Alma Mater Studiorum – Università di Bologna

DOTTORATO DI RICERCA IN

SCIENZE DELLA TERRA DELLA VITA E DELL'AMBIENTE

Ciclo XXXIII

Settore Concorsuale: 04/A2

Settore Scientifico Disciplinare: GEO/03

FRACTURE NETWORKS DEVELOPMENT, FLUID FLOW, AND DIAGENETIC PROCESSES IN SANDSTONES AND CARBONATE ROCKS

Presentata da: Leonardo Del Sole

Coordinatore Dottorato | **Supervisore**

Prof. Giulio Viola | **Prof. Marco Antonellini**

Esame finale anno 2021

ABSTRACT

Porous sandstone and carbonate rocks form important geofluid reservoirs. Interaction therein among deformation and diagenesis is critical since both processes can deteriorate or enhance reservoir quality as well as affect its texture and mechanical properties. Deformation can focus diagenetic processes and control the distribution of diagenetic products. Diagenetic processes likewise can control deformation characteristics and distribution in a sedimentary sequence. Deciphering the interaction between these processes is thus a critical prerequisite to the evaluation and prediction of the architecture and permeability structure of fault zones as well as their mechanics, to the assessment of reservoir petrophysical properties uncertainties and, ultimately, to the understanding of the structural diagenesis evolution of rock volumes.

Whilst this work concerns a common general subject and objective, its content is two-fold.

In the first part (Chapters 2 through 4), we have made a comprehensive study of the textural, (micro)structural, petrophysical, and mechanical properties of deformation bands (DBs) associated with calcite nodules in high-porosity arkosic sandstone (Loiano, Northern Apennines - Italy).

We investigate the mineralogy, texture, and microstructure of the host rock and DBs via optical and scanning electron microscopy, and digital image analysis to elucidate how sandstone mineralogy control the deformation mechanisms, cataclasis intensity, and the final band structure in arkosic sandstone. Microstructural observations on this particular mineralogy allowed us to identify different fracturing mechanisms that affect feldspar (intragranular fracturing) and quartz (spalling/flaking of edges). Cleavage-facilitated fracturing of feldspar results in (i) preferential cataclasis of feldspar with respect to quartz, and (ii) cleavage control on cataclasis, grain-shape and grain-organization within the DB. Our findings represent new insights into the deformation mechanism in arkosic sandstone.

We also aim to quantify how DBs and nodules affect the petrophysical and mechanical properties of the host rock. Porosity and permeability of the host rock and DBs are quantified via digital image analysis and the Kozeny-Carman relation. Air-permeability and uniaxial compressive strength of the host rock, DBs, and nodules are quantified through minipermeametry and the Schmidt hammer. Porosity and permeability in the DB are 1 and 3 orders of magnitude lower than in the host rock, respectively. Porosity drops by 1 order of magnitude from the host rock to the nodules. DBs and nodules degrade porosity and permeability and produce a strengthening effect of the rock volume, imparting a strong petrophysical and mechanical heterogeneity.

We used the ground penetrating radar (GPR) to detect and characterize the network of sub-seismic scale structural and diagenetic heterogeneities (SDH; DBs and nodules). GPR surveys allowed the description of the SDH spatial organization and their geometry in the subsurface.

Different textural, petrophysical, and geomechanical properties between host rock, DBs, and nodules result in different GPR response (relative permittivity, instantaneous attributes). Such response can be thus used to characterize variations in petrophysical and mechanical properties together with the organization and geometry of SDH in the subsurface, in a way to reconstruct realistic and detailed conceptual models of outcrop analogs of faulted aquifers and reservoirs in porous sandstone.

Finally, we have focused on the impact of DBs on fluid flow and diagenesis in porous sandstones in two different case studies (Loiano, Italy; Bollène, France) by combining a variety of multiscalar mapping techniques, detailed field and microstructural observations, and stable isotope analysis. We show that DBs buffer and compartmentalize fluid flow and foster and localize diagenesis, recorded by carbonate cement nodules spatially associated with the bands. Our work shows that DBs control flow patterns within a porous sandstone reservoir and this, in turn, affects how diagenetic heterogeneities are distributed. This information is invaluable to assess the uncertainties in reservoir petrophysical properties, especially where structural and diagenetic heterogeneities are below seismic resolution.

In the second part (Chapter 5), we have made a thorough study of the distribution heterogeneity of joints concentrated in chert nodules within pelagic limestones (Northern Apennines, Italy), by means of detailed field observations, photo mapping, and 3D geomechanical modelling. The objective of this study is to explain the occurrence and paleo-stress significance of 3D joint clustering in chert nodules (inclusions) within a layered carbonate sequence. The difference in stiffness between chert and limestone is about one order of magnitude. Field observations show that fracture localization occurs mostly in chert nodules as opposed to the limestone matrix. We show with a novel 3D geomechanical modelling analysis how the inclusion (ellipsoid) axes ratio influences fracture intensity and propagation within and outside the chert nodules and how the nodules record different deformation phases under different remote stress conditions. From field observations, we recognize two joint sets in the chert nodules: joints parallel (older) and normal (younger) to the plane containing the two major axes of the nodule (bedding plane). The modelling of the 3D Eshelby solution for the stress field inside the chert nodule and in the surrounding matrix is consistent with our field observations and it suggests a strong differential stress during deformation ($\sigma^r_{min}/\sigma^r_{max} < 0.3$). Chert nodules in a deformed carbonate sequence, therefore, can provide important clues on the paleo-stress conditions, the temporal sequence of events, and fracture distribution heterogeneity.

Keywords: *Structural geology, Porous sandstone, Deformation band, Carbonate rock, Joint, Structural diagenesis, Petrophysics, Geomechanics, Calcite cement, Chert nodule, Reservoir analog, Structural and diagenetic heterogeneities, Northern Apennines (Italy), Provence (France).*

ACKNOWLEDGEMENTS

First, I would like to thank my academic advisor, Prof. Marco Antonellini, for his mentoring and encouragement during this project. This work would have not been possible without his guidance.

I also wish to thank Proff. Fabrizio Balsamo (University of Parma), Roger Soliva and Gregory Ballas (University of Montpellier), Giulio Viola and Dr. Antonino Calafato (University of Bologna) for the discussions, support, and time they dedicated to me during the development of this project.

Moreover, I would like to thank Prof. Francesco Salvini (University of Roma Tre) for his mentorship which was essential for my professional growth.

I also wish to express my sincere appreciation to Dr. Peter Eichhubl (Bureau of Economic Geology, The University of Texas at Austin) and Prof. Emanuele Tondi (University of Camerino) for kindly accepting to review this thesis.

I will always remember with joy the period of studies thanks to friends and fellow graduate students with whom I shared memorable moments of fun and hard work. In particular, I would like to mention Angelo, Carlotta, Elena, Fausto, Giulia, Henri, Lorenzo, Matteo D., Matteo M., Miriana, Riccardo, and Stefano.

A special mention goes to my parents for having supported me throughout my studies and always showing appreciation for what I do. I dedicate this thesis to them and to the memory of my beloved grandpa Antonio.

Finally, I thank Amanda for being such an irreplaceable friend, a wonderful partner, and an exceptional colleague. *Tles*!

PREFACE

The research presented in this dissertation was carried out within the framework of a three-year PhD scholarship funded by the Alma Mater Studiorum - Università di Bologna. The general aim of the project has been to address issues related to the interaction between fracture and fault network development and their characteristics, fluid flow, and diagenetic processes, mainly in porous sandstones and secondarily in carbonate rocks.

This is a short explanation of the outline of the current dissertation, which is structured as a collection of papers (see *List of publications*). The thesis starts with an Introduction (Chapter 1) to provide the rationale of the research, an overview of the relevant literature, the scientific justifications of the research, and detailed research goals. The bulk of this thesis consists of four scientific papers (Chapters 2, 3, 4 and 5) published in relevant peer-reviewed international journals. As they are meant as stand-alone contributions on related topics, there is some overlap among the different papers. The research work represents my own work and my research contribution for each paper compiled in this thesis is stated in the *declaration form* below. My advisor Marco Antonellini has provided important guidance and focus during the development of this project. In the following I detail the main contents of each paper as well as the contributions that I benefited from.

Paper I (Chapter 2) presents detailed textural and microstructural investigation of deformation bands in arkosic sandstone to evaluate the impact of sandstone mineralogy on microstructure, deformation mechanisms, and cataclasis intensity within the band. It includes also the quantification of porosity, pore-size, and Kozeny-Carman permeability in the host rock and deformation bands to assess the impact of deformation (cataclasis and compaction) and cement precipitation (calcite nodule) on the petrophysical properties of the host sandstone. The result of this study was also presented at the SGI-SIMP Congress, Catania, Italy, 12-14 September 2018, and at the EGU General Assembly, Vienna, Austria, 17-22 April 2019. Marco Antonellini has suggested the area where to perform this work, contributed to the permeability modeling, and provided careful editing of the manuscript and ideas for its improvements.

Paper II (Chapter 3) combines ground-penetrating radar (GPR) surveys with *in situ* petrophysical (air-permeability) and geomechanical (uniaxial compressive strength) measurements (i) to detect and characterize the subsurface architecture of a network of deformation bands and structurally-related calcite nodules in porous sandstones; (ii) to quantify the hydromechanical properties of deformation bands and nodules as well as their heterogeneity; (iii) to define a qualitative relationship between the GPR-response and the textural, petrophysical, and geomechanical properties of the different studied features. This work shows that integrating GPR and outcrop-based data might significantly improve the structural and hydromechanical characterization of "structural and diagenetic heterogeneities" in outcrop analogs of faulted aquifers/reservoirs in porous sandstone, especially where these features are below seismic resolution. The result of this study was also presented at the EGU General Assembly, Online, 4–8 May 2020. Marco Antonellini has suggested the use of the GPR methodology and provided careful editing of the manuscript. Antonino Calafato has contributed to the processing of GPR profiles. They have both partially assisted to the fieldwork.

Paper III (Chapter 4) integrates a variety of multiscalar mapping techniques, detailed field and microstructural observations, and stable isotope analysis to elucidate the structural control exerted by deformation bands on fluid flow pattern and diagenesis recorded by calcite cement nodules spatially associated with the bands. Marco Antonellini has provided me useful suggestions for the improvement of the manuscript. The coauthors have partially contributed to the fieldwork, participated in discussing the results and provided careful editing of the manuscript.

Paper IV (Chapter 5) combines field data together with the 3-D Eshelby solution for the strains and stresses within chert nodules (inclusion) and around its carbonate matrix to provide important clues on the paleo-stress conditions, the temporal sequence of events and the distribution heterogeneity of joints (opening mode I fractures) in a deformed layered pelagic limestone sequence. The initiative for this research was taken by my supervisor Marco Antonellini. My contributions include field work, analysis and representation of the structural data, discussions, manuscript writing and revision, and figures preparations and editing.

Following the papers, the Conclusion (Chapter 6) features the main results and conclusions of the research, such as its implications, and possible future research directions. Then, the Appendices (A through D) include the *supplementary materials* related to each chapter (2 through 5). It contains supplementary data, methods, instrumentation, etc., which are useful to support the discussion in the main text, but which content does not go beyond the contents of the Chapters. All references cited in the text are listed in the Bibliography.

List of Publications

The following articles report the results of this work according to the aim and objectives of the PhD project:

Paper I **Del Sole, L.**, Antonellini, M., 2019. Microstructural, petrophysical, and mechanical properties of compactive shear bands associated to calcite cement concretions in arkose sandstone. Journal of Structural Geology, 126, 51-68.

Paper II **Del Sole, L.**, Antonellini, M., Calafato, N., 2020. Characterization of sub-seismic resolution structural diagenetic heterogeneities in porous sandstones: Combining Ground-Penetrating Radar profiles with geomechanical and petrophysical in situ measurements (Northern Apennines, Italy). Marine and Petroleum Geology, 117, 104375.

Paper III **Del Sole, L.**, Antonellini, M., Soliva, R., Ballas, G., Balsamo, F., Viola, G., 2020. Structural control on fluid flow and shallow diagenesis: insights from calcite cementation along deformation bands in porous sandstones. Solid Earth, 11(6), 2169-2195.

Paper IV Antonellini, M., **Del Sole, L.**, Mollema, P. N., 2020. Chert nodules in pelagic limestones as paleo-stress indicators: A 3D geomechanical analysis. Journal of Structural Geology, 132, 103979.

AUTHOR CONTRIBUTION

Co-author declaration

This declaration states the independent research contribution of the PhD candidate for each paper compiled in the thesis.

<table>
<tr><th>Paper No.</th><th colspan="3">Title and full bibliographic reference</th></tr>
<tr><td>Paper I</td><td colspan="3">Del Sole, L., Antonellini, M., 2019. Microstructural, petrophysical, and mechanical properties of compactive shear bands associated to calcite cement concretions in arkose sandstone. Journal of Structural Geology, 126, 51-68, https://doi.org/10.1016/j.jsg.2019.05.007.</td></tr>
<tr><td>Role of PhD candidate</td><td>Type of contribution</td><td>Overall contribution (%)</td><td>Signature of PhD candidate and tutor</td></tr>
<tr><td>First author,
Corresponding author.</td><td>Conceptualization, methodology, investigation, fieldwork, lab work, data curation, formal analysis, validation, visualization, writing – original draft, writing – editing and review.</td><td>>75%</td><td></td></tr>
</table>

<table>
<tr><th>Paper No.</th><th colspan="3">Title and full bibliographic reference</th></tr>
<tr><td>Paper II</td><td colspan="3">Del Sole, L., Antonellini, M., Calafato, N., 2020. Characterization of sub-seismic resolution structural diagenetic heterogeneities in porous sandstones: Combining Ground-Penetrating Radar profiles with geomechanical and petrophysical in situ measurements (Northern Apennines, Italy). Marine and Petroleum Geology, 117, 104375, https://doi.org/10.1016/j.marpetgeo.2020.104375.</td></tr>
<tr><td>Role of PhD candidate</td><td>Type of contribution</td><td>Overall contribution (%)</td><td>Signature of PhD candidate and tutor</td></tr>
<tr><td>First author,
Corresponding author.</td><td>Conceptualization, methodology, investigation, fieldwork, data curation, formal analysis, validation, visualization, writing – original draft, writing – editing and review.</td><td>>75%</td><td></td></tr>
</table>

Paper No.	Title and full bibliographic reference		
Paper III	**Del Sole, L.**, Antonellini, M., Soliva, R., Ballas, G., Balsamo, F., Viola, G., 2020. Structural control on fluid flow and shallow diagenesis: insights from calcite cementation along deformation bands in porous sandstones. *Solid Earth, 11(6), 2169-2195*, https://doi.org/10.5194/se-11-2169-2020.		
Role of PhD candidate	**Type of contribution**	**Overall contribution (%)**	**Signature of PhD candidate and tutor**
First author, Corresponding author.	Conceptualization, methodology, investigation, fieldwork, lab work, data curation, formal analysis, validation, visualization, writing – original draft, writing – editing and review.	>75%	

Paper No.	Title and full bibliographic reference		
Paper IV	Antonellini, M., **Del Sole, L.**, Mollema, P. N., 2020. Chert nodules in pelagic limestones as paleo-stress indicators: A 3D geomechanical analysis. *Journal of Structural Geology, 132, 103979*, https://doi.org/10.1016/j.jsg.2020.103979.		
Role of PhD candidate	**Type of contribution**	**Overall contribution (%)**	**Signature of PhD candidate and tutor**
Co-author.	Methodology, investigation, fieldwork, lab work, data curation, formal analysis, validation, visualization, writing – original draft, writing – editing & review.	15-30%	

CONTENTS

1

Introduction

1.1. Rationale and Scientific background

Porous sandstones and carbonate rocks are important reservoirs for resource extraction (groundwater, hydrocarbons, geothermal energy) and waste disposal (CO_2, polluted fluids). In this kind of rocks, the interaction between deformation and diagenesis is critical since both processes can degrade (e.g. cataclasis, clay smearing, cement precipitation) or enhance (e.g. jointing, dissolution) reservoir quality as well as affect the texture and mechanical properties of the rock volume. The importance of the interaction between deformation and deformational structures, fluid flow, and diagenetic processes has been emphasized only during the last two decades (e.g. structural diagenesis; Laubach et al., 2010). It has been shown that host rock properties and diagenetic processes may control fractures (*sensu lato*) characteristics and distribution (e.g. Cartwright, 2011; Laubach et., al., 2014; Lavenu et al., 2014, Korneva et al., 2017; Antonellini et al., 2020; Callahan et al., 2020; La Bruna et al., 2020), and that deformation may focus diagenetic processes and control the distribution of diagenetic products (e.g. Mozley and Goodwin, 1995; Garden et al., 2001; Eichhubl et al., 2009; Caine and Minor, 2009; Balsamo et al., 2012; Antonellini et al., 2017; Dimmen et al., 2017). If deformation influences diagenesis and vice versa, eventually, a feedback can develop between these processes (Fig. 1.1). In this perspective, a cross disciplinary approach between structural geology and diagenesis is needed to obtain a reliable reconstruction of structural and diagenetic evolution of rock volumes (Laubach et al., 2010), as well as to evaluate the permeability structure and mechanics of fault zones, to predict their fluid flow and seismogenic behavior (e.g. Faulkner et al., 2010), and to assess the uncertainties of deformed reservoir petrophysical properties.

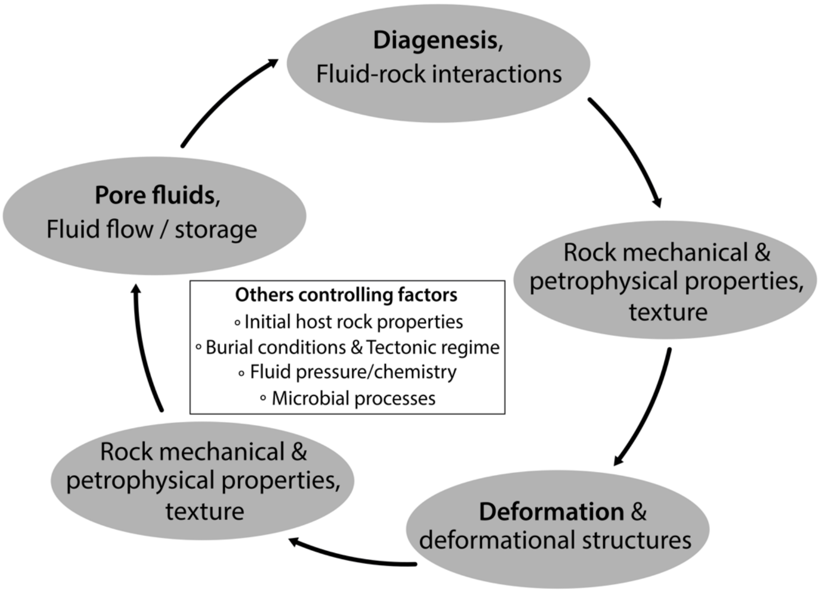

Figure 1.1. Conceptual flow diagram showing the interactions among the three main topics of deformation, fluid flow, and diagenetic processes in the shallow-crust realm. For instance, diagenetic processes (e.g. cement precipitation in porous sandstones) change the texture and the petrophysical (e.g. porosity) and mechanical properties (e.g. elastic stiffness, brittleness) of the pristine rock, affecting the subsequent deformation, i.e. type and distribution. Accordingly, new deformation structures (e.g. open-fractures, faults) and resulting fault-rocks, may affect the fluid chemistry, ease, disturb, or prevent fluids circulation, and localize further diagenetic processes and products. The latter will change the rock properties again, affecting subsequent deformation and so on. For a comprehensive review of the controls on sandstone and carbonate reservoir quality, the reader is referred to Worden et al. (2018). For a comprehensive review concerning the inter-relationships among structures, mechanics, and fluid flow the reader is referred to Faulkner et al. (2010).

Porous sandstones, deformation bands, and calcite nodules

Porous granular rocks often contain subseismic strain localization features referred to as deformation bands (Aydin, 1978; DBs from now on). They are small "fault-like" mm-thick tabular-planar structures that develop during failure at relatively shallow depths (0–4 km; e.g. Cashman and Cashman, 2000; Fossen et al., 2007). DBs are well-known in quartz-rich sand(stone)s (Aydin and Johnson, 1978; Antonellini et al., 1994a; Shipton and Cowie, 2001; Aydin et al., 2006; Fossen et al., 2007) but they have also been documented in porous carbonates (Tondi et al., 2006, 2012; Antonellini et al., 2014a, b; Rotevatn et al., 2016, 2017) and volcanoclastic rocks (Wilson et al., 2003; Cavailhes and Rotevatn, 2018). In contrast, only a limited number of studies investigated DBs in feldspar-rich sandstones so far (Rawling and Goodwin, 2003; Exner and Tschegg, 2012; Lommatzsch et al., 2015). Nevertheless, there are many feldspar-rich reservoir sandstones all over the world, which are strongly influenced by deformation and diagenesis (Gaupp et al., 1993; Chuhan et al., 2000; Gier et al., 2008).

Different types of DBs are recognized and classified kinematically as compaction, shear, and dilation band or as a function of the relative amount of shear to compaction/dilation (Du Bernard et al., 2002; Aydin et al., 2006; Eichhubl et al., 2010); or in terms of the dominant deformation mechanisms operating during their formation (particulate flow, grain fracturing and crushing, smearing, pressure-solution/precipitation; Fossen et al., 2007). Different kinematics and deformation mechanisms produce bands with different types of internal structure, hence different hydrologic and mechanical properties. Several factors, including the stress state, proximity to faults, intrinsic host rock properties, and the degree of lithification influence the spectrum of kinematics and deformation mechanisms of DBs (Antonellini et al., 1994a; Wong et al., 1997; Flodin et al., 2003; Rawling and Goodwin, 2003; Johansen et al. 2005; Fossen et al., 2007; Rotevatn et al., 2008; Eichhubl et al., 2010; Solum et al., 2010; Balsamo and Storti, 2011; Soliva et al., 2013). However, the influence of grain mineralogy and grain properties in controlling the deformation mechanisms and cataclasis intensity, as well as the resultant microstructure of the band is much less documented and constrained so far (Rawling and Goodwin, 2003; Exner and Tschegg, 2012; Cavailhes and Rotevatn, 2018).

Petrophysical properties may change significantly during shear and/or volumetric deformation in porous sandstones and they are efficient indicators to predict the fluid flow behavior of fault zones (Antonellini and Aydin, 1994; Bense et al., 2013). The effects of DBs on fluid flow can vary widely depending on their permeability contrast relative to the host rock, thickness, density, distribution, orientation, segmentation, and connectivity (Antonellini and Aydin, 1994; Manzocchi et al., 1998; Fossen and Bale, 2007; Rotevatn et al., 2013; Ballas et al., 2014; Soliva et al., 2016). In most cases DBs are associated with porosity and permeability reduction relative to the host rock (Antonellini and Aydin, 1994; Fisher and Knipe, 2001; Ballas et al., 2015). Dilation bands, instead, display an enhancement of porosity and permeability (Antonellini et al., 1994; Du Bernard et al., 2002).

Although DBs have been extensively studied, their practical influence on fluid flow and reservoir performance has been (and still is?) a matter of debate for several years. Several authors demonstrated from production, flow tests, and flow-based models (Harper and Mofta, 1985; Lewis and Couples, 1993; Antonellini et al., 1999, 2014a; Sternlof et al. 2004; Medici et al., 2019; Romano et al., 2020) that DBs introduce a permeability anisotropy, compartmentalize reservoirs, and cause poor well performance. Other authors concluded from theoretical and physical modelling and flow simulations that DBs can have significant effect on fluid flow and production only where high permeability contrast between DBs and host rock and/or high cumulative DBs thickness exist (Matthäi et al., 1998; Walsh et al., 1998; Fossen and Bale, 2007; Rotevatn et al., 2009; Torabi et al., 2013).

Furthermore, it has been shown, from theoretical modelling and laboratory measurements, that DBs networks affect mechanical properties of granular materials during and after their development (Aydin and Johnson, 1978; Underhill and Woodcock, 1987; Main et al., 2001; Kaproth et al., 2010). However, only a few attempts have been made to quantify the effect of DBs on the mechanical properties (i.e. Young’s modulus, uniaxial compressive strength) of the host material so far

(Alikarami et al., 2013; Pontes et al., 2019), even though they are essential input parameters during reservoir simulation and geomechanical modeling (e.g. Zoback, 2010).

Pore-filling calcite cement is a common diagenetic feature in porous siliciclastic reservoirs, and it leads to porosity loss, reduction in permeability, and, in turn, overall reservoir quality deterioration (Ehrenberg, 1990; Morad et al., 2010). Carbonate cement is commonly concentrated within a few specific horizons or nodules with various shapes and arrangements (e.g. Bjørkum and Walderhaug, 1990; McBride, 1996), making porosity and permeability prediction more challenging (e.g. Dutton et al., 2002; Davis et al., 2006; Lee et al., 2007).

The interplay between deformation localization and diagenesis create "structural and diagenetic heterogeneities" in which the effects of cement add up to those caused by deformation and they may (i) increase sealing capacity of faults and compromise reservoir integrity (Knipe, 1993; Caine and Minor, 2009; Eichhubl et al., 2009; Faulkner et al., 2010; Pei et al., 2015); (ii) change the mechanical properties of the host rock (e.g. Dvorkin et al., 1991), influencing fault-zone architecture and its deformative response during subsequent deformation (Flodin et al., 2003; Johansen et al., 2005; Williams et al., 2016; Pizzati et al., 2020). However, the effect of the assemblage "DBs – cement" on the petrophysical and mechanical properties of the host rock has received little attention so far (Leveille et al., 1997; Fisher and Knipe, 1998; Ogilvie and Glover, 2001), and even less so regarding calcite cement (Alikarami et al., 2013).

Different processes account for enhanced fluid flow and for the presence of diagenetic products in DBs (Antonellini et al., 1994; Fowles and Burley, 1994; Ogilvie and Glover, 2001; Du Bernard et al., 2002; Sigda and Wilson, 2003; Parry et al., 2004; Balsamo et al., 2012). These mechanisms, however, appear to be limited to specific conditions, assuming that DBs behave as fluid conduits. Much less attention has been paid to fluid flow and diagenesis leading to (post-DB formation) calcite cementation in association with low-permeability cataclastic DBs so far. Studies of cement precipitation in these DBs are mostly limited to quartz cement (Fisher and Knipe, 1998; Milliken et al., 2005; Eichhubl et al., 2010) and experimental (Lander et al., 2009; Williams et al., 2015).

Properly characterizing the influence of DBs and related cements on fluid flow in reservoirs/aquifers is difficult mainly because our limited knowledge of sub-seismic structures in those reservoirs. DBs small offsets (from a few millimeters to 20–40 mm) make them structural heterogeneities below seismic resolution. Still too many limits prevent the optimal detection of sub-seismic faults on seismic reflection profiles, despite many progresses have been made in the field of seismic imaging to detect them (e.g. Lohr et al., 2008). Therefore, other methods need to be employed for improving the detection and characterization of sub-seismic resolution structural and diagenetic heterogeneities in porous sandstones.

Carbonate rocks, chert nodules, and fractures

Carbonate rocks form important geofluid reservoirs (hydrocarbons, water, CO2), including where fluid flow is generally influenced by opening-mode fractures. Knowledge of the paleo-stress conditions at the time of deformation is critical to assess if brittle structures (i.e. joints) are present in a carbonate sequence and to determine whether these structures played a role during diagenesis (Ferraro et al., 2019). In carbonate rocks, besides dissolution and replacement, the porosity is achieved mainly by fracturing and faulting. As the fracture networks control reservoir permeability, fracture development and distribution must be characterized for a better understanding of fluid flow.

Faults and fractures could represent fluid conduits or pose barriers to fluid circulation, depending on the permeability of the host rock relative to that of the fault zone or fracture corridors (Cooke et al., 1999; Antonellini and Mollema, 2000; Aydin, 2000; Wennberg et al., 2006; Agosta et al., 2010). The geometry of the fracture assemblages and the geometric and genetic relationships between opening mode fractures and faults that develop in carbonate rocks depend on the tectonic setting, detailed lithology, and pre-existing structures (Mollema and Antonellini, 1999; Antonellini and Mollema, 2000; Graham et al., 2003; Antonellini et al., 2008; Aydin et al., 2010; Lavenu et al., 2014; Michie et al., 2014; Korneva et al., 2017; Ferraro et al., 2019; La Bruna et al., 2020).

The association of chert nodules (stiff inclusion) and pelagic carbonate rocks (soft matrix) has been described in the literature (Alvarez et al., 1976) with special reference to the strengthening effect that the nodules have on the carbonate sedimentary sequence (Petracchini et al., 2015a, b). The role of chert nodules on the occurrence and distribution heterogeneity of fractures (joints) in a deformed layered pelagic limestone sequence, however, has never been investigated so far.

Stiff inclusions embedded in a soft matrix experience elevated stresses when the rock package is stressed (Eshelby, 1957; Jaeger and Cook, 1979; Eidelman and Reches, 1992; Davis et al., 2017). Eshelby (1957) resolved the full 3D problem for the stress and strain fields inside and outside an ellipsoidal inclusion embedded in a matrix with different mechanical properties from those of the inclusion itself. Jaeger and Cook (1979) present the elastic solution for the homogeneous stress field inside a circular 2D inclusion embedded in a softer/stiffer matrix. The solutions presented by Eshelby (1957) and Jaeger and Cook (1979) have been applied to explain fracture localization in pebbles (Eidelman and Reches, 1992), fracture concentrations within micro-granitoid enclaves in granite (Mondal and Acharyya, 2018) or within elliptical clasts embedded in chlorite schist (Acharyya and Mondal, 2019). In the studies mentioned above, paleo-stress information was deduced from an estimate of the minimum rock breakage loads and the minimum crustal depth during deformation as a function of the inclusion aspect ratio, the ratio between the remote stresses, and the fracture toughness (Lawn, 1993). The analyses presented so far, however, relied mostly on a 2D solution for circular or elliptical stiff inclusions embedded in a soft matrix without considering the third spatial dimension.

1.2. Scope of this study

This project uses a multidisciplinary approach (fieldwork, analytical methods, modeling) that involves structural geology, sedimentary petrology, fracture mechanics, and geochemistry to address issues relating to the interaction among fracture and fault networks development, fluid flow, host rock properties, and diagenetic processes in porous sandstones and carbonate rocks. Specifically, it aims to understand how deformation and deformational structures (i.e. DBs in porous sandstone) impact on the hydromechanical properties of rock volume, affect fluid flow, focus diagenetic processes and control the distribution of diagenetic products (i.e. carbonate nodules); how host rock properties (i.e. sandstone mineralogy) or diagenetic processes (i.e. chert nodules in limestone) control, respectively, faulting (i.e. DBs) and fracturing (i.e. joints) characteristics and their distribution during deformation.

To fill the technical and knowledge gaps discussed in previous subsection (*1.1*), the detailed objectives of the present study have been to:

– Advance current knowledge of the development of deformation bands (DBs) in high-porosity arkosic sandstone. We investigate the mineralogy, microstructure, and texture of the host rock and DBs via optical and scanning electron microscopy, 2D digital image analysis, manual point counting, and XRD to elucidate how sandstone mineralogy and mineral properties affect the deformation mechanisms, cataclasis intensity, and the final band microstructure in feldspar-rich sandstone (see **Paper I**).
– Enrich current knowledge of the effect of DB-related deformation, calcite cement in nodules, and the assemblage "DB – nodule" on the texture and petrophysical and mechanical properties of the host sandstone, as well as their heterogeneity/anisotropy, by means of 2D digital image analysis, Kozeny-Carman permeability, air-minipermeametry, and the Schmidt hammer (see **Papers I and II**). We also aim to discuss the impact of structural and diagenetic heterogeneities on fluid circulation and on subsequent deformation (see **Papers II, III, and IV**).
– Give new insights into the subsurface imaging and characterization of sub-seismic scale structural and diagenetic heterogeneities in outcrop analogs of faulted porous sandstone reservoirs by combining ground-penetrating radar (GPR) surveys and outcrop-derived information to (i) detect and characterize subsurface architecture of DBs and associated calcite nodules; (ii) define consistent GPR "facies" for each of the analyzed features (sandstone, DBs,

nodules); and (iii) qualitatively relate the GPR-response of each analyzed feature to their textural, petrophysical and mechanical properties previously quantified *in situ* (see **Paper II**).

- Advance current understanding of the control exerted by low-permeability cataclastic DBs on flow pattern and diagenetic heterogeneities (calcite nodules) origin and distribution in porous sandstones by combining a variety of multiscalar mapping techniques (string mapping, UAV photography), detailed field and microstructural (optical, scanning electron and cathodoluminescence microscopy) observations, and stable isotope ($\delta^{13}C$ and $\delta^{18}O$) analysis (see **Paper III**).
- Give new insights into the occurrence, distribution, and paleo-stress significance of 3D joint clustering in chert nodules (inclusions) within a deformed layered pelagic limestone sequence. Specifically, we aim to determine how the 3D inclusion shape and applied remote stress control fracture development within and around the chert nodules, by combining detailed field observations with the 3D Eshelby solution for the strains and stresses within chert nodules and around its (soft) carbonate matrix (see **Paper IV**).

2

Microstructural and petrophysical properties of deformation bands associated to calcite cement nodules in arkose sandstone

The content of this Chapter has been published in **Del Sole, L.**, Antonellini, M., 2019. Microstructural, petrophysical, and mechanical properties of compactive shear bands associated to calcite cement concretions in arkose sandstone. Journal of Structural Geology, 126, 51-68.

ABSTRACT

Diagenetic concretions are common in sandstones, but little is known about a possible structural control on such features, and even less so in arkose. We studied compactive shear bands (CSB) with cataclasis in high-porosity arkose associated with spatially heterogeneous carbonate cementation. We investigated the mineralogy, microstructures, grain-size and grain-shape, porosity and pore-size, for both host rock and CSBs. We documented the relationship between CSBs and concretions and quantified the effect of both deformation and cementation on petrophysical and mechanical properties of the assemblage bands-nodule with respect to the pristine rock. Microstructural observations on this particular mineralogy allowed us to identify different fracturing mechanism that affect feldspar (intragranular fracturing) and quartz (spalling/flaking of edges). Cleavage-facilitated fracturing of feldspar results in *i)* preferential cataclasis of feldspar with respect to quartz, and *ii)* cleavage control on cataclasis, grain-shape and grain-organization within the CSB. The spatial association between concretions and CSBs suggests that CSBs played a role in cement precipitation. The combined effect of deformation and cementation on mechanical properties is reflected on the rock-strength measurements that show a rock strengthening in the assemblage bands-nodule. Our findings represent new insights into the deformation mechanism in arkose, the relationship between structures and diagenesis as well as their effect on petrophysical and geomechanical characteristics.

2.1. INTRODUCTION

Porous sandstones are important reservoirs for geofluids. In this kind of granular materials, the interplay between deformation localization and cementation during diagenesis is critical since both processes can strongly reduce rock porosity and permeability (Antonellini and Aydin, 1994; Fowles and Burley, 1994; Knipe et al. 1997; Gibson, 1998; Lothe 2002) thus baffling the fluid flow. It is crucial, therefore, to understand the interaction of structures and diagenesis (Laubach et al., 2010). Deformation bands are well-known strain localization structures in quartz-rich porous sandstones (Aydin, 1978; Antonellini et al., 1994a; Shipton and Cowie, 2001; Aydin et al., 2006; Fossen et al., 2007; Eichhubl et al., 2010) but they have also been documented in carbonate rocks and porous and granular rock types (Tondi et al., 2006; Antonellini et al., 2014b; Cavailhes and Rotevatn, 2018). In contrast, only a limited number of studies presented microstructural investigations on cataclastic deformation in porous feldspar-rich sand(stone)s so far (Rawling and Goodwing, 2003; Exner and Tschegg, 2012; Lommatzsch et al., 2015).

Different types of deformation bands are recognized and classified in terms of kinematics or the dominant deformation mechanisms (see Aydin et al., 2006; and Fossen et al., 2007 for reviews). The deformation mechanisms depend on mineralogy, grain properties, porosity, cementation and stress state. Tectonic regime controls deformation bands distribution and their clustering (e.g. Soliva et al., 2016). In this work, we focus on compactive shear bands (CSB from now on) with cataclasis (as defined by Aydin et al., 2006) in high-porosity arkose sandstones. CSBs are analogous to the compactional shear bands (kinematic classification), and to the cataclastic bands (deformation mechanism classification) as defined by Fossen et al. (2007). CSBs represent one of the principal deformation features of fault zones in porous sandstones (Aydin, 1978; Antonellini et al., 1994; Aydin et al., 2006; Fossen et al., 2007; Soliva et al., 2013). When CSBs occur in a cluster, they form a zone of compactive shear bands (ZB from now on). In CSBs with cataclasis, the grain crushing is the main microstructural deformation mechanism. CSBs with cataclasis are characterized by reduction of grain size and porosity via grain crushing, compaction, and rearrangement of grains by rotation and boundary sliding (e.g. Menendez et al., 1996). The permeability decrease within the bands is a function of cataclasis intensity (e.g. Ballas et al., 2015). In turn, the degree of cataclasis is determined by different factors, such as the confining pressure occurring during deformation, tectonic regime, and host rock (HR from now on) properties such as porosity, grain size and sorting (e.g. Antonellini et al., 1994a; Rotevatn et al., 2008; Ballas et al., 2015). However, the influence of grain mineralogy and grain properties (cleavage, strength) in controlling the deformation mechanisms and cataclasis intensity in the bands is much less documented and constrained (Rawling and Goodwing, 2003; Exner and Tschegg, 2012; Lommatzsch et al., 2015; Cavailhes and Rotevatn, 2018), and even less in arkosic sandstone. In general, CSBs are associated with a strong porosity and permeability reduction relative to HR (Antonellini and Aydin, 1994; Torabi et al., 2013; Ballas et al., 2015), so that they act as baffle/barrier to fluid flow. Despite this, some studies presented evidence of preferential water retention and enhanced fluid flow within the deformation bands in vadose zones (Sigda and Wilson, 2003; Cavailhes et al., 2009; Wilson et al., 2006; Balsamo et al., 2012), due to their high capillary pressure. In such conditions, deformation bands may act as pathways for preferential fluid flow. Fluid-flow-related diagenetic/reactive processes, such as dissolution and precipitation, are not often reported associated with CSBs in siliciclastic rocks, whereas they are important during compaction and shear localization in carbonate rocks (e.g. Tondi et al., 2006; Rotevatn et al., 2016).

In sandstone reservoirs, pore-filling calcite cement is a common diagenetic feature and may occur pervasively throughout the rock sequence or concentrated in some horizons as concretions with various shapes and arrangement (e.g. McBride, 1996). In these cemented structures, the porosity is almost entirely obliterated by cement whereas the surrounding HR is usually poorly cemented. Numerous articles were published on carbonate concretions (Berner, 1968; Bjørkum and Walderhaug, 1990; Wilkinson and Dampier, 1990; Cibin et al., 1993; McBride et al., 1995, 2003; Milliken et al., 1998; Morad et al., 2000; Mozley and Davis, 2005) but only a few of them, and mostly in recent times, focused on the possible link between deformation structures and concretions (e.g. Mozley and Goodwin 1995; Garden et al., 2001; Eichhubl et al., 2004, 2009; Balsamo et al., 2012; Dimmen et al., 2017). Coalescence of concretions along a plane, may form extensive cement tabular structures that, if located within geofluids reservoirs, may promote compartmentalization (e.g. Lee et al., 2007) and they may degrade fluid flow properties at a variety of scales (e.g. Caine and Minor, 2009; Eichhubl et al., 2009). From this perspective, we think that it is important to consider the possibility of concretions to form in association with CSBs within siliciclastic rocks and understand their spatial organization, extension, continuity, density, their hydraulic role in terms of fluid flow circulation as well as their mechanical influence on the HR. This will be useful during geofluids exploration, reservoir simulation modeling, and geomechanical evaluation of a drilling site.

The terms nodules and concretions are used almost interchangeably in the literature (e.g. Tucker, 2003). In some cases, these terms are used to differentiate cemented bodies by their geometry (e.g. Nichols, 2009). They are structures created by local mineral precipitation. In our case the cementing medium (calcite) precipitated enclosing grains of the host sediment (i.e. poikilitic growth). For the purpose of this work, it was not necessary to differentiate these diagenetic structures based on their shape, so that the terms *nodules* and *concretions* will be used as synonyms.

Petrophysical (e.g. porosity, permeability, and capillary entry pressure) and mechanical (e.g. rock strength) properties may change significantly during volumetric deformation in porous sandstones.

Such granular rocks have grains that may move exploiting the pore space and are subjected to stress concentration at contact points, which causes grain fracturing and cataclasis. The influence of deformation bands during reservoir production could be minor depending on the permeability contrast and/or band frequency (Fossen and Bale, 2007; Rotevatn et al., 2013), but diagenetic effects linked to the deformation may cause production complications (Edwards et al., 1993; Leveille et al., 1997). These diagenetic effects change the bulk petrophysical and mechanical properties of the HR to an extent that is larger than that of the CSBs alone. In our field case, CSBs and concretions are spatially related, and whether or not the deformation preceded fluid circulation and diagenesis, such spatial association suggests an area of interaction between structures and diagenesis (Laubach et al. 2010). In the event that deformation preceded the fluid circulation and the cementation, this association could be used for investigating: (i) the role of CSBs in affecting HR petrophysical properties and in controlling the distribution of diagenetic products; (ii) the hydraulic behavior of CSBs; (iii) the effect of such later diagenetic structures plus the bands on the petrophysical and mechanical properties of the HR.

In this paper, we (i) investigate the mineralogy, microstructures, grain -size and -shape, for both HR and CSBs, in order to elucidate how sandstone mineralogy and mineral properties (e.g. crystal habit, cleavage, strength) can affect the microstructure, the deformation mechanisms and cataclasis (as reflected by grain shape, grain orientation, and grain size distribution), within CSBs in arkose sandstones; (ii) we quantify porosity, pore-size, and Kozeny-Carman permeability, in both HR and CSBs, to assess the impact of CSB-related deformation mechanisms (cataclasis and compaction) on the petrophysical properties of the HR; lastly, we (iii) examine the spatial relationships between CSBs and metric/decametric-scale calcite-cement concretions, and quantify the effects of both deformation and cementation on petrophysical and mechanical properties of the assemblage bands-nodule with respect to the HR. Following the points *(ii)* and *(iii),* we argue about which mechanism could have promoted the cement precipitation, and where and why these mechanisms may have occurred.

2.2. STUDY AREA

The outcrop of our study area is in the Emilian Apennines, that is part of the Northern Apennines fold-and-thrust belt, which developed since the Late Cretaceous as a result of the collision between the Adria microplate and the European plate (e.g. Cibin et al., 2001). In particular, we focused on the Loiano Sandstones that are proximal turbidite deposits of poorly consolidated, immature, and high porosity sandstones. The Loiano Sandstones outcrop between the *Secchia* Valley in the west and the locality of *Loiano* in the east (Fig. 2.1a). The Loiano Sandstones is a lenticular sandstone and conglomerate body (dark green in Fig. 2.1a) interpreted as the subaqueous part of a gravity-dominated delta-fan (Papani, 1998) synchronous with the middle Eocene Apennines orogenic collision. The Loiano Sandstones thickness is between 300 and 1000 meters. The terrigenous sand and gravel supply for the Loiano Sandstones came from the recycling of the deformed Ligurian flysch units, that at the time of Loiano Sandstones deposition was subaerial (Cibin et al., 2001). Referring to the work of Antonellini and Mollema (2002), who described different outcrops within the Loiano Sandstones, this study was performed in the *Fondovalle Savena* sector, at 44°17’40” N latitude and 11°17’26” E longitude (Fig. 2.1a-b). The Loiano Sandstones are part of the *Montepiano Formation*, which, is part of the Epiligurian *Montepiano-Loiano-Ranzano* (MLR) Sequence. The MLR was deposited on the Northern Apennines accretion prism (Cibin et al., 2001) within episutural basins that are in stratigraphic discordance with the deformed Ligurian units below. The timing of MLR deposition spans from the Middle Eocene to the Upper Oligocene and the Loiano Sandstones are included between the Late Lutetian and the Bartonian time. The sedimentation in the Epiligurian basins occurred in a back position with respect to the front of deformation (*piggy-back* basins). These basins were passively transported towards the NE from the late Oligocene to the present. This peculiar structural position allowed for continuous sedimentation and with no significant rotation of depositional axes from the Upper Eocene to the Miocene. The Epiligurian sediments were mildly affected by multiple tectonic episodes (Cibin et al., 2001 and references therein). The Epiligurian basins are small in size (a few tens of km in width and length; Fig. 2.1a) and rather discontinuous. Estimated burial depths (in meters) referred to the top of the Loiano Sandstones are: 800-1000 (Cibin, 1993), 700-1200 (McBride et al., 1995), and 1250-1600 (Milliken et al., 1998). Cibin (1993), however, claims that on the basis of the stratigraphic section and analysis of the fluid inclusions, the maximum burial depth of the Loiano Sandstones is 3 km. This would constrain the diagenetic processes in the Loiano Sandstones to those of low-depth diagenesis such as compaction and cementation (Cibin et al., 1993).

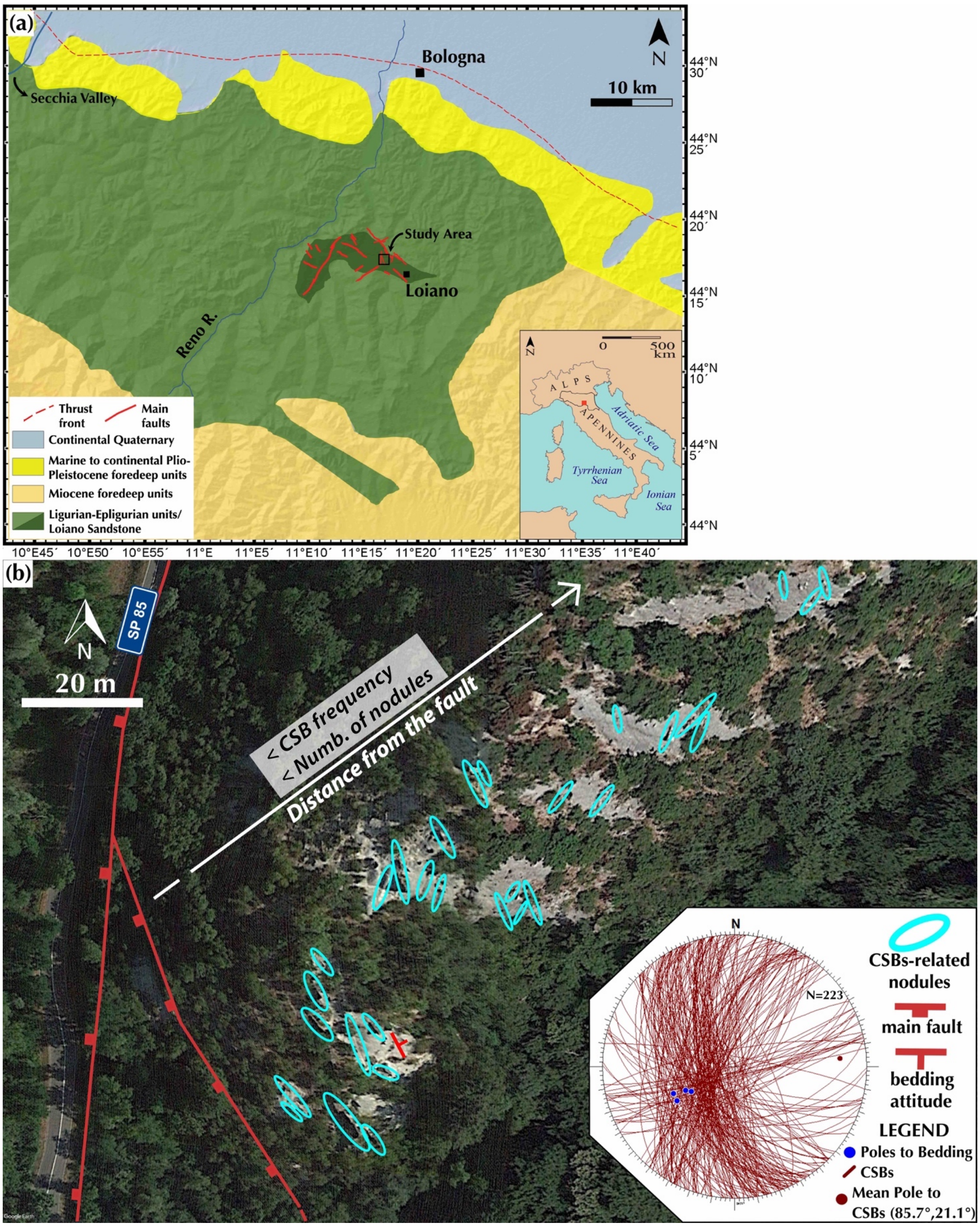

Fig. 2.1 – (a) Geological sketch map with location of the field site and of the Loiano Sandstones (dark green) in the Northern Apennines. The red dashed line is the thrust front in the subsurface, red lines are the main faults in the studied sector. The red square in the inset shows the position of the study area in the Italian peninsula. **(b)** – Aerial photograph of the outcrop. Its position is indicated by the black square in (**a**). Some of the CSBs-related concretions (light blue ellipsoid) are also reported. The qualitative density trend of CSBs and nodules with respect to the normal main fault is indicated by the white arrow. The lower-hemisphere equal-area projection of CSB's planes and poles to bedding is shown in the bottom-right inset.

2.3. MATERIALS AND METHODS

2.3.1. Outcrop characterization

We measured the orientation of the structures in the field to evaluate the structural framework of the Loiano Sandstones. Deformation bands orientation was measured using a Brunton™ geological compass. The deformation bands traces were mapped onto outcrop photographs to document their geometry and the relationships among various deformation band sets. Stereographic projection (Fig. 2.1b) and azimuthal analysis (Fig. 2.2b) of structural data were made using the *Daisy3* software (Salvini, 2004). Oriented samples were collected from cemented HR (here referred as nodule or concretion; e.g. Figs. 2.2a and 2.3c-f) with and without CSB's and they were used for thin sections preparation and XRD analyses.

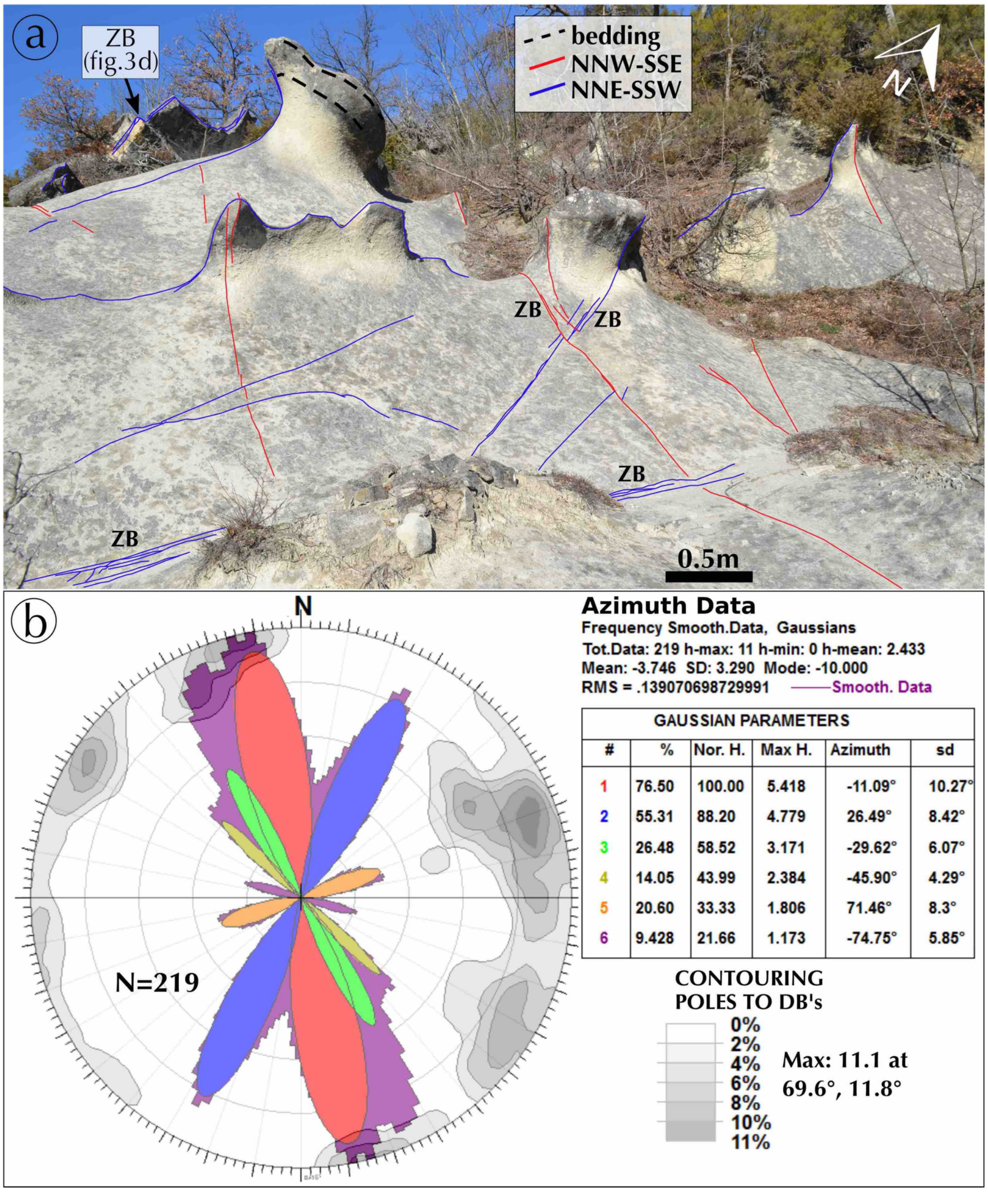

Fig. 2.2 – (a) Overview photograph of the outcrop showing concretions and their association with CSBs and ZB (colored lines). The different colors of the lines represent the two main sets of CSBs in the outcrop: NNW-SSE (red) and NNE-SSW (blue). An example of bedding-parallel concretion is also shown in the upper part of the photograph where bedding is indicated by black dashed lines. **(b)** – CSB's azimuth frequency rose diagram for measured outcrop data, with Gaussian Parameters table: normalized height (Nor. H) and Max height (Max. H) of the Gaussian curves calculated from the frequency distribution histograms, the azimuth given in ±90°, and standard deviation (sd) for each CSB set population. The frequency of each set is ranked (1-6) by color. In transparency the contouring of poles to CSBs.

2.3.2. Geomechanical analysis

The aim of our work with the Schmidt hammer is to understand the variations of rock uniaxial compressive strength (UCS) across the CSBs and concretions with respect to the HR, since both CSBs and cement can affect rock mechanical properties (e.g. compressive strength, Young's modulus, etc.). Rebound values were obtained using an L-type Schmidt hammer made by DRC® (Menditto et al., 2013) with an impact energy of 0.735 N×m. We measured rebounding indexes along a transect (Fig. 2.13a-b) that intercepts different domains: the poorly consolidated Loiano Sandstones (HR), the concretions with and without CSBs, and ZBs. We also measured rebound indexes in each one of these domains (poorly consolidated Loiano Sandstones [HR], the concretions with and without CSBs, and ZB) separately at different locations (Fig. 2.13c), to obtain reference values for comparison with the values measured along the transect. Boxplots of single feature measurements (Fig. 2.13c) were made with the R software (R Core Team, 2018). At least five Schmidt hammer measurements were done on each location, using a square grid with a cell size of 0.04 m to avoid repeating the measurements exactly on the same spot. The data point reported in the plot (Fig. 2.13a) is the average value calculated from the five measurements.

The rebound index I read on the Geohammer is correlated with the UCS (in MPa) by the following formula (Menditto et al., 2013):

$$UCS = a \times I^b \tag{2.1}$$

where a and b are two constants values obtained experimentally that depend on the angle between the hammer axis and the sample surface. We used different empirical curves, provided by the manufacturer, to obtain UCS values from measurements with different rebound angles (see Menditto et al., 2013 for instruments technical specifications). Normally, during in-situ measurements with the Schmidt hummer, fracture discontinuities (*sensu lato*) are avoided, because they could affect the mechanical response of the rock. Deformation bands, however, are not discontinuities in the rock as they are not associated with a parting surface.

2.3.3. Microstructural analysis

Combining optical and electron microscopy analysis with 2-D digital image processing on polished thin sections, we identified various mineral phases and quantified the following properties: the fraction of each mineral phase, porosity, grain and pore size (area, Feret's diameter: the longest distance between any two points along the selection boundary, i.e. particle major axis), the principal grain shape parameters (roundness, circularity, aspect ratio), and grain angle with respect to a chosen reference system in the CSBs and in the HR samples of Loiano Sandstones. Manual point counting was performed with a Zeiss™ microscope on 300 spots using an electro-mechanical microscope slide stepper (produced by J. SWIFT) coupled with an electronic counter (see A.1 in Appendix A). The grain size distributions in the HR, as well as the length of the 2-D grains longer axis, were measured with the graduated cross-line of the eyepiece and then converted in millimeters. Point counting results were used to compare rock composition and grain size distribution with those obtained from SEM image analysis. Scanning electron microscopy (SEM) images were obtained using a JEOL JSM-5400 microscope using backscattered electrons (BSE). The observations and descriptions of the CSB's microstructure were done on BSE images. Digital image analysis, to investigate the particles properties, was performed on 8-bit secondary electrons (SE)-SEM images after application of a threshold. Segmentation of the final SE image into grain and void pixels was done using the threshold optimization method of ImageJ (e.g. Antonellini et al., 1994b; Ferreira and Rasband, 2012). The surface area of each high resolution (3000 dpi) image is about 10.26 mm^2. At the working distance used, the images were acquired with a pixel resolution or minimum detectable dimension of 8.36 μm. Compositional maps were obtained using an Energy-Dispersive X-ray Spectroscopy (EDS) (*IXRF Systems*) coupled with the SEM (see A.2 in Appendix A).

2.3.3.1. *Petrography and petrophysics*

Each mineral phase was analyzed separately by EDS distribution element mapping. The fraction of each mineral phase was calculated as the ratio of the number of pixels belonging to that mineral phase over the total pixels of the map (e.g. $\%\, quartz = No. quartz\ pixels/Tot. pixels$). The quartz ($SiO_2$) fraction was calculated by the use of the silica [Si] element map. With the same approach, K-feldspar ($KAlSi_3O_8$) and Na-plagioclase ($NaAlSi_3O_8$) fractions were measured using potassium [K], aluminum [Al], and sodium [Na] maps. Our operative definition of total porosity is the sum of the skeleton porosity (pores closed by cement) and the remnant porosity (voids, i.e. present-day porosity). The HR and CSB skeleton porosities were measured by calcium [Ca] element mapping, because of the calcite cement filling the pores in the nodules. The determination of porosity was done after manual removal of any detrital carbonate clasts from the images. The remnant porosity, on the other hand, was measured using carbon [C] and chlorine [Cl] maps, with the same approach used for the quantification of mineral phases. The thin sections, in fact, were epoxy (Cl-base) impregnated and prepared with carbon, so that any possible original rock pore can be detected by these elements. The direct association between a chemical element [e.g. K] and a certain mineral phase [K-feldspar] is a reasonable assumption, because in our case the rock mineralogy turned out to be rather homogeneous, as demonstrated by microscope analysis and XRD. X-ray powder diffraction (XRD) analysis was performed in two different sectors within the same rock sample (CL1), scraping two powder samples one directly from the CSB surface and the other from the adjacent cemented HR. The objective of the XRD analysis is to evaluate the mineralogical phases and obtain a semi-quantitative modal mineralogy for both CSB and pristine HR. The measurements were made with a Philips diffractometer (40 kV, 30 mA) using Cu-K-alpha radiation.

2.3.3.2. Grain- and pore-size distributions

Grain and pore sizes were measured using the same element maps mentioned before, after application of an area/diameter conversion algorithm (Eq. 2.2). Violin plots of pore sizes distributions (Fig. 2.6e) were made with the *R* software (R Core Team, 2018) and the *ggplot2* package (Wickham, 2016). We used the surface-equivalent sphere diameter D_s, which is defined as the diameter of a sphere with the same surface as the particle surface S_p (Pabst and Gregorova, 2007) and that is expressed as:

$$D_s = \left(\frac{6}{\pi} \times S_p\right)^{1/2} \tag{2.2}$$

The total grain size distribution was measured starting from the single-mineral-phase grain size distribution and then computing the relative percentage of each mineral phase in the considered sample.

Where grain size reduction is a key feature in CSBs, the assessment of particle size distribution is fundamental for understanding the deformation micro-mechanisms and quantifying the degree of comminution. According to a number of authors (e.g. Sammis et al., 1987; Blenkinsop, 1991; Billi et al., 2003; Rawling and Goodwin, 2003), fault-rocks have self-similar (fractal) characteristics in terms of number and size of particles. For this reason, we analysed the grain size distributions, that here are presented as exceedance frequency plots (Rawling and Goodwin, 2003; Torabi et al., 2007; Torabi and Fossen, 2009; Exner and Tschegg, 2012), and computed their fractal dimension D. In order to observe a self-similar distribution, the number of elements having a linear dimension greater than a certain value, must have an exponential dependence on that dimension (Turcotte, 1997). The degree of self-similarity may be measured with the parameter *D*,

$$N_{(>r)} = C \times r^{-D} \tag{2.3}$$

where *N* is the number of grains with an area greater than a certain value r normalized by the total number of grains, *C* is a constant, and *D* represents the power dimension of the best fit grain size distribution, which is known as the fractal number/dimension (Turcotte, 1997; Sammis et al., 1987). *D* values were estimated as the slope of the cumulative distribution linear portions in a *log (N) - log (r)* plot (Rawling and Goodwin, 2003). We selected the fractal ranges having power-law fits with

$R^2 > 0.9900$ to identify the most linear portion of each particle size distribution and its upper and lower fractal limits (Blenkinsop, 1991). As indicated by the linear best fit of data on log-log graphs (Fig. 2.11), the particle populations have a power-law size distribution. Here, *D* is given as two-dimensional; the 3-D exponent can be obtained just by adding 1 to the two-dimensional *D* (e.g. Blenkinsop, 1991).

2.3.3.3. *Grain-shape parameters*

Grain shape descriptors were evaluated to define the rock framework and the texture evolution from the HR to the CSB due to cataclasis and grain reorganization by rotation and translation during shear. Analysis of selected SE images allowed us to compute different grain shape descriptors. Roundness, defined also as the inverse of Aspect Ratio, defines the general shape of the particle (envelope). The Circularity, on the other hand, is characteristic of the periphery outline of the particle (or perimeter in 2-D). The expressions for Roundness, Circularity, and Aspect Ratio are in *section A.3* (Appendix A). These elaborations were applied both to the HR and the CSBs. The areas chosen for the elaborations have been carefully selected so as to be the most representative of the whole thin sections.

2.3.3.4. *Permeability modeling: Kozeny-Carman relation*

The Kozeny-Carman (KC) model (Kozeny, 1927; Carman, 1937) is an empirical relationship for estimating porous medium permeability (k) from its porosity (ϕ):

$$k = B \times \frac{\phi^3}{\tau^2 \times {S_s}^2} \tag{2.4}$$

where B is a geometric factor accounting for the irregularities of pore shapes, τ is the tortuosity, and S_s is the specific surface area (pore surface area divided by the sample volume). This method was validated in a number of studies (e.g. Torabi et al., 2008; Ballas et al., 2012, 2014; Rotevatn et al., 2016). We used image-computed porosity to estimate the permeability. The image-computed porosity was obtained from 2-D thin sections images using the techniques explained in *Section 2.3.3.1*. In this work, we used a slightly modified version (Eq. 2.5) of the classical KC (Eq. 2.4; see Xu and Yu [2008] for a review of the KC equations) to calculate permeability (m^2) based on grain size distributions, which is defined as follows:

$$k = \frac{\phi^3}{(1-\phi)^2} \times \frac{V_s^2}{2 \times \tau^2 \times {S_g}^2} \tag{2.5}$$

Where V_s is the solid volume (m^3) and S_g is the surface area of the grains (m^2). Differently from the classic KC that uses the average grain size, here the real particle size distribution was used in the calculations, so that

$$V_s = \sum_{i=1}^{n} \frac{4}{3}\pi N_g f_i r_i^3 \quad (2.6)$$

and

$$S_g = \sum_{i=1}^{n} 4\pi N_g f_i r_i^2 \quad (2.7)$$

Where N_g is the total number of grains in the unit volume, f_i is the fraction of grains in a given grain size class, and r_i is the average radius in the grain class.

Permeability was calculated both for HR and CSB. The calculations were done without considering the presence of cement within the pores. The KC equations for permeability cannot be applied to concretions (cemented HR and CSB) where most of the pores have been filled by cement, because the concept of granular media (necessary for the applicability of KC relation) is no longer pertinent. Parameters and results of permeability analyses are shown in Table 2.1.

2.4. RESULTS

2.4.1. Outcrop characterization

The outcrop with the CSBs is within the damage zone of a normal fault striking NW-SE and dipping SW (Fig. 2.1b). Orientation frequency analysis was performed for each CSB set. The lower-hemisphere equal-area projection of CSBs plane azimuth (stereoplot in Fig. 2.1b) and the azimuth frequency rose diagram of Figure 2.2b show the principal directions for 219 deformation bands. These structures occur in 4 main sets with NNW-SSE, NNE-SSW, ENE-WSW and ESE-WNW orientations (Fig. 2.2b). The mean orientation is similar to that of the Apennines (ca. NNW-SSE). At the outcrop scale, single CSB in sandstones exhibit an extensive reduction in grain size, a lower porosity, a whitish color with respect to the surrounding pristine HR (Fig. 2.3a-b), and they weather out in positive relief. Slip of single CSBs ranges from 4-5 mm up to 20-40 mm (Fig. 2.3a-b). When CSBs occur in a cluster (localization of many CSBs in a narrow zone), they form a ZB. ZBs thickness ranges between 0.8 and 60 cm (Figs. 2.2a; 2.3a-b) with up to around 40 CSBs, and they accommodate offsets up to 0.5 m. Where CSBs branch and merge they form typical structures such as eye and ramp structures that are often recognized at the outcrop (Figs. 2.3a-b) and thin section scale (Fig. 2.8e). The CSBs in Loiano Sandstone are spatially associated with carbonate diagenetic structures in the form of isolated or multiple spheroids or irregular-shape nodules and tabular concretions (Figs. 2.1b, 2.2a and 2.3c-f), which are evident thanks to their differential erosion (weather out in positive relief) with respect to the poorly cemented HR. The nodular concretions range in diameter (major horizontal axis) from 0.2 m to 3 meters, whereas tabular concretions have a thickness ranging from 0.15 to 0.8 meters and a long axis ranging from 3 up to 15 meters in length. Concretions, in volume, constitute about 20% of the exposed outcrop. We focused on deformation-band-parallel concretions that represents roughly 75% of the total concretions in this area; the remaining concretions are bed-parallel (Fig. 2.2a). Concretions develop along single CSBs (Figs. 2.2a and 2.3c), ZB (Figs. 2.2a and 2.3d-e), at the intersection line among different sets of deformation bands (Figs. 2.2a and 2.3f) or along bedding (Fig. 2.2a). The association between CSBs and concretions is both spatial and geometrical, and manifest itself in the form of i) parallelism and spatial overlap between CBSs and concretions (Figs. 2.1b, 2.2a and 2.3c-f), ii) confinement of the concretions by the CSBs (Figs. 2.2a and 2.3d), and iii) geometric congruence between the CSB trend and the concretion shape (Fig. 2.3c, f). All concretions that are not bed-parallel, are spatially associated to CSBs, whereas not all CSBs are spatially associated to concretions (Figs. 2.2a and 2.3a-b). This latter case is observed whether the concretion is discontinuous along the CSB (Figs. 2.2a and 2.3b), or the CSB is not at all associated with a concretion (Fig. 2.3a).

Various sets of CSBs, spatially related with the concretions, as well as to its shape and elongation direction, were recognized. In particular, this link is apparent for two main sets: the NNW-SSE (no.1 [red], no.3 [green] and no.4 [yellow] in Fig. 2.2b) and the NNE-SSW one (no. 2 [blue] in Fig. 2.2b). These two sets are also the most frequent in outcrop and form significant clusters (Figs. 2.1b and 2.2b); they are the structural directions that mainly associate with the concretions (Figs. 2.1b and 2.2a). Field observations indicate that the NNW-SSE and NNE-SSW sets have cross-cutting relationships typical of faults forming synchronously, i.e. they cut each other (Figs. 2.2a and 2.3a, f). The other two CSB sets are the ENE-WSW one (no.5 [orange] in Fig. 2.2b) and the ESE-WNW one (no.6 [purple] in Fig. 2.2b). These latter sets (nos.5 and 6) are less frequent in outcrop (stereoplot in Fig. 2.1b and wind-rose diagram in Fig. 2.2b), crosscut the other sets (Fig. 2.3a, c), and are not spatially related with the concretions (Fig. 2.3c-f).

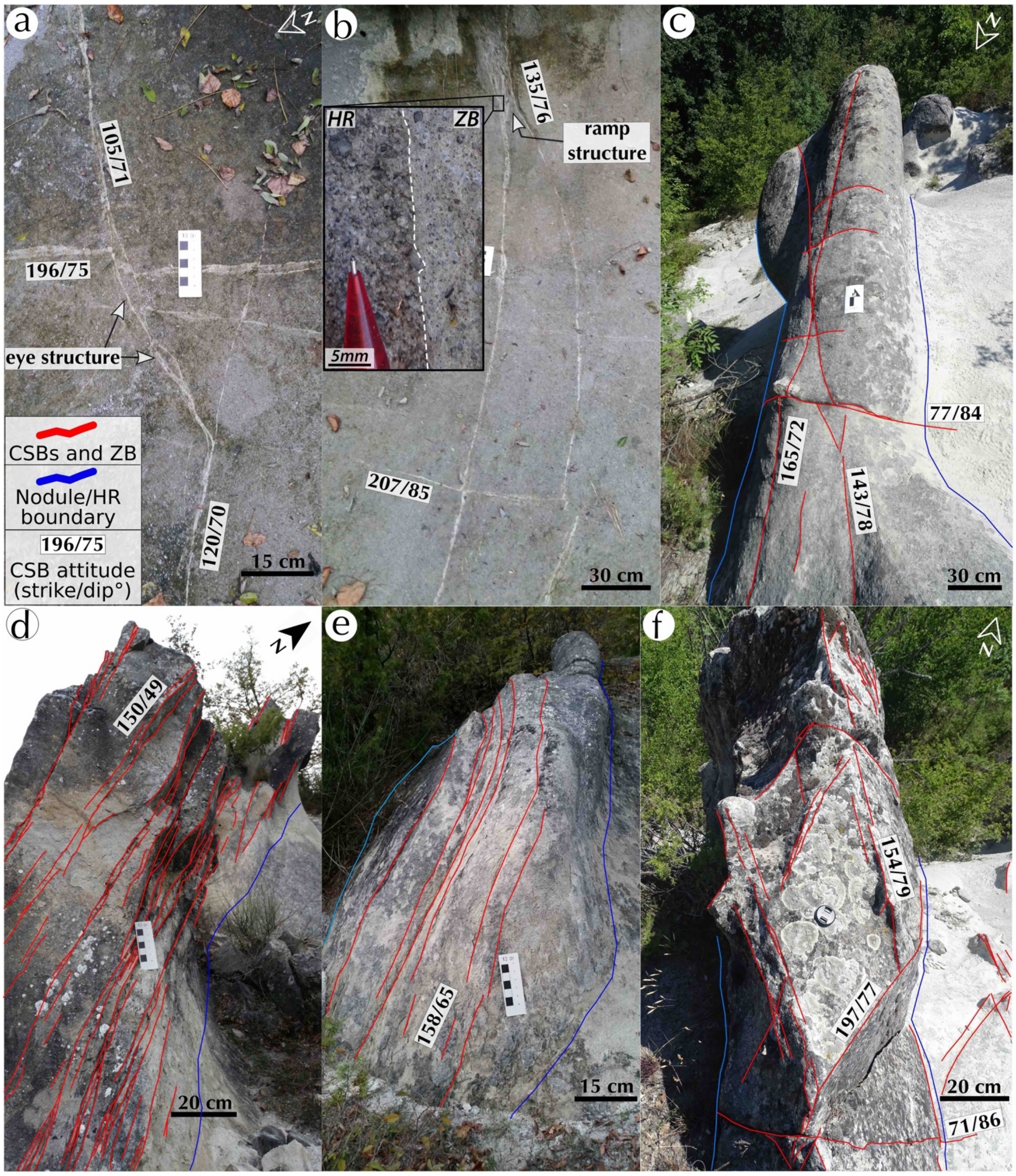

Fig. 2.3 – (a-b) Traces of different CSBs sets and relative cross-cutting relationships. **(c-f)** Typical relationships between carbonate diagenetic structures (nodules) and CSBs (red lines). The inset in (**b**) shows that grain size and porosity reduction are visible to the naked eye. Concretions develop along single CSB **(c)**, zone of CSBs **(d, e)**, and intersection lines among different sets of CSBs **(f)**. Attitude is expressed in right-hand rule (strike/dip°). Note that the CSBs traces are anastomosing with eye and ramp structures. The boundary between nodules and HR is indicated with blue lines.

2.4.2. Petrography, microstructures and textural characteristics

Combining optical and electron microscopy analysis with digital image processing, we characterized the Loiano Sandstones as medium to coarse-grained and mostly composed by Quartz (49-60%), Feldspars (39-48%), rock fragments (up to 4%), carbonate clasts (e.g. lithoclasts, bioclasts; 1.1-4.5%), and minor accessories (e.g. micas, chlorites, heavy minerals, etc.). Manual point counting validated this composition. Thus, the Loiano Sandstones can be classified as an arkose. Composition resulted to be quite homogenous within the thin sections, both in HR and CSB, as also confirmed by XRD analysis. The predominant crystalline phases identified with XRD analysis are quartz, followed by K-feldspar, plagioclase, calcite, and traces of mica/illite (see A.4 in Appendix A for XRD diffractometers). Mica/illite both in the HR and in the CSB have an abundance less than 3%, which is constrained by the XRD lower detection limit.

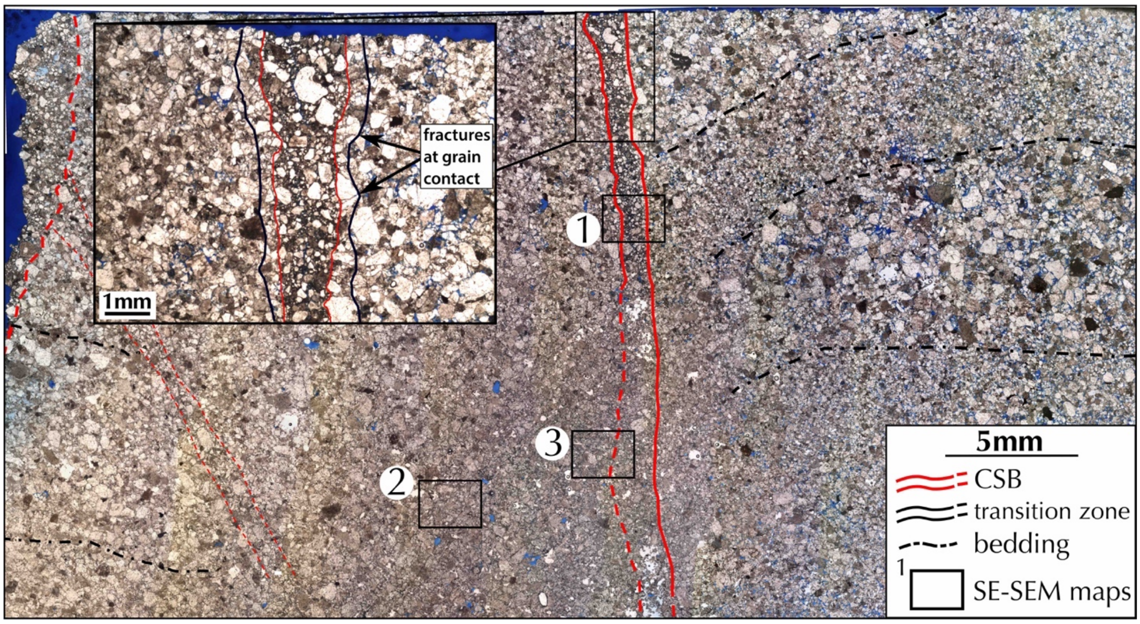

Fig. 2.4 – Thin section photo-mosaic showing CSB's microstructure. The location of some of the SE-SEM maps discussed in the paper, are also shown: (1) Map1DB (Fig. 2.6d, h), (2) Map3HR (Fig. 2.6c, g) and (3) Map2DB (Fig. 2.8d). The drag of strata shows that the left section of the image moves down with respect to the right one along the CSB. The inset is an enlargement of the CSB, where the coarse particles are surrounded by a dark fine-grained matrix. The fine matrix is not observed in the HR. The TZ (0.5-mm-wide area along both sides of the CSB's walls) is usually characterized by tighter packing and lower porosity with respect to the HR. In TZ some grains are broken (fractures at grain-contact). Microscope photos in plane-polarized light.

The CSB's microstructure (Figs. 2.4; 2.6d, h; 2.7; 2.8d-e; 2.10 and 2.12a-c) is characterized by grain size reduction, porosity and pore size reductions, as well as tighter packing, relative to the HR. Compared to the HR, in the CSB most of the grains are fractured and characterized by rough surfaces. A few rounded coarse grains are surrounded by an angular fine-grained matrix (flakes), thus showing poor sorting (broad grain size distribution curve; Fig. 2.6a). Some of the grains are aligned along the CSB's plane (Figs. 2.7 and 2.8e). This general pattern is observed in all samples (see also A.2 in Appendix A). Grain size and porosity reduction affect HR increasingly by approaching the CSB. Grain size significantly decreases from HR to CSB where it reaches dimensions typical for the silt size ranges (8-60 $\times 10^{-3}$ mm) (Figs. 2.6a and 2.11a). From the HR grain size distributions (Fig. 2.6a), we can see that SEM detects finer particle with respect to the optical microscope, because of its large magnification and the automatic particle and mineral recognition system. There is also a bias towards smaller diameters, because large particles partially fall outside the SEM-Map. Despite this, the HR grain size distribution is similar in the optical and SEM images as well as the manual point counting (Fig. 2.6a).

We refer to the 0.5-mm-wide area located along the wall of the CSB and on both sides of the CSB as transition zone (Figs. 2.4 and 2.5) to distinguish it from the surrounding HR (farther than 0.5 mm from both sides of the CSB), which was "virtually" not affected by deformation. The transition zone is characterized by a grain size range quite similar to that of the HR (see curves in Fig. 2.6a), still a grain size reduction is observed in the transition zone, where there are smaller grains with respect to the HR, and the matrix is more similar to that of the CSB (Fig. 2.6a). Hence, in the transition zone the sorting is intermediate between HR and CSB. In the transition zone, grains are characterized by cracks at points of contact (Figs. 2.4; 2.5 and 2.7), rough surfaces (Figs. 2.5 and 2.7), and a partial alignment with the direction of the CSB's plane (Fig. 2.8d-e).

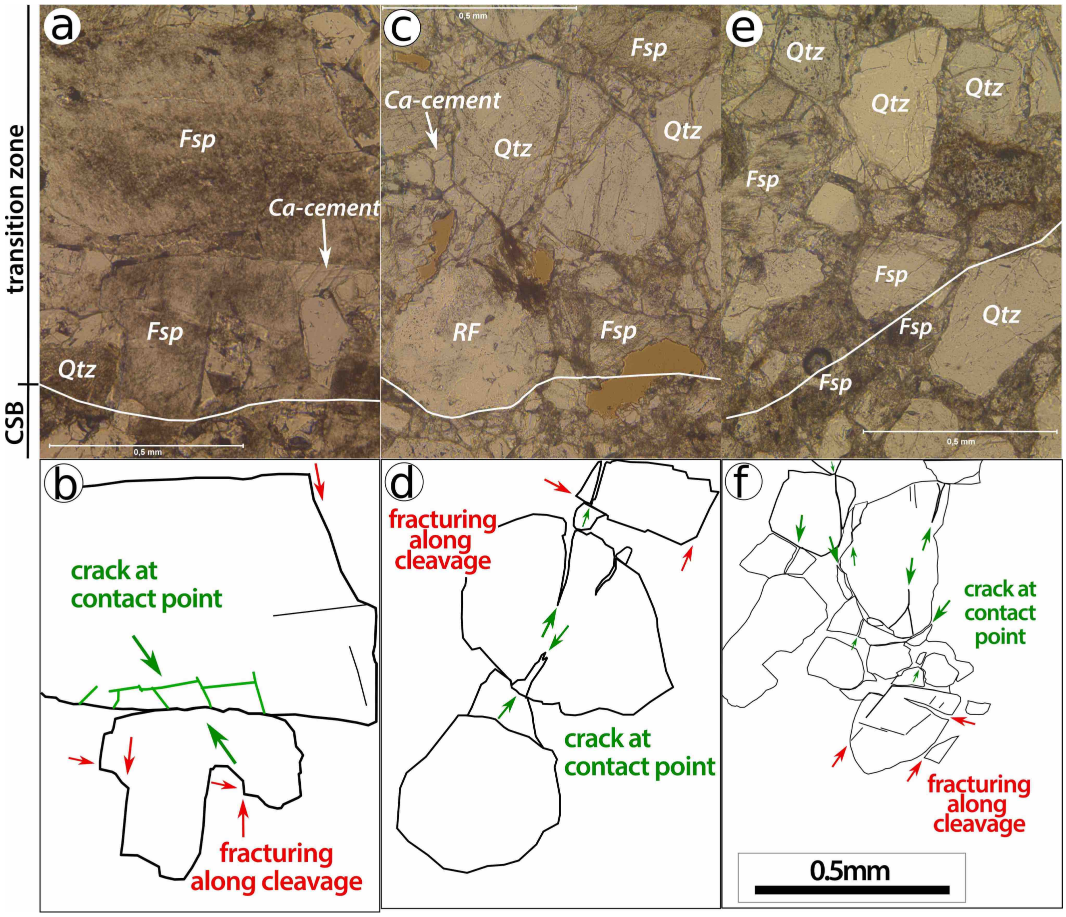

Fig. 2.5 – Photomicrographs in natural-light (**a, c** and **e**) showing the transition zone (about 0.5-mm-wide area along both sides of the CSB's walls) characteristics: poor sorting, tighter packing, and lower porosity with respect to the HR, and fractures at grain contacts (indicated by green arrows) due to stress concentration. Feldspar (Fsp) tends to break along cleavage planes (indicated by red arrows). A sketch for each photo (**b, d** and **f**) is reported to better visualize these features.

Porosity variations between HR, transition zone, and CSB are shown in Figure 2.6f. Primary porosity is predominantly made-up by intergranular pores whereas intragranular (e.g. pores within bioclasts) and oversize pores are due to dissolution of detrital grains. The total porosity is 20-26% in the HR with an average value between 23 and 24%, and 18-22% in the transition zone. The total porosity within the CSB is below 5% (based on 6 CSBs). In most of concretions the HR porosity is almost completely filled by cement, so that the remnant porosity (voids) has low values (down to 1.3%) (Fig. 2.6f). In other concretions, the remnant porosity is significant (up to 11%) (e.g. Map4HR in Appendix A). The 2-D skeleton porosity within the CSB is reduced by one order of magnitude with respect to the HR, from 22.4% to 4.5%, whereas the porosity is 19.6% along the CSB's walls (transition zone) (Fig. 2.6f-h).

The pore size diminishes along with grain size and porosity (Fig. 2.6e). The violin plots in Figure 2.6e show the pore-size distributions for HR, transition zone, and CSB. The violin plot is similar to a boxplot, because it includes the median value and a box indicating the interquartile range, except that violin plot also shows the kernel probability density (x-axis) of the data at different values. The pore size distribution curves are right-skewed in all three sectors (CSB, transition zone, HR), meaning that the bulk of the pore size distribution is concentrated towards the "small" pore size values. Pore size median value is around ~0.012 mm both for CSB and transition zone, whereas median value for HR is a little higher (~0.020 mm). The maximum pore size within the CSB (mean 0.014 mm) is less than 0.100 mm, but most of the pores have a size between 0.008 mm (minimum detectable size) and 0.010 mm (Fig. 2.6e). The pore sizes distribution curves for HR (mean 0.041 mm) and transition zone (mean 0.031 mm) show secondary peaks greater than the median value, along the long "tail of the curve", where only a few pores are larger than 0.2 mm, just below 0.5 mm (Fig. 2.6e).

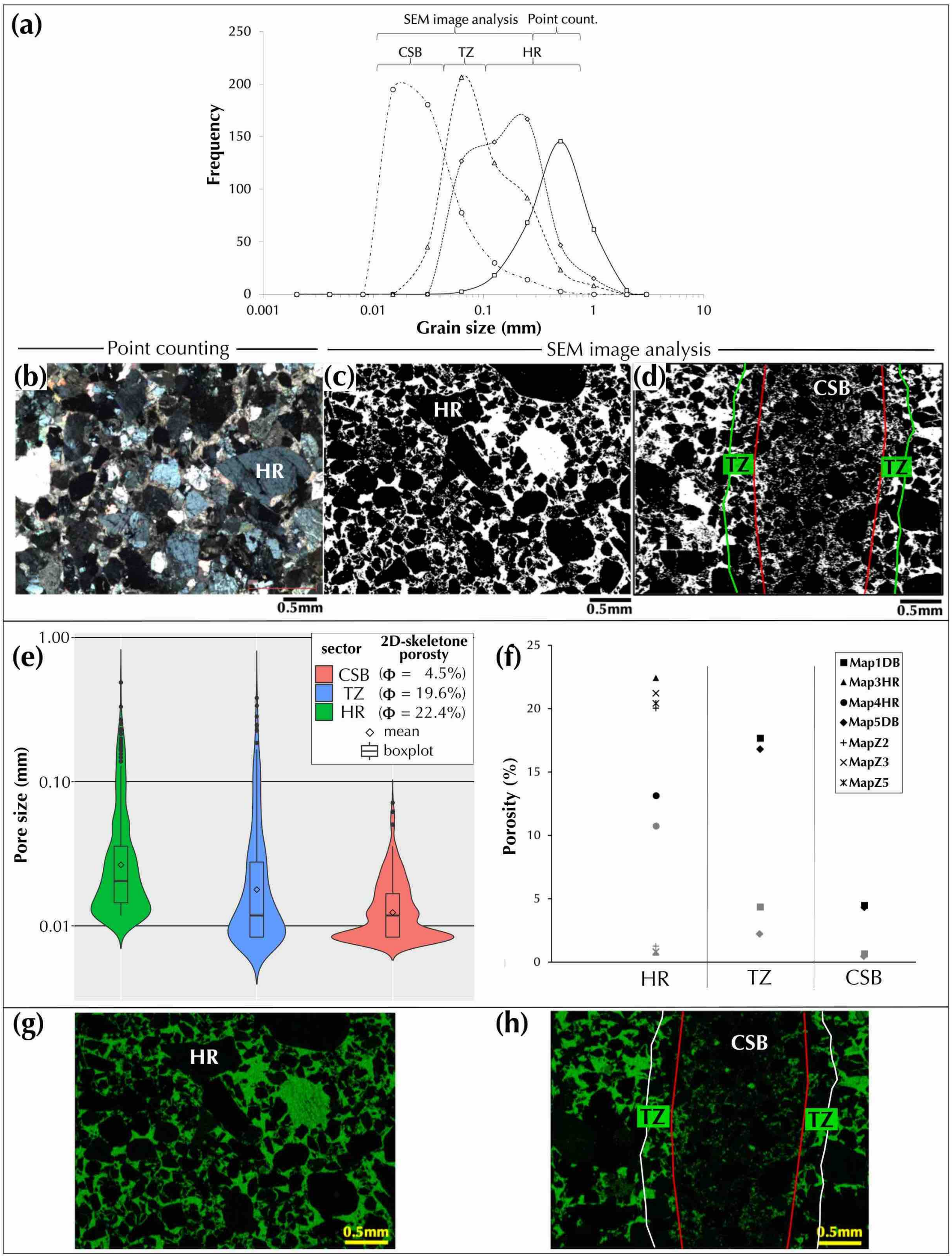

Fig. 2.6 – (a) Grain size distribution curves calculated for HR both from manual point counting **(b)** and SEM image analysis **(c)**. Transition zone (TZ), and CSB curves were calculated only from SEM images analysis **(d)**. **(e)** Violin plots of 2D-pore sizes distribution (see the text for explanation). The x-axis shows the kernel probability density of the data at different values. **(f)** Porosity data from different sectors of the thin section: black dots represent the skeleton porosity calculated from EDS - Ca distribution element maps (e.g. **g-h**), whereas grey dots represent empty pores (voids), calculate from EDS - C+Cl distribution element maps (See Appendix A for more maps). Total porosity can be obtained adding together skeleton porosity and voids. Refer to Figure 2.4 for the SEM-maps location.

In addition to grain fracturing and grain size reduction, we observed that elongated sand grains (high aspect ratio) show a preferred orientation, and that the long axes tend to be aligned parallel to the plane of the CSB (Figs. 2.7; 2.8e and 2.10). In particular, figure 2.8a shows the feldspar grains angle distribution for the HR (4 samples) and CSB. In the image analysis reference frame considered (inset in Fig. 2.8a), the CSB is at around 90 degrees. The purpose of this histogram is to show that: i) feldspar grains within the HR do not exhibit a preferential angle, each sample (denoted by a different fill colour of the bar) tend to keep a nearly constant frequency value within all angle ranges; on the contrary, ii) the long axes of feldspar grains within the CSB exhibit a preferential orientation (~90°), which is parallel to the plane of the CSB. Moreover, it was observed that the aspect ratio of feldspar grains tends to slightly increase from the HR (1.83) to the CSB (2.07) (Fig. 2.8b).

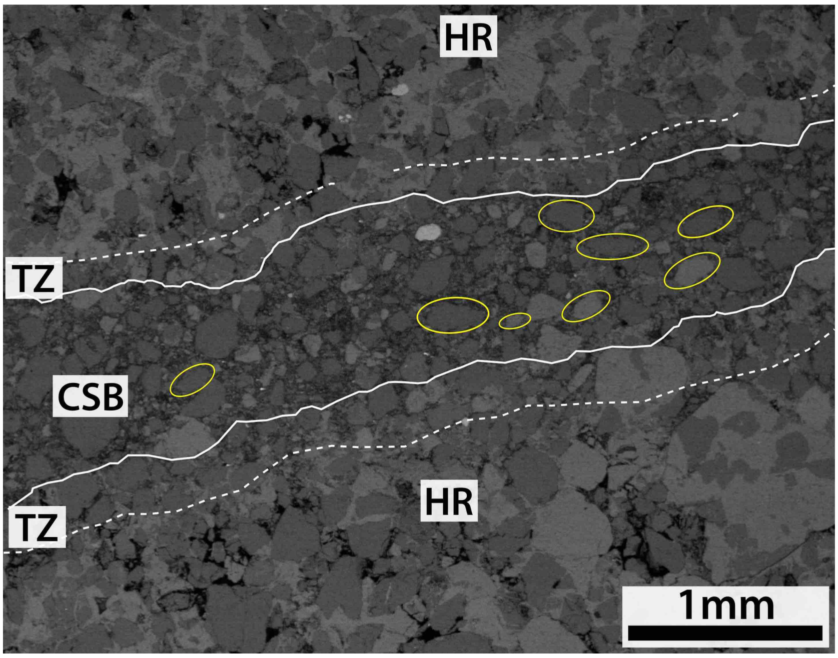

Fig. 2.7 – Preferential alignment of major elongated grains (mainly feldspars), along the plane of the CSB as shown by BSE photomicrograph (yellow-line ellipse). Such alignment is sometimes observed also along the CSB-side of the TZ. Grains assume a random orientation in the HR.

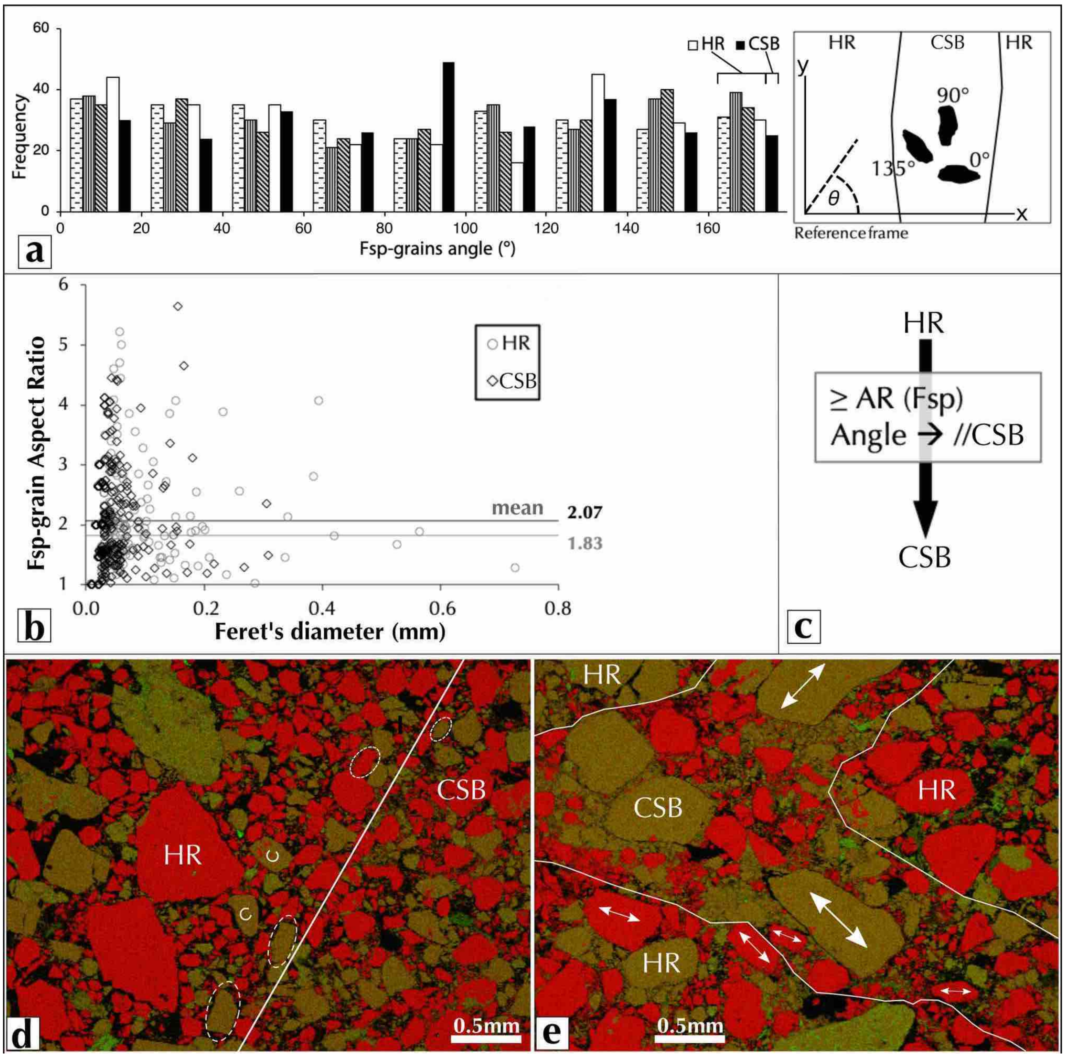

Fig. 2.8 – Example of grain orientation and grain shape evolution from the HR to the CSB. **(a)** Feldspar grains angles (°) distribution for HR (4 samples) and CSB (1 sample). The reference frame (inset) is used for grain angle calculation with image processing. **(b)** Distribution of the feldspar-grain aspect ratios as a function of the Feret's diameter. The lines represent the mean value of aspect ratio for HR (gray) and CSB (black). **(c)** The general trend is that grains tend to align along the plane of the CSB. **(d-e)** Grains arrangement within and around the CSB is shown also by SEM-EDS – Al distribution element maps (Map2DB and MapZ6) where red grains are quartz and light brown grains are feldspars; the longer axis of the grain is indicated by the white arrows.

Similarly, to what observed for feldspars aspect ratio (Fig. 2.8b), roundness, and circularity decrease from the HR (roundness = 0.59; circularity = 0.70) to the CSB (roundness = 0.54; circularity = 0.68) (Fig. 2.9). Roundness in quartz grains, on the other hand, stays constant from the HR to the CSB (0.58) and circularity increases from the HR (0.71) to the CSB (0.75) (Fig. 2.9).

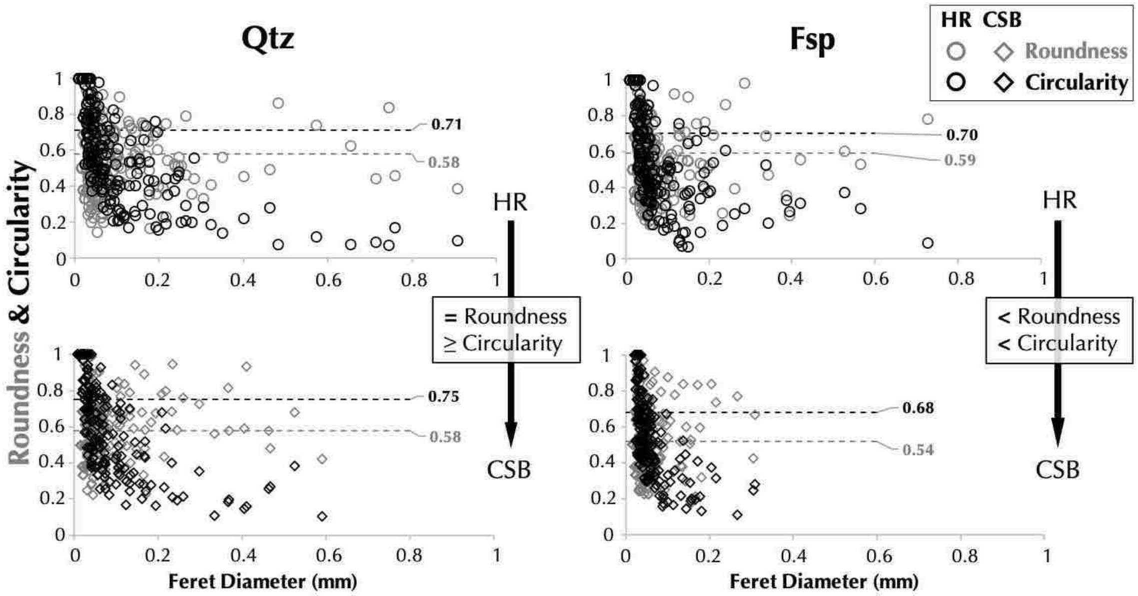

Fig. 2.9 – Example for the evolution of grain shape descriptors from the HR to the CSB. Distribution of the particle roundness (in grey) and circularity (in black) for quartz (Qtz) and feldspar (Fsp) in HR (upper diagrams) and CSB (bottom diagrams) as functions of the Feret's diameter. A roundness of 1 describes a perfect circle; a roundness approaching 0 describes an infinitely elongated particle. Dotted lines in each graph represent the mean values.

Considering that the Loiano Sandstones are arkose sandstones, it is important to evaluate if different fracturing mechanisms operate on different mineral phases (e.g. feldspar and quartz), because it could have important effects on the CSB microstructure, as well as on the grain size distribution. The feldspar grains show a grain-size reduction mainly by intragranular fracturing within the CSB; fracturing is preferentially oriented along cleavage planes (Figs. 2.5 and 2.10). Quartz grains, on the other hand, do not show any preferential fracture direction and break by spalling and/or flaking of edges along concoidal fractures (Fig. 2.10).

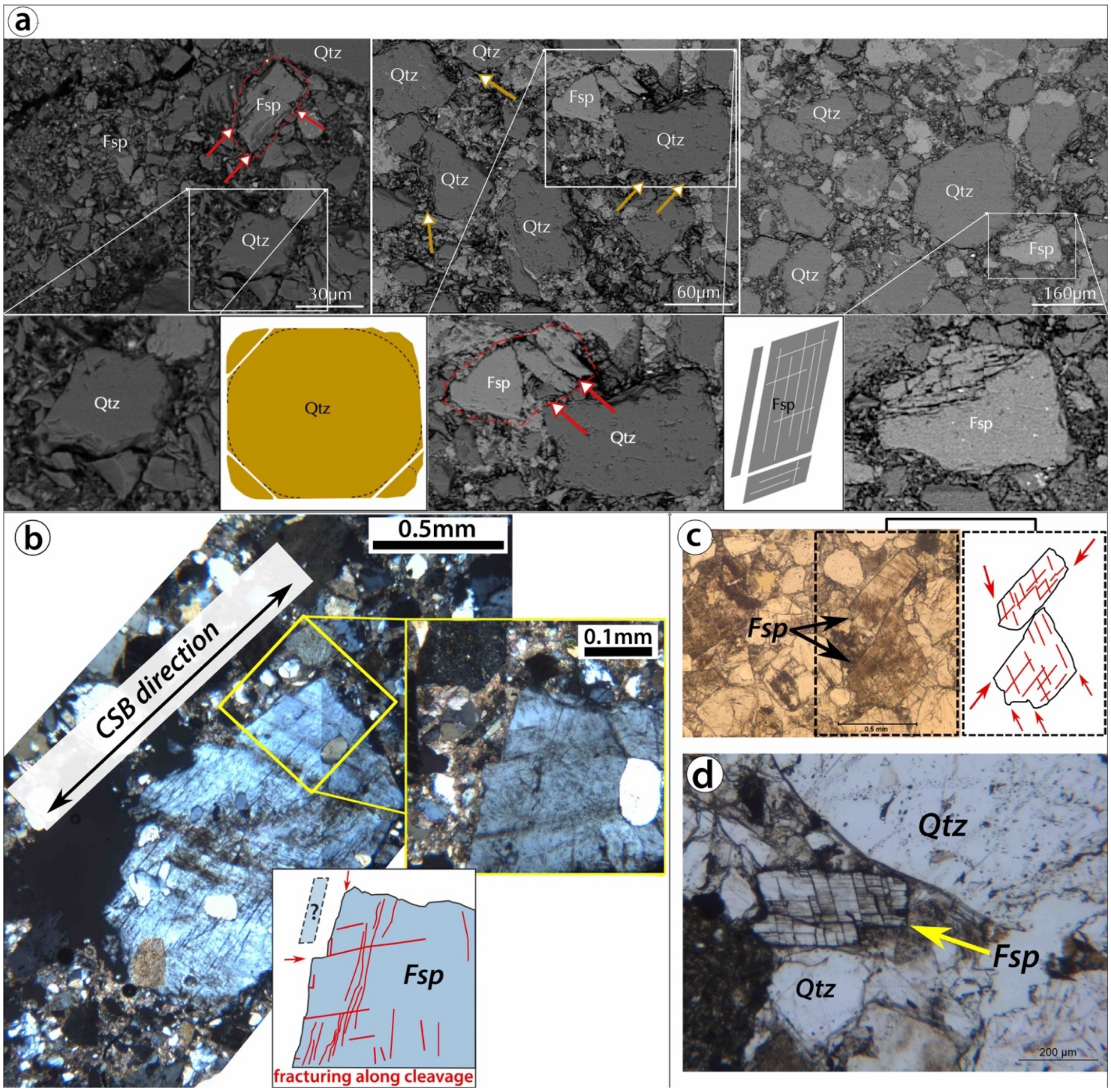

Fig. 2.10 – Mineralogical control on fracture mechanism in **(a)** BSE (15. kV) and **(b-d)** natural-light microscope images. Examples that show as **(a)** quartz (Qtz) mainly breaks via spalling and flaking of edges (golden arrows) whereas **(a-d)** feldspars (Fsp) break mainly by cleavage-controlled intragranular fractures (red arrows). Sketches for fracturing mode are reported for both minerals. The cleavage controls cataclasis **(a-d)**, grain shape, and grain orientation within the CSB, accounting for the preferential cataclasis of feldspar. Feldspar breakage produces elongated and less rounded grains **(a-d)** and fragments with respect to quartz **(a, c-d)**, and tend to align along the CSB's plane **(a-b)**.

Figure 2.11 shows the results of grain size distributions analysis in plots of *grain area* against *exceedance frequency* plotted in a log-log space. Figure 2.11a compares the total grain size data of HR and CSB: from the HR to the CSB, the number of sand sized particles decreases and concurrently the amount of fine grains increases, then the CSB curve (D=0.70) is steeper than that of the HR (D=0.45). With the aim of quantify the contribution of both quartz and feldspar to the grain size reduction within the CSB, we analysed the grain size distributions of both for quartz (Fig.2.11b) and feldspar (Fig. 2.11c) separately (e.g. Exner and Tschegg, 2012). Quartz and feldspar display a comparable HR grain size distribution. On the contrary, the grain size distributions of quartz and feldspar, in the CSB, are significantly different. Although the curves for quartz and feldspar both increase their slope from the HR to the CSB (i.e. both mineral phases undergo to grain size reduction), the increase of slope for feldspar from the HR (D = 0.56) to the CSB (D = 0.84; Fig. 2.11c) is more pronounced with respect to that of the quartz (HR: D = 0.38; CSB: D = 0.53; Fig. 2.11b).

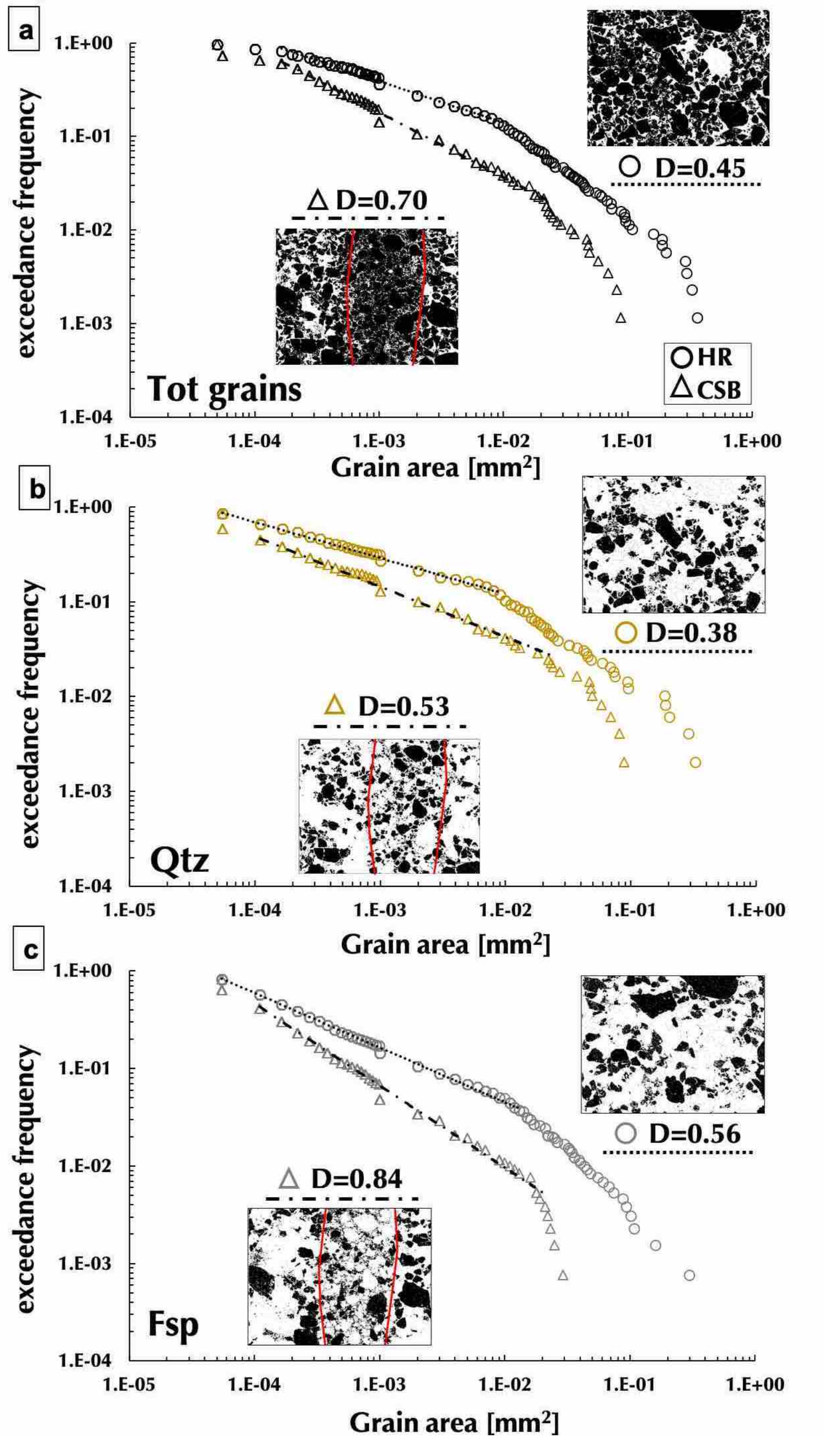

Fig. 2.11 – Plot of exceedance frequency against grain area for **(a)** total grains, **(b)** quartz grains, and **(c)** feldspar grains, in the HR (upper curves with circles) and CSB (lower curves with triangles). Two-dimensional power law exponents (D) and fractal range (black straight lines) for each distribution are also reported.

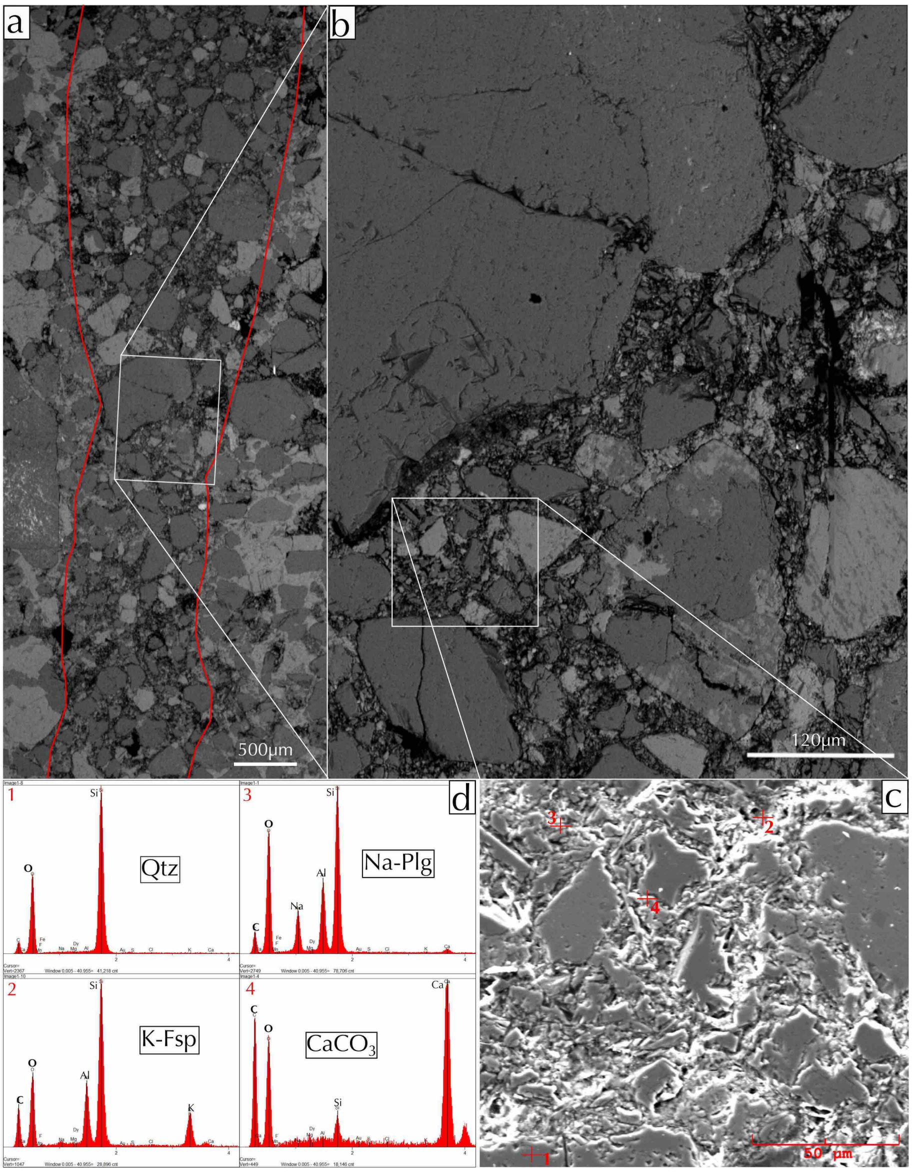

Fig. 2.12 – (a-b) BSE images (15. kV) of the CSB at different magnifications. They show the microstructure and texture of the CSB described in the paper. The enlargement **(c)** shows the position where the EDS-spectra **(d)** were measured. Within the CSB, the largest particles are made of quartz (spectrum 1); finer particles are characterized by multiple phase spectra (Si + O + Al + K + Na + C + Ca) that represent a comminuted "mix" of K-feldspars (spectrum 2), plagioclases (spectrum 3), quartz, and $CaCO_3$ (authigenic cement, detrital carbonate grains; spectrum 4).

2.4.3. Permeability analysis

Here, we present the permeability results obtained with the Kozeny-Carman relation (Equations 2.5, 2.6 and 2.7). The input parameters and model results are shown in Table 2.1. Concomitantly with porosity reduction, we observed a drop of permeability of 3 orders of magnitude from the pristine HR (2.94E+00 Darcy) to the CSB (5.00E-03 Darcy). Advective velocity decreases by 2 orders of magnitude from HR to CSB.

In the concretions (cemented HR and CSB), the cementation filled most of the sandstone pores generating a framework consisting of grains, cement, and a few remnant voids. In this contest, the KC equations for permeability cannot be applied because the concept of granular media is no longer pertinent, and other methods are needed for the estimation of the permeability (e.g. core plugs, portable air permeameters, etc.; see Chapter 3 and *Section A.5* in Appendix A).

Table 2.1

Kozeny-Carman (KC) permeability: input parameters and results for the host rock (HR) and the compactive shear band (CSB).

Parameters (Eqs. 2.5, 2.6 and 2.7)			Unit
Reference length	0.01		m
Reference volume	1.00E-06		m3
Effective length multiplier	5.2		-
Fluid density	1000		Kg/ m3
Fluid dynamic viscosity	0.001		Pa×sec
Flow length	0.01		m
Effective length	0.052		m
Tortuosity	5.2		-
Kozeny function	54.08		-
B	1.2		-
	HR	**CSB**	
Porosity	2.24E-01	4.50E-02	-
Voids volume	2.24E-07	4.50E-08	m^3
Solid volume	7.76E-07	9.55E-07	m^3
Surface area grains	8.46E-03	1.85E-02	m^2
Average grain diameter	1.22E-04	7.17E-05	m
Specific surface area	9.57E+03	2.00E+04	m^{-1}
Intrinsic permeability	2.94E+00	5.00E-03	Darcy
Hydraulic conductivity	9.60E+00	8.11E-02	K/n

2.4.4. In situ rock uniaxial compressive strength

The UCS values obtained with the Schmidt hammer are summarized in Figure 2.13. Results from 48 spot measurements along the transect (Figs. 2.13a-b) show different UCS values for different features of the Loiano Sandstones: pristine HR arithmetic mean is 23.72 MPa, nodules (Nod) arithmetic mean is 47.27 MPa, and nodules with ZB (Nod+ZB) arithmetic mean is 61.31 MPa. In addition to the transect results, 149 local measurements, obtained separately from each of the features mentioned above (pristine HR, nodules, nodules with ZB), are shown in Figure 2.13c. These latter data show the same UCS trend observed in the transect: the arithmetic mean for pristine HR is 23.80

MPa (mode = median = 23.86 MPa), for nodules (Nod) is 48.96 MPa (mode = 37.03 MPa; median = 47.42 MPa), and for nodules with ZB (Nod+ZB) is 69.54 MPa (mode = median = 66.94 MPa). In general, we observe that UCS values for nodules (Nod) are higher than values for pristine HR both in transect (Fig. 2.13a) and single measurements (Fig. 2.13c). The UCS values in nodules with ZB are higher than values measured in nodules without CSBs or associated with a single CSB. The UCS boxplots data (Fig. 2.13c) show that there is a narrow range of UCS variability (SD = 4.14) within the pristine HR, whereas nodules and concretions without CSBs or associated with a single CSB (SD = 15.80), and nodules with ZB (SD = 13.87) have a higher UCS variability.

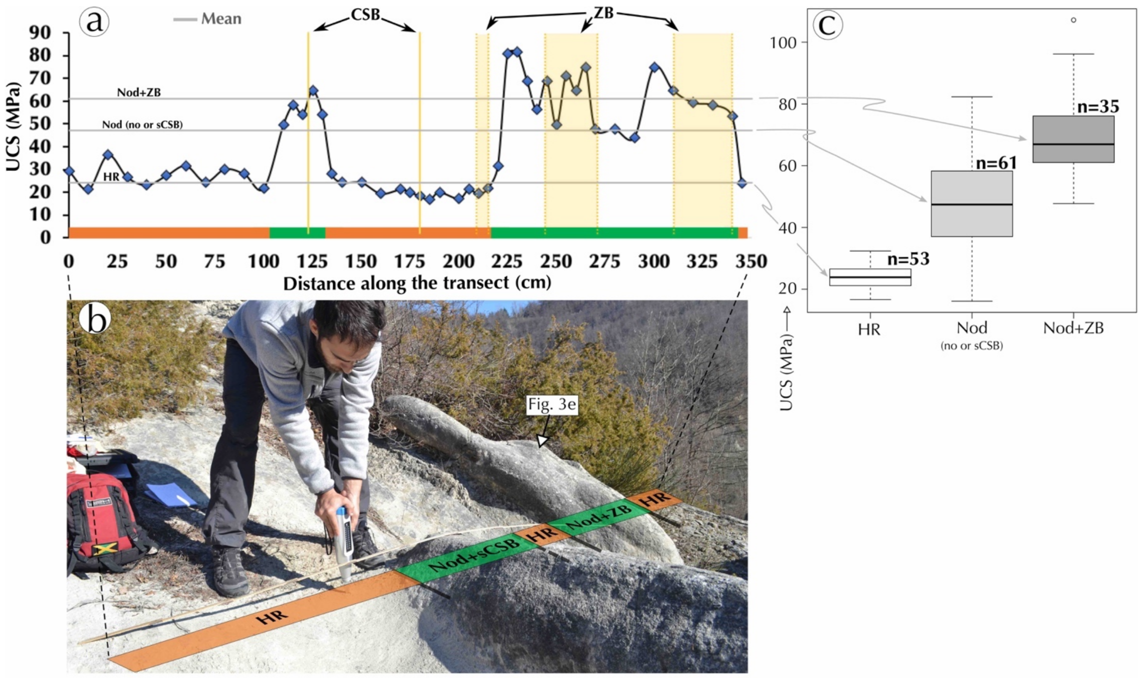

Fig. 2.13 – (a) Geomechanical transect across the pristine HR, nodules, CSBs, and ZBs. Transect position and measurement method is shown in **(b)**. **(c)** – Boxplot of UCS for each single feature: HR, nodules without and with a single CSB (Nod), and nodules associated to zones of CSBs (Nod+ZB). The black thick line in the boxplot is the 2nd quartile (median), the lower and upper box sides are the 1st and 3rd quartiles respectively. The lower and upper whiskers define, respectively, the minimum and maximum observed values in the data range excluding the outliers (dots). Number of measurements - n - is indicated on each boxplot.

2.5. DISCUSSION

In the following, we will discuss several aspects of the texture and microstructure of CSBs with cataclasis and their petrophysical properties. Then, we consider the association between CSBs and carbonate diagenetic structures, and their impact on bulk petrophysical and geomechanical properties. Finally, we discuss about the implications for sandstone reservoirs or aquifers.

2.5.1. CSB's microstructure – Mineralogical control on fracturing

The results concerning the mineralogy and grain size of Loiano Sandstones, obtained with the characterization techniques, both optical and SEM imaging, are consistent with each other and with the data from the literature (Gazzi and Zuffa, 1970; Cibin et al., 1993), pointing out that Loiano Sandstones, in the studied sector, can be classified as a medium- to coarse-grained arkose.

The CSB core is characterized by a broad grain-size distribution curve, with a few large, rounded, and nearly undisturbed sand-size grains surrounded and cushioned (e.g. Blenkinsop, 1991) by an angular fine-grained matrix with little pore size (Figs. 2.4; 2.6e, h; 2.8e). The porosity in the transition zone (Fig. 2.6f) is reduced although is more similar to the HR porosity. The pore-size (Fig. 2.6e) is also reduced, hence this zone is distinguished by a tighter packing relative to the HR. Grain shape (Fig. 2.8b-c and 2.9) and arrangement (Figs. 2.7 and 2.8a) within the CSB change during progressive deformation and accordingly change the CSB's internal (micro)structure. Microstructural observations (Fig. 2.7) and grain angle analyses (Fig. 2.8a) show that sand grains within the CSB are preferentially oriented, and the long axes tend to be aligned parallel to the plane of the band (Figs. 2.7, 2.8a, d-e), as observed by other authors (e.g. Rath et al., 2011). This behavior was observed preferentially in grains with a longer axis (higher AR) and is typical for feldspars (Figs. 2.7 and 2.8a, c). For example, Nicchio et al. (2018) described a peculiar deformation fabric characterized by a well-developed foliation (S-C-C'-type like structures) that essentially developed just by preferential alignment of feldspar fragments produced by intense comminution within deformation bands. The increase in aspect ratio (Fig. 2.8b-c) of the feldspar particles from the HR to the CSB, let us think that the tendency of the grains to dispose themselves parallel to the shear direction is linked to the feldspar grain habit (higher aspect ratio) (Figs. 2.7 and 2.8d-e, 2.10). The grain habit of a comminuted material in a micro-fault zone, on the other hand, is controlled by the micro-fractures characteristics as well as the cleavage (Figs. 2.5 and 2.10).

The grain fracturing also induces particle shape alterations (Fig. 2.9): feldspar roundness and circularity decrease within the CSB (less than 5% for both properties), consistently with the aspect ratio evolution (Fig. 2.8b). Quartz shape variations are opposite: circularity increases (below 5%) and roundness remains constant. Tavani et al. (2018), studying quartz-rich calclithite, also described a similar increase in roundness of siliciclastic grains. Philit et al. (2018), studying different successions of poorly lithified quartz-rich sandstones, observed that roundness evolution varies with respect to the degree of cataclasis: it decreases in the first stages (0-8% of cataclasis) and then slightly increases (up to ca. 40% of cataclasis). Based on quartz evolution within CSBs (roundness stays almost constant, circularity increases; Fig. 2.9), we can say that the CSBs in the Loiano Sandstones are in an advanced state of cataclasis (>8% of cataclasis, referring to Philit et al., 2018). If we look at the quartz behavior in terms of shape variations, there is a certain agreement between our data and the two previously mentioned studies (Philit et al., 2018; Tavani et al., 2018). In our case, however, the feldspar shape variations show an opposite trend (both roundness and circularity decrease; Fig. 2.9). Therefore, it is proper to investigate for different quartz and feldspar behavior, especially when a significant quantity of feldspar is present (e.g. arkose), and when different fracturing mechanisms act on different mineral phases. If different mineral phases are subject to different fracture mechanism, the grain size distribution and the shape descriptors of those minerals, within the CSB, could evolve in a completely different way during the progress of cataclasis. This increases particle shape heterogeneity during deformation band development.

The feldspar grains within the CSB show a grain-size reduction mainly by intragranular fracturing preferentially oriented along cleavage planes (Figs. 2.5 and 2.10) similar to what observed by Rawling and Goodwin (2003). The high slope of the feldspar grain size distribution curve (Fig. 2.11c) indicates that the contribution of feldspar grains to the increase in fine grains content within the CSB prevails. The grain size distribution in the HR, on the other hand, is similar for quartz and feldspar (Fig. 2.11b-c), demonstrating a selective feldspar cataclasis in the CSB (e.g. Exner and Tschegg, 2012). Hence, in Loiano Sandstones, the mineralogy controls the degree of fracturing. Probably, the increase in the D value from quartz to feldspar within the CSB is related to the different fracture mechanisms that characterize each mineral phase (e.g. Tullis and Yund, 1987; Rawling and Goodwin, 2003) as we demonstrate in this study (Figs. 2.5 and 2.10). As observed by Exner and Tschegg (2012; Fig. 8a), also our HR quartz distribution curve (Fig. 2.11b) displays a distinctive "kink", which in our case is around a grain area of 0.01 mm^2. The quartz curve keeps a similar trend within the CSB whereas the feldspar curve has a more linear trend (Fig. 2.11c). Feldspar grains are more prone to break with respect to quartz, given that fractures take advantage of particle weaknesses such as cleavage planes (Figs. 2.5 and 2.10). This explains the preferential grain size reduction of feldspars (Fig. 2.11c) compared to that of quartz (Fig. 2.11b) (e.g. Tullis and Yund, 1987). As a result, the quartz is optically recognizable within the CSB, because it is well-represented in the coarse grain size class whereas feldspars are concentrated in the fine grain size class and difficult to identify ate the microscope (Figs. 2.4, 2.10 and 2.12). Lommatzsch et al. (2015), studying CSB in uncemented arkosic sediments, show how the weakening of feldspar structure caused by alteration, and the decomposition of biotite (mechanical deformation and chemical alteration), result in a preferred fracturing of those two mineral phases. Preferential cataclasis of weaker grains has been shown also in porous volcaniclastics rocks by Cavailhes and Rotevatn (2018). The latter authors documented how the cataclasis affect preferentially weak volcanic glass. Feldspar, pyroxene, and amphibole are relatively less comminuted and cataclasis is controlled by cleavage planes.

In the Loiano Sandstones, the different nature of feldspars and quartz mineral phases may explain the microstructure, textural characteristics, and the grain fracture mechanisms of CSBs. Feldspar cleavage planes guide the fracturing (intragranular fractures), leading to more elongated (> aspect ratio; < roundness and circularity) grains and particle fragments (Figs. 2.7, 2.8d-e, 2.10). These elongated fragments, in turn, are prone to rotate and align on the plane of the CSB during shear (Figs. 2.7 and 2.8a, 2.d-e) as previously observed by other authors (Goodwin and Tikoff, 2002; Nicchio et al., 2018). Figures 2.5 and 2.10 shows that the shape of the crushed feldspar grains is controlled by the cleavage direction. On the other hand, quartz is not affected by cleavage (Fig. 2.10a, d), so that intragranular fracturing is less common. Spalling and flaking of quartz grains produce more rounded particle fragments, which are less likely to align with the CSB plane. Furthermore, quartz grains are stronger than feldspar resulting in less intense comminution (Figs. 2.4, 2.11b-c and 2.12a).

2.5.2. Petrophysical properties

More than one mechanism caused porosity and permeability reduction in the Loiano Sandstones, namely localized shearing associated with cataclasis and cement precipitation in the pore space. In Loiano Sandstones, the CSB porosity is reduced by an order of magnitude (Fig. 2.6f) following grain crushing and the resulting change in grain-size distribution (Figs. 2.6a and 2.11) similar to what observed by other authors (Aydin 1977; Antonellini et al., 1994a; Fossen 2007). We also observed a pore-size reduction from the HR to the CSB (Fig. 2.6e). The reduction of porosity produces a corresponding decrease in KC permeability up to three orders of magnitude with respect to the HR (Table 2.1). These values are consistent with data obtained from other authors for cataclastic shear bands (Antonellini and Aydin, 1994; Fossen et al., 2007; Torabi and Fossen, 2009; Ballas et al., 2012). Porosity decrease, owing to reduction/closing of pore-throat sizes, imply a reduction in permeability (Reis and Acock, 1994). Porosity and permeability evolve through time and space: in the Loiano Sandstones they are controlled by the degree of cataclasis and the rate of chemical precipitation. Cataclasis within the CSB produced an intensely comminuted matrix, causing an increase of specific surface area and tortuosity, that in turn reduced the permeability (Sulem and Ouffroukh, 2006; Torabi et al., 2008). Cement precipitation caused the filling of voids in the HR adjacent to the CSB and within the CSB, reducing the porosity up to 1 order of magnitude (grey dots in Fig. 2.6f) with respect to pre-cementation conditions (black dots in Fig. 2.6f). The combined effect of cataclasis, compaction, and cementation, produced relatively wide zones (up to ca. 80 cm-thick) of low permeability (down to 10^{-3} Darcy), which can extend for a few tens of meters in length (i.e. tabular concretions; Figs. 2.1b, 2.2a and 2.3c-f). Cementation contributes to the porosity and permeability deterioration effect caused by grain crushing and compaction in the CSB. Cement precipitation is not homogeneous in the carbonate nodules within the Loiano Sandstones (Fig. 2.6f). This could be linked to porosity and permeability anisotropy related to deformation (e.g. pore size and connectivity; Farrel et al., 2014) that in turn controlled the fluid circulation and the cementation process. Consequently, the present-day porosity of nodules is not homogeneous and, therefore, also their permeability. This inhomogeneity is reflected upon the Schmidt hammer measurements (*see Section 2.5.4*) and it explains the variability (scatter) of UCS data for the concretions (SD = 15.80), whereas UCS data distribution for the pristine HR is more homogeneous (SD = 4.14) (Fig. 2.13c).

Despite the high feldspars content in the Loiano Sandstones, the XRD patterns did not show any significant clay minerals content both in the HR and in the CSB. In this case, as suggested by Nicchio et al. (2018) in similar settings, the deformation mechanism was merely physical (cataclasis), and the calcite cementation process was a later one. These authors stated that if there is important fluid flow in the CSB zone, authigenic clay minerals would be expected to form, due to the high concentration of comminuted feldspar fragments. This situation, however, may not apply to the Loiano Sandstones, because cementation occurred just after the CSB development, leaving no time for further reaction of the comminuted grains with circulating fluids. Various authors (Cibin et al., 1993; McBride et al., 1995; Milliken et al., 1998) proposed that calcite cement formed at or just before the maximum burial depth for the Loiano Sandstones. This hypothesis was supported being the intergranular volume (IGV = intergranular porosity + cement + matrix; Paxton et al., 2002) of cemented sand (i.e. concretions and nodules) similar (slightly higher) to that of the pristine poorly lithified host sandstone.

2.5.3. Deformation bands as cement localization sites

The timing of CSBs formation and calcite cementation in Loiano Sandstones is still under investigation and will be presented in a future work. Here, however, we discuss some preliminary results. There is evidence that supports the hypothesis that the formation of the CSBs precede the cementation. Field observations show that the concretions are preferentially developed along the CSBs, being all not bed-parallel concretions (25% of the total concretions; Fig. 2.2a) associated to CSBs (75% of the total concretions; Figs. 2.2a and 2.3b-f). On the contrary, not all the CSBs are associated to concretions (Figs. 2.2a and 2.3a). The association between CSBs and concretions is manifested through a parallelism and spatial overlap between the two. In some cases, the CSB is located within the concretions, in other cases they also bound the concretions. Moreover, we observed a clear congruence between the elongation direction of the concretions and the CSBs. Figure 2.1b shows that the elongation direction of the concretions follows the same trend of the principal CSBs sets (stereoplot in Fig. 2.1b; Fig. 2.2b), that in turn follow the trend of the main faults (Fig. 2.1). In case cementation is the first event, we should expect: (i) no spatial association between CSBs and concretions, and that ii) concretions are cut by the CSBs. On the contrary, we observe that the structures are overprinted by the cement, at least for those CSBs sets (NNW-SSE, NNE-SSW) associated with concretions. Lastly, deformation bands are restricted to porous granular media (e.g. Aydin et al., 2006; Fossen et al., 2007), since the processes linked to the formation and evolution of the bands (e.g. grain rotation, translation) requires a certain amount of porosity. Hence, the presence of cement would prevent the formation of the CSBs in the low-porosity concretions.

In the following, we discuss about which mechanism could have promoted the precipitation, and where and why these mechanisms may occur. Grain surface area is a critical parameter for cement precipitation (Walderhaug, 1996; Lander et al., 2008). The kinetics (reaction rates), in fact, is directly controlled by the grain-fluid interface (e.g. Noiriel, 2015). Furthermore, the reactive transport properties can be influenced by the specific surface area (SSA) variations (Noiriel et al., 2009). It is important to bear in mind that SSA is inhomogeneous in the rock volume and it evolves through time (Noiriel et al., 2009; Gouze and Luquot, 2011), in our case during cataclasis and cementation. Cementation in a sandstone is promoted where there is a local increase in SSA that could both allow the initiation of cement precipitation and the acceleration of the precipitation rate (Walderhaug, 1996; Lander et al., 2008). Teng et al., (2000), with Atomic Force Microscopy observations, showed that growth of calcite at low supersaturation concentrations ($\sigma < 0.8$) occurs by step flow at surface defects (i.e. screw dislocations, pits, fractures and grain boundaries). Nucleation theory states that the energy barrier for nucleation depends on the degree of fluid supersaturation with respect to the nucleating mineral and on the interfacial free energy (i.e. surface tension) (e.g. De Yoreo and Vekilov, 2003). In our case, the low permeability and high surface area of the comminuted CSB core material, lower the energy barrier for nucleation of cement, so that a high degree of supersaturation is not needed to induce authigenic cementation at grain contacts (Wollast, 1971; Berner, 1980). Nucleation spots are available in the Loiano Sandstones, because of fine-grained reactive feldspars and mechanically crushed grains (e.g. Phillips, 2009). Grain size control on quartz sandstones cementation was observed both directly and experimentally (Heald and Renton, 1966; Walderhaug, 1996; Lander et al., 2008). The cataclasis of sand grains within the CSB increases the reactive surface area. Considering that feldspar dominates the cataclasis, the degree of feldspar fracturing in the Loiano Sandstones is the basis for cement precipitation. Cataclasis has multiple effects on advective flow velocity. It causes *(i)* a decrease of the hydraulic conductivity (*K*) and *(ii)* an increase of flow velocity linked to the porosity reduction (e.g. Noiriel, 2015). The decrease of K (three orders of magnitude) on reducing advective flow velocity is prevalent on the flow velocity increase caused by porosity reduction (one order of magnitude). As a result, there is a net decrease in advective flow velocity in the CSBs.

We hypothesize that carbonate cement precipitation is promoted (1) where fluid flow slows down (low permeability and advective velocity) (e.g. Fetter, 2002) and (2) where a large amount of grain surface area (fresh and highly reactive) is available (fine grain-size) (e.g. Lander et al., 2008). These two conditions occur in the CSB due to cataclasis development (grain crushing and comminution). Compactive shear bands in the Loiano Sandstones were areas where advective fluid flow was slowing down and they might have acted as a place of preferential nucleation of the carbonate nodules as observed in the field. The association between CSBs and concretions is clear in the field only for some of the measured sets, the NNW-SSE one and the NNE-SSW one (Fig. 2.2b). Likely, the ENE-WSW and ESE-WNW sets (Fig. 2.2b), being not associated to nodules and crosscutting the other sets (Fig. 2.3), are the youngest structures and likely they were not present at the time of cement precipitation.

2.5.4. Mechanical properties

The combination of different mechanical rock properties, such as Young's modulus, hardness, strength, surface smoothness, density and cementation are reflected in the hammer rebound values (Katz et al., 2000). In porous rocks, a negative correlation between mechanical (e.g. UCS) and petrophysical properties (porosity and permeability) was documented in the literature (Palchik, 2006; Schöpfer et al., 2009; Alikarami et al., 2013; Torabi et al., 2018). The effect of porosity on UCS is observed also in the Loiano Sandstones. As expected, higher UCS values were measured in nodules with respect to the pristine HR. The cemented sandstones also weather out in positive relief. Cementation in sandstones increases rock strength both for calcite (Alikarami et al., (2013); using the Schmidt hammer) and for quartz cements (Bernabé et al., (1992); using the triaxial tests). The cement precipitates at the grain contacts inhibiting rotation and sliding of particles in a way to increase rock cohesion. Our study is the first where the Schmidt hammer is used to evaluate the mechanical properties of deformation bands associated with diagenetic nodules. Our field measurements show that nodules associated with zones of CSBs have higher UCS values (~70 MPa) with respect to nodules without CSB (~49 MPa). This indicates that the rock strength increase is not caused by cementation only, but also by cataclasis and compaction associated to the ZB. Where a single CSB is present, the UCS measurements are unaffected by its presence. Consider, in fact, that the tip of the Schmidt hammer has a thickness of ca. 1 cm, hence 1 order of magnitude greater than CSB average thickness (ca. 1 mm). On the other hand, where a ZB is present (i.e. a narrow zone (50-60 cm) with up to 40 CSBs) the effect of cataclasis and compaction is more intense and detectable by the Schmidt hammer measurement. In a few previous studies (Torabi and Alikarami, 2012; Alikarami et al., 2013), a higher rock strength/elasticity within deformation bands with respect to the adjacent HR was also measured with the Schmidt hammer and ultrasonic laboratory measurements. According to these studies, the strength/elasticity increase was due to cataclasis and porosity reduction forming a dense microstructure within the deformation band. Rock strength measurements where cement is present (Nod; Nod+sCSB; Nod+ZB in Fig. 2.13) are more variable with respect to HR measurements, because of diagenetic processes such as cementation, which may be inhomogeneously distributed (Chang et al., 2006).

Combination of cataclasis (angular grains and non-unimodal GSD), and compaction leads to interlocking of grains and asperities, promoting strain hardening (Aydin and Johnson, 1978; Underhill and Woodcock, 1987). In granular materials, the angularity and surface roughness of particles have critical effects on the frictional strength (e.g. Mair et al., 2002). The grain crushing causes a textural change in terms of grain sorting, grain reorientation and grain shape: poor sorting and clast roughening (> angularity) promote the increase of band friction (e.g. Underhill and Woodcock, 1987; Philit et al. 2018) and finally the higher packing within the band produces a dense microstructure (*physical healing*; c.f. Shipton and Cowie, 2003) with increased cohesion (Kaproth et al., 2010). The combined effect of cataclasis, compaction, and cementation in the Loiano Sandstones produces a strengthening effect of the nodules with CSBs with respect to the HR, and at the same time involves a rock deterioration in terms of petrophysical properties.

2.5.5. Implications for geofluids

Considering that porous sandstones are important reservoirs and aquifers, including many feldspar-rich sandstones (e.g. Chuhan et al., 2000; Gier et al., 2008), assessing the role of deformation bands in controlling fluid flow patterns and diagenetic processes is helpful to predict aquifer/reservoir behavior during geofluids exploration, management, and exploitation (e.g. water wells placement, hydrocarbon production, CO_2 storage management). Deformation bands may potentially impact porosity and permeability of porous sandstone promoting reservoir compartmentalization (Edwards et al., 1993; Lewis and Couples, 1993;) or reducing reservoir injectivity, because of pore clogging. Hence, they significantly affect reservoirs and aquifers production (Antonellini and Aydin, 1994; Sternlof et al., 2006; Qu et al., 2017; Rotevatn et al., 2017) especially where a large permeability reduction, a high deformation bands frequency, a high connectivity (Fossen and Bale, 2007; Rotevatn et al., 2013), and diagenetic effects are present. Deformation bands in the Loiano Sandstones are characterized by: (1) A drop in porosity by one order of magnitude from pristine HR to CSB. (2) A drop of 3 orders of magnitude in permeability from pristine HR to CSB. (3) A drop of two orders of magnitude in advective velocity from pristine HR to CSB. (4) A drop in porosity of one order of magnitude from pristine HR to the nodule. The association of deformation bands with carbonate concretions in the Loiano Sandstones, therefore, has the potential to strongly affect reservoir or aquifer production. The characterization of deformation bands (attitude, frequency, extension, connectivity, thickness of zones, etc.), their impact on petrophysical properties, and possible association with diagenetic effects (nodules and concretions) should also be taken into consideration during reservoir/aquifer flow simulations and management.

2.6. CONCLUSIONS

The excellent exposures shown in this paper allowed documenting the association between deformation bands and carbonate concretions in the Loiano Sandstones, which are a high porosity reservoir/aquifer analogue for arkose sandstone. Microstructural observations of CSBs in this particular mineralogy allowed us to discuss: (i) the preferential cataclasis of feldspar, and (ii) the cleavage control on cataclasis, grain-shape, and grains organization within the CSB. In terms of structural diagenesis, this research shows a case in which deformation affects the fluid flow, focuses the diagenetic processes, and controls the distribution of diagenetic products. Furthermore, we show interesting results about the rock strength increase caused by the assemblage CSBs-concretions. The major conclusions that we obtained from this work are the following:

(1) CSBs in the Loiano Sandstones are characterized by two main processes: cataclasis and compaction. Within the CSB both cataclasis and grain crushing reduce the grain size distribution, producing an angular fine-grained matrix that surrounds a few large, rounded, and nearly undisturbed sand-size grains.
(2) The presence of feldspars controls cataclasis development within the CSB. The mineralogy, in fact, controls the grain size distribution and the shape of cataclasis-related grains. Feldspar contribution to the increase in fine grains content within the CSB prevails with respect to the quartz.
(3) Feldspars are characterized by a persistent cleavage that makes them weaker and more prone to fracture with respect to quartz. The cleavage controls fragment shape: elongated (high aspect ratio) and low in roundness and circularity. Quartz grains, on the other hand, do not show any preferential fracture direction, so that grain crushing will occur at defects and weakness points (i.e. edges). The microstructure and texture of the CSB is influenced by the alignment of elongated grains (mostly feldspars) along the plane of the band during progressive shear. The mineralogy controls the deformation mechanisms and the cataclasis. In turn, different fracturing mechanism between feldspar (intragranular fracturing) and quartz (spalling and/or flaking of edges) explain the preferential cataclasis of feldspar grains within the CSB.

(4) The joint effect of compaction and cataclasis decrease CSB porosity by an order of magnitude with respect to the pristine HR. The porosity and pore-size decrease within the CSB causes a change in pore connectivity and a decrease in permeability up to three orders of magnitude from pristine HR to CSB. The calcite cement precipitation enhances the porosity and permeability reduction effect caused by the deformation.

(5) Cementation affects porosity/permeability in the Loiano Sandstones. Porosity drops one order of magnitude from the pristine HR to the concretions. Sheet-like nodules and concretionary bodies of cemented sandstone localized on pre-existing low permeability CSBs further extend and enhance the permeability reduction associated with the CSBs. The variations of petrophysical properties due to the nodules and the cataclastic faults may have a strong influence on the migration, trapping, and production of geofluids in a sandstone reservoir/aquifer.

(6) Nodules and concretions, regardless of the presence of CSBs, show higher UCS values (~49 MPa) with respect to the pristine HR (~24 MPa). Nodules associated to ZB are those with the highest UCS values measured in outcrop. Cataclasis, compaction, and cementation contribute to increase the strength of the Loiano Sandstones, and in particular of the assemblage CSB – concretion.

Supplement – Supplementary material to this Chapter can be found in the Appendix A.

References – The references related to this Chapter can be found in the Bibliography.

Acknowledgments – We thank Atle Rotevatn and an anonymous reviewer for their constructive and positive reviews, leading to improvement of the original manuscript, and Stephen E. Laubach for his editorial work.

3

Characterization of sub-seismic resolution structural and diagenetic heterogeneities in porous sandstones

The content of this Chapter has been published in **Del Sole, L.**, Antonellini, M., Calafato, A., 2020. Characterization of sub-seismic resolution structural diagenetic heterogeneities in porous sandstones: Combining ground-penetrating radar profiles with geomechanical and petrophysical in situ measurements (Northern Apennines, Italy). Marine and Petroleum Geology, 117, 104375.

ABSTRACT

Deformation bands and structurally-related diagenetic heterogeneities, here named Structural Diagenetic Heterogeneities (SDH), have been recognized to affect subsurface fluid flow on a range of scales and potentially promoting reservoir compartmentalization, influencing flow buffering, and sealing during production. Their impact on reservoir hydraulic properties depends on many factors, such as their permeability contrast with respect to the undeformed reservoir rock, their anisotropy, thickness, geometry as well as their physical connectivity and arrangement in the subsurface. We used the Ground Penetrating Radar (GPR) for detection and analysis of the assemblage of deformation bands – carbonate nodules, in high-porosity arkose sandstone in Northern Apennines of Italy. 2D GPR surveys allowed the description of the SDH spatial organization, their geometry, and their continuity in the subsurface. Petrophysical (air-permeability) and mechanical (uniaxial compressive strength) properties of host rock, deformation bands, and calcite-cement nodules were evaluated along a 30-m thick stratigraphic log to characterize the permeability and strength variations of those features. The assemblage "deformation bands – nodules" degrade porosity and permeability and produce a strengthening effect of the rock volume, imparting a strong mechanical and petrophysical heterogeneity to the pristine rock. Different textural, petrophysical, and geomechanical properties between deformation bands, nodules, and host rock result in different GPR response (permittivity). Thus, GPR response could be used to extend outcrop data (petrophysical and geomechanical) of SDH to 3D subsurface volumes in a way to reconstruct realistic and detailed outcrop analogs of faulted aquifers and reservoirs in porous sandstones.

Graphical abstract

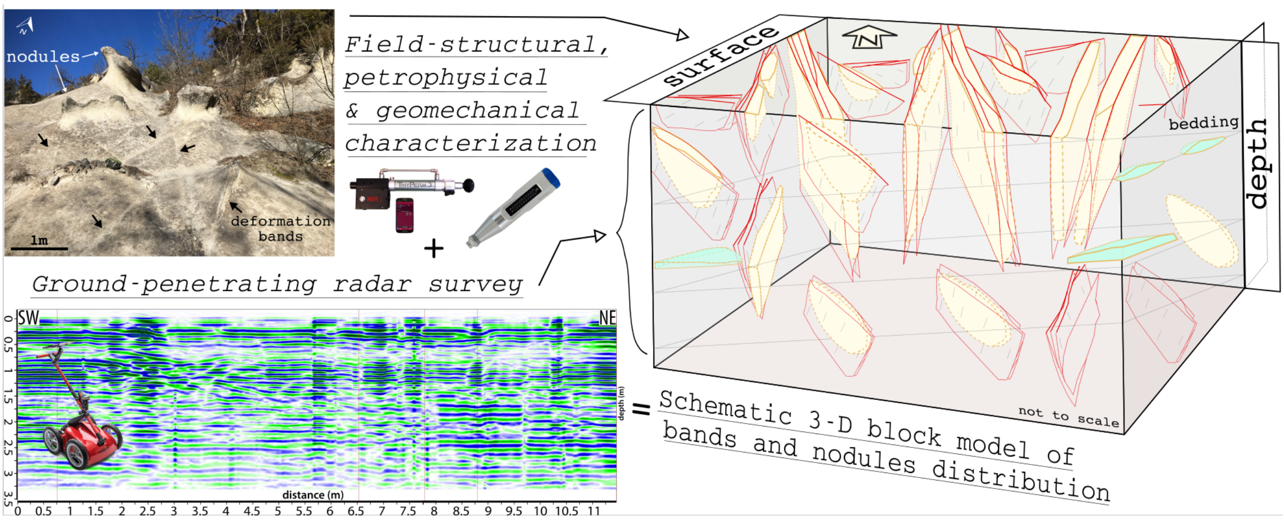

3.1. INTRODUCTION

3.1.1. Deformation bands: attributes

Reservoirs in porous granular rocks (commonly porosity ≥ 0.15; e.g. Fossen et al., 2007) often contain deformation bands, which are small "fault-like" mm-thick tabular-planar structures that develop during failure at relatively shallow depths (typically 0-4 km; e.g. Fossen et al., 2007). They are well-known in sand(stones) (Antonellini and Aydin, 1994; Aydin et al., 2006; Fossen et al., 2007), but also in carbonates (Tondi et al., 2006; Rath et al., 2011) and volcanoclastic rocks (Wilson et al., 2003). A variety of factors control the spatial distribution of deformation bands and their impact on the hydraulic properties of reservoirs. The most important factors are the host rock properties, kinematics and deformation mechanisms, tectonic regime, burial conditions occurring during deformation, amount of offset, and diagenetic evolution of those structures (Antonellini et al., 1994a; Fisher and Knipe, 2001; Fossen et al., 2007; Ballas et al., 2014, 2015). Deformation bands may inhibit (compaction, cement precipitation, clay smearing), buffer (cataclasis) or even enhance (dilational fracturing) the fluid flow in a deformed porous rock (Antonellini and Aydin, 1994; Mollema and Antonellini, 1996; Gibson, 1998; Antonellini et al., 1999; Aydin, 2000; Bense et al., 2003; Sternlof et al., 2006; Fossen et al., 2007). In most cases, deformation bands are associated to a porosity decrease up to 1 order of magnitude with respect to the host rock that, in turn, promotes a permeability reduction from 1 up to 3 orders of magnitude with respect to the host rock (Antonellini and Aydin, 1994; Antonellini et al., 1994a, 1999; Fisher and Knipe, 2001; Jourde et al., 2002; Shipton et al., 2002; Fossen et al., 2007). Some exceptions are represented by disaggregation bands with a dilational component (Du Bernard et al., 2002; Bense et al., 2003) where an enhancement of porosity and permeability of the fault rock is observed.

In this work, we focus on compactive shear bands (CSB from now on) with cataclasis (Aydin, 1978; Aydin and Johnson, 1978) in high-porosity arkose sandstones spatially associated to calcite-cement nodules (Del Sole and Antonellini, 2019; Chapter 2), and here we refer to them as Structural and Diagenetic Heterogeneities (SDH). Despite their small offsets, from a few millimetres to 1-2 cm, deformation bands and zone of deformation bands (localization of many bands in a narrow zone; ZB from now on) may affect subsurface fluid flow on a range of scales, promoting reservoir compartmentalization, and causing flow buffering or sealing during production (Harper and Mofta, 1985; Edwards et al., 1993; Antonellini and Aydin, 1994; Fowles and Burley, 1994; Gibson, 1998; Manzocchi et al., 1998; Walsh et al., 1998; Antonellini et al., 1999, 2014a; Main et al., 2001; Rawling et al., 2001; Sternlof et al., 2006; Ambrose et al., 2008; Rotevatn and Fossen, 2011; Fachri et al., 2013; Ballas et al., 2014; Zuluaga et al., 2016), so that they need to be considered during geologic CO_2 sequestration, Enhanced Oil Recovery (EOR), and well production. Some studies (Matthai et al., 1998; Walsh et al., 1998; Fossen and Bale, 2007), on the other hand, have shown that major effects on fluid flow and production arise only where there is a high permeability contrast between the bands and the host rock, a large cumulative bands thickness, and/or diagenetic effects linked to the deformation. Along with changes in the hydraulic properties, deformation bands networks affect mechanical properties (e.g. frictional and cohesive strength) of granular materials (Aydin and Johnson, 1978; Underhill and Woodcock, 1987; Main et al., 2001; Anthony and Marone, 2005; Schöpfer et al., 2009; Kaproth et al., 2010; Alikarami et al., 2013). This is even more true if faults are associated to diagenetic effects (e.g. Dvorkin et al., 1991) as in the Loiano Sandstones, where the cementation further increase the porosity reduction caused by mechanical crushing and grains reorganization in the CSBs (Del Sole and Antonellini, 2019; Chapter 2). Pore-filling calcite cement is a common diagenetic feature in sandstone reservoirs (e.g. Morad, 1998), and may occur pervasively throughout the rock sequence or concentrated in some horizons as nodules with various shapes and arrangement (e.g. Bjørkum and Walderhaug, 1990). Furthermore, selective cementation linked to deformation bands in sandstones seems to be a common process (e.g. Antonellini et al., 1994a; Fowles and Burley, 1994; Eichhubl, 2001; Balsamo et al., 2012; Del Sole and Antonellini, 2019). The effects of cement within sandstone reservoirs add up to those caused by deformation structures and they may: (*i*) affect fluid flow properties and deteriorate the reservoir quality (Kantorowicz et al., 1987; Bjørkum and Walderhaug, 1990; Antonellini et al., 1999; Dutton et al., 2002; Lee et al., 2007; Caine and Minor, 2009; Eichhubl et al., 2009), (*ii*) change the mechanical properties of the rock volume, as well as fault-zone architecture and its deformative response during subsequent deformation (Dewhurst and Jones 2003; Johansen et al., 2005; Rath et al., 2011; Williams et al., 2016), and thus (*iii*) generating a strong hydraulic (Sternlof et al., 2004; Davis et al., 2006; Rotevatn et al., 2009; Farrell et al., 2014) and mechanical (Al-Harthi, 1998; Baud et al., 2005; Del Sole and Antonellini, 2019) heterogeneity. Hence, SDH need to be characterized in geometry, extension, together with their geomechanical and petrophysical properties. Those just mentioned are essential parameters during reservoir simulation (Fachri et al., 2013; Antonellini et al., 2014a) and reservoir geomechanical modelling (e.g. Zoback, 2010).

3.1.2. Sub-seismic resolution faults: characterization and detection

Porous sandstones are good geofluids reservoirs (e.g. Antonellini et al., 1999; Fisher and Knipe, 2001) but, because of their low resistance to failure, they often develop strain localization structures such as deformation bands. Their small offsets make them structural heterogeneities below seismic resolution and could be referred as Sub-Seismic Resolution Faults (SSRF from now on) or simply sub-seismic faults (e.g. Walsh et al., 1998). Along with other brittle structures (i.e. slip surfaces, joints, etc.), deformation bands are small-scale structural features which occur in the damage zone (e.g. Shipton and Cowie, 2001), the process zone (Cowie and Shipton, 1998), and the termination (Rotevatn and Fossen, 2011) of seismically mappable "major" faults or around non-tectonic structures such as shale and salt diapirs (e.g. Antonellini et al., 1994a). As mentioned earlier (*Section 3.1.1*), multiple studies have shown that SSRF may compartmentalize reservoirs and aquifers influencing subsurface fluid circulation. Besides, the hydraulic behavior of seismic-scale faults can be predicted through the analysis of their associated SSRF (e.g. Tueckmantel et al., 2010). Many progresses have been made in the field of seismic imaging to detect SSRF, e.g. the use of seismic attributes (dip azimuth, curvature, and coherency) (e.g. Lohr et al., 2008), the analysis of amplitude variations in 3D seismic models (Lohr et al., 2008), and the use of stochastic techniques to extrapolate the SSRF from seismic resolution faults (Marrett and Allmendinger, 1992). Nevertheless, still too many limits prevent the optimal detection of SSRF. These limits include processing errors, seismic noise in situations of complex fault architecture, and the seismic (vertical) resolution. Nowadays, the typical lower vertical resolution limit obtained by seismic line processing is in the order of 5-10 m offsets (Hustoft et al., 2007). Thus, SSRF cannot be properly imaged on seismic reflection profiles processed with standard and enhanced techniques (Walsh et al., 1998; Jones et al., 2008; Lohr et al., 2008). SSRF imaging, therefore, requires an integration of seismic with other methods such as reservoir modelling and fluid flow simulations via deterministic (Rotevatn et al., 2009; Rotevatn and Fossen, 2011) and stochastic approaches (Maerten et al., 2006; Fachri et al. 2013; Antonellini et al., 2014a), geomechanics-based structural restoration (e.g. Maerten et al., 2006, 2019) that incorporate information from boreholes (e.g. Shipton et al., 2002), and outcrops (e.g. Jones et al., 2008). Yet, the 2D surface field characterization of deformation bands alone does not allow to describe their spatial organization, their persistency, and continuity in the subsurface. The need to explore other methods to imagine SSRF brought us to use the ground penetrating radar (GPR from now on) to detect CSBs in the subsurface. GPR has been used with success to characterize the structure of sedimentary bodies and facies architecture (Young et al., 2003; Neal, 2004; Lee et al., 2007; Magalhães et al., 2017; Leandro et al., 2019). In structural geology, most of the GPR-based studies are in the field of paleoseismology and active tectonics (Salvi et al., 2003; Slater and Niemi, 2003; Ercoli et al., 2014). The literature about detection and structural characterization of fracture networks is far less extensive and it is focused on open fractures characterization in "non-porous" hard rocks (Grasmueck et al., 1996; Theune et al., 2006; Baek et al., 2017) and mostly in "non-natural" conditions (i.e. pits, quarries, mines, nuclear waste depositories). Only Medeiros et al. (2010) and Brandes et al. (2018) detected deformation bands in sandstones via GPR imaging.

The current study aims to characterize a sandstone reservoir analog with pervasive SDH linking outcrop-derived and subsurface information. In particular, the objectives of this work are (*i*) to detect and describe the subsurface architecture of deformation bands and associated cement nodules, i.e. their location, distribution, and geometry, via multiple GPR surveys; (*ii*) to quantify CSBs and nodules mechanic and hydrologic properties and their heterogeneity; (*iii*) to discuss the relationships that exist between the GPR-response and petrophysical and geomechanical properties. The importance of our work is to show that a GPR survey might assist and improve the structural characterization of fracture networks and SDH in outcrop analogs of faulted aquifers and reservoirs in porous sandstones.

3.2. STUDY AREA

3.2.1. Geological setting

The study area is in the Northern Apennines fold-and-thrust belt (Emilia Romagna Region, Italy), which developed since the Late Cretaceous as a result of the collision between the Adria microplate and the European plate (Cibin et al., 2001). Our work focused on the Loiano Sandstones (Cibin et al., 1993, 2001) that are part of the Epiligurian Succession, that is composed of Middle Eocene to Middle Miocene siliciclastic rocks deposited in piggy-back basins. These basins were formed on the top of the Northern Apennines accretion prism, in discordance with the underlying Ligurian units, synchronously with the Middle Eocene orogenic collision (Cibin et al., 2001). From Oligocene onwards, these basins were passively transported in a northeastward direction, and simultaneously a system of foredeep basins recorded the progressive migration of the thrust front onto the Adria continental margin (Ricci Lucchi, 1986). Extension in the internal (western) domains followed and overprinted progressively the contraction and northeastward thrusting in the external (eastern) sectors of the chain since the Miocene (Carmignani et al., 1995). The Loiano Sandstones were deposited between the Late Lutetian and the Bartonian time, thus they represent one of the oldest siliciclastic bodies of the Epiligurian Succession, and they have been interpreted as a fan-delta to proximal turbidite deposit (Papani, 1998), overlined by pelagic and hemipelagic marls (Monte Piano *Fm*). The studied outcrops are located at 44°17′40″ N latitude and 11°17′26″ E longitude (Fig. 3.1) and they are partially analogs to those presented by Antonellini and Mollema (2002) and Del Sole and Antonellini (2019; Chapter 2).

3.2.2. Loiano Sandstones properties

The Loiano Sandstones are high-porosity (20-26%; predominantly intergranular), medium- to coarse-grained, poorly consolidated, immature sandstones and conglomerate of arkosic composition. The Loiano Sandstones form a relatively small lenticular deposit (a few tens of km in width and length), with a thickness ranging from 300 to 1000 m. In the studied outcrops, the Loiano Sandstones are characterized by multiple sets of deformation bands (Figs. 3.1, 3.4 and 3.5) spatially associated to carbonate nodules (Figs. 3.2, 3.4, 3.5 and 3.9b) formed by local precipitation of calcite cement that encloses grains of the host sediment (i.e. poikilitic growth). Most of the nodules, roughly 75% of the total nodules in the area, are CSBs-parallel (Figs. 3.4, 3.5a-b and 3.9b) whereas the remaining 25% are bedding-parallel (Figs. 3.5a-b and 3.9c). The localization of nodules along the trace of a single CSB (or ZB), or the confinement of nodules in between CSBs (or ZB) is a clear demonstration of the spatial association between nodules and deformation bands (Del Sole and Antonellini, 2019). In the field, a geometrical congruency between the trend of CSBs and shape of non-bedding-parallel nodules is always clear. The CSBs are characterized by grain-size reduction (Fig. 3.5c, e) and grain-surface roughening via mechanical grain fracture acting preferentially on feldspar grains, porosity and pore-size reduction via compaction, and grain-reorganization by rotation and grain-boundary sliding. Both cataclasis and compaction, within the CSB, cause porosity reduction (1 order of magnitude), that in turn reduces the permeability by 3 orders of magnitude with respect to the host rock (Del Sole and Antonellini, 2019; Chapter 2). Cement precipitation reduces the porosity in the nodules, CSBs, and ZB further decreasing porosity. In most of the nodules (without CSBs), the host rock pores are almost filled by cement, so that the residual porosity is small (1-5%). It is not the scope of this work to characterize and describe in detail neither Loiano Sandstones features nor dimensional and microstructural properties of deformation bands and nodules. Here we sum up some of that information. For a more comprehensive description about attributes of CSBs (e.g. thicknesses, geometry, amount of slip, petrophysical properties) and nodules (e.g. size, geometry, petrophysical properties) in Loiano Sandstones, the reader is referred to Del Sole and Antonellini (2019) and references therein.

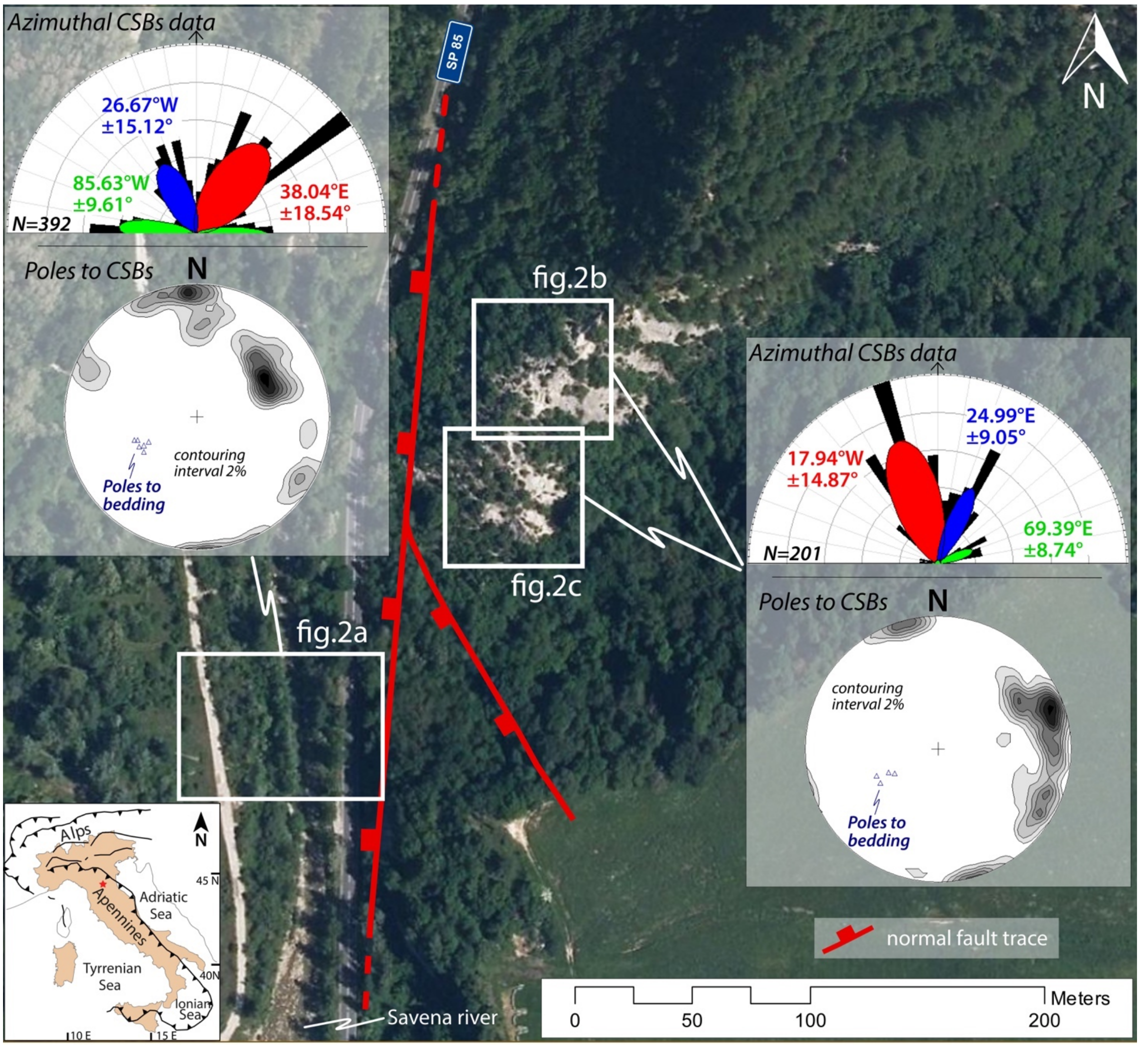

Fig. 3.1 – Aerial photograph of the outcrops. Azimuth frequency rose diagrams of the mapped deformation bands, and lower-hemisphere equal-area projection of poles to deformation bands and poles to bedding. The azimuth (± 90°) and the standard deviation (±sd) are reported for each population. Frequency of each set is ranked by colour: red (1°), blue (2°), green (3°). Stereographic projections and wind-rose diagrams of structural data were made using the *Daisy3* software (Salvini, 2004). The inset shows the position of the study area (red dot) in the Italian peninsula.

3.3. METHODS

3.3.1. In situ geological characterization

A detailed 30 meters-thick stratigraphic section log was made with the Jacob's staff method (Fig. 3.10a), along the stratigraphic succession that outcrops in the Western sector of the outcrop (Fig. 3.2a). The log reports the stratigraphy with its lithologic and textural (grain size) variations as well as the presence and distribution of CSBs, ZB, and nodules. Grain size was evaluated with a comparator chart directly in the field. Grain size and mineralogical data of Loiano Sandstones has already been extensively presented in other works (see Del Sole and Antonellini, 2019 and references therein; Chapter 2). The log in Figure 3.10a has been used as a reference frame for air-permeability (Fig. 3.10c; *Section 3.3.3*) and UCS (Fig. 3.10b; *Section 3.3.4*) measurements, to quantify the impact of each single feature (i.e. host rock properties, CSBs, and cement) on the rock-volume petrophysical and geomechanical properties. In order to observe variations of these properties within those different features, we followed the same approach described in Del Sole and Antonellini (2019; Chapter 2). The trend of the CSBs as well as nodule patterns within the host rock were documented in the field (Fig. 3.2) and on high-resolution photographs (Figs. 3.4 and 3.5).

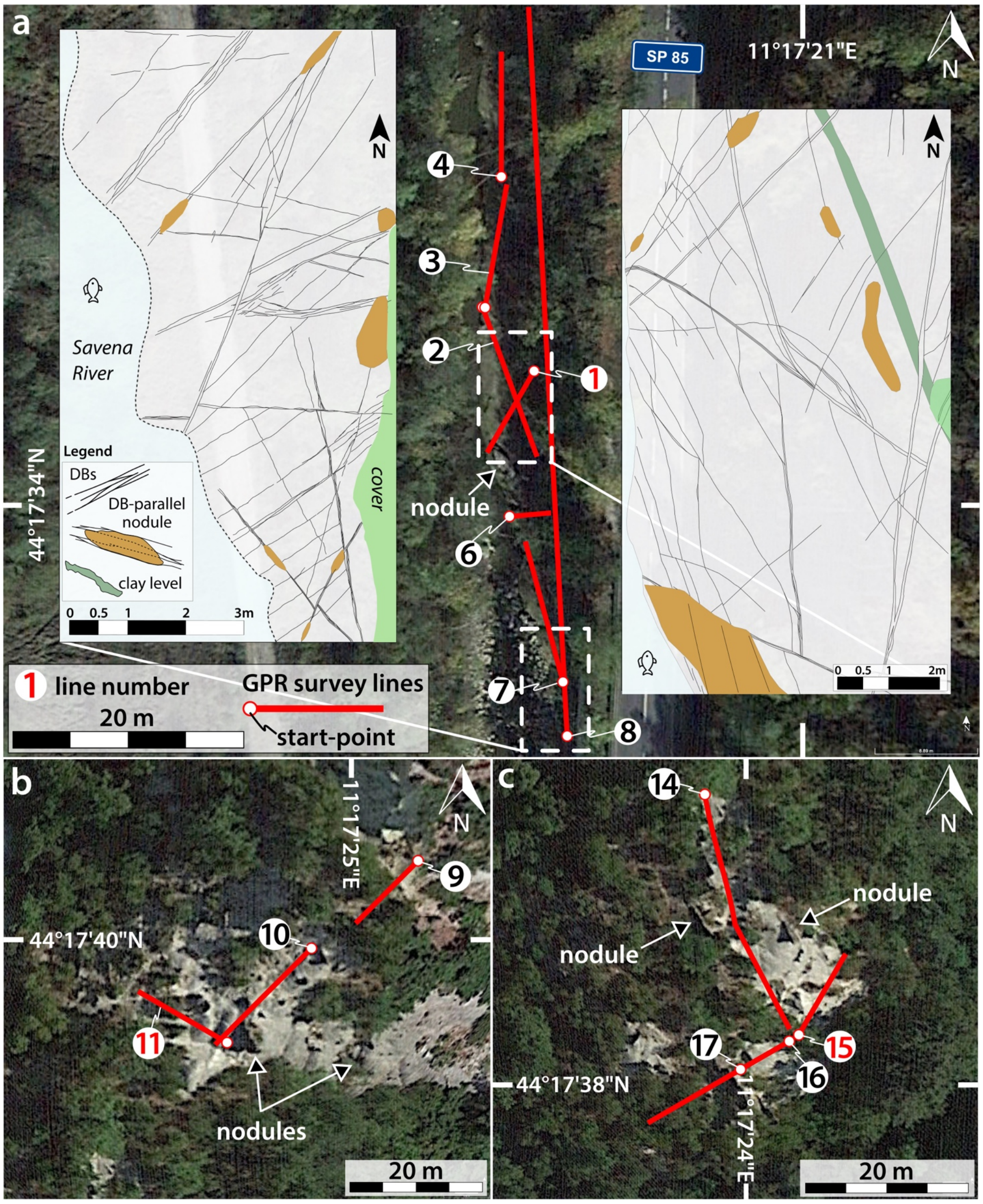

Fig. 3.2 – GPR survey line traces. Each profile is indicated by a number and by a start-point (white small circles). Profiles with red numbers are those shown in the paper. The geometry and distribution of deformation bands (DBs) and nodules is reported in two field maps in **(a)**. Some metric- to decametric-scale nodules are indicated. Latitude and Longitude are reported in degrees (°), minutes ('), and seconds (''). The location of **a**, **b** and **c** are reported in Fig. 3.1.

3.3.2. GPR: theory, data acquisition and processing

The geophysical survey was done using a Cobra Dual 10 GPR (©Radarteam Sweden AB). This instrument is equipped with two shielded antennas (bistatic configuration), two channels, and operating bandwidth from 100 to 900 MHz with a central frequency of 500 MHz. The GPR uses a broad bandwidth electromagnetic pulse (time-domain impulse radar) that spreads through the ground acting as a sounding device. The operation principle is based on the measurement of the amplitude of the electromagnetic wave reflected where a contrast of dielectric permittivity (ε_r) is present and in the detection of the wave-travel-time to the receiving antenna after the pulse has been emitted (Annan, 2009). The depth (z) at which the reflection took place can be calculated from the time interval between the emission and the reception of the electromagnetic wave, and from its propagation velocity in the traversed medium. The construction of the GPR profile is achieved by vertically flanking all recordings related to each emitted pulse. The GPR is equipped with four wheels that ensure the coupling between the GPR antenna and the rock surface (see Fig. 3.3). The geometric matching between the survey lines (traces) and the position is ensured by a wheel equipped with encoder that links the rotation of the wheel with the distance travelled. The vertical resolution is a function of (i) the wavelength (λ) of the emitted signal and (ii) the dielectric permittivity of the medium that controls the velocity (v) of the electromagnetic wave. Vertical resolution is independent of depth and is around $\lambda/4$ (e.g. Neal, 2004). The horizontal resolution is obtained from the Fresnel radius and is about $(z \times \lambda/2)^{0.5}$, and it is lower the deeper the signal penetrates. Recording at different frequencies allow investigations at different depths (Olhoeft, 1998). Data were recorded using two channels simultaneously: the first one at high frequency (500 MHz) for shallow imaging (1.88 m), and the second one at low frequency (300 MHz) for deeper imaging (3.75 m). Higher resolution in depth means lower horizontal resolution, thus we used both channels data.

Careful observations were made in the field of the geometry and distribution of CSBs and the carbonate nodules (Figs. 3.2, 3.4, and 3.5) to arrange a suitable network of GPR survey lines (Fig. 3.2). Fourteen GPR-lines were recorded (Fig. 3.2). In particular, GPR lines were taken normal to the major CSBs trends, in the direction of their dip (Fig. 3.2). Hence, the study of the outcrop was essential to understand the structural framework, plan the survey, and interpret the profiles. The GPR surveys were carried out in March 2019. In particular, during the acquisition, the mean temperature was 12°C and mean humidity was 50%. What we call "Eastern outcrop" (see *Section 3.4.1*) is close to the water table (see proximity to the river in Fig. 3.2a, 3.5a-b), and it is in "wet" conditions. What we call "Western outcrop" (Fig. 3.2b-c) is a bit higher than water table level when compared with the Eastern outcrop. Anyway, despite being not completely saturated, some water is still present in the Eastern outcrop; it is mostly bonded pore water of meteoric origin or derived from "capillary suction" from the saturated zone below. All GPR profiles were processed following a standard procedure (Fig. 3.3) and elaborated with the *Prism 2 software* (*RADAR Systems, Inc.*). A first step consists of background noise signal removal. The noise is caused by the strong reflection of the ground that generally masks the amplitude of the signal of interest. The automatic gain control (AGC) has not been applied systematically because of its feature of indiscriminately levelling the entire track. Thus, the gain function (Fig. 3.3) has been modified, manually, by adapting it point by point to reinforce or suppress the signal, i.e. the amplitude of reflections, only in certain areas of the profile to enhance the target of interest. The profiles have been migrated only in two cases (lines: 1 and 7). This choice was motivated by the decrease in visibility of interesting structures and by the inability of the software to migrate different areas of the profile characterized by different wave propagation velocities. Finally, the depth conversion of the wave travel time was carried out. Concerning the choice of ε_r and the resulting EM propagation velocity, we chose an appropriate value that characterize wet, not-completely-saturated, poorly-consolidated sandstones (see Tab. B.1 in Appendix B). The same ε_r value was applied in both outcrops due to similar saturation conditions. At each profile, we considered a constant EM propagation velocity for the whole depth. We think that this assumption is reasonable considering that at the scale representative of each profile (length and depth), the medium (host rock) is quite homogenous (i.e. sandstone). Clay and gravel levels are only sporadic and of limited thickness (from a few mm to a few cms). Different permittivities in the range of wet sandstones (see e.g. Cassidy, 2009) were tested, and the results changed slightly. For example, with $\varepsilon_r = 10$ the velocity would be equal to 9.5×10^7 m/s, and the penetration depth would be 2.37 m in the shallow range (500 MHz) and 4.74 m in the deep one (300 MHz). Please refer to Appendix B for further information about GPR's setup, EM material properties, and GPR profiles resolution. As a further processing step, the instantaneous attributes (e.g. Lemke and Mankowski, 2000) such as instantaneous amplitude or trace envelope and instantaneous phase were considered. Instantaneous amplitude is a function of the contrast in dielectric permittivity of the substrate and has always a positive value. This attribute allows identifying areas that have higher (bright spots) or lower (dim spots) dielectric permittivity than the surrounding zones. The instantaneous phase tends to emphasize the geometry and lateral continuity of the lithological and sedimentary structures.

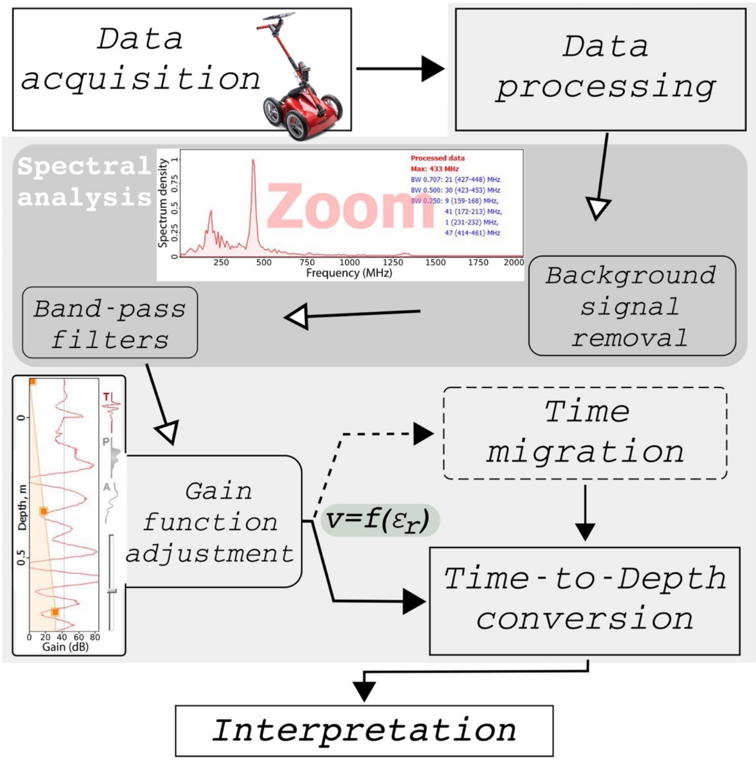

Fig. 3.3 – Flowchart that summarizes the procedure used on GPR data from the acquisition, through the processing steps (light grey), to the interpretation. The section in dark grey (background signal removal and band-pass filters) involves the spectral analysis: here, a graph example of spectrum density (y-axis) as a function of frequency (MHz) is shown. Then, the gain function adjustment: here, a graph example of signal gain function (dB) versus depth (meters) is shown. Time migration, in dotted line box, was applied only on two sections. In order to perform both time migration and time-to-depth conversion, the waves velocity in the medium need to be known. In turn, the velocity is a function of the dielectric permittivity (ε_r).

3.3.3. In situ air-permeability measurements

The assessment of petrophysical properties is essential to understand how SDH affect the host rock properties and to evaluate what might be the impact of these structures on the subsurface fluid flow (see *Sections 3.1.1* and *3.1.2*). Del Sole and Antonellini (2019; Chapter 2) computed with the Kozeny-Carman relation the permeability for bands where only cataclasis and compaction are present and could not account for the effect of cement precipitation. In the present paper, bulk-permeability was evaluated *in situ* by mean of air permeameter tests. Permeability was measured, using a TinyPerm 3 (*New England Research, Inc.*) portable air permeameter. The instrument has a rubber nozzle with a central hole (5 mm in diameter) and an outer seal (15 mm diameter). Considering the tip-seal internal radius and the flow-geometry, the permeameter sample a volume of about 1 cm^3 (Antonellini and Aydin, 1994). Hence, we tried to measure permeability only in ZB at least 1 cm thick. Prior to permeability measurements, sampling surfaces were carefully scraped and brushed to remove weathering effects and dust. The nozzle was wrapped up with “putty rubber” to avoid air slippage between the nozzle and the sampling surface. Measurements were repeated multiple times, at least 3

(7 on average), on each location to sort out anomalous measurements. The replicability of the results is supported by other independent measurements, such as image analysis (Del Sole and Antonellini, 2019; Chapter 2) and falling head permeability tests on core plugs (unpublished data; see *Section A.5* in Appendix A). A total of 348 permeability measurements were collected for the host rock (n=174), CSBs (n=56), and nodules (n=118). Boxplots that show the results of measurements done on each single feature (Fig. 3.12) were made with the *R* software (R Core Team, 2018).

3.3.4. In situ Schmidt hammer rebound index measurements

Since fracture networks and related diagenetic effect (here named SDH), affect also mechanical properties of the host rock (see *Section 3.1.1*), the variations of uniaxial compressive strength (UCS from now on) were evaluated measuring rebound values using an L-type Schmidt hammer made by DRC® (Diagnostic Research Company), with an impact energy of 0.735 N×m and a measurement range of 10–200 N/mm2 (MPa). Measurements were repeated multiple times, at least 4 (9 on average), on each location, using a square grid with a cell size of 0.04 m to avoid repeating the measurements exactly on the same spot and to sort out anomalous measurements. A total of 523 rebound measurements were collected for host rock (n=302), nodules (n=156) and CSBs (n=65). Boxplots that show the results of measurements done on each single feature (Fig. 3.12) were made with the *R* software (R Core Team, 2018). The rebound of a spring-loaded mass impacting against the chosen rock surface is converted in a rebound index (*I*) readable on the Schmidt hammer. Then, the index *I* can be correlated empirically, via a calibration chart, to the UCS, the shear modulus (rigidity), or other rock physical properties (e.g. Aydin and Basu 2005; Chang et al., 2006). Here, the index *I* is correlated with the UCS (in MPa) by the following formula, $\mathrm{UCS} = \mathrm{a} \times \mathrm{I}^{\mathrm{b}}$ (Eq. 2.1; Menditto et al., 2013), where *a* and *b* are two empirically derived correlation parameters that depend on the angle between the hammer axis and the sample surface. We used different empirical curves, provided by the manufacturer, to obtain UCS values from measurements with different rebound angles (see Menditto et al., 2013 for instrument technical specifications).

In this paper, besides assessing the difference in petrophysical and mechanical properties between host rock, deformation bands, and nodules, we distinguish different types of nodules. We differentiate isolated or multiple nodules with CSBs, bedding-parallel isolated-nodules without CBSs, and nodular-beds, to evaluate separately the effects of CSBs and cement on petrophysical and mechanical properties. Where possible, permeability and UCS in CSBs, ZB, and nodules were estimated both parallel and normal to the rock face in a way to measure any anisotropy in the petrophysical and mechanical properties (Figs. 3.11 and 3.12). Other than evaluate the impact of deformation and diagenesis on the petrophysical and mechanical properties of the host rock, our objective is to correlate, in a qualitative way, those two characteristics with the GRP response of each feature, let's say a GPR "facies" (Huggenberger, 1993; Lee et al., 2007; see *Section 3.5.3*).

3.4. RESULTS

3.4.1. Outcrop data

The outcrops presented here are in proximity of a high angle (~75°) normal fault striking nearly N-S and dipping W (Fig. 3.1). We subdivide the studied area in two sub-sectors considering their position with respect to the fault; a Western sector in the hangingwall (Figs. 3.1 and 3.2a) and an Eastern sector in the footwall (Figs. 3.1 and 3.2b-c). Figure 3.1 shows rose diagrams for the azimuthal CSBs data, and lower-hemisphere equal-area projection of poles to CSBs and poles to bedding (NE dipping). Azimuth frequency rose diagrams shows that CSBs occur in three main sets with NW-SE, NE-SW, and roughly E-W orientations (Fig. 3.1). No major differences exist between the Eastern and Western sector in terms of trend of the main populations of CSBs. Secondary differences are: (i) the most frequent set in the Western sector is the NE-SW one (38.04°E±18.54; red line in Fig. 3.1), followed by the NW-SE one (26.67°W±15.12; blue line) whereas the most frequent set is the NW-SE one (17.94°W±14.87; red line) followed by the NE-SW one (24.99°E±9.05; blue line) in the Eastern sector; (ii) the least frequent set (green lines) is WNW-ESE (85.63°W±9.61) in the Eastern sector, and ENE-WSW (69.39°E±8.74) in the Western one (Fig. 3.1); (iii) the CSBs attitude in the Western sector shows, on average, higher dip angles with respect to those in the Eastern sector. In the field, CSBs are recognized as thin bands with a different color from that of the host rock, generally whitish (Figs. 3.5c-e and 3.9a-b). In most cases CSBs weather out in positive relief with respect to the surrounding poorly consolidated host rock (Figs. 3.5c, e and 3.9b). The distinctive feature of the Loiano Sandstones in the area studied is a spatially heterogeneous carbonate cementation. The carbonate cement is in the form of tabular concretions, isolated or multiple spheroids, and irregular shape nodules (Figs. 3.4, 3.5a-b, 3.9b-c, 3.11). These diagenetic structures are also more resistant to weathering with respect to the poorly cemented host rock. Neither bedding-parallel isolated-nodules nor nodular-beds are related to CSBs, but they are organized along bedding surfaces. Nodular beds are continuous pervasively-cemented layers (Fig. 3.5a-b). They differ from bedding-parallel isolated-nodules, because of their tabular geometry (thickness between 35-50 cm) and continuity along the bedding plane for several meters (up to 15 m in length) (Fig. 3.5a-b; see also Del Sole and Antonellini, 2019). Sometimes, extensional fractures and veins develop within the nodules (Fig. 3.4d-e) but they do not propagate into the host sandstone (see *Section C.8* in Appendix C for details). For additional nodule characteristics the reader is referred to Del Sole and Antonellini (2019; Chapter 2). Most of the stratigraphic succession in the log of Figure 3.10a is composed by medium- to coarse-sandstones. The bedding is easy to observe thanks to the nodular beds, a few levels of clay and silt, and sporadic well-defined thin levels of very fine- to medium-gravel (Figs. 3.5a-b and 3.9a).

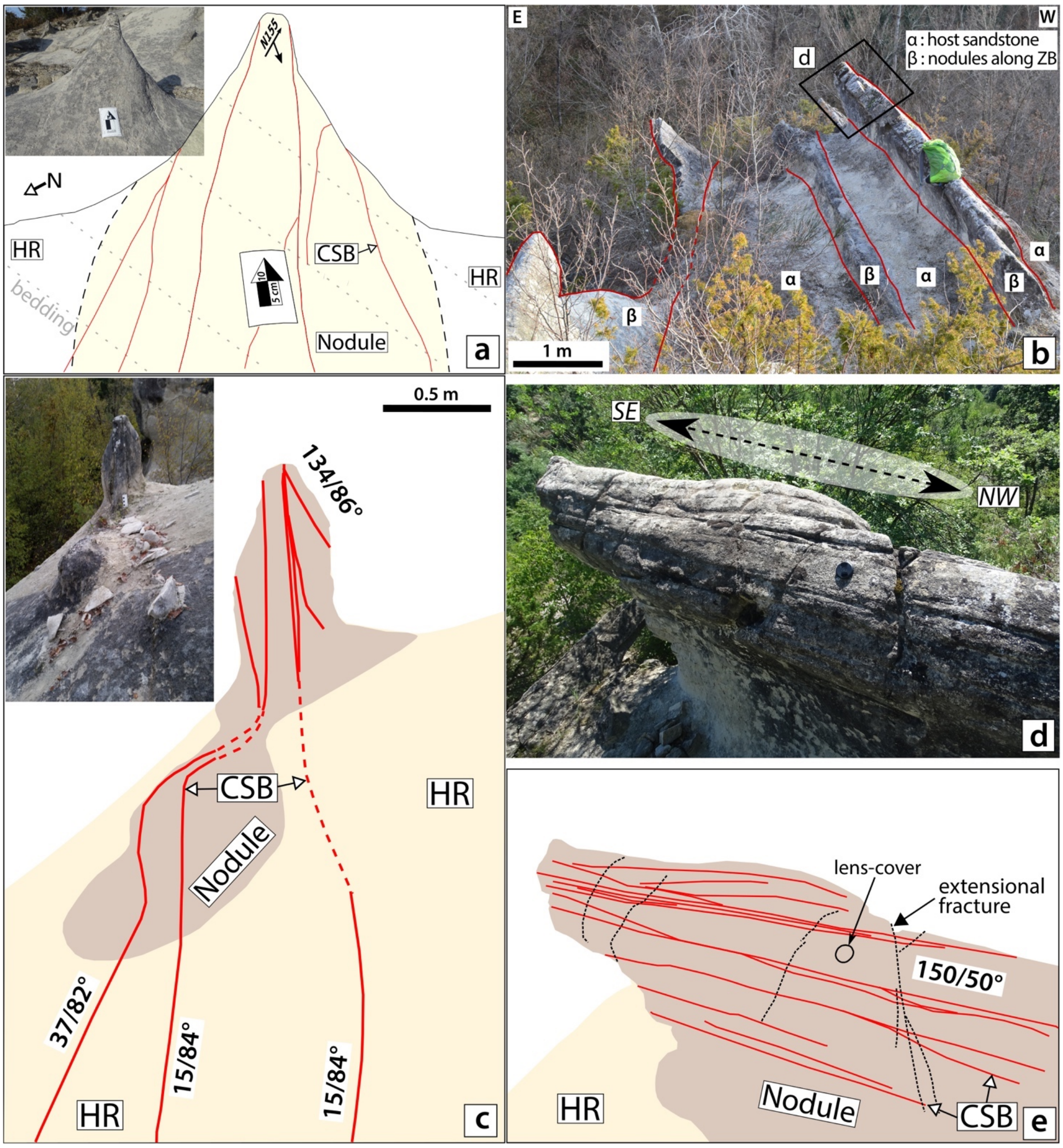

Fig. 3.4 – **(a-e)** Typical relationships between carbonate diagenetic structures (nodules) and CSBs/ZB. Nodules along CSBs and ZB are isolated **(a, c)** or tabular **(b, d-e)**. Post-CSB opening fractures cut through the assemblage "nodule – CSB" and they do not propagate into the soft and poorly consolidated host rock (HR). The lens-cover for scale is 55 mm. Azimuth is expressed in right-hand rule (strike/dip°). These examples are form the Eastern sector (Fig. 3.2b-c).

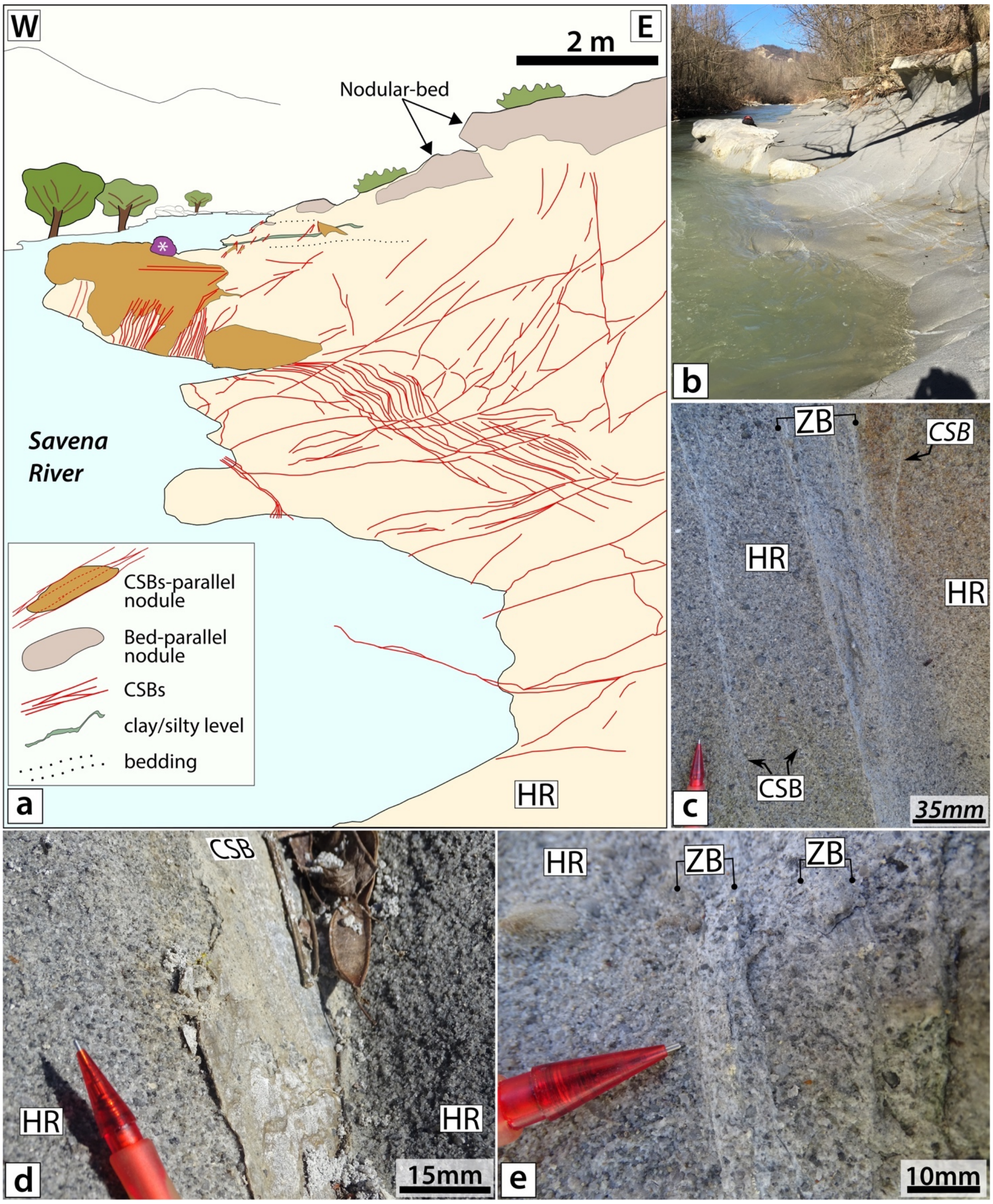

Fig. 3.5 – **(a-e)** Field evidence of CSBs and nodules in the Western sector (Fig. 3.2a). **(a)** Sketch from a field photo **(b)** that summarizes the geometry and distribution of CSBs and nodules as well as their spatial relationships. Asterisk (*) indicates a small backpack for scale (50 cm). **(c, d, e)** Close-up on CSBs; they are present as single structures or organized in zone of bands (ZB). CSBs exhibit a whitish colour with respect to the host rock (HR), a clear reduction in grain size, a lower porosity, and a positive relief **(c, e)**.

3.4.2. Ground-penetrating radar data

The interpretations of selected GPR profiles are shown in Figs. 3.6, 3.7, and 3.8. In the profiles, the position of bedding planes, CSBs, and nodules were interpreted. The reflections dipping to the NE in NE-SW trending profiles represent bedding planes (Figs. 3.6 and 3.8); bedding in the NW-SE trending profiles (Fig. 3.7), which is also the layering strike direction, is nearly horizontal. In general, reflections from the bedding do not have a good continuity. All GPR profiles show the presence of nearly vertical (Figs. 3.6, 3.7 and 3.8) and SW-dipping linear features (Fig. 3.6) that systematically offset reflectors related to primary sedimentary structures, i.e. bedding. Those linear features are interpreted as CSBs or ZB plane intersection with the GPR profile. Zone of bands are interpreted either as offsets of GPR reflections (Figs. 3.7 and 3.8) or as inclined reflections (Figs. 3.6 and 3.7). These geometries can be well recognized using the instantaneous phase (Figs. 3.6d). In most cases, CSBs and ZB are expressed as linear features where the electromagnetic reflectors have strong amplitudes (Figs. 3.6, 3.7 and 3.8). In other cases, CSBs are expressed as low amplitude bands (Fig. 3.6; see ellipse in 3.6c). Nodules are expressed as high amplitude zones that appear as "bright spots" in the instantaneous amplitude attribute images (Figs. 3.6c, 3.7c and 3.8c). Bedding-parallel nodules (Fig. 3.6a) were distinguished from CSBs (or ZB)-parallel nodules considering (i) the bedding attitude, (ii) the surface evidence along the survey line, and (iii) the presence, in the profile, of linear features interpretable as CSBs (or ZB) associated with the concretion. In general, dip angles of CSBs and ZB in GPR profiles are coherent with those measured in the field (Fig. 3.1). In GPR profiles, CSBs and ZB are nearly subvertical, mostly in the Eastern sector (Figs. 3.7 and 3.8), or they are south-westward dipping, especially in the Western sector (Fig. 3.6). In some cases, it seems that the presence of cement (i.e. nodules) masks the signal associated to the CSBs in the GPR profiles (Fig. 3.7). The number of interpreted elements is larger near the surface than in the deeper sectors, because of the better control between outcrop data and GPR profile at the surface. Nevertheless, there are multiple cases in which we were able to interpret CSBs (and ZB) and nodules that do not reach the surface (Figs. 3.6, 3.7 and 3.8). In figure 3.9 we compare the different features (bedding planes, CSBs, bedding-parallel nodules, CSBs-parallel nodules) observed in the GPR profiles, so that it is possible to define a GPR "facies". This allows a quick and reliable profile interpretation, and the identification of structures also at depth.

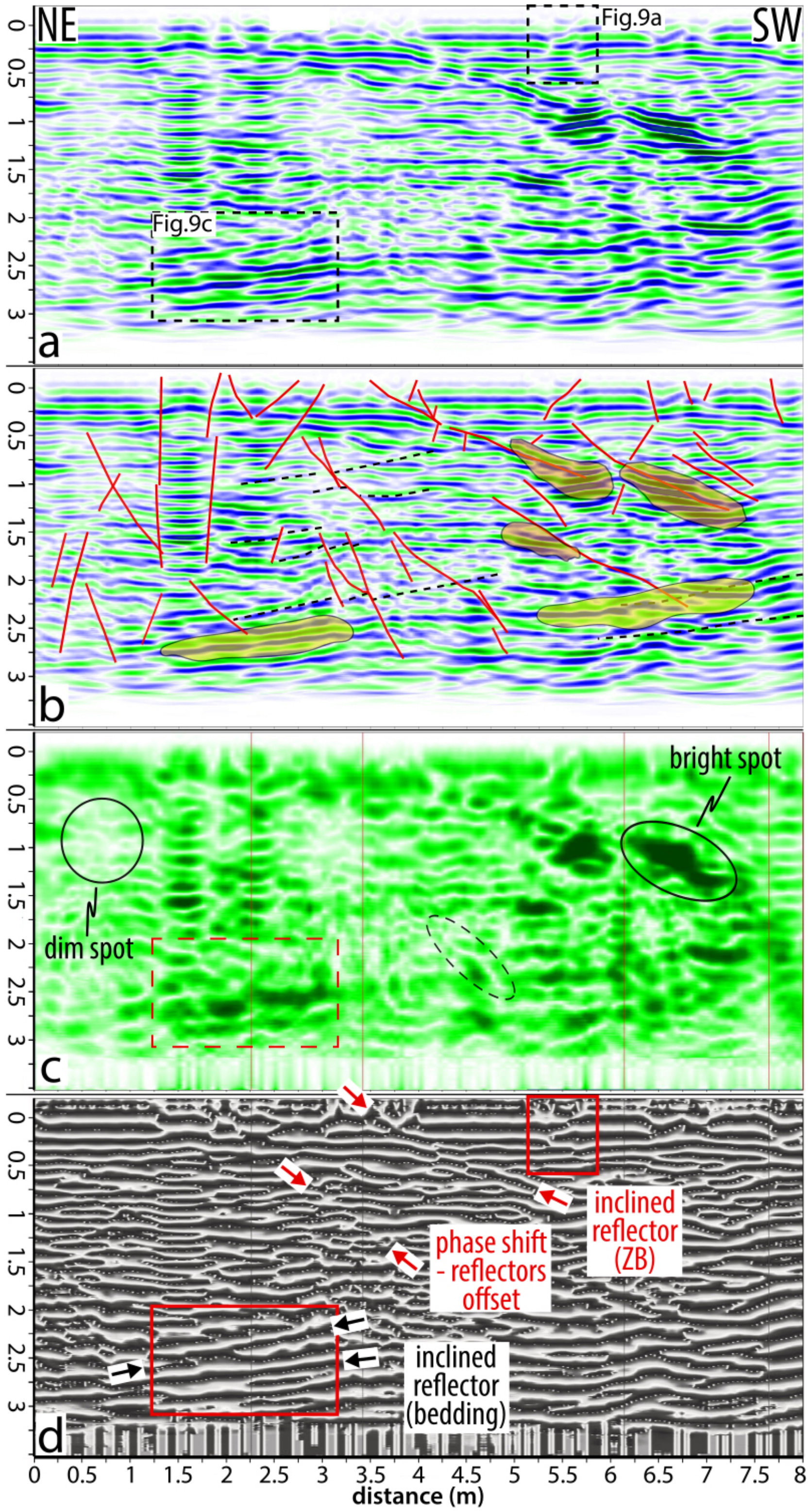

Fig. 3.6 – **(a-d)** GPR line "DAT_0001_CH_2_migrated" recorded in the Western sector outcrop (Fig. 3.2a). **(a)** Uninterpreted GPR line. **(b)** Interpreted GPR line. Bedding planes (black dashed lines) are identified as NE-dipping reflectors. Vertical and SW-dipping linear features that offset bedding reflectors represent CSBs and ZB (red lines). ZB are expressed also as inclined reflectors. The areas in brown and yellow are CSBs/ZB-parallel nodules and bedding-parallel nodules (NE-dipping), respectively. **(c-d)** Instantaneous attributes: **(c)** instantaneous amplitude or trace envelope and **(d)** instantaneous phase. Those indicated as dim spot and bright spot in trace envelope are low-amplitude (e.g. porous sandstones) and high-amplitude (e.g. nodules) areas, respectively. The dashed line ellipse indicates a case in which a low-amplitude band coincides with a CSB. Horizontal and vertical distances are in meters.

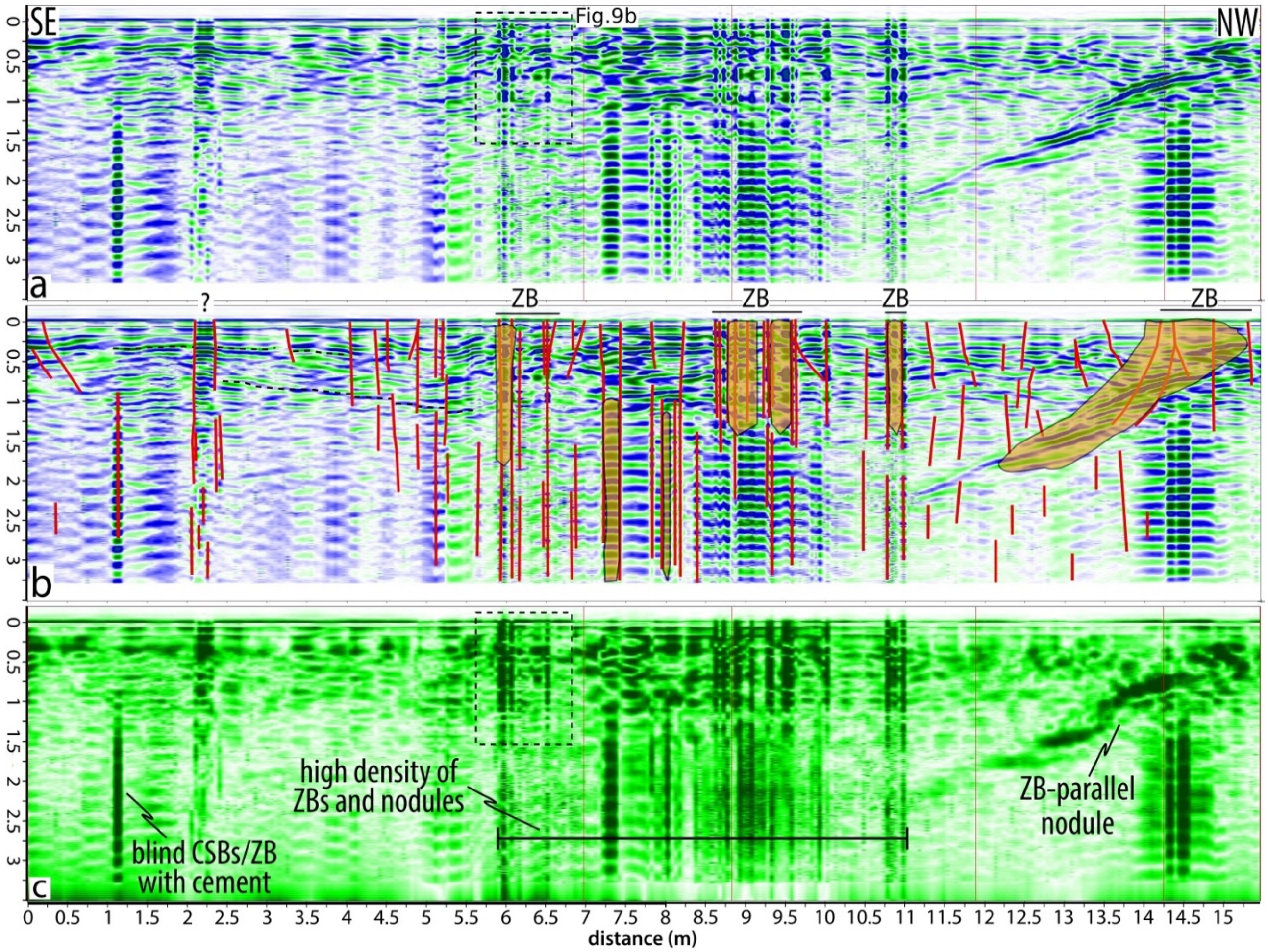

Fig. 3.7 – **(a-c)** GPR line "DAT_0011_CH_2" acquired in the Eastern sector outcrop (Fig. 3.2b). **(a)** Uninterpreted GPR line. **(b)** Interpreted GPR line. Here, the bedding (black dashed lines) is nearly horizontal. Mostly vertical linear features that offset bedding reflectors represent CSBs and ZB (red lines). ZB are expressed also as inclined reflectors. The areas in brown are CSBs/ZB-parallel nodules **(c)** Instantaneous amplitude (trace envelope) profile. Zone of bands and associated nodules are expressed as high-amplitude areas (bright spot), while the surrounding porous sandstones are expressed as low-amplitude (dim spot) areas. Nodules and "blind" CSBs/ZB that do not reach the surface were identified. Horizontal and vertical distances are in meters.

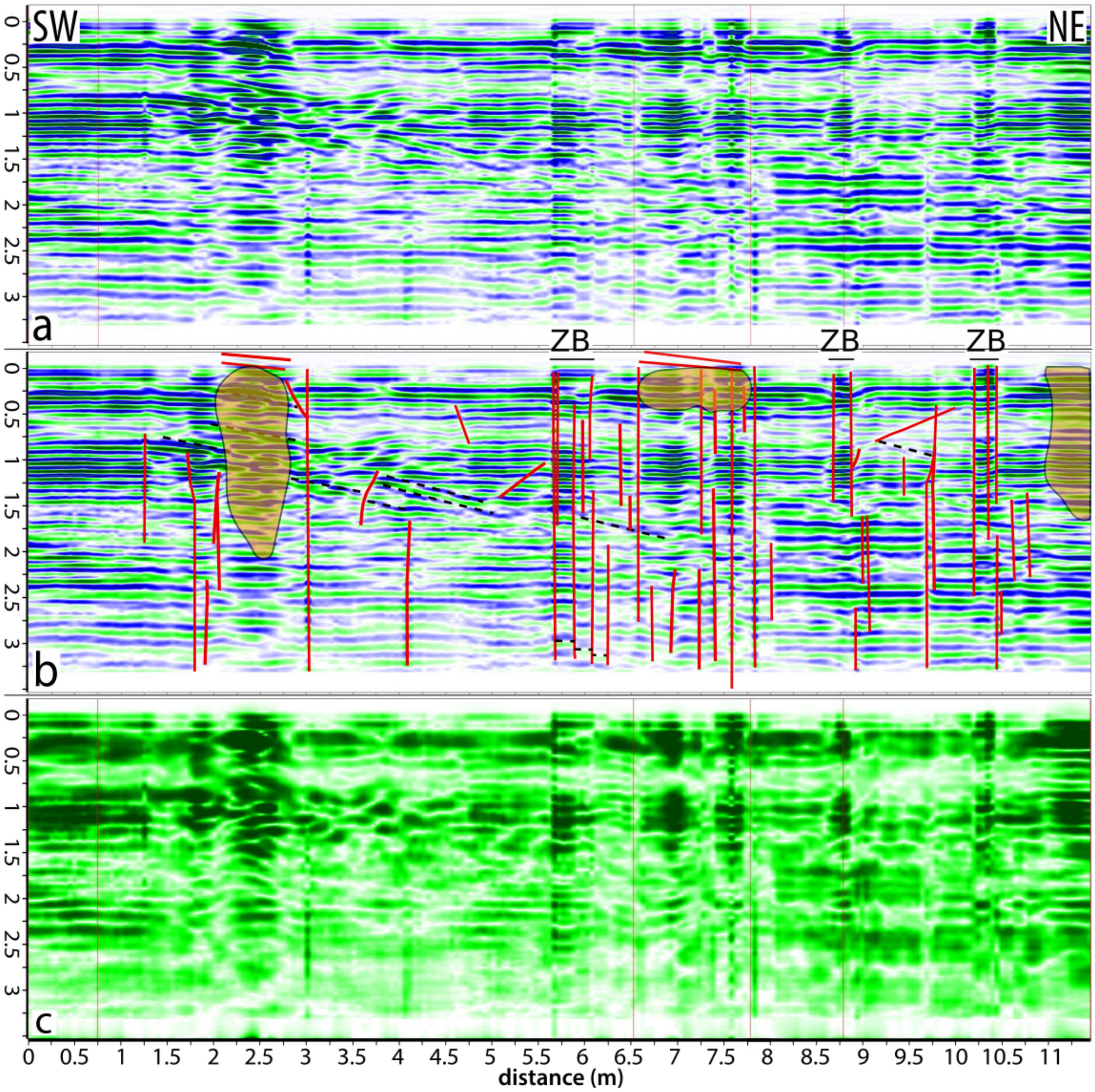

Fig. 3.8 – **(a-c)** GPR line "DAT_0015_CH_2" acquired in the Eastern sector outcrop (Fig. 3.2c). **(a)** Uninterpreted GPR line. **(b)** Interpreted GPR line. Bedding planes (black dashed lines) are identified as NE-dipping reflectors. Mostly vertical linear features that offset bedding reflectors represent CSBs and ZB (red lines). The areas in brown are CSBs/ZB-parallel nodules. The nodule at about 7 meters of distance from the beginning of the profile is associated to a cluster of CSBs that is parallel to the profile trend (NE-SW). **(c)** Instantaneous amplitude (trace envelope) profile. Zone of bands and associated nodules are expressed as high-amplitude areas (bright spot), while the surrounding porous sandstone is expressed as a low-amplitude (dim spot) area. Horizontal and vertical distances are in meters.

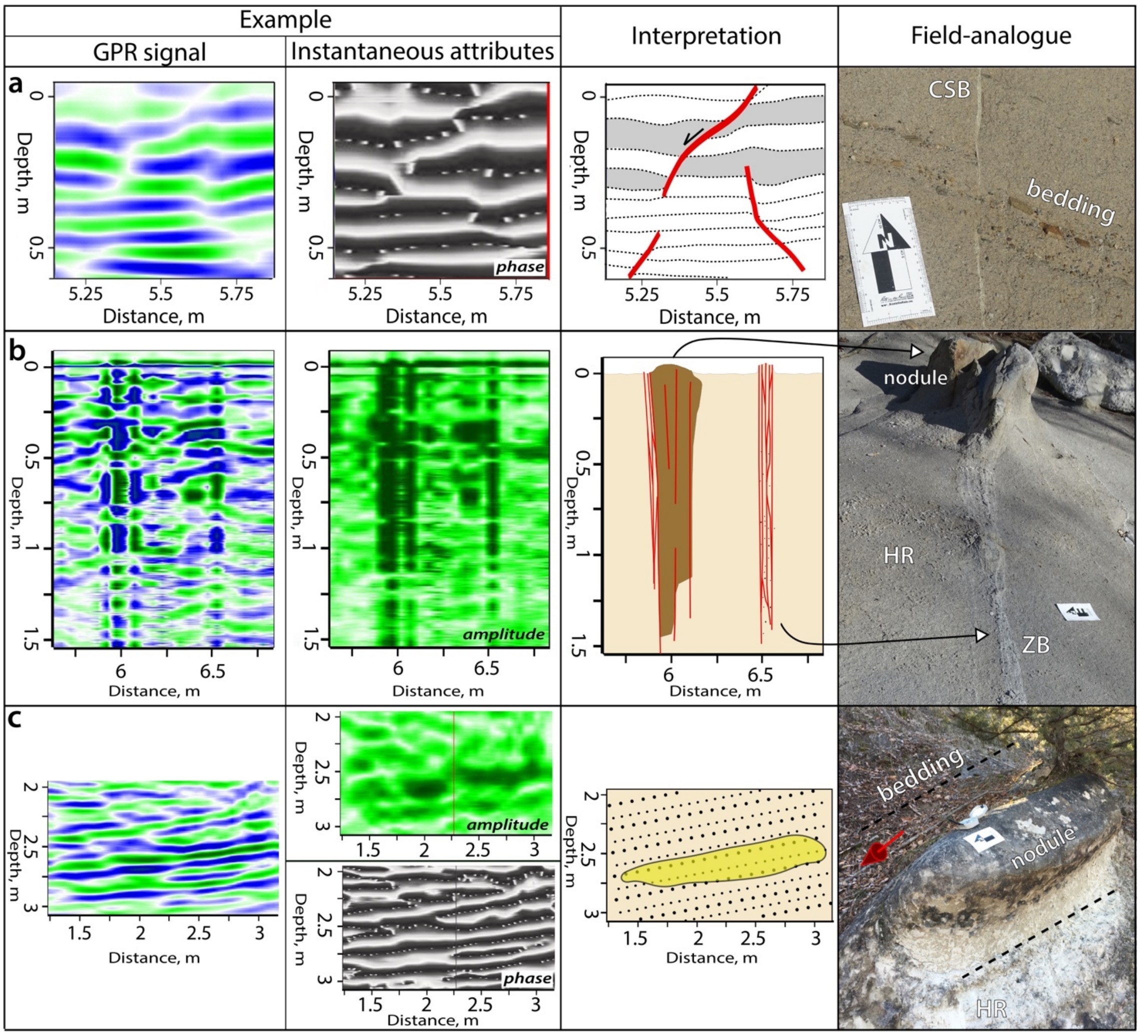

Fig. 3.9 – **(a-c)** GPR "facies" for CBSs and ZB, nodules (CSB-parallel and bedding-parallel), and bedding surfaces. For each feature the GPR signal (1st column), the instantaneous attributes: amplitude and phase (2nd column), an interpretative sketch (3rd column), and a photo of the field-analog (4th column) are shown for comparison. **(a)** and **(c)** were taken from the GPR line in Fig. 3.6; **(b)** was taken from GPR-line in Fig. 3.7.

3.4.3. In situ geomechanical characterization

Results of *in situ* compressive strength measurements are shown in Figs. 3.10b and 3.11, and Table 3.1. Figure 3.10b shows UCS results measured along the stratigraphic log of Fig. 3.10a and reports error bars that define the 95% confidence level for each data point. Focusing on Fig. 3.10b, our results show that the host rock has the lowest strength among the measured features. Host rock UCS values represent rock strength after compaction but before any deformation or cement precipitation occurred. Host rock UCS values have a low variability both at the scale of the single measurement, i.e. narrow error bars (Fig. 3.10b), and at the scale of the entire sampled succession. This low variability is proved by: (i) all blue points in Fig. 3.10b are clustered in a narrow vertical line that ranges from 0 to 30 MPa, and (ii) boxplot of UCS values (Fig. 3.11a) shows that both whiskers and interquartile range have a low standard deviation (Table 3.1). UCS values for CSBs and nodules depart from host rock values having higher strength and variability with a high standard deviation (Figs. 3.10b and 3.11a; Table 3.1).

The distribution of the UCS values for each single feature (host rock, deformation bands, nodules) was also considered, and the results are shown in Fig. 3.11 and Table 3.1. The boxplots show the following: (1) The lowest values were recorded along the relatively undeformed low-consolidated protolith (Fig. 3.11a). (2) Host rock UCS values decrease with increasing grain-size (Figs. 3.11b and 3.10b); very-fine to medium grained sandstone (VFM) shows the highest values; medium to very-coarse sandstone (MVC) shows intermediate values; gravel beds (G) show the lowest values. Instead, clay-silt (CS) levels show the lowest host rock UCS values of the entire rock volume. (3) UCS values of CSBs (Figs. 3.10b and 3.11a) have intermediate values between those recorded in the host rock and those recorded in the nodules. (4) Normal to CSB UCS values tend to be higher when compared with parallel to CSB UCS values (Fig. 3.11c). (5) Nodules have the highest strength (Figs. 3.10b and 3.11a) among all considered features. (6) Among all nodules, the lowest UCS values were reported along isolated nodules without CSBs; CSBs-parallel nodules show intermediate values; the highest UCS were reported for continuous nodular beds (Fig. 3.11d). (7) Lastly, if we consider measurements taken parallel and normal to the nodular beds (Fig. 3.11e), we observe that parallel-measured values are systematically higher than the normal ones.

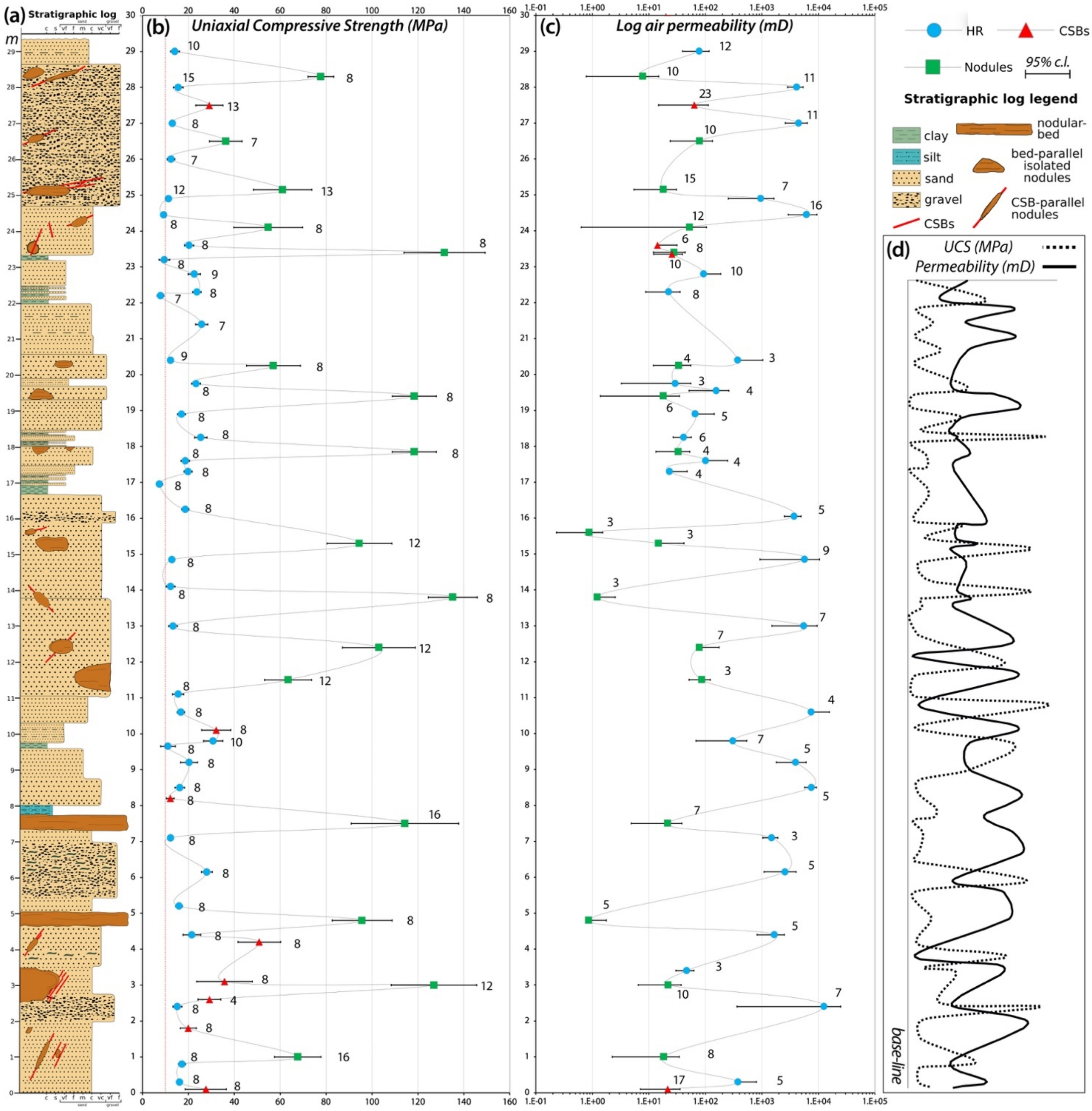

Fig. 3.10 – **(a-c)** Stratigraphic, geomechanical, and petrophysical logs of the 30 meters-long outcrop succession shown in Fig. 2a. **(b-c)** Scatter plot with error bars (95 % confidence level) of **(b)** UCS values (MPa) derived from Schmidt hammer rebound measurements and **(c)** air-permeability values (mD) derived from portable permeameter measurements. Data points are subdivided into host rock (blue circles), CSBs (red triangles), and nodules (green squares). The number of measurements in each location is reported on the right side of the corresponding point. Vertical red dashed line in **(b)** indicates the lower bound (~10 MPa) of the instrument measurement range. HR stands for host rock. **(d)** The paired UCS (dotted line) and air-permeability (solid line) curves trend highlight the inverse pattern between those properties along the considered stratigraphic section.

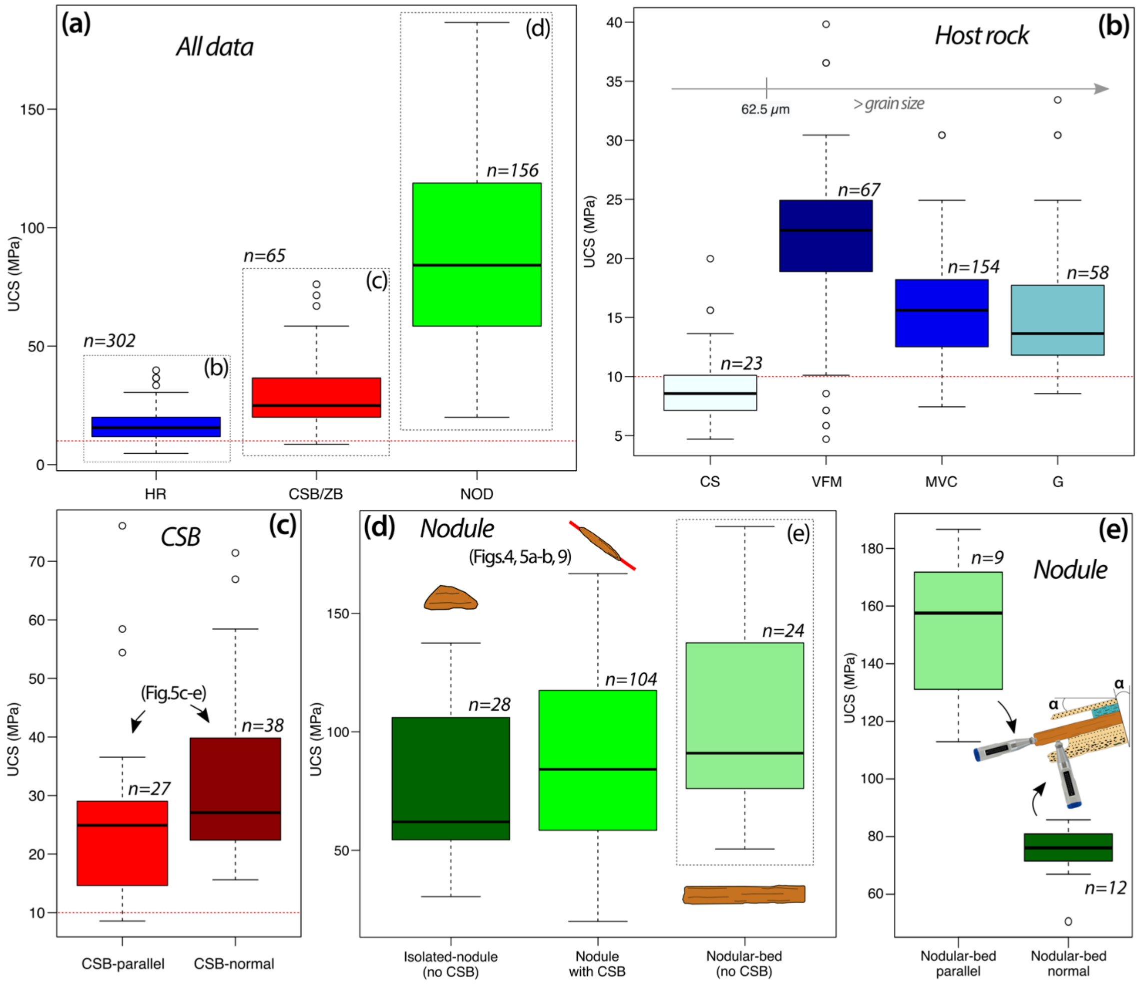

Fig. 3.11 – *In situ* compressive strength (MPa) measurements results. **(a)** - Total UCS data for host rock (HR; blue), CSBs (red), and nodules (NOD; green). **(b)** - UCS values for host-rock as a function of grain-size: gravel beds (G), medium to very coarse-sand (MVC), very-fine to medium sand (VFM), and silt/clay (CS). **(c)** - UCS values for CSBs as a function of measurements taken parallel (par) and perpendicular (perp) to the CSB's plane. **(d)** – UCS values for each nodule type: bedding-parallel isolated-nodule (without CSBs), nodule with CSBs, and nodular-beds (without CSB). **(e)** – UCS values for nodular-beds as a function of measurements taken parallel and perpendicular to the nodule greater dimension. Horizontal red dashed line in **(a)**, **(b)** and **(c)** indicates the lower bound (~10 MPa) of the instrument measurement range. The black thick line in the boxplots is the 2nd quartile (median), the lower and upper box sides are the 1st and 3rd quartiles respectively. The lower and upper whiskers define, respectively, the minimum and maximum observed values in the data range excluding the outliers (dots). Number of measurements - n - is indicated on each boxplot. See Table 3.1 for statistical parameters of the results.

Table 3.1
Uniaxial Compressive Strength data and statistical parameters.

Uniaxial Compressive Strength (MPa)									
	Feature	**Data N**	**Median**	**Mean**	**Std. Dev.**	**Mode**	**Min**	**Max**	**Fig. ref.**
UCS by feature	HR	302	15.61	16.77	6.40	15.61	4.70	39.82	*3.11a*
	CSB/ZB	65	24.92	29.59	14.81	24.92	8.56	76.07	
	NOD	156	84.17	89.61	38.26	76.07	19.98	186.62	
HR UCS by grain size	CS	23	8.56	9.58	3.61	8.56	4.70	19.98	*3.11b*
	VFM	67	22.38	21.96	7.47	22.38	4.70	39.82	
	MVC	154	15.61	16.01	4.51	15.61	7.44	30.44	
	G	58	13.64	15.65	6.03	11.81	8.56	33.42	
CSB UCS by measurement angle	CSB-normal	38	27.09	31.91	13.83	19.98	15.61	71.43	*3.11c*
	CSB-parallel	27	24.92	26.34	15.78	24.92	8.56	76.07	
Nodule UCS by nodule type	Nodule with CSBs	104	84.17	88.64	38.12	76.07	19.98	166.73	*3.11d*
	Isolated-nodule (no CSBs)	28	62.01	77.35	31.08	118.81	30.44	137.45	
	Nodular-bed (no CSBs)	24	91.00	108.11	40.97	76.07	50.54	186.62	
Nodule UCS by measurement angle	Nodular-bed normal	12	76.07	74.86	9.93	76.07	50.54	85.81	*3.11e*
	Nodular-bed parallel	9	157.55	153.98	25.44	131.08	112.91	186.62	

3.4.4. In situ petrophysical characterization

In situ permeability measurements are reported in Figs. 3.10c and 3.12, and Table 3.2. Figure 3.10c shows permeability results (mD) measured along the stratigraphic log of Fig. 3.10a and reports error bars that define the 95% confidence level for each data point. Asymmetric error bars, with respect to the data point, are due to the logarithmic scale of the graph. Focusing on Fig. 3.10c, our results show that host rock has the highest permeability, which is representative for undeformed rock. Host rock permeability has a low variability at the scale of the single measurement, i.e. narrow error bars (Fig. 3.10c), and at the scale of the entire measured succession. Most of the host rock measurements in Fig. 3.10c (blue points), in fact, are in the range $10^3 - 10^4$ mD. Permeability values for CSBs and nodules depart from host rock values having lower permeabilities and higher variability, at least at the scale of the single measurement (Fig. 3.10c).

We considered also the distribution of the permeabilities for each single feature (host rock, deformation bands, nodules), and the results are shown in Fig. 3.12 and Table 3.2. The results were the following: (1) the highest permeabilities were recorded along the relatively undeformed low-consolidated protolith (Fig. 3.12a). (2) Host rock permeabilities increase as the sandstone grain-size increases (Figs. 3.12b and 3.10c): very-fine to medium sandstone (VFM) shows the lowest values, medium to very-coarse sandstone (MVC) shows intermediate values, and gravel beds (G) show the highest values. The permeabilities of the finest portion, represented by clay and silt, are below the instrument detectability. (3) Permeability values of CSBs (Figs. 3.10c and 3.12a) have intermediate values between those recorded in the host rock and those recorded in the nodules. (4) Normal to CSB permeabilities are lower when compared with parallel to CSB permeabilities (Fig. 3.12c). (5) Nodules show the lowest permeabilities of the entire rock volume (Fig. 3.12a and 3.10c). (6) Among all nodules, the highest permeabilities were reported for bedding-parallel isolated-nodules without CSBs. CSBs-parallel nodules show intermediate values, and the lowest permeabilities were reported for continuous nodular beds (Fig. 3.12d). (7) Lastly, if we consider measurements taken parallel and normal to the CSBs-parallel nodules (Fig. 3.12e), we observe that parallel permeabilities tend to be lower than the normal ones.

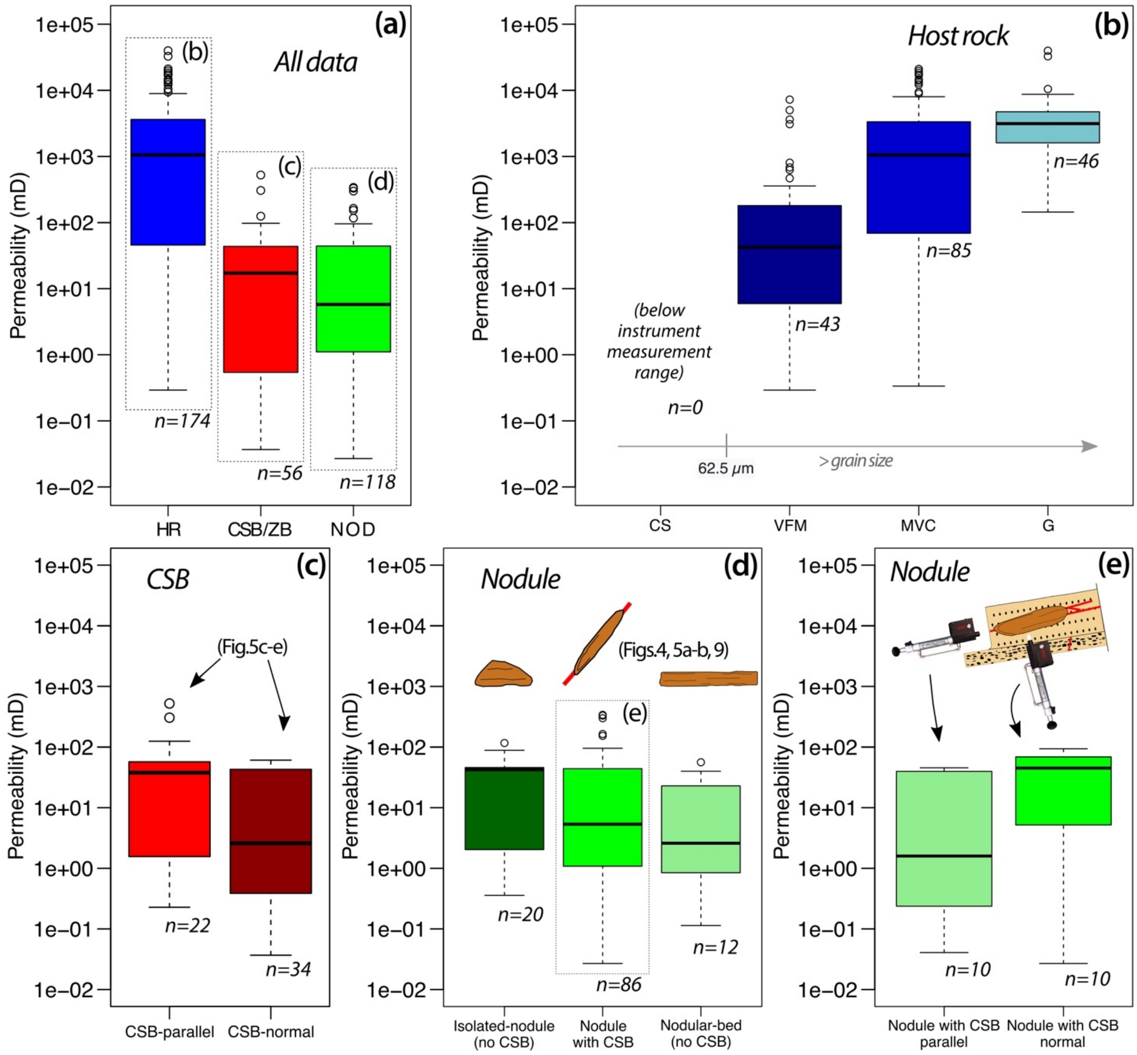

Fig. 3.12 – *In situ* air-permeability (mD) measurements results. **(a)** - Total log-air-permeability data for host rock (HR; blue), CSBs (red), and nodules (NOD; green). **(b)** - Permeability values for host-rock as a function of grain-size: gravel beds (G), medium/very coarse-sand (MVC), very-fine/medium sand (VFM), and silt/clay (CS). **(c)** - Permeability values for CSBs as a function of measurements taken parallel (par) and perpendicular (perp) to the CSB's plane. **(d)** – Permeability values for nodule as a function of type: bedding-parallel isolated-nodule without CSBs, nodule with CSBs, and nodular-beds (without CSB). **(e)** – Permeability values for CSBs-parallel nodules as a function of measurements taken parallel and perpendicular to the nodule greater dimension. The black thick line in the boxplot is the 2nd quartile (median), the lower and upper box sides are the 1st and 3rd quartiles respectively. The lower and upper whiskers define, respectively, the minimum and maximum observed values in the data range excluding the outliers (dots). Number of measurements - n - is indicated in each boxplot. See Table 3.2 for statistical parameters of the results.

Table 3.2
Air-permeability data and statistical parameters.

	Air-permeability (mD)							
	Feature	**Data N**	**Median**	**Mean**	**Std. Dev.**	**Min**	**Max**	**Fig. ref.**
Permeability by feature	HR	174	1053.46	2963.35	5409.98	0.29	39729.44	*3.12a*
	CSB/ZB	56	17.16	38.65	80.65	0.04	522.41	
	NOD	118	5.76	31.70	56.49	0.03	339.65	
HR permeability by grain size	CS	0	-	-	-	-	-	*3.12b*
	VFM	43	42.39	541.87	1460.33	0.29	7240.14	
	MVC	85	1054.98	3210.15	5154.18	0.34	21072.26	
	G	46	3137.55	4470.86	7202.89	143.90	39729.44	
CSB permeability by measurement angle	CSB-normal	34	2.59	20.86	23.14	0.04	60.77	*3.12c*
	CSB-parallel	22	37.81	66.14	122.03	0.23	522.41	
Nodule permeability by nodule type	Nodule with CSBs	86	5.34	33.80	63.76	0.03	339.65	*3.12d*
	Isolated-nodule (no CSBs)	20	42.22	33.94	31.45	0.36	116.42	
	Nodular-bed (no CSBs)	12	2.59	12.91	19.73	0.11	56.01	
Nodule permeability by measurement angle	Nodule with CSBs normal	10	45.01	41.59	32.25	0.03	93.57	*3.12e*
	Nodular with CSBs parallel	10	1.59	14.19	20.15	0.04	45.40	

3.5. DISCUSSION

The objective of this discussion is to integrate the results of in situ petrophysical and mechanical analyses, and the potential of GPR in detecting sub-seismic faults and nodules in the subsurface. This integration allows a reliable SDH volumetric characterization, and it helps extending outcrop-based measurements to the subsurface, improving outcrop reservoir analog reconstruction.

3.5.1. GPR's potential for structural and diagenetic heterogeneities detection

The GPR interpretation of CBSs, ZB, and nodules in the subsurface presented in Figures 3.6, 3.7, and 3.8 is supported by careful observations along the GPR surface traces and by the definition of GPR facies (Fig. 3.9). The contrast in dielectric properties (i.e. relative permittivity) between CSBs (and ZB) and nodules with respect to the surrounding rock causes distinct reflection patterns, with high reflectors amplitude, that are detected in the GPR profiles. Other factors that likely influence our ability to detect CSBs and nodules from the surrounding rock are the dimensions of the target (i.e. thickness of CSBs and ZB, dimension of nodules) or instrument resolution. Considering our field observations (see *Section 3.4.1*) and the resolution of our acquisitions (see Tab. B.2 in Appendix B), the "geological significance" of reflectors that we image in GRP profiles could be (1) nodules, (2) low-angle zones of deformation bands, and (3) lithologic differences, such as sandstones levels with different texture (grain-size, porosity, etc.) or sporadic levels of gravels and clay. From field observations we know that the thickness of zone of bands ranges between 0.8 and 60 cm (e.g. Figs. 3.2a, 3.4, and 3.5) and carbonate nodules volume ranges from 0.001 m^3 to > 10 m^3 (see also Del Sole and Antonellini, 2019; Chapter 2). The resolutions obtained by the choice of parameters (see Tabs. B.1 and B.2 in Appendix B) are in the range of zone of bands and nodules dimensions and would enable their detection, thus supporting our GPR profiles interpretations (Figs. 3.6-3.8). The instantaneous amplitude attribute allowed to identify discrete zones that have higher or lower reflectivity with respect to the surrounding areas. Lithological discontinuities attributed to the presence of nodules (with and without CSBs) with more cement than the host rock (Figs. 3.6c, 3.7c, 3.8c and 3.9b-c) were also identified in our GPR survey. The instantaneous phase attribute helped us in the identification of CSBs and other discontinuities or their lateral terminations (Figs. 3.6d and 3.9a, c) emphasizing the geometry and lateral continuity of lithological and sedimentary structures. Bedding reflections were identified in the shallow-NE-dipping reflections (Figs. 3.6 and 3.8). The presence of a dense network of deformation bands and cement-nodules could be one of the reasons why the reflections from the bedding do not have a good lateral continuity. We interpret the abundant SW-dipping (Fig. 3.6) and sub-vertical (Figs. 3.6, 3.7, 3.8) linear features as CSBs and ZB. The slight difference in dip angles between the two studied sectors might be the presence of the normal fault (Fig. 3.1), and some of the bands being in its damage zone and some being in the background. In most cases CSBs and ZB appear as high-amplitude (bright) bands. The offset of CSBs and ZB generate an offset in the (bedding) reflectors that is easy to identify in the GPR lines (Figs. 3.6, 3.7, 3.8). Zone of bands are expressed either as offsets of GPR reflections (Figs. 3.7 and 3.8) or as inclined reflectors(s) (Figs. 3.6 and 3.7). In the latter case, ZB-related inclined reflector has an aspect similar to that of bedding-related inclined reflectors, forming a reflection like that caused by a contrast in permittivity at a bedding interface. The presence of cement in nodules and within CSBs may facilitate the detectability of both those features (e.g. Lee et al., 2007). Furthermore, CSBs have lower porosity and smaller pore sizes, high surface/volume ratio of framework particles (lower grain size) with respect to the host rock. These characteristics enhances capillary forces able to retain water preferentially along the CSB trace and increasing its water content, so that to improve even further their detectability (Topp et al., 1980; Huggenberger, 1993; Slater and Comas, 2009). Only in a few cases, the CSBs appear as a low-amplitude (dim) linear features; this may be due to a lack of cement in their microstructure or even to late-stage re-activation of these CSBs as opening fractures (Fig. 3.4d-e). Given the complexity of deformation bands networks, field structural characterization alone is not enough to portray their geometry and arrangement in the subsurface. On the other hand, GPR surveys alone could be of difficult interpretation, regarding the organization of deformation bands network, for several reason: (1) the need to know the general structural framework (e.g. typology and attitude of structures, etc.), (2) the presence of noise in the signal, and (3) the need to know the exact velocity profile for time-to-depth conversion. Therefore, a joint field-structural characterization together with 2D (or even 3D) GPR surveys is an excellent technique to characterize the structural architecture of porous sandstones. Figure 3.13 shows a 3D conceptualization of the structural information obtained by integrating both GPR and field surveys. Our results show that GPR is a reliable subsurface imaging tool to detect and investigate SSRF and related diagenetic effects in faulted porous sandstone by data collected directly *in situ*, in natural outcrop conditions, and with low acquisition and processing times and costs. Our approach could be also applied to outcrop-based characterization of sub-seismic scale polygonal faults (Antonellini and Mollema, 2015; Verschuren, 2019).

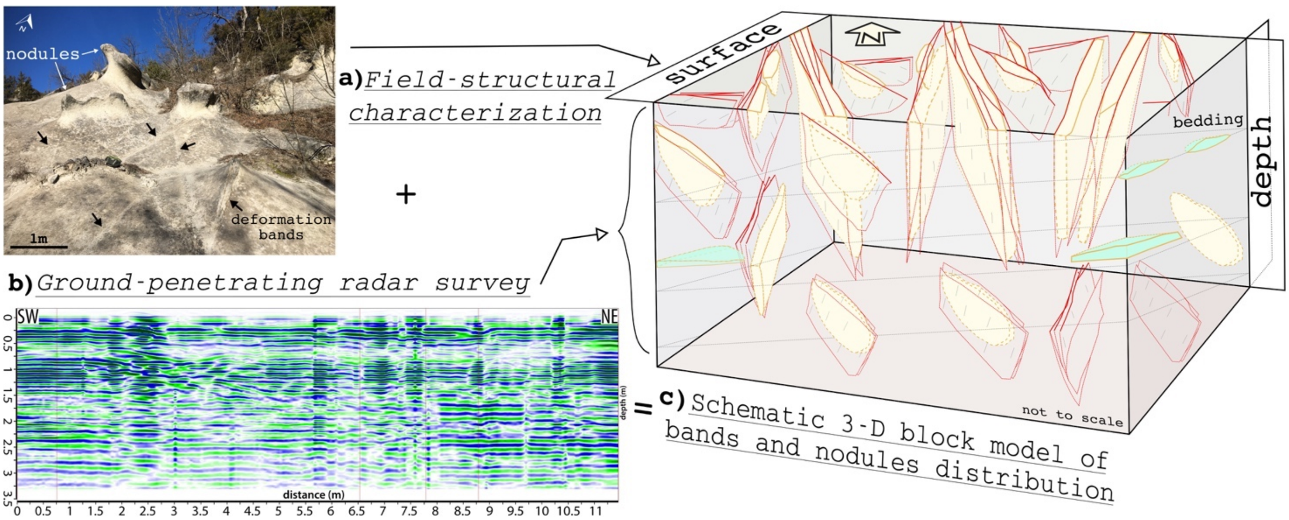

Fig. 3.13 – Schematic representation of the workflow followed in this study where we combined a field-structural characterization, geomechanical and petrophysical measurements, and 2D GPR surveys to reconstruct the structural architecture of CSBs and nodules in the subsurface. In **(a)**, cement-nodules and deformation bands are indicated by white and black arrows respectively. **(b)** The GPR profile is the same of Fig. 3.8a. **(c)** Schematic 3D block model where nodules (light yellow) along deformation bands (red lines) and bedding-parallel nodules (light green) are reported.

3.5.2. Geomechanical and petrophysical properties and their heterogeneity

It has been widely recognised that structural and diagenetic heterogeneities (SDH), such as deformation bands and associated diagenetic effects, control the geomechanics and flow properties of aquifers and reservoirs (see *Sections 3.1.1* and *3.1.2*). In our measurements (Figs. 3.10, 3.11 and 3.12; Tables 3.1 and 3.2), we observed the highest permeability and lowest UCS in the undeformed host rock with respect to all other measured features. This is due to the low cohesion of the Loiano Sandstones (Del Sole and Antonellini 2019). Host sandstone UCS values comparable to those we measured, were also found by other authors (e.g. Fjær et al., 2008; Pontes et al., 2019) in similar sandstones (i.e. poorly consolidated, high porosity). Permeability within CSBs is, on average, two orders of magnitude lower than the host rock, while their strength is, on average, almost 2 times higher than the adjacent HR (UCS_{CSB}/UCS_{HR}=1.76). Permeability reduction within the bands follow the reduction of porosity (e.g. Antonellini and Aydin, 1994; Fowles and Burley, 1994; Jourde et al., 2002; Shipton et al., 2002) accompanied by changes in pore connectivity and pore-throat geometry (e.g. Farrell et al., 2014), which is caused by mechanical crushing and grains reorganization within the band. The strength increase within the band could be related to the strain hardening behaviour associated to CSBs development (Aydin and Johnson, 1978; Underhill and Woodcock, 1987; Kaproth et al., 2010) and to the presence of the cement (Alikarami et al., 2013). Deformation bands UCS values similar to those we measured, were also found by other authors (Pontes et al., 2019; Pizzati et al., 2020). Nodules represent the less permeable and at the same time the most hardened feature of the rock volume having permeability that is, on average, 3 orders of magnitude lower than the host rock, while its strength is, on average, more than 5 times higher than host rock (UCS_{NOD}/UCS_{HR}=5.34). The permeability reduction in the nodules could be simply related to the cement precipitation that fills up almost all pores, reducing pore connectivity and increasing flow tortuosity (e.g. Dullien, 1991). Cement precipitates at the grain contacts inhibiting rotation and sliding of particles thus, increasing the cohesion and strength (Dvorkin et al., 1991; Bernabé et al., 1992; Del Sole and Antonellini, 2019). Contrasts in UCS between bands and nodules, similar to those we observed in Loiano, were found by Pizzati et al. (2020). The less permeable and the strongest features in outcrop are the nodular-beds followed by nodules associated to CSBs and ZB, while bedding-parallel isolated nodules show the lowest decrease in permeability as well as the lowest increase in UCS when compared to other nodules. Nodular-beds are not related to CSBs and their cement is of the same composition and it encloses the same framework grains of other nodules. Thus, their lower permeability and higher strength are probably due to a higher degree of pore-filling cement. Several authors (e.g. Dvorkin et al., 1991; Bernabé et al., 1992) demonstrated that even a small amount of cement would increase the stiffness of the system. Nodules associated with bands exhibit a permeability that is, on average, 1 order of magnitude lower and UCS values that are, on average, 1.5 times higher than those measured in bedding-parallel isolated nodules. Reduced permeability and increased strength could be explained by combining (1) cementation, that reduces porosity increasing the cohesion, (2) grain crushing that increases friction by clast roughening and decrease porosity by reducing grains size and sorting, and (3) compaction that enhances the degree of packing, reducing porosity and increasing cohesion (e.g. Bernabé et al., 1992; Underhill and Woodcock, 1987; Antonellini and Aydin, 1994; Anthony and Marone, 2005; Kaproth et al., 2010; Del Sole and Antonellini, 2019). Points (2) and (3) are linked to the presence of CSBs in nodules but they are of secondary importance when evaluating their effect on nodule permeability. Considering the flow geometry of the field permeameter and the volume sampled during measurement, the dominant factor controlling permeability in a thick nodule (from tens of cm's to meter-scale) would be the presence of cement rather than a few mm-thick band. Another factor that seems to control the permeability and UCS response is the grain size. Host rock permeability increases as the grain-size of the sandstone increases. Similarly, UCS decreases as the grain-size of the sandstone increases in accordance with what described by other authors (Brace, 1961; Fredrich et al., 1990; Přikryl, 2001). Some of the measured UCS values fall below the lower bound of the instrument measurement range (clay-silt levels). Although these values are not absolute UCS values, we think that they are representative if considered relative values with respect to UCS values of sandstones, CSBs, and nodules.

In summary, the combination of cataclasis and compaction within the bands and cementation associated to nodules causes rock deterioration in terms of their flow properties and, at the same time, an increase of their compression strength. Thus, an inverse relation exists between permeability and UCS (Fig. 3.10d), in agreement with what documented by other authors in porous rocks (e.g. Chang et al., 2006; Schöpfer et al., 2009; Alikarami et al., 2013). Our results show also that mechanical and petrophysical properties of Loiano Sandstones are strongly anisotropic at various scales. At the scale of the single structure, this heterogeneity is manifested through significant different results when measuring, both UCS and permeability, normal and parallel to a zone of deformation bands and nodules. UCS values measured normally to the plane of the CBSs is, on average, 17.45% higher than those measured parallel to the bands surface. Similarly, the CSB normal permeability is 1 order of magnitude lower than the parallel one. This result is in accordance with those reported by other authors (Antonellini and Aydin, 1994; Sternlof et al., 2004; Farrell et al., 2014). On the contrary, UCS measurements on nodular-beds, show that the UCS measured normal to the nodule greater dimension is significantly lower (34.12%) when compared to the parallel UCS. This effect is probably related to some shape-preferred orientation of minerals with their long axis oriented parallel to the bedding (e.g. Přikryl, 2001) or to nodular-beds shape (oblate ellipsoid). As already observed by Del

Sole and Antonellini (2019; Chapter 2), another factor of heterogeneity is that nodules and CSBs show a wide scatter of UCS if compared to the host rock values. Although less pronounced, a similar difference in scattering between host rock, bands, and nodules has also been observed for the permeability results. This effect could be related to a non-homogeneous cementation process. In addition, a large-scale permeability anisotropy results from: (i) a spatially heterogeneous cementation (geometry and distribution of nodules) (Dutton et al., 2002; Davis et al., 2006; Lee et al., 2007), and (ii) the presence of deformation bands and their properties, i.e. permeability contrast, thicknesses, geometrical architecture, and associated diagenetic effects (Antonellini and Aydin, 1994; Shipton et al., 2002; Sternlof et al., 2004; Fossen and Bale, 2007; Rotevatn et al., 2009; Farrell et al., 2014; Del Sole and Antonellini, 2019). The assemblage of bands and nodules could induce a mechanical anisotropy at the scale of the rock-volume and strengthen the sandstone in a way analogous to the behaviour of laminae-reinforced industrial composite materials (Jones, 2014; Petracchini et al., 2015).

3.5.3. Permittivity as a proxy for mechanical and petrophysical characteristics

The relationships among grain size and sorting, porosity, permeability, cementation, UCS, and the GPR response are worth to be investigated in further detail. GPR measurements are primarily controlled by changes in water content affecting the dielectric properties of sediments (i.e. ε_r). Water content is governed by grain size and capillary properties (Topp et al., 1980; Huggenberger, 1993; Slater and Comas, 2009). CSBs, nodules, and the assemblage "deformation bands – nodules" produce high amplitude reflectors, because of their porosity differences (Davis and Annan, 1989) that result in a clear contrast between their relative permittivities. Nodules and bands characterized by high-amplitude signal (high ε_r), therefore, are the clearest features detectable in the GPR profiles. Their detectability can be improved upon by analyzing GPR attributes (Lemke and Mankowski, 2000; Lee et al., 2007; Forte et al., 2012). Given the existing correlations between petrophysical properties and permittivity (Topp et al., 1980; Davis and Annan, 1989; Knoll and Knight, 1994; Slater and Comas, 2009), it is possible to estimate the petrophysical properties from GPR profiles via calibration with direct measurements from cores and outcrops (Szerbiak et al., 2001). We observe that areas of low porosity and permeability, such as bands and nodules, are also areas with high GPR-signal amplitude (higher ε_r). The pristine rock, on the contrary, which has high porosity and permeability, is characterized by a low GPR-signal amplitude (lower ε_r). Likewise, we observe that areas of high UCS, such as bands and nodules, are also areas with high GPR-signal amplitude (higher ε_r). The pristine rock, on the contrary, which has low UCS, is characterized by a low GPR-signal amplitude (lower ε_r). Thus, we could define a relationship also between relative permittivity and UCS. In Fig.

3.14, we summarize the paired morphological, geophysical (GPR-signal), geomechanical (UCS), and petrophysical (permeability) patterns. This simplified sketch shows that the topographic profile (Fig. 3.14a) has the same pattern as the GPR (Fig. 3.14b) and the UCS (Fig. 3.14c) profiles, while all of them mirror the petrophysical one (Fig. 3.14d). In the Loiano Sandstones, cataclasis and pore filling cement govern petrophysical properties variability, which in turn influences hydraulic, mechanical, and dielectric properties of the rock volume. We suggest that, once petrophysical and mechanical properties have been evaluated directly, it is possible to extend those values in the subsurface and estimate those properties at the scale of the reservoir, directly from GPR data (Szerbiak et al., 2001; Lee et al., 2007).

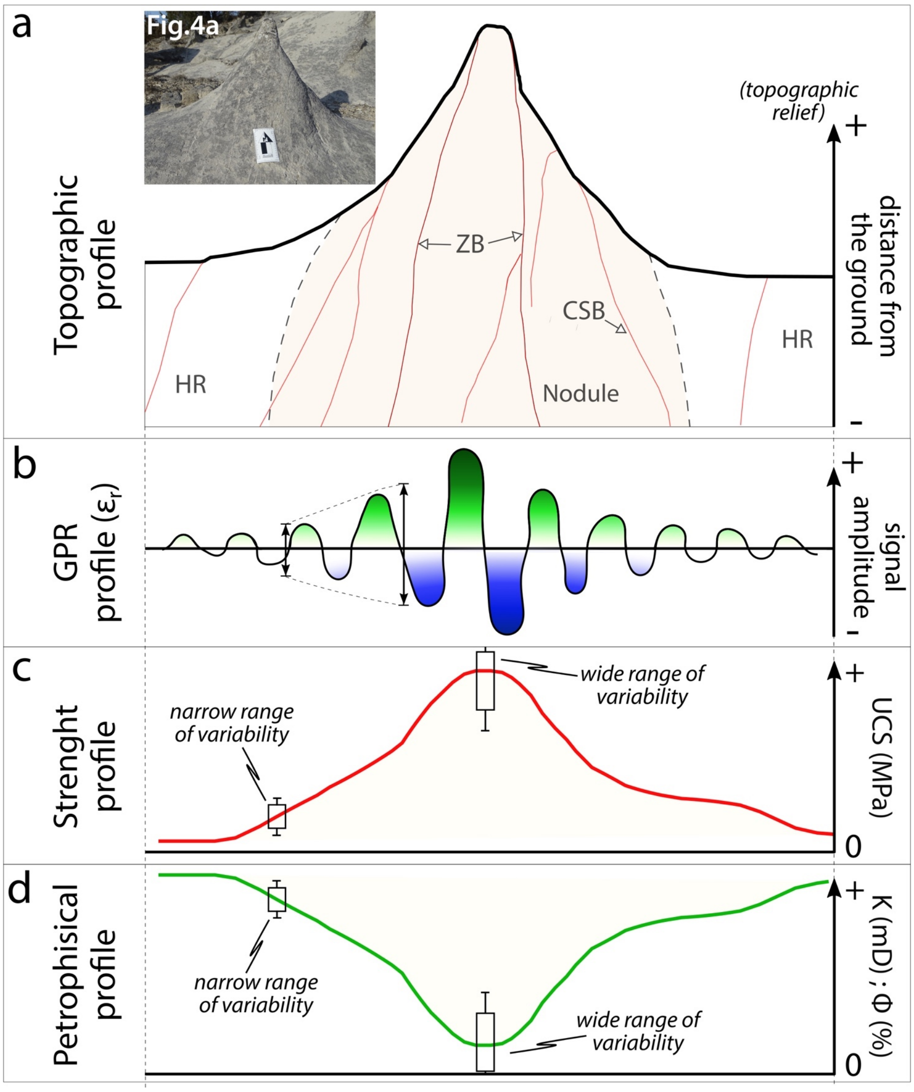

Fig. 3.14 – Schematic representation of **(a)** topographic [meters], **(b)** geophysical [permittivity], **(c)** geomechanical [UCS], and **(d)** petrophysical [K – permeability, ϕ – porosity] profiles across host rock, nodule, and CSBs and ZB. Topography, permittivity, and geomechanical properties show the same pattern whereas the petrophysical profile mirrors the previously mentioned properties profiles. The figure in **(a)** is the same shown in Fig. 3.4a. The black boxes in **(c)** and **(d)** are box plots that show how UCS (Figs. 3.10b and 3.11a-e) and permeability (Figs. 3.10c and 3.12a-e) variability in nodules and CSBs/ZB is higher than host rock UCS variability.

3.5.4. Implications for subsurface reservoir and aquifer characterization

The approach used in this work is useful to characterize shallow aquifers and reservoirs structural architecture in sandstones and to extract input data for flow simulations and geomechanical modelling where SDH are present. A reservoir development plan needs to take SDH effects into account, so that the best exploitation strategy can be deployed, and bypassed pay minimized. Although GPR is typically employed as near-surface geophysics tool, our approach could be extended at greater depth, i.e. at reservoir depth conditions, using methods such as borehole radar (e.g. Olsson et al., 1992; Wänstedt et al., 2000) or other advanced radar instruments (e.g. *SHARAD;* Smith and Holt, 2015). However, it is crucial to take into account the variation of different parameters with depth (e.g. fluid-pressure and saturation, rock mechanical properties, etc.) in order to extend this approach to the subsurface. Although no specific attention was given to the control exerted by regional structural framework on the observed deformation bands, such information could be critical when extrapolating information to the subsurface. We could argue that the compatibility between strike of deformation bands (Fig. 3.2) and larger scale normal faults in this sector of the Northern Apennines (Fig. 3.1; Antonellini and Mollema, 2002; Picotti et al., 2009) indicate that they were formed contemporaneously within a similar stress field. However, the presence of multiple sets of bands, with different trends (Fig. 3.1; Del Sole and Antonellini, 2019), different apparent slip (mainly normal and strike-slip), and ambiguous crosscutting relationships (conflicting relationships) leads us to think that the Loiano Sandstones recorded multiple tectonic phases in post-Eocene times (*Section 3.2.1*; Cibin et al., 2001; Antonellini and Mollema, 2002); a clear sequence of deformation has not been defined so far.

The networks of observed (from outcrops) and interpreted (from GPR profiles) deformation bands and nodules are pervasive and have a good degree of interconnection. These characteristics, coupled with their low permeabilities, may cause hydraulic compartmentalization of the reservoir analog. The presence of low-permeability thick and elongated nodules associated or not (bedding-parallel) with CSBs, enhance the permeability reduction due to the CSBs alone and locally control flow line direction. The potential impact of structural discontinuities and nodules on fluid migration is quantified by the permeability *in situ* measurements. Mechanical parameters, such as UCS, are fundamental for modelling a wide range of wellbore stability problems. GPR showed its worth as a valuable tool to estimate the geometry and spatial distribution of flow baffles and small-scale flow barriers such as deformation bands (Brandes et al., 2018) and cement-nodules (Lee et al., 2007) within sandstones, and also it could provide estimates of permeability and porosity through calibration with direct measurements (Szerbiak et al., 2001; Lee et al., 2007) providing important input for reservoir development, and enormously improving the outcrop analog reconstruction. The information on

UCS, petrophysical properties and SSRF network characteristics from reservoir analogs is essential to integrate large-scale seismic surveys and well-log information.

3.6. CONCLUSIONS

We have shown that the integration of field mapping, in situ permeability and UCS measurements, and 2D GPR surveys is a powerful tool to characterize the structural architecture, the petrophysical, and mechanical properties of a sandstone reservoir analog in the presence of SDH. In particular, the most significant conclusions of our work are:

(1) Ground-penetrating radar offers promising prospects for imaging sub-seismic SDH in the subsurface and improve their characterization and distribution in sandstone reservoirs. GPR is a high-resolution and non-invasive tool with very low data acquisition and processing times, and it should be considered during aquifer and reservoir characterization.

(2) Nodules are the most cohesive domains in the outcrop as well as the less permeable ones: their UCS is more than 5 times higher and their permeability is 3 orders of magnitude lower than the host rock. Nodular-beds and CSBs-parallel nodules are the strongest (UCS is between 5 and 6 times larger than host rock) and less permeable ones (on average 3 orders of magnitude lower than host rock and somewhere up to 5). The presence of cement strengthens fault rocks considerably. Deformation bands UCS is almost 2 times larger whereas permeability is 2 (CSB-parallel) and 3 (CSB-normal) orders of magnitude (up to 5) lower than the host rock.

(3) Normal-to-band UCS is higher than parallel-to-band one. Similarly, normal-to-band permeability is 1 order of magnitude lower than parallel-to-band one. UCS in nodular beds is higher where measured parallel to the nodular body greater dimension than where measured normal to it.

(4) Our results suggest that a network of SDH, such as low porosity deformation bands and nodules within highly porous host rock, degrades porosity and permeability in a reservoir and produces a general strengthening effect. At the same time, they impart a strong mechanical and petrophysical anisotropy to the rock volume.

(5) The assessment of reservoir heterogeneities (e.g. SDH) is the basis for reservoir quality prediction modelling. In this study, we show that GPR can be useful to characterize variations in petrophysical and mechanical properties together with the geometry and organization of bands and nodules in the rock volume.

(6) Zones with high permittivity (ε_r) correspond to areas of positive relief, high strength, and low permeability. These areas can be identified as deformation bands and cement nodules. The results of this study indicate that the GPR response (i.e. relative permittivity, instantaneous attributes)

could be used as a proxy for petrophysical and geomechanical characterization of faulted porous sandstone reservoirs.

(7) Once petrophysical and mechanical properties have been evaluated directly in situ, we could extend those values in the subsurface to 3D volumes, directly from GPR data, improving the prediction of fluid behavior in sandstone aquifers and reservoirs. Integrating GPR and outcrop-based data we could improve significantly sub-seismic resolution SDH characterization obtaining a realistic and detailed conceptual model of the outcrop analog.

Supplement – Supplementary material to this Chapter can be found in the Appendix B.

References – The references related to this Chapter can be found in the Bibliography.

Acknowledgments – We thank Cédric Bailly and an anonymous reviewer for their constructive and positive reviews, leading to improvement of the original manuscript, and Nicolas E. Beaudoin for his editorial work. We are grateful to Giulio Viola and Luigi Cantelli for lending the TinyPerm 3 Portable Air Permeameter and the GPR, respectively.

4

Structural control on fluid flow and shallow diagenesis: insights from calcite cementation along deformation bands in porous sandstones

The content of this Chapter has been published in **Del Sole, L.**, Antonellini, M., Soliva, R., Ballas, G., Balsamo, F., Viola, G., 2020. Structural control on fluid flow and shallow diagenesis: insights from calcite cementation along deformation bands in porous sandstones. Solid Earth, 11(6), 2169–2195.

ABSTRACT

Porous sandstones are important reservoirs for geofluids. Interaction therein between deformation and cementation during diagenesis is critical since both processes can strongly reduce rock porosity and permeability, deteriorating reservoir quality. Deformation bands and fault-related diagenetic bodies, here called "structural and diagenetic heterogeneities", affect fluid flow at a range of scales and potentially lead to reservoir compartmentalization, influencing flow buffering and sealing during geofluids production. We present two field-based studies from Loiano (Northern Apennines, Italy) and Bollène (Provence, France) that elucidate the structural control exerted by deformation bands on fluid flow and diagenesis recorded by calcite nodules associated with the bands. We relied on careful *in situ* observations through geo-photography, string mapping, and UAV photography, integrated with optical, scanning electron and cathodoluminescence microscopy, and stable isotope ($\delta^{13}C$ and $\delta^{18}O$) analysis of nodules cement. In both case studies, one or more sets of deformation bands precede and control selective cement precipitation. Cement texture, cathodoluminescence patterns, and their isotopic composition suggest precipitation from meteoric fluids. In Loiano, deformation bands acted as low-permeability baffles to fluid flow and promoted selective cement precipitation. In Bollène, clusters of deformation bands restricted fluid flow and focused diagenesis to parallel-to-band compartments. Our work shows that deformation bands control flow pattern within a porous sandstone reservoir and this, in turn, affects how diagenetic heterogeneities are distributed within the porous rocks. This information is invaluable to assess the uncertainties in reservoir petrophysical properties, especially where structural and diagenetic heterogeneities are below seismic resolution.

4.1. INTRODUCTION

Porous rocks, such as sandstone and carbonate, are important reservoirs for geofluids. Structural and diagenetic processes commonly affect the petrophysical properties and reservoir quality in these rocks. The importance of the interaction between deformation and structures, fluid flow, and diagenetic processes has been emphasized only during the last 2 decades (e.g. see the recently coined term *structural diagenesis*, Laubach et al., 2010; Mozley and Goodwin, 1995; Eichhubl et al., 2009; Balsamo et al., 2012; Philit et al., 2015; Antonellini et al., 2017, 2020; Del Sole et al., 2020). If deformation influences diagenesis and vice versa, a feedback can eventually develop between these two processes. Early diagenesis influences the mechanical properties of rocks (Antonellini et al., 2020) and, in turn, their mechanical stratigraphy (Laubach et al., 2009; La Bruna et al., 2020). "Structural and Diagenetic Heterogeneities" (referred to as SDHs from now on) can determine the textural characteristics (e.g. grain size, grain shape, relative proportion of grains and matrix material) as well as the petrophysical and mechanical properties of the rock volume hosting them (Antonellini and Aydin, 1994; Aydin, 2000; Faulkner et al., 2010; Bense et al., 2013; Pei et al., 2015; Del Sole et al., 2020). Cement precipitation in granular porous siliciclastic rocks leads to porosity loss, reduction in permeability (Tenthorey et al., 1998; Morad et al., 2010), and, in turn, overall reservoir quality deterioration (Ehrenberg, 1990; Morad et al., 2010). Carbonate cement is commonly concentrated within a few specific horizons or nodules with various shapes and arrangements (Kantorowicz et al., 1987; Bjørkum and Walderhaug, 1990; Mozley and Davis, 1996), making porosity and permeability prediction more challenging (Davis et al., 2006; Morad et al., 2010). Furthermore, cement increases the mechanical strength of the host rock (Dvorkin et al., 1991, Boutt et al., 2014), influencing fault-zone architecture and potential fault reactivation (Dewhurst and Jones, 2003; Flodin et al., 2003; Wilson et al., 2006; Williams et al., 2016; Pizzati et al., 2020).

Granular or porous sediments and sedimentary rocks commonly contain sub-seismic resolution strain localization features referred to as deformation bands (Aydin, 1978; DBs from now on). The effects of DBs on fluid flow can vary significantly depending on several factors, such as their permeability contrast relative to the host rock, their thickness, density, distribution, orientation, segmentation, and connectivity (Antonellini and Aydin, 1994; Gibson, 1998; Manzocchi et al., 1998; Sternlof et al., 2004; Shipton et al., 2005; Fossen and Bale, 2007; Torabi and Fossen 2009; Rotevatn et al., 2013; Soliva et al., 2016). In some cases, DBs may act as conduits for fluids (Parry et al. 2004; Sample et al. 2006; Petrie et al., 2014; Busch et al., 2017). In most cases, however, they are associated with significant porosity and permeability reduction relative to the host rock (Antonellini and Aydin, 1994; Shipton et al., 2002; Sternlof et al., 2004; Balsamo and Storti, 2010; Ballas et al., 2015; Fossen et al., 2017; Del Sole and Antonellini, 2019), thus inducing permeability anisotropy and reservoir compartmentalization. This might negatively impact production from faulted siliciclastic systems (Edwards et al., 1993; Lewis and Couples, 1993; Leveille et al., 1997; Antonellini et al., 1999; Wilkins et al., 2019) and flow-based models and simulations (Sternlof et al. 2004; Rotevatn and Fossen, 2011; Fachri et al., 2013; Qu and Tveranger, 2016; Romano et al., 2020).

Cement has been found in association with DBs. Localization of cement along these structural features may significantly enhance porosity and permeability reduction caused by mechanical crushing and reorganization of grains, thus increasing their sealing or buffering potential (Edwards et al., 1993; Leveille et al., 1997; Fisher and Knipe, 1998; Parnell et al., 2004; Del Sole et al., 2020). The occurrence, distribution, and petrophysical properties of cement along DBs therefore need to be properly characterized and implemented into reservoir quality modeling to predict porosity, permeability, and their heterogeneity (e.g. Morad et al., 2010).

Models of calcite cementation, in particular, are fundamental for predicting sandstone and fault-rock properties such as porosity, permeability, compressibility, and seismic attributes. Diagenetic processes related to fluid flow mechanisms and evolution within DBs are not fully constrained; in particular, how DBs steer the origin and distribution of calcite cement remains poorly understood. Different processes account for enhanced fluid flow within DBs, such as unsaturated flow relative to the host rock in arid to semiarid vadose zones (Sigda et al., 1999; Sigda and Wilson, 2003; Wilson et al., 2003) and transient dilation in the early stage of DB formation (e.g. Antonellini et al., 1994a; Main et al., 2000). Also, these mechanisms have been employed to explain the occurrence of cement and other processes (e.g. cementation, hydrocarbon inclusion entrapment, removal of iron oxide coatings) in and around the band (Fowles and Burley, 1994; Labaume and Moretti, 2001; Ogilvie and Glover, 2001; Parnell et al., 2004; Parry et al., 2004; Sample et al., 2006; Wilson et al., 2006; Cavailhes et al., 2009; Balsamo et al., 2012; Lommatzsch et al., 2015). These mechanisms, however, appear to be limited to specific conditions (e.g. cement precipitation in the early stage of DB formation or in vadose environments) and they assume that DBs behaved as fluid "conduits" in order to explain the occurrence of cement or other authigenic products within these structures. Nevertheless, a significant number of studies on DBs show that in most cases they are baffle or seals to fluid flow (see Ballas et al., 2015 for a review). Much less attention has been paid to fluid flow and diagenetic mechanisms leading to (post-DB formation) selective cementation in association with low-permeability baffle DBs, and studies of cement precipitation in these DBs are mostly limited to quartz cement and are mostly experimental (Fisher and Knipe, 1998; Milliken et al., 2005; Lander et al., 2009; Eichhubl et al., 2010; Williams et al., 2015). Different mechanisms, then, need to be invoked to explain the occurrence of (carbonate) cement in association with DBs in a broader set of conditions.

The aim of our work is to elucidate the influence of DBs on fluid flow and their role in fostering diagenesis and localizing diagenetic products in porous sandstones. The novelty of our work is that by using a multiscalar and cross-disciplinary approach integrating structural and diagenetic analysis, we assess the control exerted by DBs on flow pattern, diagenetic heterogeneities origin, and spatial distribution by means of the systematic characterization of the occurrence, as well as the spatial and microstructural relationship between DBs and cement nodules in two porous sandstone reservoir analogs. We examine two field sites in Italy and France where calcite cement nodules are spatially associated with DBs. The comparison between the two locations with different geological settings makes it possible to derive general conclusions that can be extended to other cases in which DBs and diagenetic processes interact. Our study also allows for the evaluation of the impact of both structural and structural-related diagenetic heterogeneities on present-day fluid circulation and on subsequent deformation.

4.2. GEOLOGICAL FRAMEWORK

4.2.1. Loiano field site, Northern Apennines (Italy)

The Loiano study area is in the Northern Apennines (Emilia-Romagna region, Italy), 20 kilometers to the south of the city of Bologna (Fig. 4.1a). The Northern Apennines are an orogenic wedge formed in response to the upper Cretaceous-Eocene closure of the Ligurian-Piedmont ocean (Marroni et al., 2017) and the subsequent Oligocene-Miocene convergence and collision between the Adriatic Promontory and the Sardinia-Corsica Block of African and European origin, respectively (Vai and Martini, 2001). Our work focused on the Loiano Sandstones of the Epiligurian Successions (Fig. 4.1a-c), the middle Eocene to middle Miocene siliciclastic infill of thrust-top, piggyback basins discordant to the underlying Ligurian units, which migrated passively to the NE during the Apennines orogeny atop of the entre orogenic wedge (Vai and Martini, 2001). The 300-1000 m thick, late Lutetian-Bartonian Loiano Sandstones are a fan delta to proximal turbidite deposit (Papani, 1998). They are medium- to coarse-grained, poorly consolidated, immature arkosic sandstones and conglomerates deposited in a relatively small lenticular basin (a few tens of Kms in width and length; Fig. 4.1a, c). They are composed of 49 to 60% quartz and 39–48% feldspar, the rest being rock fragments, detrital carbonate clasts, and minor accessories (Del Sole and Antonellini, 2019).

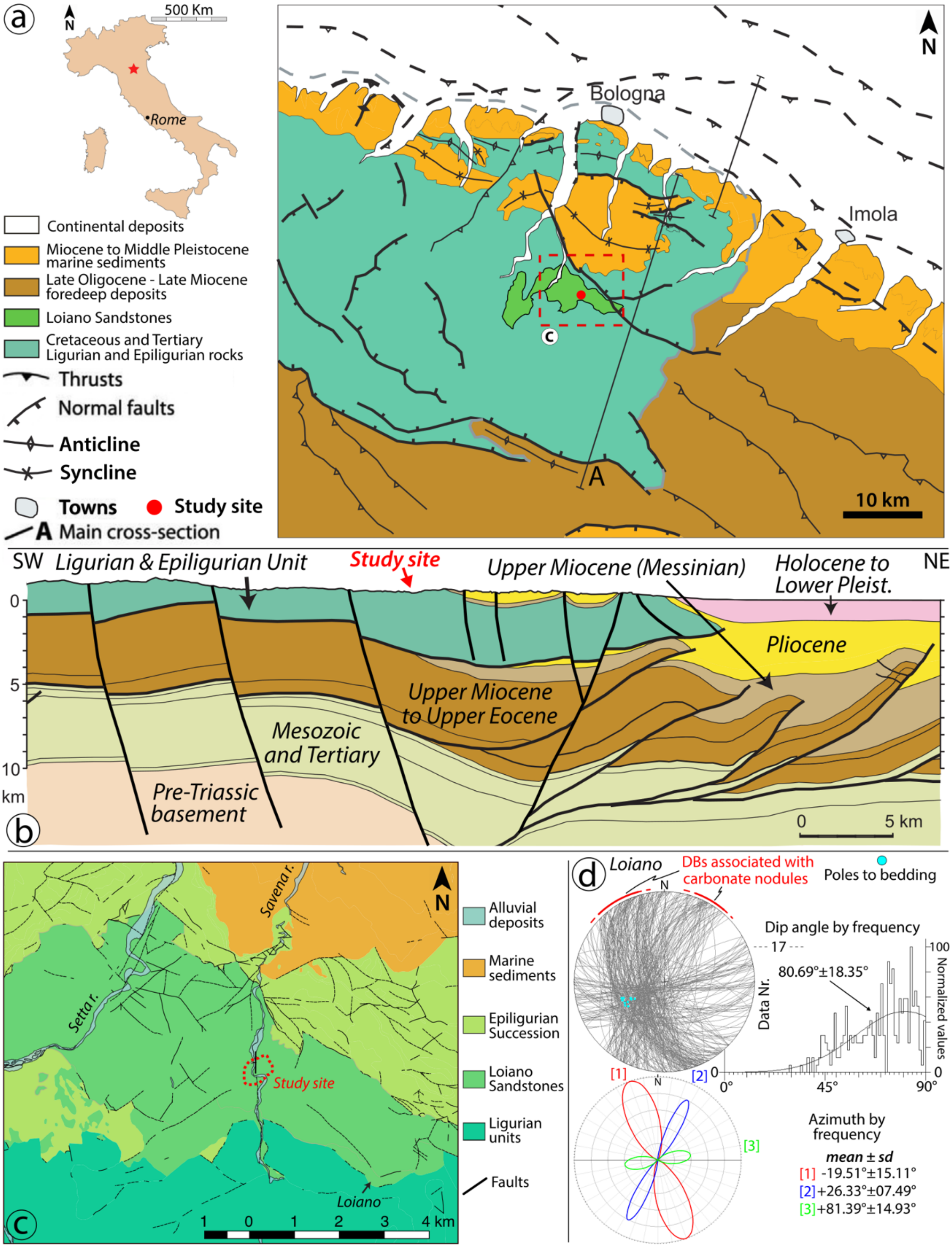

Fig. 4.1 – (a) Schematic geologic map and **(b)** cross-section of the Northern Apennines near Bologna (Italy), modified from Picotti and Pazzaglia (2008). **(c)** Geologic map of the study area and location of the studied outcrops (red dotted line). This map is constructed from data on the Regione Emilia-Romagna (http://www.regione.emilia-romagna.it/, last access: 17 December 2019). The location of **(c)** is indicated by a red square in **(a)**. **(d)** Lower-hemisphere equal-area projection indicates the orientation of the different sets of DBs (298 data points) and poles to bedding at the study site. DBs associated with carbonate nodules are highlighted by a red line. DBs azimuth (strike; N ± 90°) frequency rose diagram and dip angle (°) plotted against frequency. Best-fit Gaussian curves superimposed on the corresponding data histograms (frequency distributions). Gaussian peaks and related standard deviations (± sd) are indicated for each population.

4.2.2. *Bollène field site, Provence (France)*

The Bollène site is in the Southeast Basin of Provence (France), 15 kilometers to the north of the city of Orange (Fig. 4.2a). The Southeast Basin is a triangular region between the Massif Central to the northwest, the Alps to the east, and the Mediterranean Sea to the south. It is a Mesozoic cratonic basin on the edge of the Alpine orogen, approximately 200 km long and 100 to 150 km wide. Three main tectonic episodes affected the region (Arthaud and Séguret, 1981; Roure et al., 1992; Séranne et al., 1995; Champion et al., 2000): SSW-NNE Pyrenean contraction from the Paleocene to Oligocene, NW-SE Gulf of Lion extension from the Oligocene to early Miocene (rifting), and, lastly, SW-NE Alpine contraction from the Miocene to Quaternary (Fig. 4.2a). The site of Bollène is exposed in a quarry (Figs. 4.2c) located in Turonian sand (low-cohesion sandstone), between 10 and 200 m thick in thickness and is situated north of the E-W Mondragon anticline (Fig. 4.2b, c). The Turonian sands at the Bollène quarry are laminated and fine- to coarse-grained with modal and bimodal grain size distributions; they formed in deltaic and eolian environments (Ferry, 1997). The host sands are not cemented. They are composed of 88 to 92% quartz, the rest being feldspar. The median grain diameter (D_{50}) is 0.31 mm, i.e. medium sand. Their porosities range from 20 to 43%, and the precise value at study site is 22% (Ballas et al., 2014).

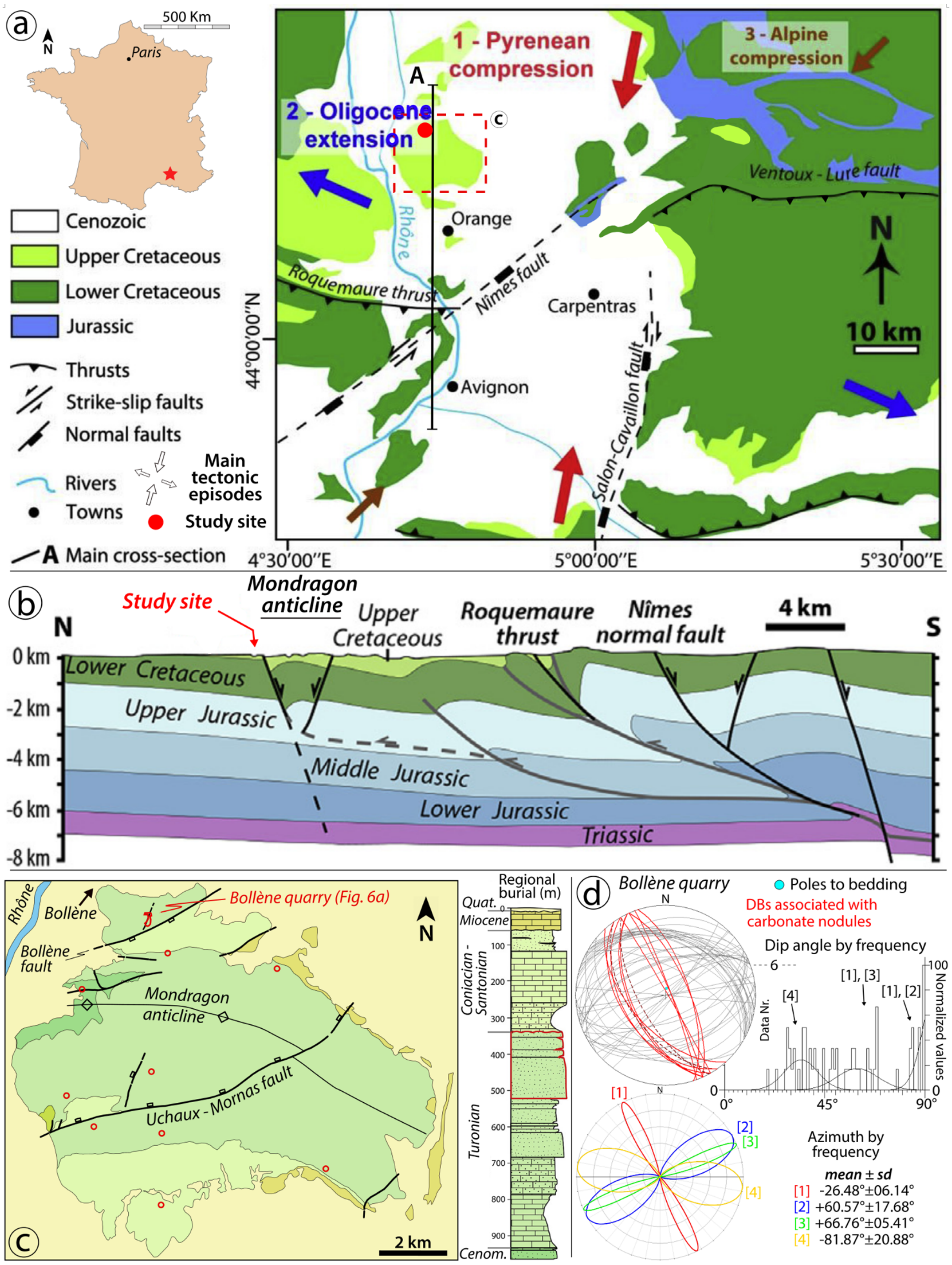

Fig. 4.2. **(a)** Schematic geologic map and **(b)** cross section of the Southeast Basin, Provence, France. The main tectonic episodes affecting the region are reported in **(a)**. **(c)** Geologic map and stratigraphic column of the Bollène quarry. The location of the map in **(c)** is indicated by a red square in **(a)**, and red open circles indicate some past study locations (see Wibberley et al., 2007; Saillet and Wibberley, 2010; Ballas et al., 2012, 2013, 2014; Soliva et al., 2013; Philit et al., 2018). Panels **(a)** and **(b)** as well as stratigraphic column in **(c)** are modified from Philit et al., (2015, 2018). The geological map in **(c)** is modified from Ballas et al. (2012). **(d)** Lower-hemisphere equal-area projection indicates the orientation of the different sets of DBs (64 data points) at the study site. DBs associated with carbonate nodules are highlighted in red. Dotted lines indicate the main attitude of tabular carbonate nodules. DBs azimuth (strike; N ± 90°) frequency rose diagram and dip angle (°) plotted against frequency. Best-fit Gaussian curves superimposed on the corresponding data histograms (frequency distributions). Gaussian peaks and related standard deviations (± sd) are indicated for each population. The number in square brackets [n] are the same as used in Fig. 4.6b to rank different sets of DBs.

4.3. METHODS

4.3.1. Outcrop analysis

The geometry and distribution of DBs and nodules were documented by detailed field mapping at different scales for both sites. At the Loiano site, a map (370 m^2) at the 1:25 scale (1 cm ≃ 4 m) was made by standard topographic compass and tape mapping (Fig. 4.3). The Bollène quarry site pavement was mapped using a DJI PHANTOM™ drone. Photographs were taken at different heights above the ground surface and were then used to build a 3D mesh and extract high-resolution orthophotos using Agisoft PhotoScan Metashape software (© Agisoft LLC). The high-resolution orthophoto mosaic (1 px ≃ 1-1.5 mm) was used for the detailed mapping of DBs and nodules. Furthermore, DBs and nodule patterns, as well as their characteristics and spatial relationships, were documented in the field on high-resolution photographs (15 megapixels), both in Loiano (Figs. 4.4 and 4.5) and Bollène (Figs. 4.7 and 4.8). Oriented samples were collected for thin section preparation, microstructural, and stable isotopes analysis. The orientation of DBs was measured at each site and plotted in lower-hemisphere equal-area stereograms, rose diagrams, and frequency histograms (Figs. 4.1d and 4.2d) using the Daisy3 software (Salvini, 2004).

4.3.2. Microstructural analysis

Polished thin sections of host sandstones, DBs, and nodules were analyzed by standard petrographic microscopy, cold cathodoluminescence, and backscattered electron imagery using a JEOL JSM-5400 and an FEI Quanta FEG 200 environmental scanning electron microscope (SEM). These microscopy techniques were used to examine the textural characteristics (e.g. grain size, shape, arrangements, contact relationships) and microstructures of host rock and DBs, as well as the cement distribution and texture (e.g. cement type and degree of cementation, cement crystals shape and size) (Figs. 4.9, 4.10, and 4.11). In particular, cold cathodoluminescence (CL) analysis of carbonate cement in nodules was conducted with a CITL cold cathodoluminescence 8200 Mk5-1 system (operated at 14-15kV beam energy and 250µA beam current) equipped with a standard petrographic microscope (Olympus BH41). CL was used to describe the cement crystal properties (texture, fabric, luminescence) and the micron-scale spatial distribution and textural relationship among the cements, framework detrital grains, and fractures (*sensu lato*). This information is used to (i) understand the interrelation between deformation, fluid flow, and diagenesis (e.g. cement precipitation); (ii) assess the relative timing of each process; (iii) describe porosity evolution with time; and (iv) understand the mechanisms and the geochemical environment of cement precipitation when coupled with other tools (e.g. stable isotopes analyses). The CL features (color, brightness) of the carbonate minerals are controlled primarily by the relative abundances of Mn^{2+}, REEs, and Fe^{2+}. These differences, in turn, reflect specific physiochemical conditions of formation waters during mineral growth, including fluid chemistry (salinity), pH and Eh, temperature, pressure, ion activity and biological activity (e.g. Marshall, 1988; Barnaby and Rimstidt, 1989; Machel, 2000; Hiatt and Pufahl, 2014).

4.3.3. Stable isotope characterization

Stable carbon and oxygen isotope data from cements from within carbonate nodules were used to constrain the geochemical environment of precipitation and possible source of fluids. Powder samples for bulk rock carbon and oxygen stable isotopes analysis were ground with a dental drill from unweathered or altered sections of the nodules. A total of 46 sites were sampled from nodules in Loiano (n=30; Fig. 4.12a) and Bollène (n=16; Fig. 4.12b). Powders samples were analyzed with a Thermo Finnigan DELTA plus XP mass spectrometer coupled with a Thermo Finnigan Gas Bench II gas preparation and introduction system. $\delta^{13}C$ and $\delta^{18}O$ refer to the international standard VPDB (Vienna Pee Dee Belemnite). Isotope determination analytical precision was 0.10‰ and 0.15‰ VPDB for carbon and oxygen, respectively. The uncertainty was c. 0.15‰ for carbon and c. 0.20‰ for the oxygen isotopes.

4.4. DEFORMATION BANDS AND CEMENT: FIELD OBSERVATIONS

4.4.1. Loiano

At the study site, bedding strikes NW-SE and dips at an average of 38° to the NE (Fig. 4.1d). Deformation bands cluster into three different trends striking 340° (NNW-SSE), 26° (NNE-SSW to NE-SW), and 81° (ENE-WSW) (Fig. 4.1d). All DBs dip moderately to steeply mostly in the west and south quadrants (Fig. 4.1d). Deformation bands commonly occur with a positive relief and appear as whitish linear traces with minor undulations forming eye and ramp structures, whereby they branch and merge (Figs. 4.3 and 4.4). Already at the outcrop they exhibit a significant reduction in grain size and porosity in comparison to the surrounding host rocks (Fig. 4.4f). Deformation bands occur both as single features and as clusters or zones of bands, i.e. in narrow zones with variable thickness (0.8-60 cm) with subparallel DBs (up to 40). Single DBs accommodate minor offsets from a few millimeters up to 40 mm, whereas clusters can accommodate offsets up to 0.5 m (Fig. 4.4b, d). Deformation bands display a variety of apparent normal and strike-slip offsets (Fig. 4.3). Different sets of DBs show ambiguous and conflicting crosscutting relationships. Field observations indicate that the NNW-SSE and NNE-SSW sets have mutual crosscutting relationships typical of faults forming synchronously (Fig. 4.3).

The peculiar characteristic of the Loiano Sandstones is the occurrence of spatially heterogeneous carbonate cement in the form of isolated or multiple spheroids or irregular nodules and continuous tabular nodules (Figs. 4.4 and 4.5). The nodules weather out in positive relief, because they are more resistant to weathering than the weakly cemented host rock. Isolated nodules range in diameter (major horizontal axis) from 0.2 m to 3 m (Fig. 4.4c, 4.d) whereas tabular concretions have a thickness ranging from 0.10 to 0.8 m and a long axis ranging from 3 up to 15 m in length (Fig. 4.5a). Generally, the nodule shape in Loiano is similar to that of an oblate spheroid. There is no evidence of spherical nodules or prolate spheroids. The volume of the carbonate nodules ranges from 0.001 m^3 to > 10 m^3. Nodules form about 20% of the exposed outcrop volume. Two types of nodules can be distinguished depending on whether they are associated with DBs and/or clusters (i.e. DB-parallel nodules; Figs. 4.3, 4.4, and 4.5a-c) or with bedding planes (i.e. bedding-parallel nodules; Figs. 4.3 and 4.5d, e). The former represent roughly 75% of the total nodules in the study area and are the main target of this work. The association between DBs and nodules occurs in the form of (i) parallelism and spatial overlap between DBs and nodules and (ii) confinement of the nodules by the DBs. In all cases, nodules are oriented with the major axis (elongation direction) parallel to the DBs and the minor axis (i.e. thickness) perpendicular to them. Deformation band-parallel nodules are isolated ellipsoids (Fig. 4.4b, d), or, alternatively, continuous tabular objects (Figs. 4.4a and 4.5a). Nodules may be located along the DB (or zone of bands) trace (Figs. 4.4a, d and 4.5a, b), placed in between and confined by DBs (Figs. 4.4b, e, and 4.5c), or they may be asymmetrically placed on one side of the DBs (Figs. 4.4c and 4.9e). In some cases, nodules lie at the intersection of different DB planes (Fig. 4.3). Some DBs are not spatially associated with nodules (Figs. 4.3 and 4.4b). Among the multiple sets of DBs, those mostly associated with carbonate nodules are the NNW-SSE and the NNE-SSW ones. As a result, most nodules are elongated along these two structural directions (Figs. 4.1d and 4.3; see also Fig. 2.1b). The other sets are rarely associated with carbonate nodules. Nodules are never cut across by the DBs.

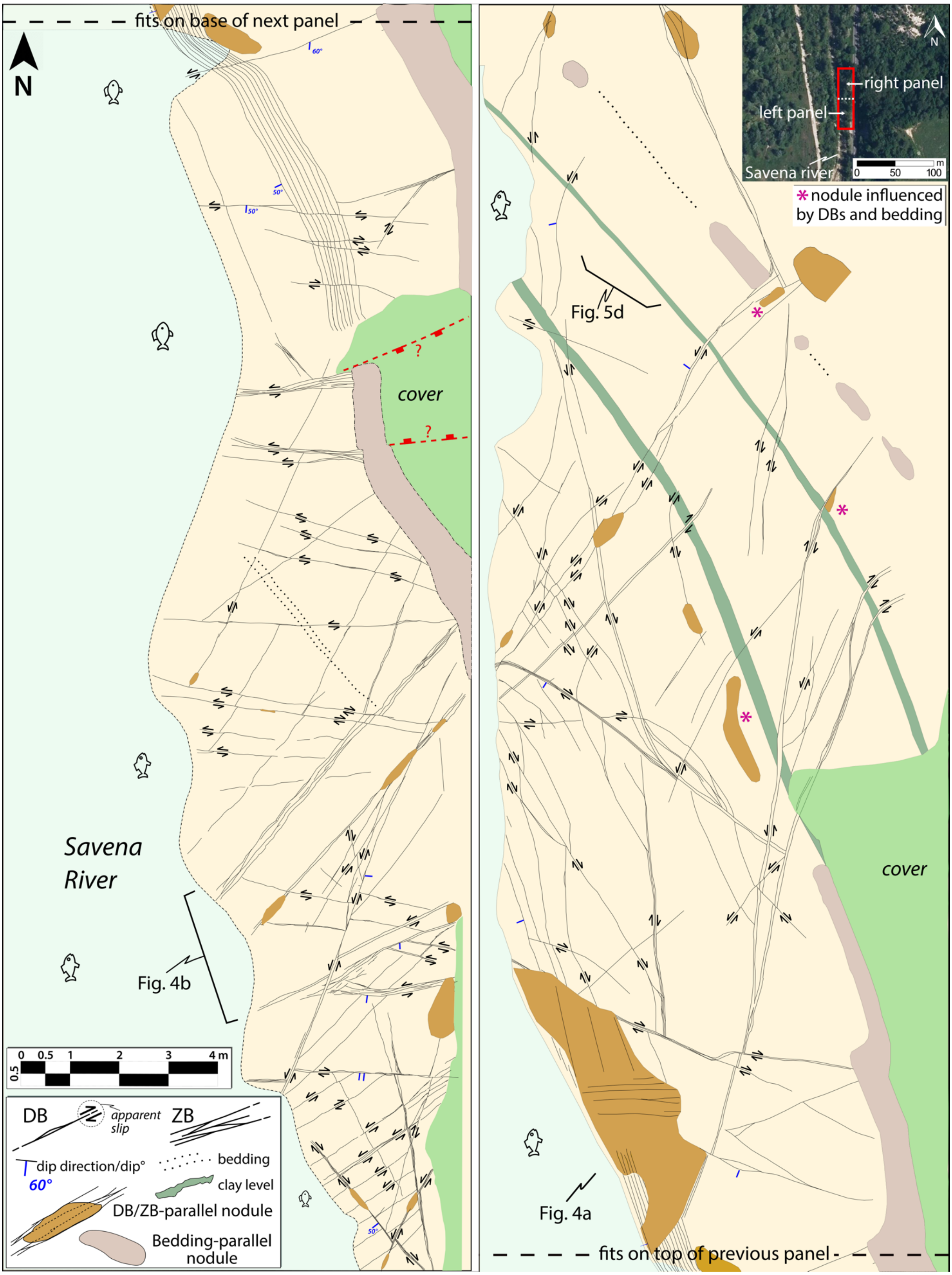

Fig. 4.3 – Outcrop map that documents the geometry and distribution of DBs and nodules in a portion of the study area in Loiano. The right-hand panel fits on top of the left-hand panel. ZB – zone of bands. The inset (© Google Earth) shows the map location in the study area.

Fig. 4.4 – Relationships between nodules and DBs. Deformation bands occur either as single structures or organized in clusters (ZB). Nodules along DBs (or ZB) are isolated **(b, d, e)** or continuous with a tabular geometry **(a)**. Nodules are located along the DB trace **(a, b, d)**, or they are asymmetrically placed on a side of the DB **(c)**. **(e)** Isolated nodule in between and confined by ZB. DBs are whiter than host rock and exhibit a positive relief, a clear reduction in grain size, and a lower porosity visible to the naked eye **(f)**. The pen in **(c, d)** is 14 cm in length. The arrow scale in **(b, e)** is 10 cm in length. The position of **(a, b)** is indicated in Fig. 4.3.

Bedding-parallel nodules are either isolated (Fig. 4.3) and multiple but laterally discontinuous (Figs. 4.3 and 4.5d, e) or laterally continuous layers with a tabular geometry (Fig. 4.3; e.g. "nodular beds" in Del Sole et al., 2020; *Chapter 3*). Nodular beds are continuous pervasively cemented layers that extend along the bedding plane for several meters (up to 15 m in length) with a nearly constant thickness of c. 35-50 cm. Nodules along bedding planes are more rounded gentle boundaries (Fig. 4.5d, e) than those associated with DBs, which are instead more tabular and exhibit angular and sharp boundaries (Figs. 4.4 and 4.5a-c). In some cases, nodule geometry and elongation direction follow both bedding surfaces and DBs (Fig. 4.3). Nodules, despite being ubiquitous in the sandstone, are mostly observed within coarse levels with a grain size equal to or larger than medium sands (0.25-0.5 mm). We did not observe any nodules in sedimentary rocks with a grain size finer than sand (siltstone and clay). Bedding-parallel nodules are commonly located in sandstone levels confined between clay-silty levels or fine-grained sand levels (Figs. 4.3 and 4.5d, e).

A set of joints and veins (Fig. 4.5a, b) was found exclusively within the carbonate nodules. They postdate DBs and nodules and do not propagate into the surrounding host sandstone (see *Section C.8* in Appendix C for details).

Fig. 4.5 – (a-c) DB-parallel- and **(d-e)** bedding-parallel nodules. **(a)** Decametric-scale continuous nodule with a tabular geometry located along a zone of bands (ZB). NE-dipping layering is shown with dotted lines. The photo is about 10 meters in depth. **(b)** Close-up of **(a)** from a map view. The lens cover is 5.5 cm in diameter. **(a, b)** Late-opening fractures cut through the assemblage "DBs – nodule" and they do not propagate into the poorly consolidated host rock. **(c)** Isolated nodules placed in between and confined by ZB. **(d, e)** The bedding is emphasized mostly by clay and silt horizons, sporadic well-defined thin levels of gravel, and the alignment of bedding-parallel nodules. **(d)** Black arrows point to multiple but laterally discontinuous bedding-parallel nodules. Here, a single DB (white line) crosses a bedding-parallel nodule without causing any offset. The position of **(d)** is indicated in Fig. 4.3. **(e)** Photomosaic showing a series of laterally discontinuous nodules just below, above, or in between several continuous impermeable clay-rich levels. The deformation pattern changes depending on the host rock properties (e.g. sorting degree, porosity ϕ, grain size; see C.1 in Appendix C for details). Cataclastic deformation is accompanied by clay smear (see inset) whereby DBs cut thin dark-colored clay levels.

4.4.2. Bollène

At Bollène, DBs occur as belonging to three different trends oriented (i) NW-SE to NNW-SSE (set 1: 334°; Figs. 4.2d and 4.6b), (ii) NE-SW to ENE-WSW (set 2: 61° and set 3: 67°; Figs. 4.2d and 4.6b), and (iii) ESE-WNW (set 4: 278°; Figs. 4.2d and 4.6b). Trend (i) can be divided into two subsets; one is characterized by normal offsets NW-SE conjugate bands with moderate dip angles (50-60°) to SW (Figs. 4.7a and 4.8a, c) and just a few to NE; a second one is characterized by dominant dextral strike-slip kinematic bands with higher dip angles (70-90°) and a NNW-SSE trend (Figs. 4.6b and 4.7f). Trend (ii) can be divided into two sets; one set is characterized by dominantly left-lateral and minor right-lateral subvertical strike-slip conjugate bands striking NE-SW to ENE-WSW (set 2 in Fig. 4.6b; Fig. 4.7a-c); a second set is instead characterized by a set of conjugate DBs with moderate dips (~60°), NE-SW orientation (set 3 in Fig. 4.6b), and undetermined kinematic (likely normal-sense). Trend (iii) is composed of ESE-WNW conjugate bands, with reverse kinematics and low dip angles (30-40°; see *Section C.3* in Appendix C). In the field, DBs appear as whitish linear traces with minor undulations and characteristic eye structures whereby they branch and merge (Figs. 4.6b and 4.7). In most cases, DBs weather out in positive relief. Frequently, DBs occur in narrow zones (a few millimeters up to 5-15 cm in thickness). Field observations indicate that ESE-WNW DBs are crosscut by NE-SW strike-slip DBs (Fig. 4.6b). The latter also crosscut the NW-SE/NNW-SSE set (Fig. 4.7a-c, f). Bedding is oriented NW-SE and dips gently (<10°) to the S (Fig. 4.2b, d). Bedding is difficult to recognize on the floor of the quarry, because of its low dip and the massive texture of the rock (Fig. 4.6b). The Turonian Sandstones outcrop on the quarry floor. There are two lithotypes. The first one is represented by massive porous sands with DBs and localized carbonate cementation (see description below). The second one is characterized by a massive calcrete level with tabular geometry (see C.4 in Appendix C for details).

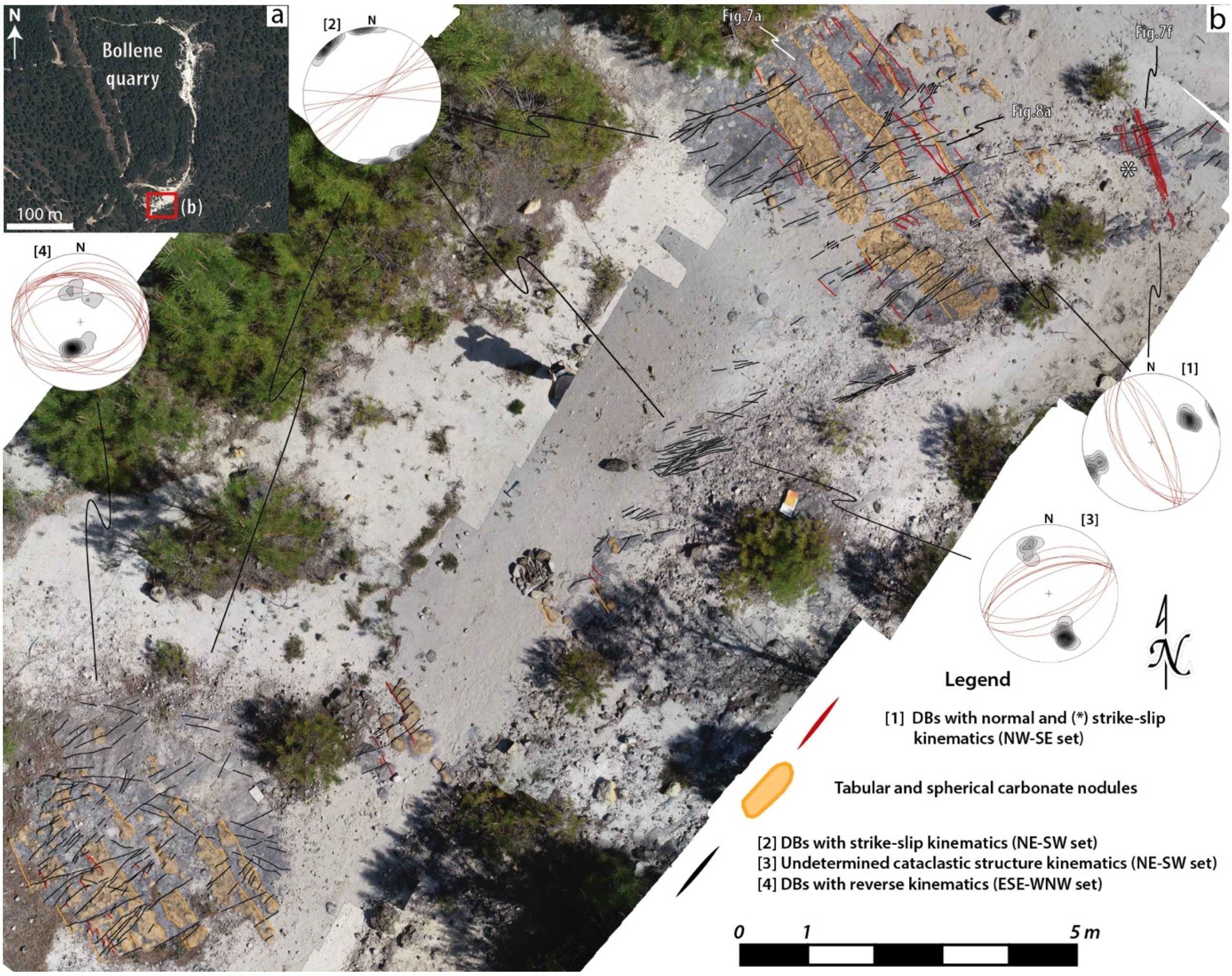

Fig. 4.6 – (a) Aerial photograph of the study site (© Google Earth). **(b)** Orthophoto that documents the geometry and distribution of DBs and carbonate nodules in the Bollène quarry. Lower-hemisphere equal-area projection indicating the orientation of the cataclastic structures measured in (1) NW-SE/NNW-SSE normal and (dextral) strike-slip bands associated with tabular and spherical nodules; (2) NE-SW/ENE-WSW strike-slip bands; (3) NE-SW bands with undetermined kinematics; (4) ESE-WNW reverse-sense bands.

The Turonian Sandstones in the Bollène quarry are characterized by a spatially heterogeneous cementation (Fig. 4.6b). These diagenetic heterogeneities occur as spherical and tabular nodules (Figs. 4.7 and 4.8). Spherical nodules are arranged as isolated bodies within the surrounding host rock (Figs. 4.7c, g and 4.8a, d, e) or aggregated in tabular clusters (Fig. 4.7a, d). Nodules weather out in positive relief. Spherical nodules range in diameter from a few millimeters (0.004-0.005 m) to a few tens of centimeters (0.2 m), whereas tabular ones have a thickness ranging from a few centimeters to 0.1 m and a long axis up to 5 m in length (Figs. 4.6b and 4.7a-c). Assessment of the nodule lateral extension is hampered by the presence of vegetation and debris cover, whereas subsurface extension cannot be measured because of the limited vertical exposures of the outcrops. Hence, the values reported here are minimum values. In general, the nodule shape may be approximated by a sphere for which length, width, and thickness are "equal" and by an oblate spheroid for which length and width are larger than the nodule thickness. Carbonate nodule volume ranges from 10^{-7} (small spherical nodules) to > 2.5 m^3 (tabular nodules assuming length and width of 5 m, and thickness of 0.1 m). In Bollène, the nodules are all spatially and geometrically associated with DBs (i.e. DB-parallel nodules; Figs. 4.6b and 4.7). This association occurs in the form of (1) parallelism between DBs and nodules, (2) geometric congruence between the DB trend and the nodule (or nodules cluster) shape, and (3) confinement of nodules in parallel-to-band compartments. In all these cases, tabular nodules and clusters of spherical nodules are oriented with the major axis (elongation direction) parallel to the DBs and the minor axis (i.e. thickness) perpendicular to them (Figs. 4.7a and 4.8a). Unlike what we have seen in Loiano, in Bollène nodules are in compartments among DBs. Carbonate nodules are associated with the NW-SE/NNW-SSE DBs set (Figs. 4.6b and 4.7a, f). Although this set is conjugate with bands dipping to the SW and to the NE, the tabular cement bodies dip only to the SW (Figs. 4.2d and 4.8a-c). No nodules are cut by the NW-SE bands. The NE-SW/ENE-WSW strike-slip bands cut through the NW-SE/NNW-SSE bands and the associated NW-SE-trending carbonate nodules (Figs. 4.7a-c, f). There is clear evidence of these crosscutting relationships both at the outcrop and at the microscale (see *Section 4.5.2*). For this reason, we focus on the NW-SE DBs and nodules in the remaining part of this study.

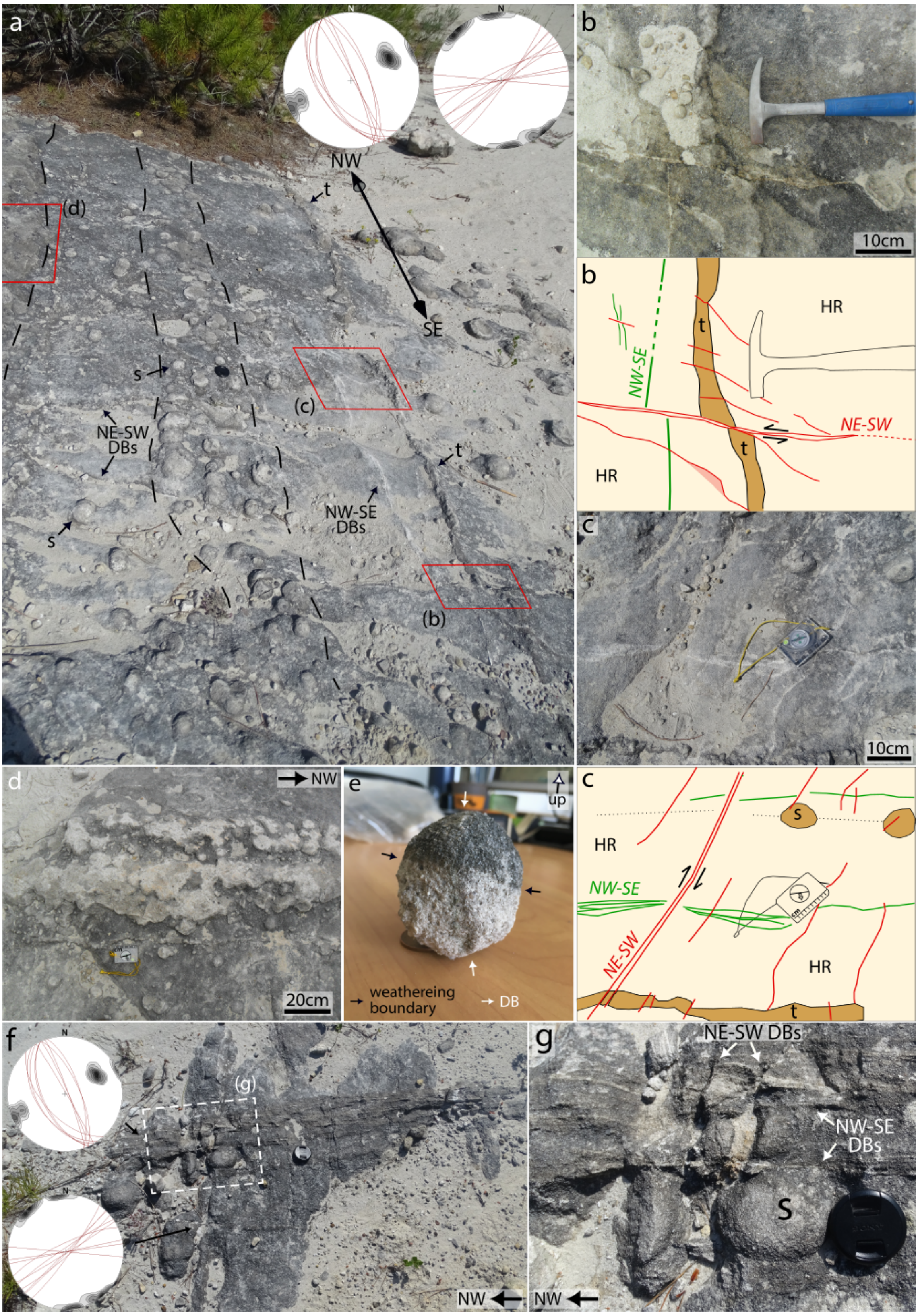

Fig. 4.7 – Calcite cement occurs isolated **(a, c, g)** or in clusters **(a, d)** of (S) spherical nodules and continuous (t) tabular nodules **(a-c)**. Nodules are arranged in compartments parallel to clusters of NW-SE normal bands **(a-c)** and to NNW-SSE dextral strike-slip bands **(f, g)**. NE-SW/ENE-WSW strike-slip bands displace both the NW-SE bands and their associated nodules **(a-c, f)**. **(e)** Spherical nodule (about 5 cm in diameter) in spatial superposition with a NW-SE DB that does not displace the cement. The lens cover in **(a, f)** has a 5.5 cm diameter. The figures **(a-d, f, g)** are in map view. The position of **(a, f)** is indicated in Fig. 4.6b. Hammer length in **(b)** is 30.5 cm.

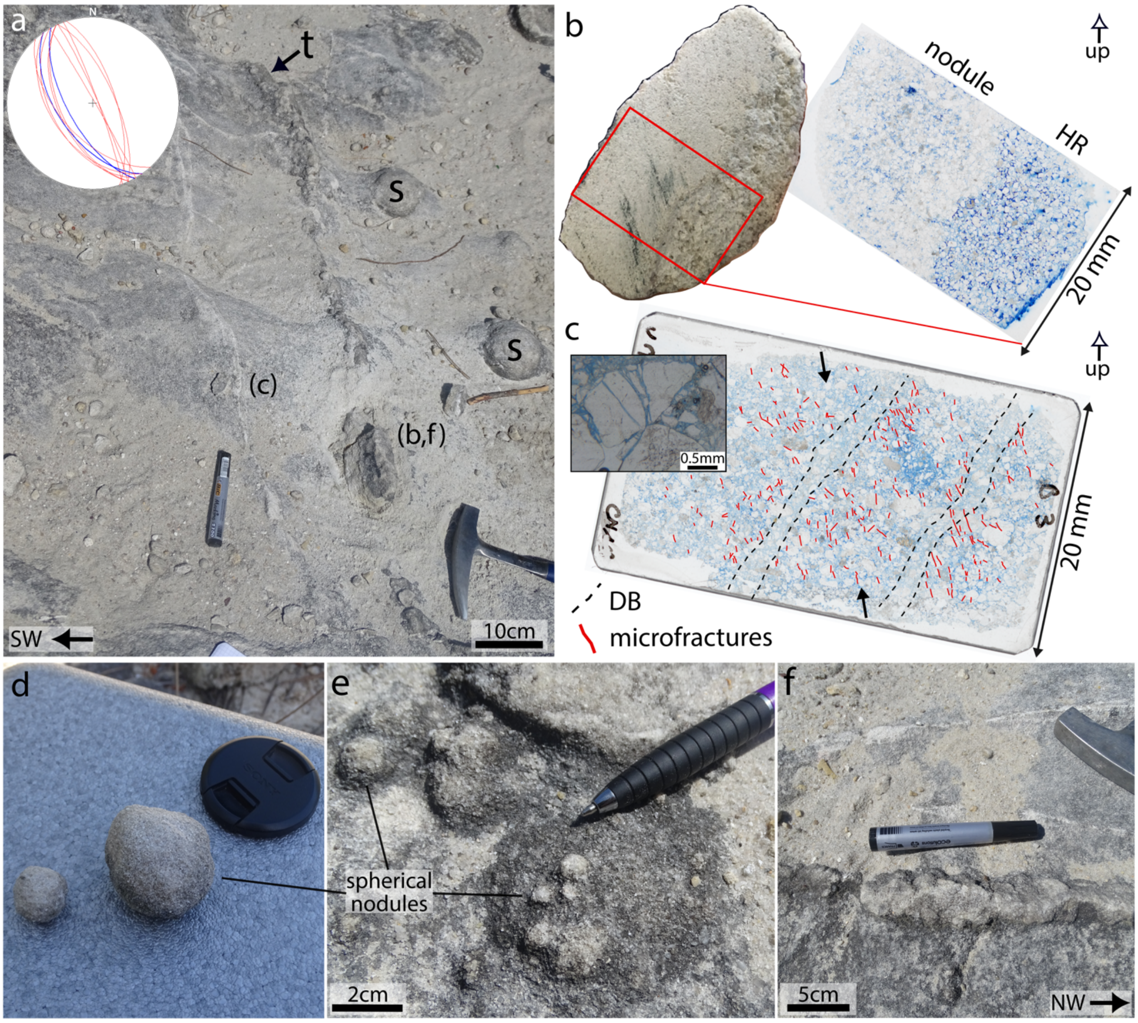

Fig. 4.8. – Typical relationships between nodules and DBs. **(a)** Continuous tabular nodule (t) and isolated spherical nodules (S) aligned parallel to the NW-SE normal-sense bands dipping SW (~55°; red lines in the inset stereoplot). The tabular bodies dip to the SW parallel to the bands (blue lines in the stereoplot in the inset). The position of **(a)** is indicated in Fig. 4.6b. **(b)** Hand specimen and polished thin sections impregnated with blue-dyed resin of a tabular nodule in **(a)**. **(c)** Polished thin sections impregnated with blue-dyed showing two sub-parallel NW-SE normal-sense bands dipping SW. Mapping of microfractures developed at grain contacts consistent with Hertzian contacts (e.g. Eichhubl et al., 2010; Soliva et al., 2013) endorses the normal kinematic of these bands (see C.1 and C.2 in Appendix C for details). "Up" refers to the topography. Close-up of spherical **(d-e)** and tabular **(f)** nodules from the field. Pen-marker length in **(a, f)** is about 13.5 cm. The lens-cover in **(d)** has a 5.5 cm diameter.

4.5. DEFORMATION BANDS AND CEMENT: TEXTURAL AND MICROSTRUCTURAL CHARACTERISTICS

4.5.1. Loiano

Host rock total porosity (minus-cement ϕ) is between 20-26% (Fig. 4.9; Del Sole and Antonellini, 2019; Chapter 2). Porosity is predominantly intergranular, whereas intragranular (e.g. pores within bioclasts) and "oversize" pores are due to dissolution of detrital grains (Figs. 4.9 and 4.10). Deformation band total porosity (minus-cement ϕ) is lower by an order of magnitude (below 5%)

than the host rock porosity (Fig. 4.9d). In the nodules, the host rock porosity is almost completely filled by cement (Fig. 4.10), so that the remnant porosity (voids) is low (down to 1.3%) (Fig. 4.9a, c). The presence of cement within the DBs enhances the porosity reduction caused by grain crushing and compaction (Fig. 4.9d). The microstructure of the DBs is characterized by reduced grain size, porosity, and pore size compared to the host rock (Fig. 4.10i-l). Within the DBs a few coarse grains are surrounded by a fine-grained matrix.

Despite the different effects of mechanical and chemical compaction as well as minor authigenic alterations (refer to C.1 in Appendix C for details), the major diagenetic components of the Loiano Sandstone are calcite cements. These cements fill mainly intergranular, and to a lesser extent intragranular (intraskeletal) pore spaces, intragranular fractures, and they encase the framework grains and all other diagenetic features. Bedding-parallel nodules (Fig. 4.10a-h) are characterized by a mosaic texture of blocky sparite to poikilotopic bright-orange to orange CL calcite cement. Crystal size is typically 40-100 μm and up to 300 μm (Fig. 4.10g, h). This cement phase is the most widespread one and it is uniform almost everywhere in terms of texture and CL pattern, if not for some minor dark CL subzones (Fig. 4.10g, h). A minor calcite cement phase is associated with detrital carbonates (bioclasts) and it shows a bright-orange CL (Fig. 4.10c-d). It occurs as pore lining formed by elongate and sharp rhombohedral calcite (dogtooth) that outlines the outer rim of the bioclasts (Fig. 4.10c) and drusy mosaic calcite that fills intraskeletal pores, outlines bioclasts, and fills intragranular fractures in bioclasts (Fig. 4.10d). This subordinate phase was observed only in bedding-parallel nodules. Pore-lining cement around bioclasts is present only where there was pore space (now filled), whereas it is absent where other grains are in contact with the bioclast. All cement phases described above (intergranular, intraskeletal, and pore lining) encase compacted grains, and cements are undeformed still preserving the original shape. Pore-filling cement in DB-parallel nodules (Fig. 4.10i-n) shows a similar texture and CL pattern to that described for the main intragranular cement phase in the bedding-parallel nodules (Fig. 4.10a-h). The main features that differentiate DB-parallel nodules from bedding-parallel ones are the finer crystal size of calcite within DBs (Fig. 4.10i-l) and the absence of a bright-orange CL cement phase described in association with bioclasts in bedding-parallel nodules (Fig. 4.10c, d). Some bright-orange CL cement was observed only in detrital form (crushed) within the DB (Fig. 4.10k). The pore filling in DBs is fine-grained sparite; no evidence was found of crushed calcite crystals belonging to the dominant calcite phase. The finer fraction within the DBs is a matrix made up of comminuted angular and fine-grained clasts (flakes) of feldspar and to a smaller degree quartz, encased by the cement (Fig. 4.10j-l). Similarly, the cement fills the microfractures that cut through coarser grains and it encase the fine-grained clasts that are present within these fractures. Although, these microfractures are frequent in the host rock sectors in proximity to the DB (Fig. 4.10i), they were also observed in bedding-parallel nodules (Fig. 4.10a, b). Host rock volumes within DB-parallel nodules are still characterized by blocky sparite cement with some minor dark CL growth subzones (Fig. 4.10i, m, n), similar to what was observed in bedding-parallel nodules.

To evaluate any sign of dissolution in nodules, we carefully checked cement crystal morphologies adjacent to poorly cemented or non-cemented host rock sectors at the edges of nodules. Here, cement crystal boundaries are regular and sharp (Fig. 4.10m, n).

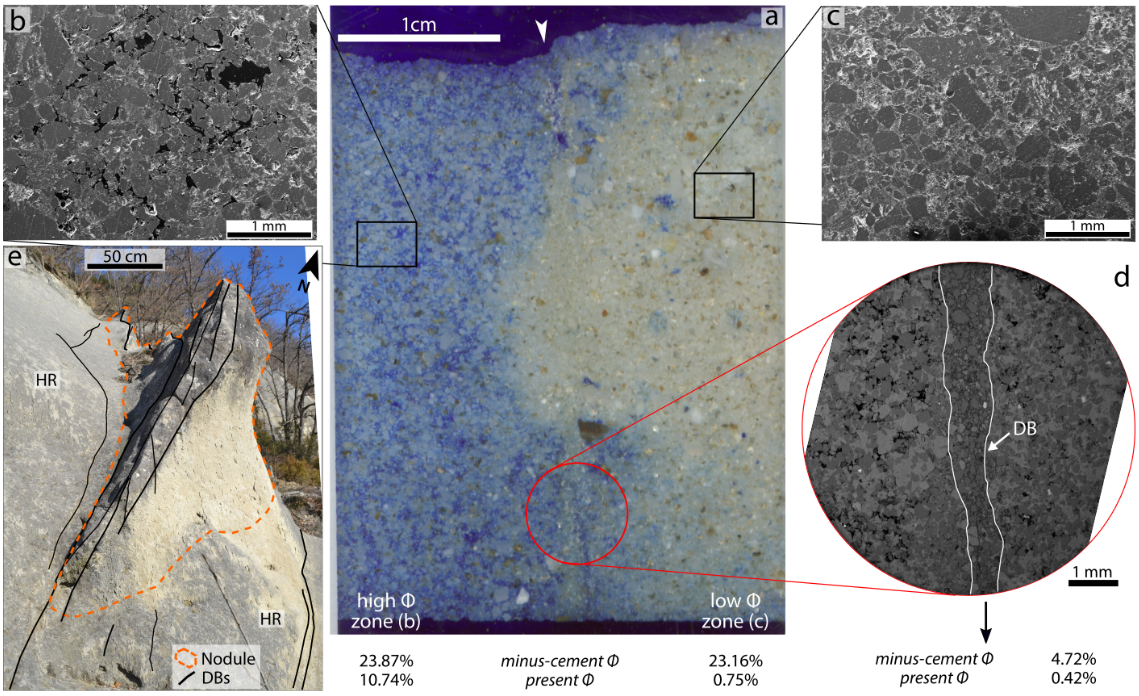

Fig. 4.9 – Host rock (HR) and DB porosity as well as relationships between cement and DBs in the Loiano Sandstones. **(a)** Polished thin sections impregnated with blue-dyed resin. The section shows a DB (arrow) separating two host rock sectors: on the right-hand side there is extensive calcite cementation, whereas on the left-hand side cementation is poor. **(b, c)** Secondary electron and **(d)** backscattered electron SEM images from different sectors of the section **(a)**. Porosity (ϕ) estimation data in **(a-d)** are from Del Sole and Antonellini (2019). **(e)** Field example for which a nodule is asymmetrically placed on a side of the DBs, similarly to what is observed in **(a)**. See text for further details.

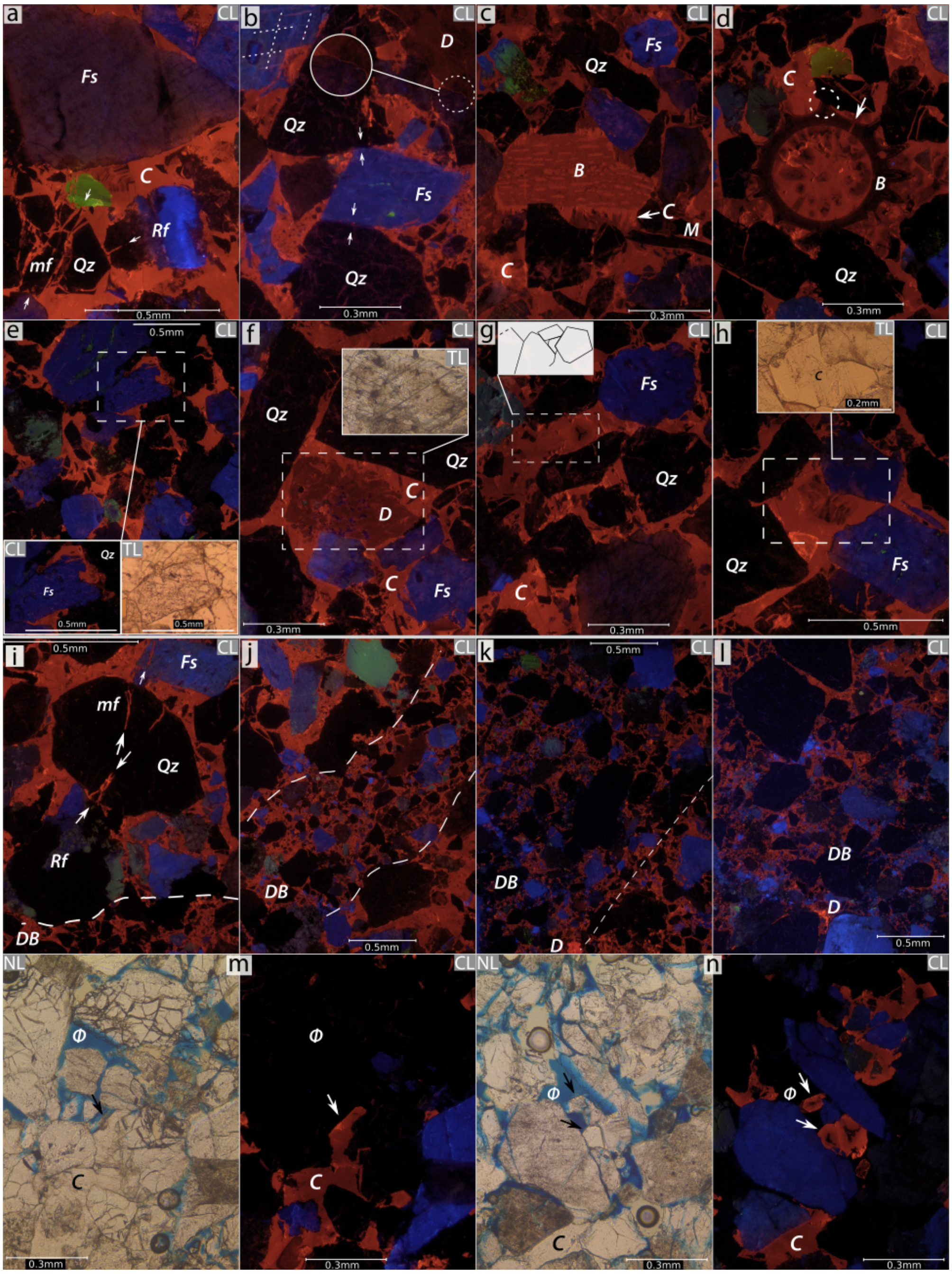

Fig. 4.10 – Natural- and CL-light photomicrographs showing the microstructure and cement textures in **(a-h)** bedding-parallel and **(i-n)** DB-parallel nodules. **(a-b, d)** Microfractures form at grain contacts due to stress concentration at contact points, and **(i)** they are common in the host rock areas close to the DB. **(b)** Feldspars break mainly by cleavage-controlled intragranular fractures (white dotted line). Some framework grains show planar to slightly undulated framework grain-to-grain contacts. Detrital carbonate clasts and **(c-d)** bioclasts are partially dissolved at grain contacts. **(e)** Some detrital grains are corroded and coated or partially replaced by cement. **(f)** Syntaxial overgrowth cement on a detrital carbonate clast (D). Bright CL **(c)** circumgranular pore lining (dogtooth texture) and **(d)** intraskeletal (drusy mosaic) calcite cement were observed only in bedding-parallel nodules. The main cement phase is characterized by bright-orange to orange CL calcite cement that fills intergranular porosity and intragranular fractures both in **(a, b, e-h)** bedding-parallel nodules and **(i-n)** DB-parallel ones. **(g-h, m-n)** Host rock volumes in nodules are characterized by blocky sparite to poikilotopic calcite cement with minor dark CL subzones, whereas **(j-l)** the cement in DBs is fine-grained sparite. **(m-n)** At nodule edges, cement crystal rims are regular and sharp, suggesting absent or negligible dissolution. Bright grains in **(k, l)** are detrital calcite (D). Qz - quartz; Fs - feldspar; M - mica; Rf - rock fragment; B - bioclast; ϕ - pore space; C - calcite cement; TL - transmitted light. See text and section C.1 in Appendix C for further details.

4.5.2. Bollène

The host sands at Bollène are weakly cemented, with the exception of localized carbonate cementation described above. Host rock grains are mostly rounded and lack a fabric (Fig. 4.11a, f). Here, we describe the microstructure of NW-SE/NNW-SSE normal-sense and strike-slip bands, as well as NE-SW/ENE-WSE strike-slip bands sets. The most recognizable features that characterize both DB sets are the reduction of grain size and porosity, as well as a tighter packing relative to the host rock (Fig. 4.11). NE-SW strike-slip bands (Fig. 4.11i-l) have a higher degree of grain comminution, porosity reduction, and tighter packing when compared to NW-SE bands (Figs. 4.8c and 4.11g-h). Most grains within the bands are fractured and angular. Despite the strong comminution, a few rounded large survivor quartz grains are preserved in the DB matrix (Fig. 4.11g, h, k). Fine angular grains that are mostly comminuted feldspar fragments and secondarily quartz and minor oxides make up the matrix. We also observed fine particles of crushed calcite cement among the matrix grains within NE-SW bands (Fig. 4.11k, l). In some cases, the grains in the host rock areas in proximity to the DB are encased by relatively undeformed carbonate cement (Fig. 4.11i, j). Some grains in the host rock are corroded and partially replaced or coated by calcite cement (Fig. 4.11c).

The main cement in spherical and tabular nodules is a poikilotopic calcite that infills intergranular pores (Fig. 4.11a-e). Most of the cement is non-luminescent (dark luminescence) under CL (Fig. 4.11c, d), but a few crystals show partial overgrowths with a bright-orange CL color (Fig. 4.11e). When the crystal has a heterogeneous CL-pattern, the non-luminescing zones are mainly in the crystal core, whereas the luminescing subzones are mostly at the crystal edges (Fig. 4.11e). A very thin film (up to c. 10μm thick or less) of bright-orange CL calcite cement commonly coats the detrital grains (Fig. 4.11c), and it is also visible under natural light (Fig. 4.11b). In the nodules, some of the intragranular microfractures at contact points are filled by cement (Fig. 4.11a); a few are not (Figs. 4.11b). The cements described above (pore filling and grain coating) are relatively undeformed (i.e. no microfractures, no twin lamellae) and still preserve the original shape, except where the NE-SE/ENE-WSW strike-slip bands crosscut the cement nodules. At the crosscutting site, indeed, and more specifically in the host rock sectors in proximity to the NE-SW/ENE-WSW bands, we observe intragranular fractures at contact points and the onset of cement comminution between quartz clasts (Fig. 4.11i, j). Fine particles of crushed detrital calcite cement are found among the cataclastic matrix grains within NE-SW/ENE-WSW strike-slip bands where they interact with nodules (Fig. 4.11k, l). At the microscale, no preferential or significant calcite cementation was observed in association with the NW-SE bands. The association between cements and these latter bands was observed only at the mesoscale (see *Section 4.4.2*).

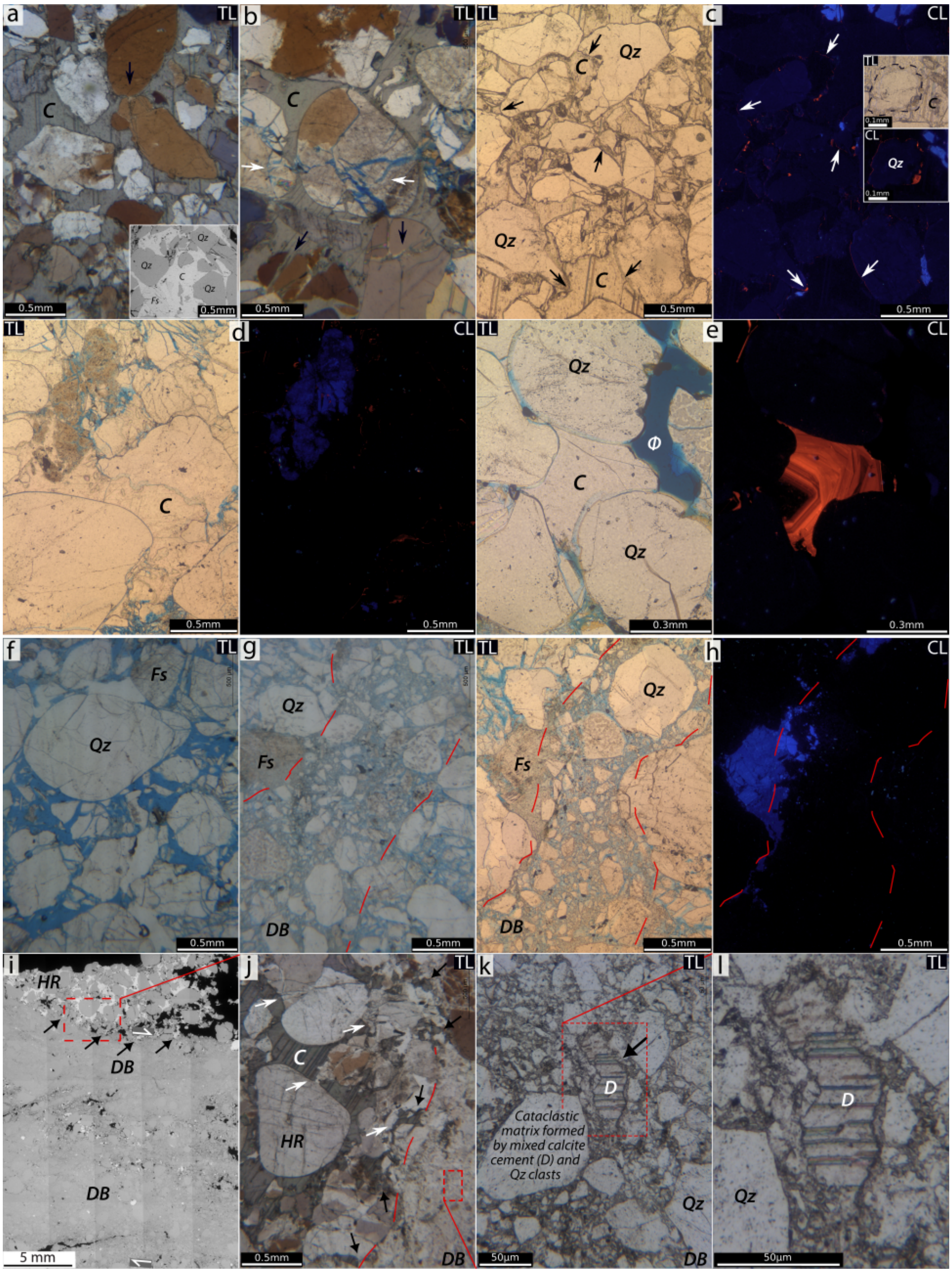

Fig. 4.11 – Natural- and CL-light photomicrographs showing the internal texture and microstructure of **(a-e)** spherical and tabular nodules and **(f-l)** DBs. **(a, b, f)** Host rock grains are mostly rounded and nearly undisturbed. Some microfractures break framework grains at contact points. In nodules, **(a)** some of the microfractures are filled; **(b)** a few are not. (g, h) Microfractures are more frequent approaching the DB and **(j)** they are preferentially oriented with respect to the band (white arrows). Cement fills intergranular pore space and intragranular fractures. **(c-e)** The major diagenetic component is poikilotopic spar cement with dominant dark luminescence and **(e)** minor bright-orange CL growth subzones. **(c)** A very thin film of bright-orange CL calcite cement often coats detrital grains. Minor diagenetic alterations are corroded detrital grains that are partially replaced by calcite cement; see inset in **(c)**. **(g, h)** NW-SE bands and **(i, l)** NE-SW strike-slip bands show a similar pattern, but NE-SW bands feature a high degree of grain comminution and porosity reduction. **(i, j)** NE-SW strike-slip bands crosscut cement nodules; intragranular fractures (white arrows) and incipient stage of cement comminution (black arrows) between quartz clasts in the host rock sectors in proximity to these bands. **(k, l)** Fine particles of crushed detrital calcite cement (D) are found among the matrix grains at the crosscutting site. The inset in **(a)** is a backscattered electron SEM image. Qz - quartz; Fs - feldspar; ϕ - pore space; C - calcite cement; TL - transmitted light. See Appendix C for details.

4.6. CEMENT STABLE ISOTOPE GEOCHEMISTRY

4.6.1. Loiano

Cement from the nodules of the Loiano samples has $\delta^{13}C$ values between -7.68 and -1.47 ‰ (VPDB) and $\delta^{18}O$ values between -4.42 and -1.35 ‰ (VPDB) (Fig. 4.12a). The cement from DB-related nodules is characterized by isotope compositions between -5.41 and -1.47 ‰ (VPDB) for $\delta^{13}C$ and between -4.42 and -1.40 ‰ for $\delta^{18}O$ (VPDB). The cement from bedding-parallel nodules has isotope compositions between -7.68 and -5.94 ‰ (VPDB) for $\delta^{13}C$, and between -2.09 and -1.35 ‰ (VPDB) for $\delta^{18}O$. Both cement groups (DB-parallel and bedding-parallel nodules) have a relatively narrow range of oxygen isotopic composition featuring a nearly vertical alignment in the $\delta^{18}O$–$\delta^{13}C$ cross-plot. DB-parallel nodules show a slightly wider span of $\delta^{18}O$ composition when compared to bedding-parallel nodules. However, carbon isotopic composition shows a wide range of variability when considering both the total isotopic composition data and the cement group data.

4.6.2. Bollène

Stable isotope analysis of the Bollène samples also defines two groups of data in the $\delta^{18}O$–$\delta^{13}C$ space (Fig. 4.12b). The cement group referring to the DB-related nodules has $\delta^{13}C$ values between -7.73 m and -4.68 ‰ (VPDB) and $\delta^{18}O$ values between -7.70 and -5.88 ‰ (VPDB). The other group is from cement sampled in a calcrete level observed within the same Turonian Sandstone a few meters above the studied outcrop (see *Section 4.4.2* and *section C.4* in Appendix C for details), and it is characterized by isotope compositions between -2.54 and -2.39 ‰ (VPDB) for $\delta^{13}C$, and between -6.58 and -6.32 ‰ (VPDB) for $\delta^{18}O$. Both cement groups have a relatively similar $\delta^{18}O$ signature and a relatively narrow range of $\delta^{18}O$ composition varying only between -7.70 and -5.88 ‰ (VPDB). In a similar way, cement sampled from the calcrete has a narrow range of $\delta^{13}C$ composition and shows the heavier $\delta^{13}C$ values in the data set. However, the $\delta^{13}C$ composition of DB-related nodules has a wider variability range and is the most depleted in the data set.

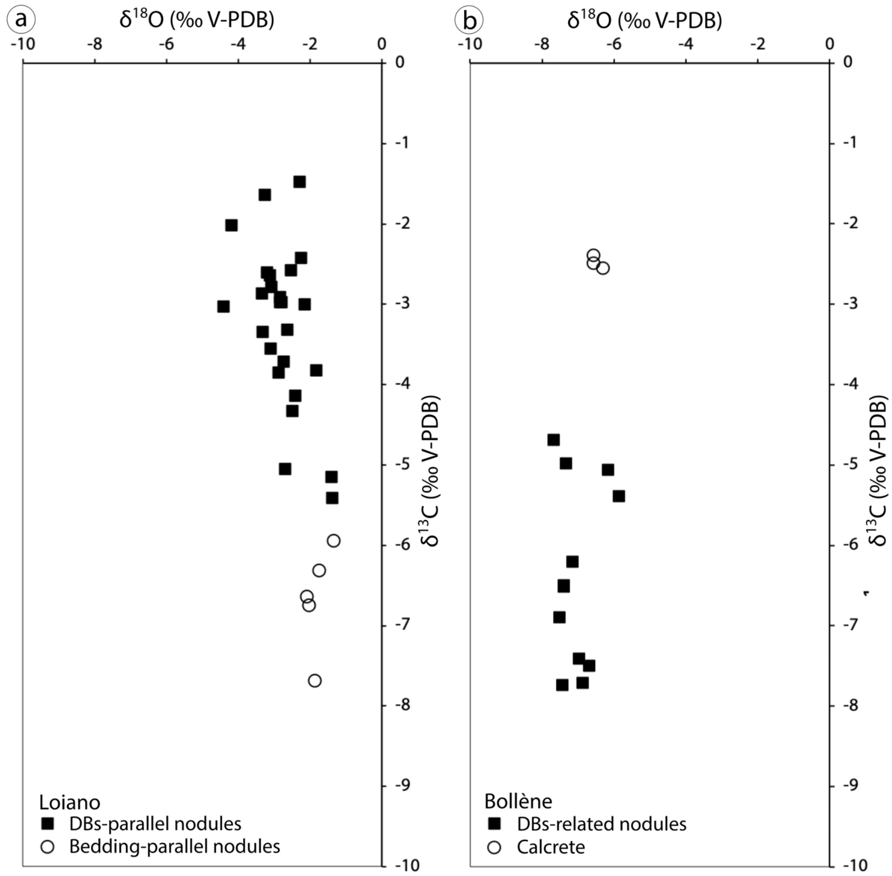

Fig. 4.12 – Stable isotope analysis results. **(a)** Cumulative isotopic data characterizing the DB-parallel nodules (black full-dots) and bedding-parallel ones (empty dots) inside the Loiano Sandstones. **(b)** Isotopic data from the DB-related nodules (black full dots) and cement sampled in the calcrete (empty dots) in the Bollène quarry (see section C.4 in Appendix C for details).

4.7. DISCUSSION

In the following, we compare the two field sites highlighting their similarities and differences concerning the interaction between deformation, fluid flow, and diagenesis. We discuss the influence of DBs on fluid flow and their role in enhancing diagenesis and localizing diagenetic products (nodules). Finally, we propose an explanation for the geochemical environment within which fluids were sourced and precipitated the nodule cement. We then explore the implications of SDHs for subsurface fluid flow and reservoir characterization.

4.7.1. Cement distribution and its relationship with deformation bands

The distinctive feature of the *Loiano Sandstones* is a spatially heterogeneous cementation in the form of nodules. Field evidence indicates that DB formation predates calcite cementation. All nodules are spatially related to DBs (Figs. 4.3 and 4.5a-c) except for those that are situated along bedding planes (~25% of the total nodules; Figs. 4.3 and 4.5d, e). In contrast, not all DBs are associated with nodules. A clear correspondence always exists between the shape and elongation direction of the nodules and the DBs direction. This pattern is also observed from aerial photographs (Fig. 2.1b; Del Sole and Antonellini, 2019). Localized cement along these structural features is itself an indication that deformation preceded cement precipitation (e.g. Eichhubl et al., 2004). If the sandstones were completely cemented at first and then completely removed except from the DBs, the cement in the DB matrix would most likely have been preserved in orange-reddish hues (oxidation residues), but nothing like that was observed. Moreover, cement morphologies adjacent to the porosity at nodule edges imply that cement dissolution has not occurred (Fig. 4.10m, n), thus excluding the possibility that nodules, both those parallel to bedding and those parallel to DBs, are relicts from an overall dissolution process. No DBs crosscut the cement, at least for those sets that are spatially related to nodules (NNW-SSE to NE-SW), indicating that cementation postdates DBs development. In support of this, the precipitation of cement and (the consequent) lower porosity would favor the formation of joints over DBs in the sandstone (Flodin et al., 2003; Aydin et al., 2006; Fig. 4.5a, b). The presence of pore-filling cement would increase the strength of the sandstone (Del Sole et al., 2020; *Chapter 3*), preventing rotation and sliding of particles, and increase rock cohesion (Bernabé et al., 1992) and grain contact area, thus yielding a uniform contact stress distribution and higher stiffness (Dvorkin et al., 1991). Extensive cement, then, would inhibit DB development. Please refer to *Section C.8* in Appendix C for further details.

Results from microstructural observations show that intergranular cement in the nodules encloses the grains within both host rock and DBs, and it overprints burial-related mechanical and chemical compaction features (Fig. 4.10a-h). This evidence suggests that the formation of authigenic cements occurred after significant compaction (Cibin et al., 1993; Milliken et al., 1998). Estimated burial depths for the top of the Loiano Sandstones are 800-1000 m (Cibin et al., 1993) and 700-1200 m (McBride et al., 1995). Transgranular microfractures at grain contacts are due to stress concentration at contact points and they are interpreted as load-bearing structures within the granular framework (Antonellini et al., 1994a; Eichhubl et al., 2010; Soliva et al., 2013). In DB-parallel nodules samples the cement that fills the transgranular fractures is in continuity (i.e. same textural and CL characteristics) with the pore-filling cement outside the fractures. The presence of undeformed cement within structural-related features such as microfractures and crushed grains (Fig. 4.10i-l), both within and outside the DBs, proves that cement precipitation occurred after (at least after the early stages of) deformation.

The bands are the main controlling factor on the location, geometry, and elongation direction of DB-parallel nodules. The occurrence and location of bedding-parallel nodules are instead controlled by grain size and contrast in grain size within the host rock. Although bedding-parallel nodules are found in all sands, they are more common within coarse-grained levels (≥ medium sands; i.e. size range: 0.25-0.5 mm). There are no nodules in sediments below the sand range or in layers with permeability below 100 mD (Del Sole et al., 2020; *Chapter 3*). Moreover, bedding-parallel nodules are often restricted to the sand level in contact with clay-silty levels above and/or below (Fig. 4.5d, e). Hence, grain size and permeability variations are the most important factors controlling diagenesis and nodule formation in Loiano. The grain size and permeability variations as dominant controls on nodules development in porous media is also reported by other authors (Mozley and Davis, 1996; Hall et al., 2004; Davis et al., 2006; Cavazza et al., 2009). In general, bedding-parallel nodules show a more rounded morphology when compared to DB-related nodules. The former nodule type owes its smooth morphology to a homogeneous and isotropic weathering; the sharp and squared shapes of DB-parallel nodules is probably due to the anisotropy introduced by the DBs in the host rock that influences the cementation. The interplay between band strength and erosion may also have an influence on nodule shape.

In the *Bollène quarry*, all calcite nodules occur in association with the DBs, in particular with the NW-SE/NNW-SSE set (Fig. 4.6b). At this site, we observe complex relationships among multiple deformational and diagenetic events. Timing of bands and nodules is inferred from crosscutting relationships. There is no evidence of low-angle ESE-WNW reverse-sense DBs crosscutting the cement nodules, whereas NE-SW to ENE-WSW-trending strike-slip DBs offset the reverse-sense bands, the NW-SE bands, and the NW-SE-trending cement nodules (Figs. 4.6b and 4.7; see also *Sections C.1 and C.3* in Appendix C). The localization and parallelism between DBs and cement are similar at the two field sites, with the exception that NW-SE-trending nodules and DBs in *Bollène* are not superposed. Here, DBs are always overprinted by cement but the spatial overlap between DBs and nodules (Fig. 4.7e) is unusual. Nodules occur in compartments that are spatially confined by DB zones. Tabular nodules and clusters of spherical nodules are oriented with the major axis parallel to the NW-SE DBs (Figs. 4.6b and 4.7a). The NW-SE bands do not crosscut the cement; therefore, calcite cementation occurred between the NW-SE bands formation (Pyrenean contraction or Oligocene-Miocene extension?) and the NE-SW strike-slip bands (Miocene-Quaternary age Alpine shortening?). Please refer to *section C.1* (Appendix C) for details on how DBs relate to the tectonics of the area. Microstructural observations show that the dominant phase of intergranular calcite cement encloses the grains within the nodules, and it overprints only a proportion of the transgranular microfractures at grain contact points. All microfractures in the nodules are filled by a cement that is in continuity (same texture and CL characteristics) with the pore-filling cement outside the grain. Unfilled microfractures (Fig. 4.11b) were not connected to the pore network, and they were potentially quickly isolated by the calcite mineral growing in the pore space. It is less likely that they formed after cement precipitation; otherwise, the cement would have been broken.

4.7.2. *Role of deformation bands in fluid flow and diagenesis*

The localized diagenesis observed in the form of nodules at Loiano and Bollène provides evidence for the effect of structural heterogeneities, such as DBs, on fluid flow in porous sandstones (Eichhubl et al., 2004, 2009; Balsamo et al., 2012; Philit et al., 2015; Del Sole and Antonellini, 2019; Del Sole et al., 2020). The petrophysical properties (porosity, permeability, capillary entry pressure) of DBs influence fluid flow and localize diagenesis and cement precipitation.

Cataclastic DBs increase flow tortuosity in reservoirs and produce capillary barriers that severely baffle the flow at the reservoir scale and limit cross-flow between host rock compartments (Harper and Mofta, 1985; Edwards et al., 1993; Lewis and Couples, 1993; Antonellini and Aydin, 1994; Leveille et al., 1997; Gibson, 1998; Antonellini et al., 1999, 2014a; Sternlof et al., 2004; Rotevatn and Fossen, 2011; Ballas et al., 2012; Medici et al., 2019; Romano et al., 2020). Smaller pores within bands result in higher capillary forces than in the host rock. This may cause higher water saturation within the bands with respect to the host rock (Tueckmantel et al., 2012; Liu and Sun, 2020). A higher degree of flow tortuosity (reduction in pore interconnectivity) and lower porosity and permeability within the bands may increase the fluid retention time regardless of the water saturation conditions (Antonellini et al., 1999; Sigda and Wilson, 2003; Wilson et al., 2006). Recently, Romano et al. (2020) documented with single and multiphase core flooding experiments that cataclastic bands can strongly influence the fluid velocity field. Other authors (Taylor and Pollard, 2000; Eichhubl et al., 2004) recognized that a slower rate of solute transport relative to the fluid within the bands causes the formation and local perturbation of diagenetic alteration fronts. In light of these considerations and the temporal and spatial relationships between bands and cements obtained from field and microstructural observations, we discuss a model for selective cement precipitation associated with DBs. In our model we assume a reservoir in saturated conditions (see also *Section 4.7.3*).

A marked grain surface roughening and reduction of grain size, porosity, and pore size characterize the DBs presented in this work. In *Loiano*, the combined effect of cataclasis and compaction in the DBs causes porosity reduction by 1 order of magnitude, permeability reduction by 3 orders of magnitude, and advective velocity reduction by 2 orders of magnitude with respect to the host rock (Del Sole and Antonellini, 2019; Chapters 2 and 3). Similarly, DBs in the *Bollène* quarry have lower permeability (up to 3 orders of magnitude) and porosity (up to 50%) (Ballas et al., 2014; see also *section C.5* in Appendix C) when compared to the host rock. A lower permeability, a higher degree of tortuosity (i.e. lower pore size), and reduced section area available for flow (i.e. lower porosity) in the DBs compared to the host rock may cause a flow "slowdown". In *Loiano*, the slowdown effect would be more pronounced when considering the normal-to-DB flow than the parallel-to-DB one given that normal-to-DB permeabilities are lower (1 order of magnitude in average) when compared to parallel-to-DB ones (Del Sole et al., 2020; *Chapter 3*). Cataclasis has competing effects on advective flow velocity; it causes (i) an increase in flow velocity linked to the porosity reduction and (ii) a decrease in the hydraulic conductivity (if the hydraulic gradient does not change). The decrease in hydraulic conductivity (3 orders of magnitude; Del Sole and Antonellini, 2019) dominates over the flow velocity increase caused by porosity reduction (1 order of magnitude; Del Sole and Antonellini, 2019). As a result, there is a net decrease in advective flow velocity in the DBs. A reduction in flow velocity (i.e. slower flow path in the DB with respect to the host rock) might increase the residence time of the fluid migrating through the reactive material (see next paragraph).

A first mechanism responsible for cement nucleation in association with DBs would be the presence of highly reactive crushed and pervasive fractured siliciclastic grains within the cataclastic DBs (e.g. Lander et al., 2009; Williams et al., 2015). The comminuted material of the DBs has a large amount of reactive surface area (nucleation spots) and very tiny pore spaces among the crushed grains. With these conditions, cement precipitation requires less free energy to occur (Wollast, 1971; Berner, 1980), whereas greater cement abundances (Walderhaug, 2000) and faster rates of cement emplacement (Lander et al., 2008; Williams et al., 2015) are promoted. Despite the fact that the role of fracturing in promoting cement precipitation in sandstones has been essentially explored for quartz cement (Antonellini et al., 1994a; Fisher and Knipe, 1998; Milliken et al., 2005; Eichhubl et al., 2010; Philit et al., 2015), we think that this mechanism can be applied to calcite cement too. There is plenty of evidence of calcite precipitation over a silica substrate (e.g. Stockmann et al., 2014), but it would require either more time or a higher degree of supersaturation (e.g. Noiriel et al., 2016) to occur (i.e. to lower the energy barrier for nucleation) when compared to a carbonate substratum. In this work we show that DBs are a preferred site of cement precipitation. Within the DB there are more nucleation spots for cement nucleation and smaller pores that lead to a fast pore clogging. DB pores close faster than host rock ones. Once the cement begins to precipitate, the fresh carbonate substrate (cement) could further enhance precipitation (e.g. Noiriel et al., 2016). This mechanism may be relevant for *Loiano* where the calcite cement fills small pore spaces among fresh quartz and feldspar surfaces created during fracturing. This process can explain why in most cases DBs are more cemented than the surrounding host rock. On the contrary, this process was less relevant in the *Bollène quarry* where the bands are not cemented by carbonate and the cementation is localized in compartments between zones of bands rather than within them. The arrangement of nodules in Bollène indicates that the low-permeability DBs hindered the cross-flow, restricted the fluid flow, and focused the diagenesis to parallel-to-bands compartments.

A second mechanism could have worked in combination with the presence of more reactive fine-grained comminution products to promote cementation in the DBs in *Loiano*. According to their experiments on an analog fault gouge, Whitworth et al. (1999) suggested a membrane behavior for faults in sandstone during cross-fault flow and solute-sieving-aided calcite precipitation. A membrane effect and solute-sieving by faults may locally increase the concentrations of components needed for calcite cementation (e.g. Ca and bicarbonate) on the high-pressure side of the membrane and induce precipitation. The DBs could have acted as a semipermeable membrane in baffling chemically reactive flow and favor cement precipitation. This process may explain a higher concentration of cement along the DBs in nodules and the asymmetric distribution of cement on one side of DBs (upstream side; Figs. 4.4c, e and 4.9a, e). An analogous mechanism was proposed by other authors to explain the occurrence of the preferred and asymmetric distribution of the authigenic alterations (carbonate and clay cements, Eichhubl, 2001; hematite bleaching, Eichhubl et al., 2004) on the upstream side of DBs in sandstones.

Other factors that may have locally favored (the initiation of) calcite cement precipitation are the growth of cement on detrital grains (*Loiano*, Fig. 4.10e; *Bollène*, Fig. 4.11c) and the presence of broken detrital carbonate clasts (e.g. shell fragments) that act as a "seed" (cement nucleation sites) (e.g. Bjørkum and Walderhaug, 1990). The latter case was observed in *Loiano*, mainly in bedding-parallel nodules (Fig. 4.9c, d). The mechanisms discussed above explain how and why cement precipitation would occur within the band and in its proximity, as observed on-site. Our field observations support the theoretical and flow simulations as well as the analog experiments, which demonstrated that DBs can negatively affect the fluid flow in porous sandstones (e.g. Antonellini et al., 2014a; Romano et al., 2020) and enhance cement precipitation (e.g. Lander et al., 2009; Williams et al., 2015).

4.7.3. Structural diagenesis scenario for carbonate nodule formation

We integrate petrographic observations and the stable isotope characterization of cements here with the mesoscale spatial organization and microscale textural relationships between nodules and DBs to discuss the geochemical conditions and potential fluid sources that controlled the formation of carbonate nodules in the studied areas. In *Loiano*, the first calcite cement to precipitate was the intraskeletal and pore-lining cement associated with bioclasts in bedding-parallel nodules (Fig. 4.9c-d). The cement fabric and textures, circumgranular dogtooth and void-filling drusy mosaic, suggest a phreatic environment (Longman, 1980; Moore, 1989; Adams and Diamond, 2017). Drusy calcite spars can result from replacement of aragonite in bioclasts in meteoric environments (Flügel, 2013). The second, more pervasive phase of cementation is documented by the intragranular cement observed in all the nodules. The mosaic of blocky sparite with coarse crystals and homogeneous distribution also point to phreatic conditions (Longman, 1980; Flügel, 2013; Adams and Diamond, 2017). The intergranular cement pattern is analogous in DB-parallel nodules and bedding-parallel nodules, meaning they probably formed in a similar phreatic environment.

Oxygen isotope data suggest a meteoric environment (Fig. 4.12a). According to the compilation made by Nelson and Smith (1996), the moderately depleted $\delta^{18}O$ and $\delta^{13}C$ values we found in both types of nodules (Fig. 4.12a) are grouped in the field of "meteoric cements" (Nelson and Smith, 1996) and are in support of precipitation under meteoric conditions. The $\delta^{18}O$ values of DB-parallel nodules cement correspond to parent fluids with oxygen isotope composition ($\delta^{18}O_{fluid}$) varying from -5.42 to -2.31‰ Vienna Standard Mean Ocean Water (VSMOW) (precipitation at 14 °C) or from -4.01 to -0.90‰ VSMOW (precipitation at 20 °C; see *section C.6* in Appendix C for details on the back calculation of $\delta^{18}O$ of parent fluids). These values are slightly less depleted if compared with the expected $\delta^{18}O$ of present-day meteoric fluids characterizing this area (-8 ÷ -6‰; Giustini et al., 2016). The isotopic signal of the cementing fluids may have been buffered by interaction with the host rock (dissolution of detrital marine shells in the sandstone framework; e.g. Fig. 4.10c-d), by mixing with local formation water (McBride et al., 1995), or, for instance, by more regional factors (e.g. atmospheric temperature, humidity, precipitation, seasonality of precipitation and recharge, vegetation; Cortecci et al., 2008; Jasechko, 2019). In this view, further investigations would be needed to properly constrain the cementing fluid conditions (e.g. clumped isotopes, fluid inclusions). The $\delta^{13}C$ composition of cement (Fig. 4.12a), however, seems to reflect soil weathering processes as the primary source of bicarbonate dissolved in the waters (Hudson, 1977; Nelson and Smith, 1996) and supports precipitation from meteoric fluids. DB-parallel and bedding-parallel nodules show a similar composition for $\delta^{18}O$; however, bedding-parallel nodules have more depleted $\delta^{13}C$ values. This might reflect a higher contribution of organic carbon from soil-derived CO_2 (Hudson, 1977), possibly indicating that bedding-parallel nodules formed in shallower conditions with respect to DB-parallel nodules. Another explanation is that the two types of nodules were formed by different episodes of water inflow with different (external) environmental conditions. The difference in isotopic composition between these two types of nodules indeed suggests different cement precipitation timing and water compositions as proposed by McBride et al. (1995) and Milliken et al. (1998). Phreatic meteoric conditions for nodule formation point to a shallow diagenesis, and it is consistent with the shallow burial depths estimated for the Loiano Sandstones (see *Section 4.7.1*).

Cementation patterns can be used to infer the paleo-fluid flow direction at the time of calcite precipitation (Mozley and Goodwin, 1995; Cavazza et al., 2009; Eichhubl et al., 2009; Balsamo et al., 2012). The different spatial arrangements between DBs and nodules in *Loiano* make the paleo-fluid flow direction reconstruction challenging. The asymmetric distribution of cement in some nodules associated with DBs can be explained by lateral fluid circulation (Fig. 4.13a), and cement would accumulate on the upstream side of the DBs (Fig. 4.4c, 4.9, and 4.13a). In other cases, cement is roughly symmetrical with respect to the bands, or it is placed where conjugate bands intersect (Figs. 4.4b, 4.5c, and 4.13a). The most likely interpretation is that both lateral flow under saturated conditions and "direct" meteoric infiltration from the surface, with percolation through the rock, contributed to the formation of nodules in *Loiano* (Fig. 4.13a).

Calcite (i.e. diffusive supply of Ca^{2+} and HCO^{3-}) is possibly derived from the infiltration of $CaCO_3$-saturated meteoric fluids carrying soil-derived CO_2 (Hudson, 1977; Nelson and Smith, 1996), and/or it is locally derived from detrital carbonate grains in the sandstone layers or from intra-formational shale beds and calcite-rich clays layers (McBride et al., 1995; Milliken et al., 1998). In both scenarios calcite precipitates in correspondence to zones of DBs (DBs-parallel nodules) and close to low-conductivity layers (bedding-parallel nodules). McBride et al. (1995) suggest that calcite precipitation along faults (DBs) in *Loiano* was induced by the mixing of locally derived formation water with meteoric water introduced along the faults or, alternatively, by a loss (exsolution) of CO_2 along the fault zones. These mechanisms, however, imply that DBs were fluid conductive. This hypothesis is at odds with our measurements of the DB hydraulic behavior (Del Sole and Antonellini, 2019; Del Sole et al., 2020; Chapters 2 and 3). More likely, carbonate DB cementation resulted from CO_2-saturated groundwater (Fig. 4.13a). We cannot exclude the possibility of a role played by normal faults in the area (Picotti and Pazzaglia, 2008; Picotti et al., 2009; Fig. 4.2a) that might have steered regional subsurface fluid circulation. These faults could have cut through top/bottom seals and driven fluid migration from above/underneath aquifers (Fig. 4.13a). Episodic fault activity can also favor (episodic) horizontal fluid migration along layering at the time of faulting, possibly explaining the occurrence of nodules (Fig. 4.13a) and their different isotopic signature (Fig. 4.12a). From our observations, we can say that the selective cementation process in the Loiano Sandstones depends on "regional" hydrological factors (e.g. topographic gradient, bedding, faults?) locally coupled to the presence of DBs.

In the *Bollène quarry*, the relative timing of DB formation and cementation in the Turonian Sandstones is complex to unravel. Carbonate cementation occurred between distinct deformation phases with multiple DBs forming (see *Section 4.7.1*). The dominant dark cathodoluminescence pattern and homogeneously distributed poikilotopic spar texture could suggest an oxidizing (high pO_2) meteoric phreatic environment (Longman, 1980; Moore, 1989; Flügel, 2013; Hiatt and Pufhal, 2014). Oxygen isotope data also support a meteoric source for the fluids (Fig. 4.12a). The range of moderately depleted $\delta^{18}O$ and $\delta^{13}C$ values of nodules in Bollène is consistent with a meteoric environment in a continental setting (Nelson and Smith, 1996). The $\delta^{18}O$ values of nodule cement correspond to parent fluids with an oxygen isotope composition ($\delta^{18}O_{fluid}$) varying between -7.85 and

-5.98‰ VSMOW (see *section C.6* in Appendix C for details on the back calculation of $\delta^{18}O$ of parent fluids). These values are consistent with the expected $\delta^{18}O$ of present-day meteoric fluids characterizing this area (e.g. Genty et al., 2014; Jasechko, 2019), thus supporting precipitation form meteoric fluids. Maximum burial depth of the Turonian Sandstone was estimated through stratigraphic constrains to be 400 ± 100 meters (Ballas et al., 2013; Soliva et al., 2013). These data support the shallow conditions for nodule diagenesis in Bollène. A phreatic environment is more probable given that in vadose conditions we should have observed meniscus cements and because massive calcrete such as observed in the study area generally forms in a groundwater environment (e.g. Alonso-Zarza, 2003). The $\delta^{18}O$ values of cement from the calcrete layer correspond to parent solutions with $\delta^{18}O$ varying from -6.70 to -6.44‰ VSMOW (see *section C.6* in Appendix C), suggesting a meteoric source of fluids. In the vadose zone, DBs would also enhance unsaturated flow relative to the host rock (Sigda et al., 1999; Wilson et al., 2006; Cavailhes et al., 2009; Balsamo et al., 2012).

Field evidence suggests that clusters of low-permeability DBs in *Bollène* impeded cross-fault flow since no cement was found in superposition with the DBs. The presence of nodules between the DB clusters indicates that the DBs forced the fluid flow and localized the diagenesis in parallel-to-band compartments. This evidence and the fact that nodules are homogenous along their elongation direction discredit the hypothesis of lateral flow. The cement could have been originated from (i) downward fluid flow directly from infiltration of meteoric waters or (ii) upward flow of basinal fluid (pressurized aquifer) along fractures and fault pathways in the carbonate rocks (Fig. 4.13b). In both cases, the water flow was potentially driven by the vertical continuity of DB clusters that have acted as propagation features of faults in overlying (i) or underlying (ii) series and aquifers (Fig. 4.13b). This scenario might explain why the cement is found only in association with the NW-SE DBs. In both cases (i and ii), the constituent necessary for the precipitation of cement in nodules (i.e. Ca and bicarbonate) would come from the surrounding carbonates. Above the Turonian Sandstones there are several carbonate layers in the upper Turonian and Santonian interval (Fig. 4.2c; Ferry, 1997), whereas below there are carbonates belonging to the Jurassic and Cretaceous series (Fig. 4.2b, c; Debrand-Passard et al., 1984). In the first case (i) continental meteoric waters saturated with meteoric carbon dioxide have dissolved the necessary constituents along their path through the rock succession toward the high-porosity Turonian Sandstones. The water percolation through the soil favored fluid acidification. Similar depleted $\delta^{18}O$ values between nodules and cement from the calcrete level (Fig. 4.12b) support the (i) hypothesis, and they may have originated from a similar surficial cement source from downward water flow in association with variations of bicarbonate concentration and/or pH in the water table. In the second (ii) hypothesis nodule cement resulted from CO_2 exsolution during the upward flow of basinal brine or CO_2-saturated groundwater in a pressurized aquifer.

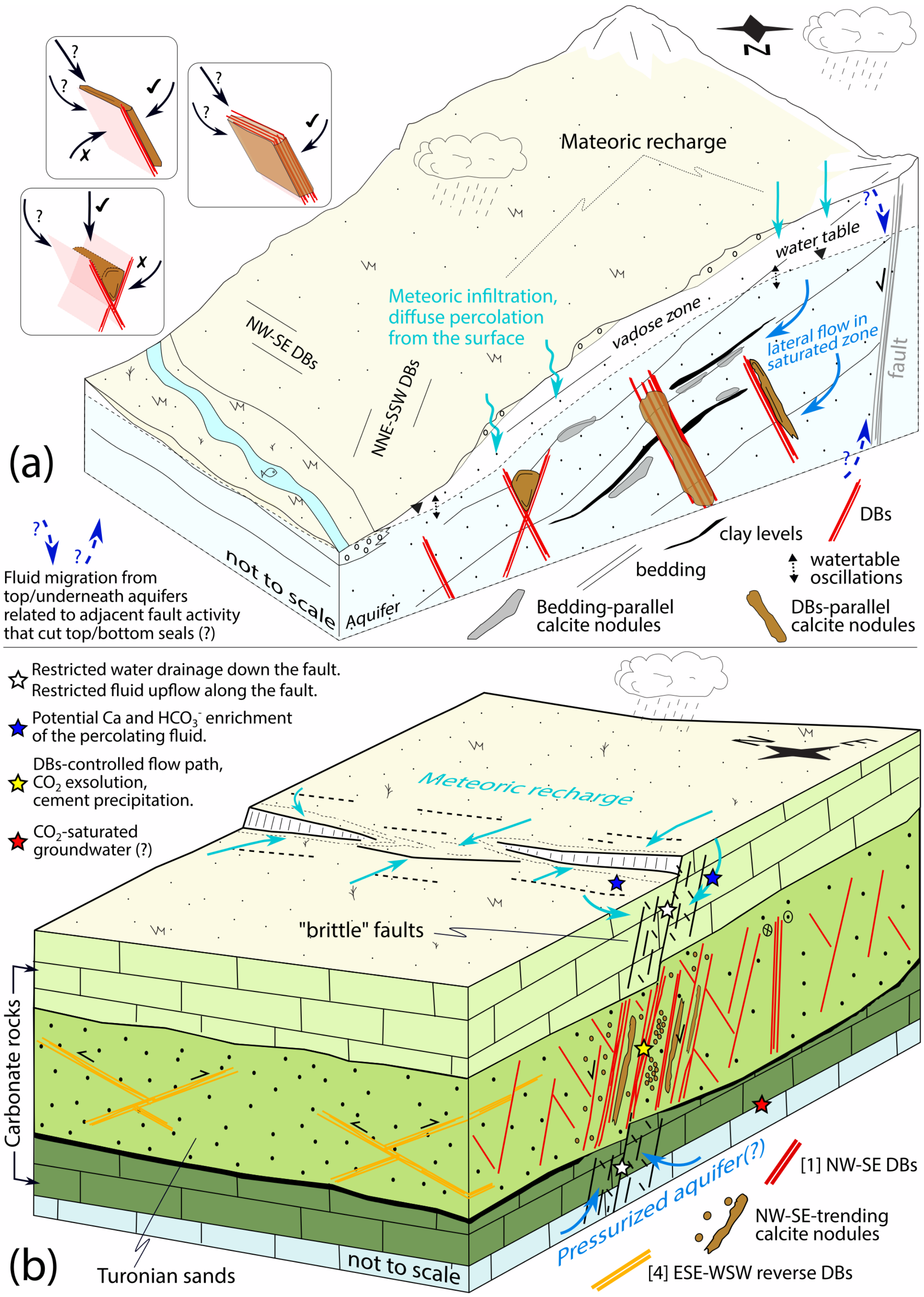

Fig. 4.13 – Generalized conceptual model for calcite nodule precipitation in the two study areas: **(a)** Loiano and **(b)** Bollène. See text (*Section 4.7.3*) for details. The inset sketches in **(a)** show possible paleo-fluid flow direction at the time of calcite precipitation for different DB-nodule configurations.

4.7.4. Implications for subsurface fluid flow, reservoir characterization, and resource development

Models for calcite cementation are of fundamental importance for predicting sandstone and fault-rock properties such as porosity, permeability, compressibility, and seismic attributes. In Loiano, zones of DBs have acted as fluid flow baffles. First, they buffered the fluid flow and localized cement precipitation, acting as areas of preferential cementation in otherwise excellent-porosity sandstones. The resulting diagenetic products enhance porosity and permeability reduction caused by cataclasis, further affecting subsequent fluid circulation. The presence of structural-related cement in the form of concretions (i) strengthens the rock volume, (ii) degrades porosity and permeability, thereby increasing the buffering effect or sealing capacity of zones of DBs, and (iii) imparts mechanical and petrophysical anisotropy to the host rock (Del Sole et al., 2020; *Chapter 3*). We think that it is important to consider the possibility of concretions to form in association with faults within siliciclastic reservoirs, especially where these structures (DBs) are below seismic resolution (e.g. Del Sole et al., 2020). It is also critical to understand SDH spatial organization, extension, continuity, density, hydraulic role in terms of fluid flow circulation, and their mechanical influence on the host rock. This information should be included in a robust reservoir characterization, and, in general, it is beneficial during geofluid exploration and energy appraisal, resource development strategies (groundwater, geothermal, hydrocarbon), well production, reservoir simulation modeling, geomechanical evaluation of a drilling site, and other environmental and industrial operations (e.g. waste fluid disposal; groundwater contaminants; geologic CO_2 sequestration; enhanced oil recovery - EOR). The incorporation of this information into aquifer or reservoir (flow) models requires implicit representation of the SDH network and the upscaling of its structural and petrophysical properties (e.g. Fachri et al., 2013; Antonellini et al., 2014a). When the cementation is heterogeneous, such as in the examples presented in our work, it could be difficult to model and predict, especially when data are spatially discontinuous (e.g. wells). In these cases, outcrop-based studies allow continuous and more reliable reconstructions of cement distribution. The characterization of the SDH network distribution (e.g. Del Sole et al., 2020; *Chapter 3*) allows us to predict where (i.e. location and volumes) and how (i.e. spatial organization) the reservoir compartments are arranged and how the fluid circulation can be affected. The kind of study that we present here might be helpful to extract those statistical parameters necessary to implement reservoir studies that account for heterogeneity in petrophysical properties and their association with seismic and sub-seismic structural heterogeneities.

4.8. CONCLUSIONS

In this contribution, we present two examples of structural control exerted by DBs on fluid flow and diagenesis recorded by calcite nodules strictly associated with DBs. The objective of this research was to constrain the role of DBs in affecting the flow pattern and in localizing cement precipitation in porous sandstones, as well as to elucidate the mechanisms involved in these processes. The major results of our study can be summarized as follows.

(1) At both study sites, one or more sets of DBs precede and control selective calcite cement precipitation in the form of nodules. The later localization of cementation along these structural features results in a complex and spatially heterogenous cementation pattern (SDHs).

(2) Selective cementation of nodules associated with DBs indicates interaction between deformation structures, fluid flow, and chemical processes. The volumetrically significant presence of cement (10-25% of the exposed outcrop volume) indicates that fluid flow and mass transport have been strongly affected by the presence of low-permeability DBs.

(3) Two main processes are discussed to explain selective carbonate cementation associated with DBs in *Loiano*. (i) The high concentration of nucleation sites on fine-grained comminution products with increased reactive surface area of the pore-grain interface and small pore throats in the DB trigger cement precipitation and fast pore clogging with respect to the host rock. (ii) Solute-sieving across the DB (membrane effect) promotes Ca and bicarbonate concentration increase on the upstream side.

(4) In *Bollène* no clear superposition among bands and cement was observed. Here, the clusters of bands acted as hydraulic barriers to cross-flow, thus compartmentalizing fluid circulation and localizing diagenesis in volumes arranged parallel to the bands.

(5) In both areas, cement textures, cathodoluminescence patterns, and their isotopic signature suggest that the cement in the nodules precipitated in a phreatic environment from fluids of meteoric origin.

(6) In a framework of late-stage diagenesis (post-DB formation) and saturated conditions (phreatic environment), the processes commonly employed to explain focused fluid flow and preferential cement precipitation associated with DBs, such as “transient dilation” and “capillary suction” (see *Section 4.1*), appear not to be pertinent. In Bollène and Loiano the DBs buffered and compartmentalized fluid flow and localized diagenesis.

(7) Further analyses, such as flow simulations and cement precipitation modeling, are deemed necessary to further explore microscale fluid flow and diagenetic mechanisms that drove preferential calcite cement precipitation along DBs in the studied porous sandstones.

(8) DBs control flow pattern and affect how diagenetic heterogeneities are distributed within a porous sandstone. The association of diagenetic cementation with DBs further increases the flow-buffering potential of these structural features. It also creates SDHs that impart a mechanical and petrophysical anisotropy to the host rock volume and can seriously affect the subsurface fluid circulation in porous sandstones. These features should be considered during reservoir characterization, especially where SDHs are below seismic resolution.

Supplement – Supplementary material to this Chapter can be found in the Appendix C.

References – The references related to this Chapter can be found in the Bibliography.

Acknowledgments – Constructive criticisms and comments by James P. Evans and Geoffrey C. Rawling greatly improved our manuscript. The authors wish to thank Randolph T. Williams for his editorial work. The authors also wish to thank Paola Iacumin, Enricomaria Selmo, and Antonietta Di Matteo for stable isotope analysis in the SCVSA Department (University of Parma). The Laboratoire Géosciences Montpellier (France) is acknowledged for hosting Leonardo Del Sole as a visiting scholar in the period between April and July 2019, during which part of the work presented in this paper was carried out.

5

Structural diagenesis in carbonate rocks

The content of this Chapter has been published in Antonellini, M., **Del Sole, L.**, Mollema, P. N., 2020. Chert nodules in pelagic limestones as paleo-stress indicators: A 3D geomechanical analysis. Journal of Structural Geology, 132, 103979.

Link to the previous Chapters – *The formation of chert nodules within a carbonate sequence is a diagenetic phenomenon, so that the preferential fracturing that we observe in chert embedded in carbonate is another aspect of structural diagenesis (Laubach et al., 2010). This (**Chapter 5**) is another example of how diagenetic processes (**Appendix C**) or host rock properties (**Chapter 2**) can control deformation characteristics and distribution in a sedimentary sequence as opposed to the case in which deformation focuses the diagenetic processes and control the distribution of diagenetic products (**Chapters 2, 3, and 4**).*

ABSTRACT

The objective of this study is to explain the occurrence and paleo-stress significance of 3D joint clustering in chert nodules (inclusions) within a layered pelagic limestone sequence. The difference in stiffness between chert and limestone is about one order of magnitude. Field observations show that fracture localization occurs mostly in chert nodules as opposed to the limestone matrix. We show with a novel three-dimensional geomechanical modelling analysis how the inclusion (ellipsoid) axes ratio influences fracture intensity and propagation within and outside the chert nodules and how the nodules record different deformation phases under different remote stress conditions. From field observations, we recognize two joint sets in the chert nodules: joints parallel and normal to the plane containing the two major axes of the nodule (bedding plane). In the nodules, the normal-to-bedding joints are interpreted to be younger than the parallel-to-bedding ones. The modelling of the 3D Eshelby solution for the stress field inside the chert nodule and in the surrounding matrix is consistent with our field observations and it suggests a strong differential stress during deformation (σ_{min}^r / σ_{max}^r < 0.3). Chert nodules in a deformed carbonate sequence, therefore, can provide important clues on the paleo-stress conditions, the temporal sequence of events, and fracture distribution heterogeneity.

Graphical abstract

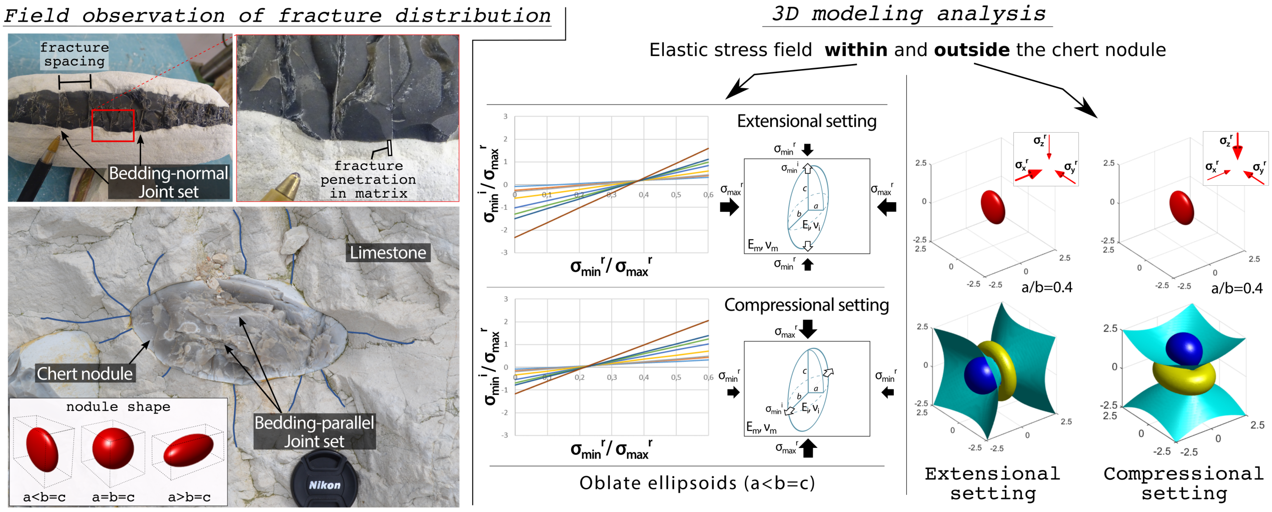

5.1. INTRODUCTION

Carbonate rocks form important geofluid reservoirs (hydrocarbons, water, CO_2, etc.), including where fluid flow is generally influenced by opening-mode fractures. Knowledge of the paleo-stress conditions at the time of deformation is critical to assess if brittle structures (i.e. joints) are present in a carbonate sequence and to determine whether these structures played a role during diagenesis (Ferraro et al., 2019). In carbonate rocks, besides dissolution and replacement, the porosity is achieved mainly by fracturing and faulting, i.e. secondary porosity. As the fracture networks control reservoir permeability, fracture development and distribution must be characterized for a better understanding of fluid-flow. Faults and fractures could represent fluid conduits or pose barriers to fluid circulation, depending on the permeability of the host rock relative to that of the fault zone or fracture corridors (Antonellini and Aydin, 1994; Antonellini and Mollema, 2000; Aydin, 2000; Cooke et al., 2006; Wennberg et al., 2006; Agosta et al., 2010). The geometry of the fracture assemblages and the geometric and genetic relationships between opening mode fractures and faults that develop in carbonate rocks depend on the tectonic setting, the detailed lithology, and pre-existing structures (Mollema and Antonellini, 1999; Antonellini and Mollema, 2000; Graham et al., 2003; Antonellini et al., 2008; Agosta et al., 2010; Aydin et al., 2010; Diaz-General et al., 2015). The association of chert nodules (stiff inclusions) and pelagic carbonate rocks (soft matrix) has been described in the literature (Alvarez et al., 1976) with special reference to the strengthening effect that the nodules have on the carbonate sedimentary sequence (Petracchini et al., 2015a, 2015b).

Stiff inclusions embedded in a soft matrix experience elevated stresses when the rock package is stressed (Eshelby, 1957; Jaeger and Cook, 1979; Mal and Singh 1991; Eidelman and Reches, 1992; Healy, 2009; Davis et al., 2017). Jaeger and Cook (1979) present the elastic solution for the homogeneous stress field inside a circular 2D inclusion embedded in a softer/stiffer matrix, claiming that this is one of the most important solutions in rock mechanics. Falzone et al. (2016) show the importance of soft and stiff inclusions in controlling the mechanical properties of cementitious composites (concrete) and Guido et al. (2015) solve the Eshelby inclusion problem to model ground displacements above a reservoir undergoing fluid withdrawal/injection. Eshelby (1957) showed that the stress field inside the ellipsoidal inclusion is uniform. Furthermore, he resolved the full three-dimensional problem for the stress and strain fields inside and outside an ellipsoidal inclusion embedded in a matrix with different mechanical properties from those of the inclusion itself. Eshelby's inclusion theory has been validated in a variety of geological problems, ranging from structural geology (e.g. Sternlof et al., 2005; Soltanzadeh and Hawkes, 2008; Katsman, 2010; Guido et al., 2015) to composite materials (layering or inclusions with strong contrast in stiffness) and rock physics (e.g. Liu and Yund, 1995; Roatta and Bolmaro, 1997a, 1997b; Mercier et al., 2005, 2012). Eidelman and Reches (1992) applied the Jaeger and Cook (1979) solution for circular inclusions to explain fracture localization in pebbles. Others employed an Eshelby two-dimensional solution for the stresses within an elliptical two-dimensional inclusion to explain fracture concentrations within micro-granitoid enclaves in granite or within elliptical clasts embedded in chlorite schist (Mondal and Acharyya, 2018; Acharyya and Mondal, 2019). In the studies mentioned above, paleo-stress information was deduced from an estimate of the minimum rock breakage loads and the minimum crustal depth during deformation as a function of the inclusion aspect ratio, the ratio between the remote stresses, and the fracture toughness (Lawn, 1993). The analyses presented so far, however, relied mostly on a 2D solution for circular or elliptical stiff inclusions embedded in a soft matrix without considering the third spatial dimension.

The novelty of our work is that by using the 3D Eshelby solution (Eshelby, 1957; Healy, 2009) for the strains and stresses within an inclusion and its carbonate matrix, we obtain clues to unravel the paleo-stress conditions and the sequence of deformation as well as fracture connectivity in layered rocks. In particular, the objectives of this work are two-fold. First, we use the Eshelby method to determine how the three-dimensional inclusion shape and the ratio of the remote stresses may influence fracture intensity and propagation within and outside the nodules. Second, we show how chert nodules may record different deformation phases under different remote stress conditions.

Our work can be also applied to a variety of situations and to other carbonate sequences in Italy and around the world (Maliva and Siever, 1989; Maliva et al., 2005; Antonellini et al., 2008; Petracchini et al., 2015a). More generally, however, it can be extended to problems where stiff inclusions are embedded into a rock matrix, such as with clasts in conglomerate (Eidelman and Reches, 1992; Acharyya and Mondal, 2019) and microgranitoid enclaves (Mondal and Acharyya, 2018). The method can also be used to investigate effects of pore spaces in tight gas sands (Ruiz and

Cheng, 2010), concretions in a sandstone matrix (Quesada et al., 2009; Del Sole and Antonellini 2019), brittle fracturing in shale gas reservoirs (Sone and Zoback, 2013), as well as structures at a crustal scale (Andrew and Gudmundson, 2008; Ding et al., 2011).

5.2. GEOLOGIC SETTING OF THE STUDY AREA

Our study area is the *Monte Conero* in central eastern Italy. This is an ENE-vergent, highly asymmetrical anticline, with layers in the eastern limb dipping between 70° and 90° and layers in the western limb dipping 22° (Fig. 5.1). The *Monte Conero* is located in the central part of the Pliocene Adriatic foredeep and represents the outermost portion of the exposed *Umbria-Marche* foreland thrust-and-fold belt (Northern Apennines, Italy), which formed in the latest phase of the Alpine-Himalayan orogenesis (Diaz-General et al., 2015; Montanari et al., 2016).

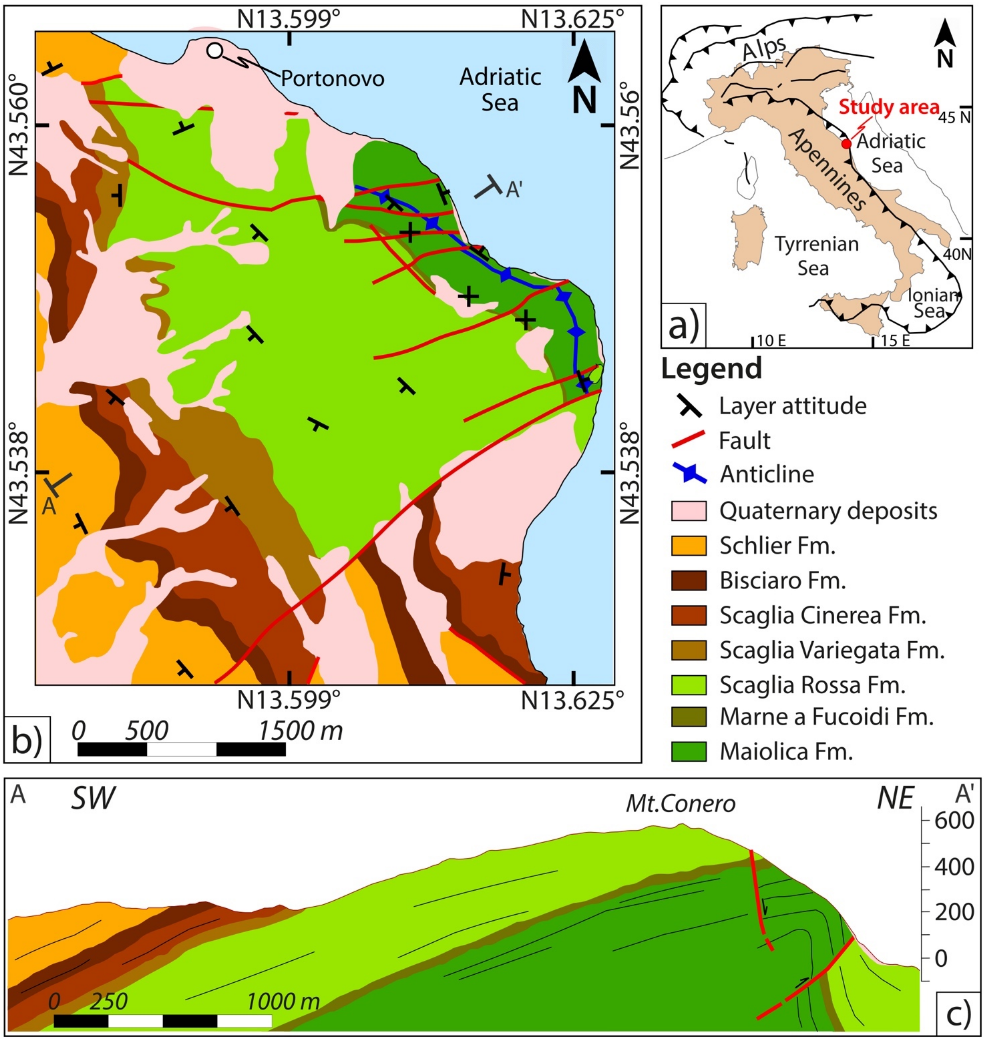

Fig. 5.1 - Index map for the study area. **(a)** Location of the study area in the Italian peninsula. **(b)** Schematic geologic map and **(c)** cross section of the Monte Conero area (modified from Diaz-General et al., 2015).

The stratigraphic sequence (from oldest to youngest) exposed at the *Monte Conero* starts in the middle section of the *Maiolica Formation* (*Fm*) and it extends all the way up to the *Schlier Fm* (Upper Tortonian) (Montanari and Sandroni, 1995). The *Maiolica Fm* (Tithonian-Lower Aptian stages) is the oldest formation that crops out and it is composed of well-defined layers containing white micrite and chert nodules. The thickness of the *Maiolica Fm* at the *Monte Conero* varies between 20 and 400 meters (Bortolotti et al., 1994), and the average single layer thickness is between 0.4 and 0.6 meters. The overlying *Scaglia Rossa Fm* (Lower Turonian to mid-Eocene stages) is part of the *Scaglia* unit and typically consists of pink and red limestone layers. The complete *Scaglia* unit rock sequence spans from the Aptian age into the Eocene epoch. It is composed of well-defined limestone and marly-limestone layers. The *Scaglia Rossa Fm* is composed of micrite with alternation of marl and chert layers. The formation thickness ranges from 200 to 400 meters (Bortolotti et al., 1994), and the single layer average thickness varies between 0.1 and 0.15 meters.

The deformation processes leading to the present-day structural setting of the *Monte Conero* began during Miocene time: an extensional tectonic event, probably connected with the flexure of the Adriatic foreland lithosphere, affected the Apennines during late Burdigalian and early Messinian time (Deiana et al., 2002; Mazzoli et al., 2002 and references therein) and resulted in formation of NW-SE striking normal faults. Some of these normal faults were later reactivated as reverse or back-thrust faults (Deiana et al., 2002). The main orogenic phase started between the end of mid-Messinian (after *Gessoso-Solfifera Fm* deposition) and the lower Pliocene. The *Monte Conero* anticline developed in this period, with deformation progressing from West to East (Montanari and Sandroni, 1995; Alberti et al., 1998; Argnani, 1998; Barchi et al., 1998). The anticline is intersected by two conjugate strike-slip fault systems oriented at high angle to the fold axis (Cello and Coppola, 1984; Coltorti et al., 1987; Coccioni et al., 1997; Sarti et al., 2011; Diaz-General et al., 2015): a right-lateral NE-SW fault system and a left-lateral transpressive E-W-system. The strike-slip faults formed during the Pliocene horizontal shortening event, the same that led to the formation of the *Monte Conero* anticline and they may be interpreted as tear faults (Diaz-General et al., 2015). These faults cut through a transgressive surface, which crops out at the summit of the mountain, that in turn cuts Pliocene marine deposits. This indicates that deformation of the *Monte Conero* continued during the early Pleistocene but slows in the western sector of the Apennines, where an extensional phase develops. Pleistocene contraction has continued until now in the coastal area where it is associated with uplift (average 3 mm/year; Coltorti et al., 1987; Mayer et al., 2003; Sarti et al., 2011) and seismicity (Crescenti et al., 1977). Relatively fast uplift, coastal erosion, and fracturing are the main triggers for the landslides at *Monte Conero* (Montanari et al., 2016). The main deformation structures in the *Maiolica* and *Scaglia Rossa* matrix are veins and bedding-parallel stylolites (pressure solution seams). There are multiple sets of veins in the Maiolica and Scaglia Fm; the veins are normal to bedding and have a general trend oriented NE-SW (Fig. 2 in Diaz-General et al. 2015 and also our Fig. 5.5c, f) The age relationships and the distribution of these features is reported in Diaz-General et al. (2015). Here, we focus on the deformation concentrated in the chert inclusions, which is characterized by opening mode I fractures (i.e. joints) (Pollard and Segall, 1987; Pollard and Aydin, 1988; Schultz and Fossen, 2008).

5.3. FIELD OBSERVATIONS

5.3.1. Field methods

Careful measurements were made in the field of the geometry and characteristics of the chert nodules and the host rock in the two rock types (*Maiolica and Scaglia Fm*). The dimension of the nodules (semi-axes *a*, *b*, and *c* when possible) (see Fig. 5.2 for axes terminology convention) as well as fracture patterns and intensity within and outside the chert inclusions were documented in the field or on high-resolution photographs (15 megapixels) with the methods of scanlines (Priest and Hudson, 1976, 1981). Chert rock samples including the surrounding limestone were sliced and used for the 3D analysis by means of high-resolution photo mapping. Field evidence points out that the fractures in the nodules are joints (mode I), because no splay joints or offsets (indicative of shear) were observed. Detailed observations on the chert nodules allowed us to distinguish the temporal relationships among the different joint sets using the methodology explained in Antonellini and Mollema (2019).

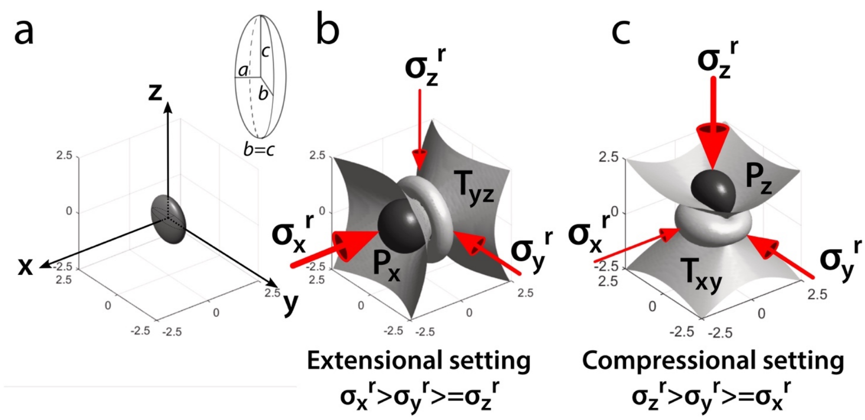

Fig. 5.2 - Reference system for the ellipsoids. **(a)** Cartesian reference system centered on the ellipsoid and definition of the three ellipsoid semi-axes *a, b*, and *c.* In order to conform to the reference system, the *yz-plane* is parallel to bedding and the *x* is perpendicular to it (see also sketches in Fig. 5.10 that explain the orientation of the stress state). **(b)** Definition of the remote stresses and the T_{yz} *and* P_x reference mean stress regions (dark spheroids) outside the ellipsoid in an extensional tectonic setting ($\sigma_x^r > \sigma_y^r >= \sigma_z^r$). **(c)** Definition of the remote stresses and the T_{xy} and P_z reference mean stress regions (dark spheroids) outside the ellipsoid in a compressional tectonic setting ($\sigma_z^r > \sigma_y^r >= \sigma_x^r$).

5.3.2. Field and (micro)structural observations

Chert nodules are ubiquitous in almost all pelagic carbonate formations cropping out at the *Monte Conero* anticline (Fig. 5.3; *Maiolica*, *Marne a Fucoidi*, *Scaglia Rossa*). Chert is present mainly as nodules, lenses and, less commonly, as continuous layers. The longest axes of chert nodules axes to be aligned parallel to bedding planes. Fracture intensity is always higher in the nodules than in the host rock regardless of the type of limestone that hosts the nodules and the shape of the nodules (Figs. 5.4 and 5.5). The boundary between the chert nodule and the matrix is marked by a chert rind with a smooth transition from chert to limestone (Fig. 5.4). For this reason, we consider the boundary nodule-host rock a welded boundary.

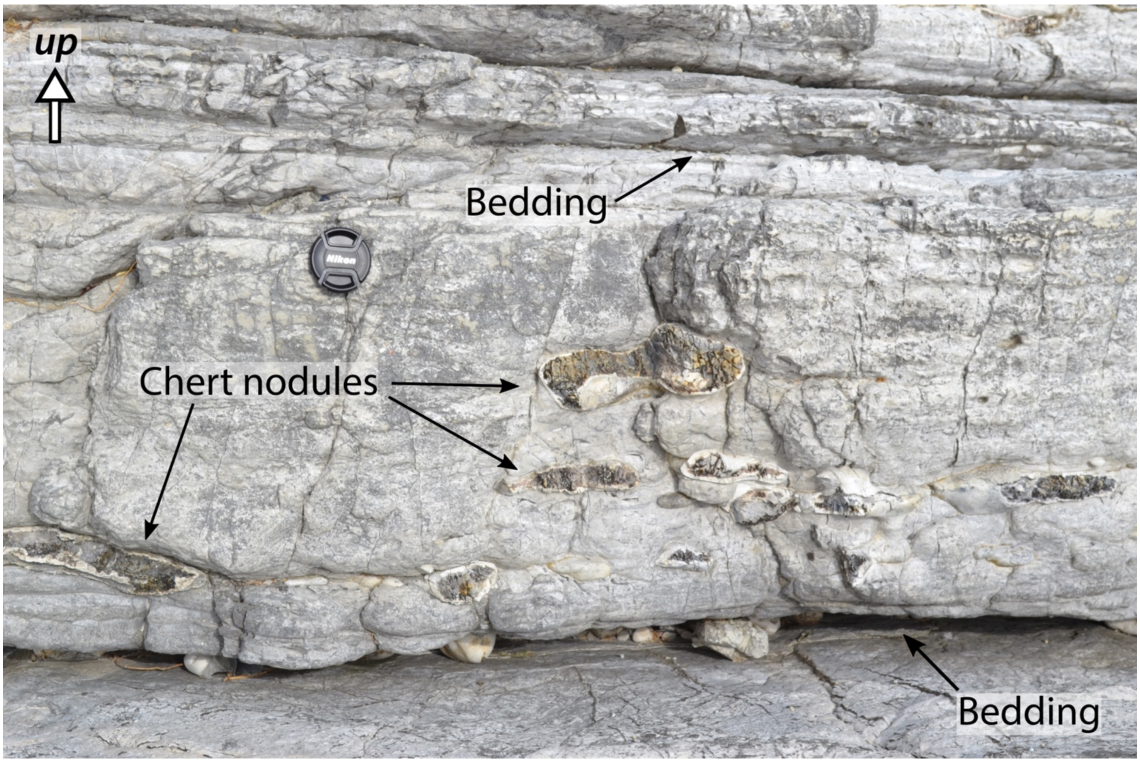

Fig. 5.3 – Chert nodules with different shapes in the Maiolica Fm at Monte Conero (Italy). The lens cap is 5.5 cm in diameter. "Up" refers both to the topography and the stratigraphy.

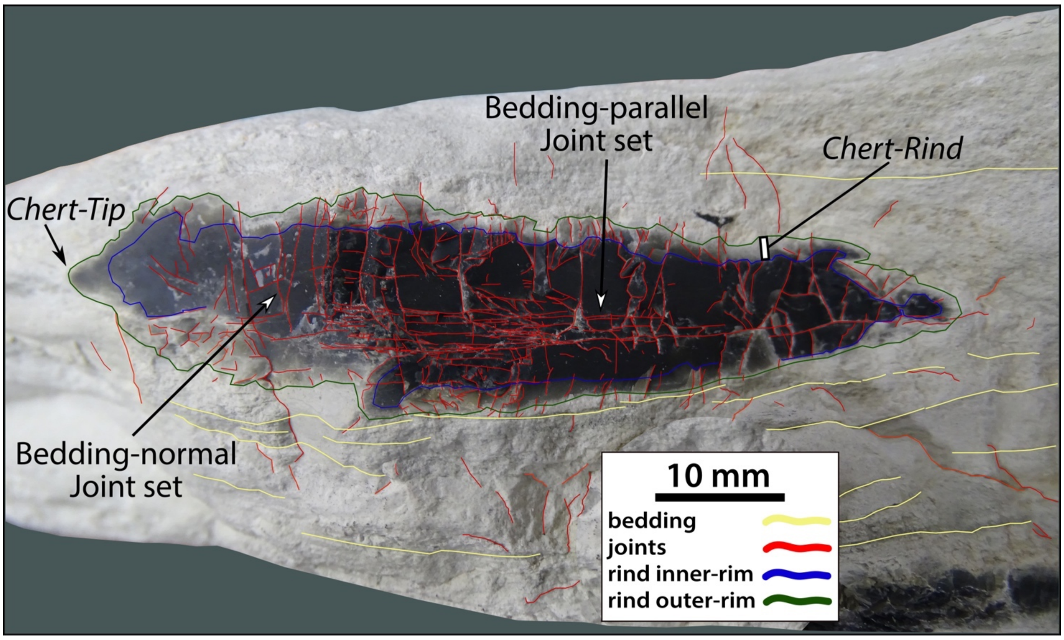

Fig. 5.4 – Chert nodule in the Maiolica Fm at Portonovo shore (Monte Conero, Italy). Note that the bedding and the joints are mostly confined within the nodule. Two predominant sets of joints are present: one set is parallel-to-bedding and one set is normal-to-bedding. A few joints propagate for a short distance from the nodule into the limestone matrix. Tip and rind of chert nodule are also reported.

The dark-grey/black chert (Figs. 5.3, 5.4 and 5.5) is typical of the upper and younger part of the sequence (Aptian-Albian boundary) whereas the older cherts have a lighter color (yellow, green). Chert layers are distinctive of the lower *Scaglia Rossa* section (Cenomanian-Turonian boundary) where they typically have a reddish-brown color (Fig. 5.5a, b). The following description of the nodules is from the oldest to the youngest. The gray-black nodules in the *Maiolica Fm* (Fig. 5.5d, e) have mostly an oblate shape ($a<b=c$) with the b- and c-axes laying on the bedding plane and the a-axes normal to bedding; their a-axes range in length from 3 cm to 14 cm (see Fig. 5.6a), as also observed by Diaz-General (2013).

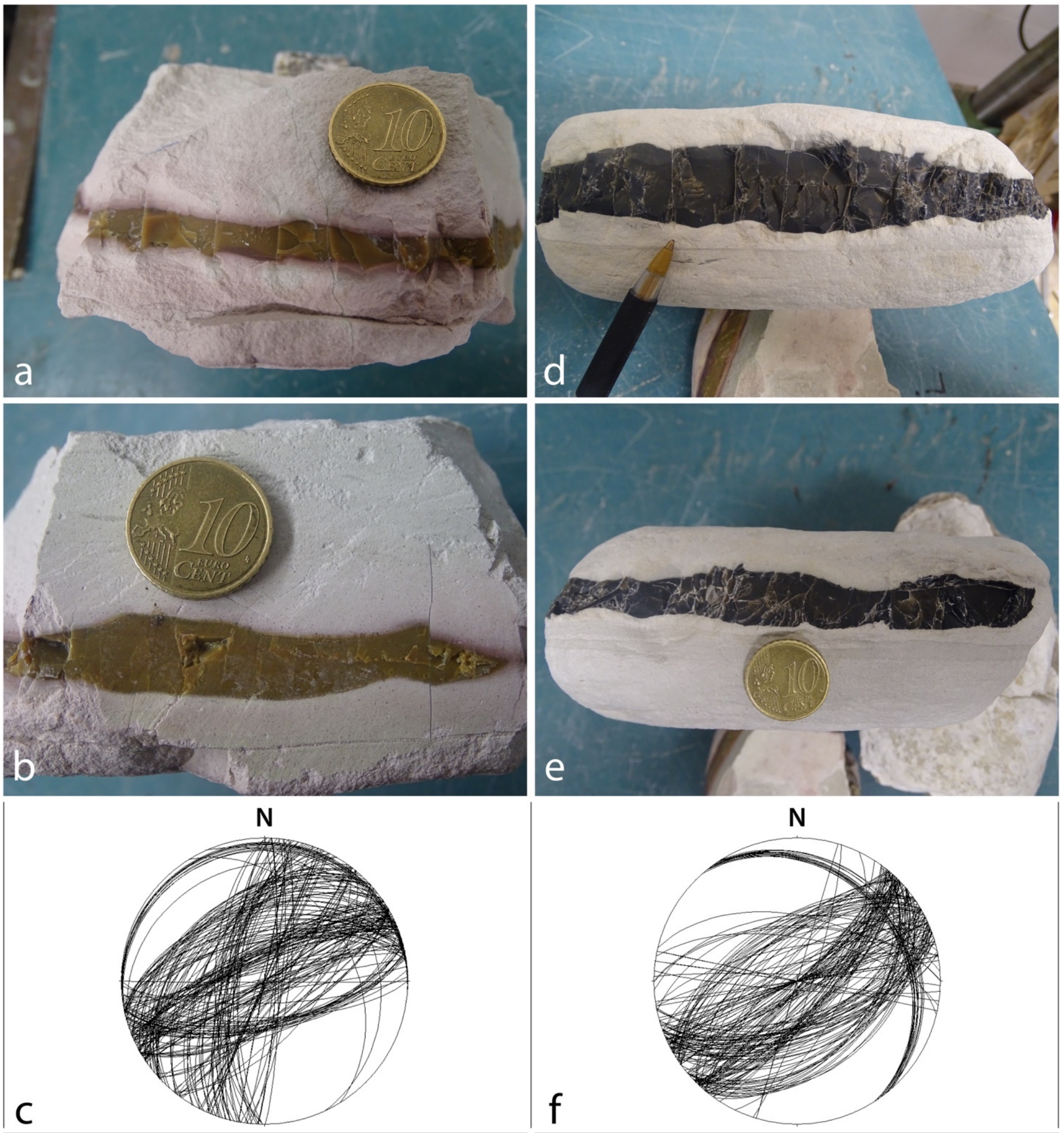

Fig. 5.5 – *Mode-I* fractures (joints) within chert inclusions **(a)** Chert inclusion in the Scaglia Rossa Fm. The spacing of the joints is around 10 mm. **(b)** View of the same sample on a section at 90° from **(a)**. Note that the normal-to bedding-joints are not visible. **(c)** Equal angle stereonet projection of the veins mapped in the whole Monte Conero area within the Scaglia Fm 76 data points (original field data from Diaz-General et al. 2015). **(d)** Chert inclusion in the Maiolica Fm. The spacing of the joints is about 10-15 mm. **(e)** View of the same sample on a section at 90° from **(c)**. Note that the sample breaks up along the planes of the joints visible in **(c)**. **(f)** Equal angle stereonet projection of the veins mapped in the whole Monte Conero area within the Maiolica Fm 351 data points (original field data from Diaz-General et al. 2015).

The chert nodules in the *Scaglia Rossa Fm* have both oblate and prolate shapes; oblate shapes are predominant. In prolate ellipsoids, the average lengths of the *b* and *c* axes are around 8-10 cm whereas *a* axes are 25-30 cm long. Oblate chert nodules in the *Scaglia Rossa Fm* usually have *a-semi axes* 3-10 cm long and *b*, *c* semi axes 15-40 cm long (Diaz-General, 2013; this work; Fig. 5.6a, b). Figure 5.4 shows the joints within a chert nodule in the *Maiolica* limestone. The most important observations are the following: **(1)** Joints are pervasive in the chert whereas the limestone matrix is almost intact. **(2)** Two predominant different sets of joints occur in the chert nodule. One set of joints developed parallel to the plane containing the *b* and *c* axes and the bedding plane. A second set of joints is normal to the first one and to bedding with orientations similar to that of the veins in the limestone; their plane contains the *a*- axis of the ellipsoid (Fig. 5.4). Some joints (both sets) do not reach the chert rind and almost all joints are confined within the chert inclusion especially where the *a*/*b* ratio of the ellipsoid is small (Figs. 5.5 and 5.7a). In chert nodules with large *a*/*b* ratios, joints tend to extend into the limestone matrix (Fig. 5.7a), from 1 mm for an *a*/*b* = 0.1 to 40-50 mm for an *a*/*b* = 0.6. The fracture penetration for the same *a*/*b* is less for the bedding-parallel joints than for the normal-to-bedding-ones (Fig. 5.7a). For parallel-to-bedding joints, penetration into the matrix ranges from 1 mm for an *a*/*b* = 0.1 to 5-6 mm for an *a*/*b* = 0.5-0.6. The joints become veins where they extend into the limestone matrix. **(3)** The fractures that cut across the chert/carbonate boundary extend only a few millimeters to a few centimeters into the host rock and their traces seem to anastomose. Nodules with large *a*/*b* ratios show joints that extend into the matrix whereas ellipsoids with small *a*/*b* ratios do not (Figs. 5.5, 5.7a, 5.8, and 5.9). **(4)** Joint spacing within the chert nodules depends on the *a*/*b* ratio of the chert ellipsoids. It varies from 2-3 mm for *a*/*b* = 0.1 to 10 mm for *a*/*b* = 10 mm (Figs. 5.5 and 5.7b).

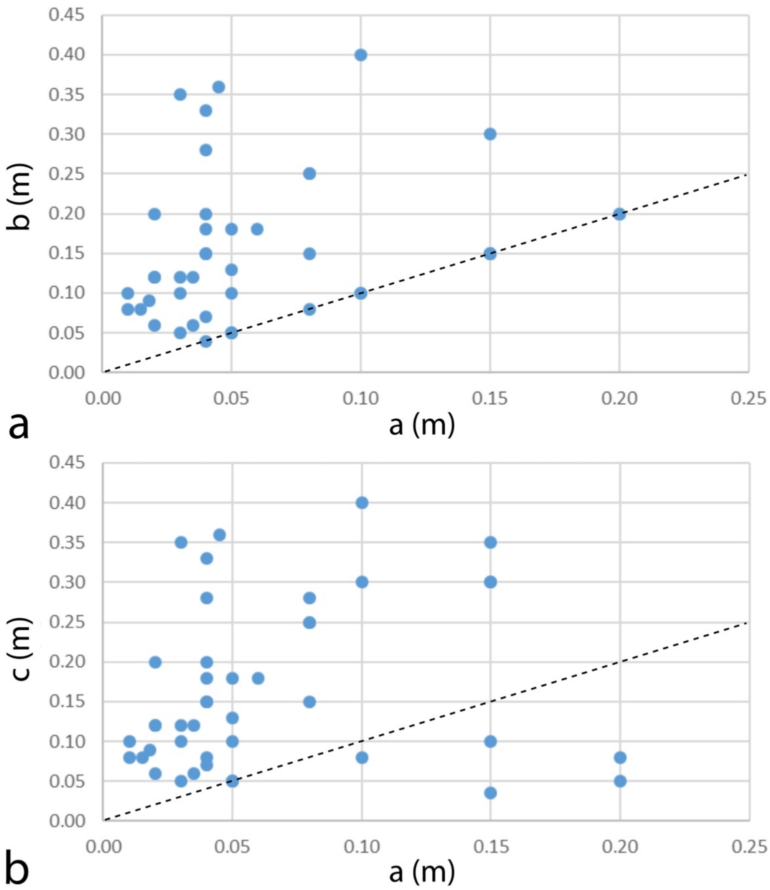

Fig. 5.6 – Chert ellipsoid dimensions measured in the field within the Maiolica and Scaglia Rossa Fm. The terms *a, b,* and *c* refer to the lengths of the semi-axes. **(a)** *a* vs. *b*. **(b)** *a* vs. *c*. The data points above the straight line represent oblate ellipsoids those below represent prolate ellipsoids.

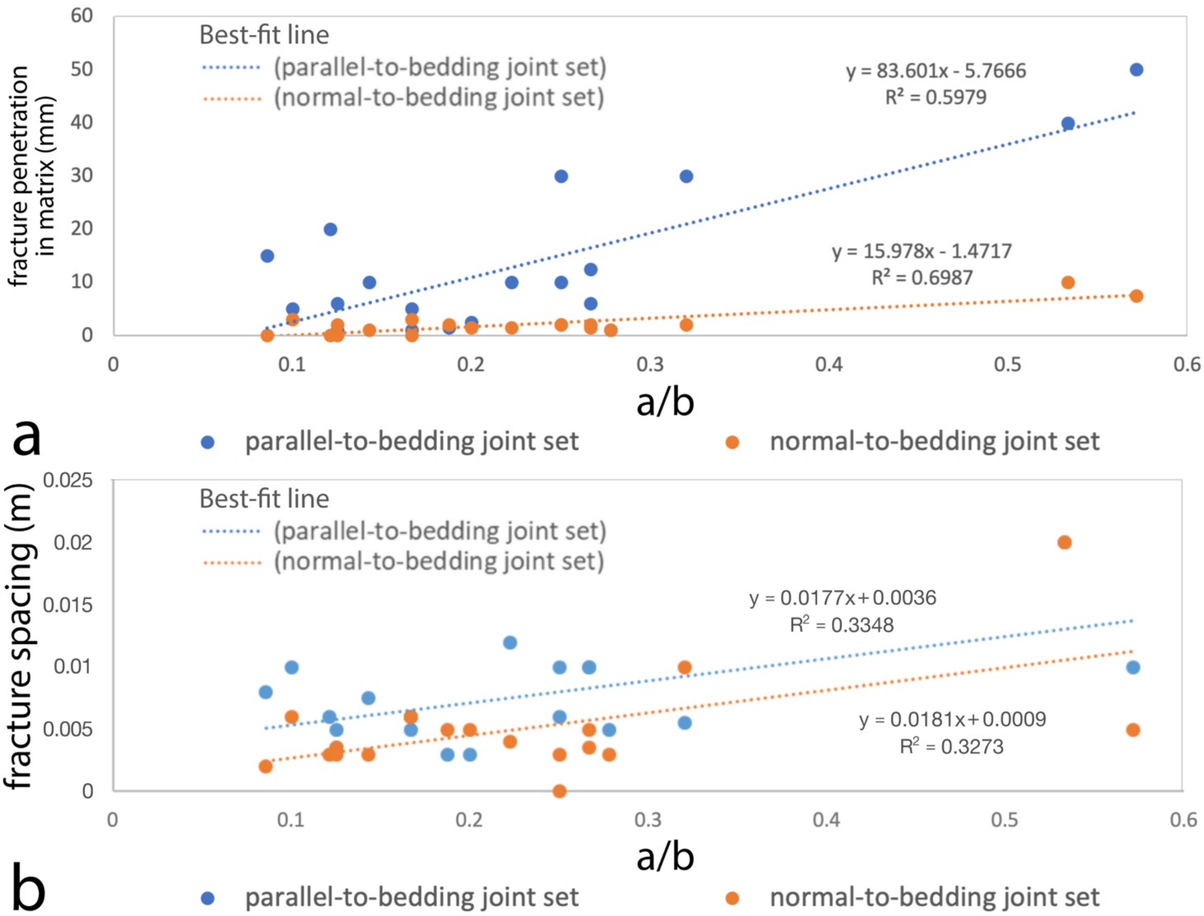

Fig. 5.7 – (a) Joint propagation distance from the chert inclusion boundary into the matrix for oblate ellipsoids. **(b)** Joint spacing within the chert inclusion as a function of the *a*/*b* ratio. The penetration distance **(a)** and the spacing **(b)** are represented for both the parallel-to-bedding and the normal-to bedding joint set. The best-fit trend is represented in **(a)** and **(b)** by the dotted lines. The equations of regression are also shown on the figures.

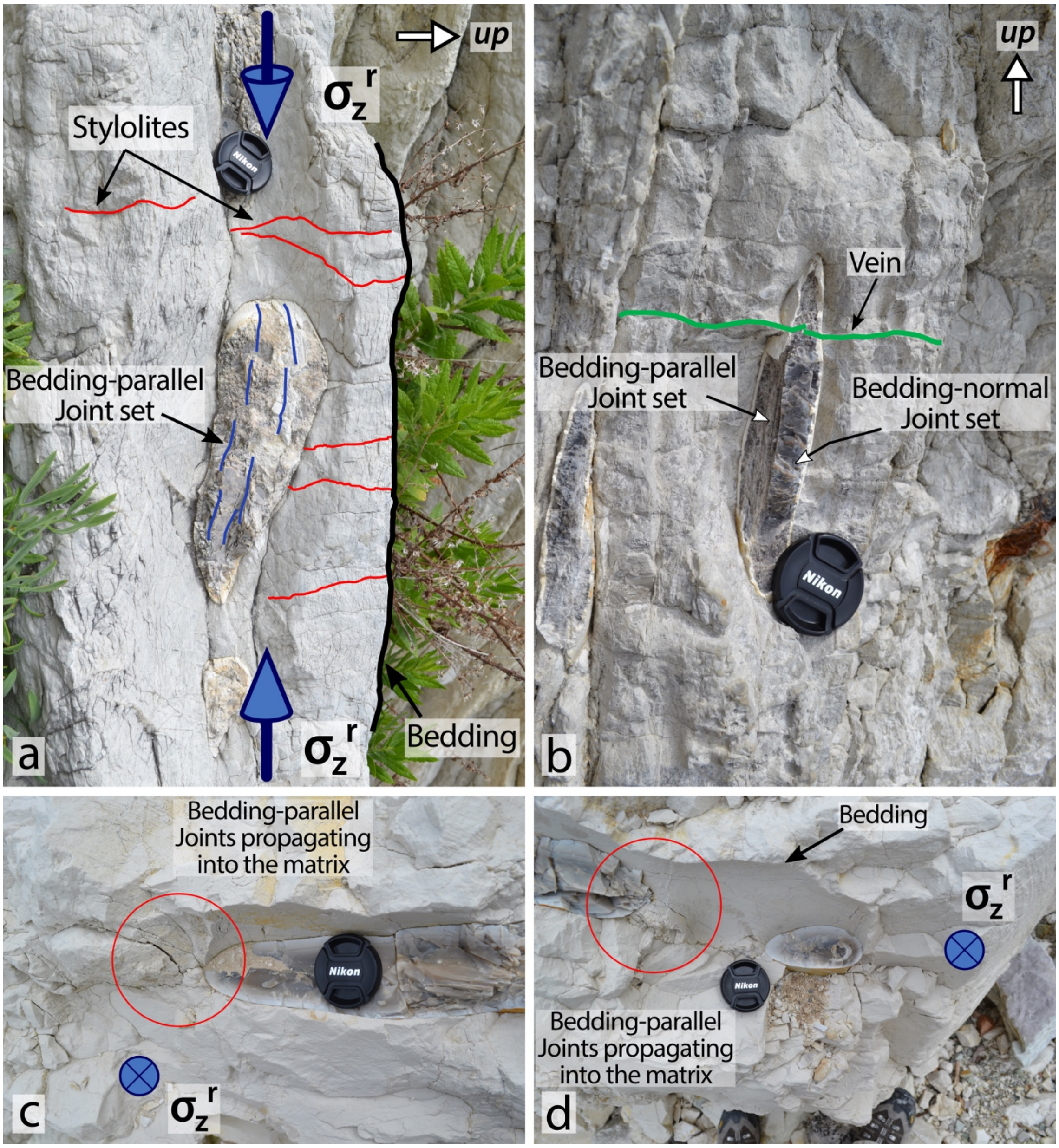

Fig. 5.8 – Chert inclusions in the Maiolica Fm (Monte Conero). **(a)** Chert inclusion where parallel-to-bedding joints do not propagate into the P_z volume aligned with the σ_z^r direction. **(b)** Chert inclusion affects the propagation of a vein (green line). Note also that the parallel-to-bedding joints do not penetrate into the P_z volume. Up direction is topographic. **(c)** Chert inclusion where parallel-to-bedding joints propagate into the T_{xy} toroidal volume lying on the *xy-plane*. The remote stress σ_z^r is normal to the photograph. **(d)** *Similar situation to that described in* **(c)**.

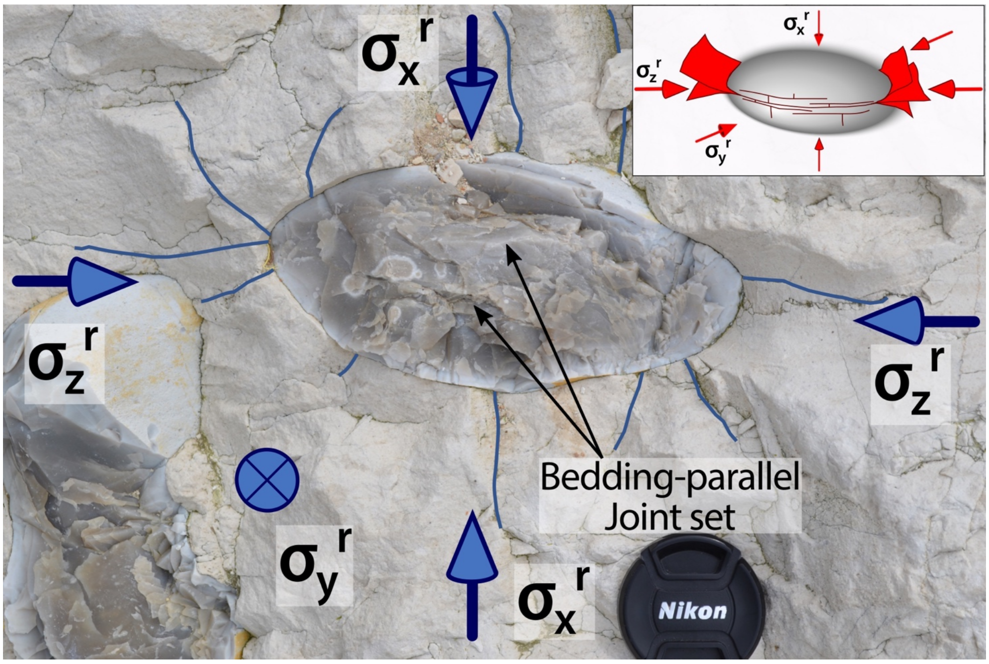

Fig. 5.9 – Chert inclusions in the Maiolica Fm (Monte Conero). The blue lines are fractures propagating from the nodule into the T_{xy} toroidal volume (see Fig. 5.2). The direction of the regional principal stresses at the time of fracturing is indicated by the arrows. The inset in the upper right corner represents bedding-parallel joints propagating into the matrix under the stresses thought to have acted on the nodule.

5.4. MODELLING

The purpose of the modelling presented in this section is to show if the stresses inside and outside the inclusion would allow the opening of tensile fractures as a function of ellipsoid shape and stress boundary conditions. The nodules are treated as elastic stiff inclusions embedded into a soft matrix (limestone); the contrast in stiffness is one order of magnitude. The remote stress applied (Table 5.1) consider a stress ratio $\sigma_{min}{}^r/\sigma_{max}{}^r$ from 0.1 to 0.5 for both an extensional and compressional tectonic setting. Please refer to Appendix D for a synoptic table of all symbols used in this paper.

5.4.1. Field methods

The shape of the chert inclusion is approximated by a 3D ellipsoid. In the case of a 2D ellipse, the aspect ratio (α = ratio between lengths of the major and minor axes of an ellipse) describes its shape; for 3D ellipsoids, however, we need additional parameters to define the exact shape. For simplicity, we consider ellipsoids with semi-axes of lengths a, b, and c (Fig. 5.2a) where b equals c ($b = c$). In the case of oblate ellipsoids $a < b = c$ and in the case of prolate ellipsoids $a > b = c$. In order to keep a fixed reference and to be able to distinguish between oblate and prolate ellipsoids, we use the system described in Fig. 5.2a where the three semi-axes a, b, and c are aligned along the x, y, and z axes respectively and use the a/b ratio to describe the shape of the ellipsoid. If $a/b < 1$, the ellipsoid is oblate, if $a/b > 1$ the ellipsoid is prolate, and if $a = b$ the ellipsoid is a sphere.

5.4.2. *Boundary conditions and rheology*

In our study, we model chert nodules as stiff (100 GPa Young modulus, 0.12 Poisson ratio) inclusions embedded into a soft (10 GPa Young modulus, 0.25 Poisson ratio) carbonate matrix (pelagic limestone) (Table 5.1). The mechanical properties of the chert inclusions and the matrix (*Maiolica* and *Scaglia* Fm - Table 5.1) were derived from the literature (Schmidt, 1976; Pabst and Gregorova, 2013; Perras and Diederichs, 2014; Petracchini et al., 2015b; Antolini et al., 2016; Wierer and Bertola, 2016; Aliyu et al., 2017). The boundary between the chert nodule and the host rock is welded as also confirmed by field observations (Fig. 5.4; no discontinuity at the boundary).

Figures 5.2b and 5.2c show the reference frame for the remote stress conditions (tension positive; compression negative): the applied remote stresses σ_x^r, σ_y^r, and σ_z^r are aligned along the x, y, and z axes respectively. Given that in our modeling we keep a fixed x-y-z reference frame (x pointing up), the principal stresses defining an extensional tectonic setting are $\sigma_x^r > \sigma_y^r >= \sigma_z^r$ (Fig. 5.2b) and those defining a compressional tectonic setting are $\sigma_z^r > \sigma_y^r >= \sigma_x^r$ (Fig. 5.2c). The principal stresses within the inclusion σ_x^i, σ_y^i, and σ_z^i are also aligned along the x, y, and z axes respectively. Figures 5.2b and 5.2c define reference regions for the mean stress outside the ellipsoid by means of isosurfaces with equal value of the ratio between mean stress and the absolute value of the maximum applied remote stress ($\bar{\sigma} / |\sigma_{max}^r|$). Visualization of these regions is necessary to be able to describe the mean stresses around the inclusions and the propagation of the joints from the inclusion into the matrix. Figure 5.2b defines reference regions for an extensional tectonic setting: T_{yz} a toroidal region (defined by the light grey isosurface) on the yz plane and P_x a balloon-shaped region (defined by the dark grey isosurface) around the *x-axis*. Figure 5.2c, on the other hand, defines reference regions for a compressional tectonic setting: T_{xy} a toroidal region (light grey) on the xy plane and P_z a balloon-shaped region (dark grey) around the *z-axis*.

Table 5.1.
Mechanical properties of the chert and *Maiolica/Scaglia Fm* and boundary conditions used for the modelling.

Mechanical properties			
E chert		100 GPa*	
ν–chert		0.12*	
E *Maiolica/Scaglia Fm*		10 GPa*	
ν *Maiolica/Scaglia Fm*		0.25*	
Remote boundary conditions			
Extensional tectonic setting - $\sigma_x^r > \sigma_y^r >= \sigma_z^r$			
σ_x^r	σ_y^r	σ_z^r	$\sigma_{min}^r/\sigma_{max}^r$
-1.0	0	0	0
-1.0	-0.1	-0.1	0.1
-1.0	-0.2	-0.2	0.2
-1.0	-0.3	-0.3	0.3
-1.0	-0.4	-0.4	0.4
-1.0	-0.5	-0.5	0.5
-1.0	-0.1	-0.2	0.1
-1.0	-0.1	-0.3	0.1
-1.0	-0.2	-0.4	0.2
Compressional tectonic setting - $\sigma_z^r > \sigma_y^r >= \sigma_x^r$			
σ_x^r	σ_y^r	σ_z^r	$\sigma_{min}^r/\sigma_{max}^r$
0	0	-1.0	0
-0.1	-0.1	-1.0	0.1
-0.2	-0.2	-1.0	0.2
-0.3	-0.3	-1.0	0.3
-0.4	-0.4	-1.0	0.4
-0.5	-0.5	-1.0	0.5
-0.1	-0.2	-1.0	0.1
-0.1	-0.3	-1.0	0.1
-0.2	-0.4	-1.0	0.2
Hydrostatic stress- $\sigma_z^r = \sigma_y^r = \sigma_x^r$			
-1.0	-1.0	-1.0	1.0
(*) Schmidt, 1976; Pabst and Gregorova, 2013; Perras and Diederichs, 2014; Petracchini et al., 2015b; Antolini et al., 2016; Wierer and Bertola, 2016; Aliyu et al., 2017			

5.4.3. Methodology

5.4.3.1. Stress and strain fields from Eshelby Method

The stress and strain fields inside and around the "inclusion" were computed (Fig. 5.2) using the Eshelby inclusion's model (Eshelby, 1957, 1959; Mura, 2012) with a MATLAB™ code developed by Healy (2009) (code available at https://doi.org/10.1016/j.cageo.2008.11.012) and slightly modified for our purpose.

The closed-form Eshelby solution used is based on an isotropic inclusion (ellipsoid) embedded within an isotropic matrix. Both Young's modulus (E) and Poisson ratio (ν) for the matrix and the inclusion need to be specified (see Table 5.1 for the values used) in order to compute the required stiffness tensors ($\mathbf{C}$). Loads on the inclusion-matrix system can be prescribed in terms of the inclusion eigenstrain (or eigenstress) and/or the remote strain (or stress) (Healy, 2009). The term "eigenstrain" (Mura, 2012) represents a plastic stress-free strain within the inclusion such as fracturing, thermal expansion/contraction, volumetric changes due to pore pressure changes. The term "eigenstress" refers to the stress within the inclusion. According to Eshelby (1957), the stresses and strains within the inclusion are homogeneous (i.e. they have the same magnitude everywhere within the inclusion). The strain and stress fields inside the inclusion (Ju and Sun, 1999) are

$$\boldsymbol{\varepsilon} = \boldsymbol{\varepsilon}^0 + \boldsymbol{S}:\boldsymbol{\varepsilon}^{**} \tag{5.1}$$

$$\boldsymbol{\sigma} = \boldsymbol{\sigma}^0 + (\boldsymbol{C}^0 \cdot [\boldsymbol{S} - \boldsymbol{I}]):\boldsymbol{\varepsilon}^{**} \tag{5.2}$$

where $\boldsymbol{\varepsilon}^0$ is the remote strain, $\boldsymbol{\varepsilon}^{**}$ is the eigenstrain, $\boldsymbol{\sigma}^0$ is the remote stress, $\boldsymbol{C}^0$ is the stiffness tensor of the matrix, $\boldsymbol{I}$ is the 4th-order identity tensor, and $\boldsymbol{S}$ is the 4-th order Eshelby tensor, and "**:**" denotes the tensor contraction. $\boldsymbol{S}$ is a function of the ellipsoid dimensions and the Poisson ratio of the matrix (Mura, 2012).

The external stress and strain fields outside the inclusion can be computed as follows

$$\boldsymbol{\varepsilon}(\boldsymbol{x}) = \boldsymbol{\varepsilon}^0 + \boldsymbol{G}(\boldsymbol{x}):\boldsymbol{\varepsilon}^{**} \tag{5.3}$$

$$\boldsymbol{\sigma}(\boldsymbol{x}) = \boldsymbol{\sigma}^0 + (\boldsymbol{C}^0 \cdot \boldsymbol{G}(\boldsymbol{x})):\boldsymbol{\varepsilon}^{**} \tag{5.4}$$

where $\boldsymbol{x}$ is a position vector and $\boldsymbol{G}(\boldsymbol{x})$ is a 4th-order tensor that is a function of the ellipsoid geometry, Poisson's ratio of the matrix, and the coordinate position (Ju and Sun, 1999, 2001).

We modelled the stresses inside and outside a chert inclusion under a wide variety of applied remote stress boundary conditions spanning from an extensional to a compressional tectonic setting (see Table 5.1). The model results for the homogeneous stresses within the inclusions are presented in the form of plots of the stress ratios $\sigma_{min}{}^{r}/\sigma_{max}{}^{r}$ vs. $\sigma_{min}{}^{i}/\sigma_{max}{}^{r}$ where $\sigma_{min}{}^{r}$ is the least compressive remote stress, $\sigma_{max}{}^{r}$ is the largest compressive remote stress and $\sigma_{min}{}^{i}$ is the least compressive stress (most tensile) within the inclusion. We also used plots of $\sigma_x^i/\sigma_{max}^r$, $\sigma_y^i/\sigma_{max}^r$, $\sigma_z^i/\sigma_{max}^r$ vs. *a/b* ratio. These plots allow us to identify where the stress field is tensile in the inclusion (negative $\sigma_{min}^i/\ \sigma_{max}^r$ ratio) and by how much inclusion stresses are enhanced with respect to the remote stresses. We use a positive-tension and negative-compression stress sign convention.

The model results for the stresses outside the inclusion are presented in terms of average or mean stress $\bar{\sigma}$. The importance of mean stress is proven with lab experiments that reveal a transition from brittle to ductile behavior with increasing confining stress ($\bar{\sigma}$); rocks subject even to very small mean tensile stress (of order 1 to 10 MPa) fail by cracking (Pollard and Segall, 1987; Pollard and Fletcher, 2005). We choose to plot the mean stress in three dimensions to highlight the areas where the rock may fracture.

Pollard and Segall (1987; p. 310) define the mean stress as

$$\bar{\sigma} = \frac{(\sigma_{xx}+\sigma_{yy}+\sigma_{zz})}{3} \tag{5.5}$$

where σ_{ii} are the three normal stress components in the three cartesian directions. For uncompressible materials $\bar{\sigma}$ is equivalent to the octahedral normal stress (Pollard and Segall, 1987). The three-dimensional mean stress values are represented by colored isosurfaces representing the stress ratio $\bar{\sigma}/|\sigma_{max}^r|$ where blue is for $\bar{\sigma}/|\sigma_{max}^r| = -0.025$ (compression), cyan is for $\bar{\sigma}/|\sigma_{max}^r| = 0$, and yellow is for $\bar{\sigma}/|\sigma_{max}^r| = +0.025$ (tension). The remote boundary conditions investigated are reported in Table 5.1. Different inclusion shapes were modeled under the same remote stress boundary conditions. Given that most chert inclusions have an oblate shape with major semi-axes *b* and *c* laying along the bedding surface, in this paper we will concentrate on data for *a/b* ratios ranging from 0.01 to 1 (oblate ellipsoids). Our modeling, however, considered *a/b* ratios ranging from 0.01 to 100 including, therefore, both prolate and oblate ellipsoids.

5.4.3.2. Fracturing criteria

The tensile strength of the fractured chert inclusions was examined using the methodology explained by Eidelman and Reches (1992). This methodology follows the fracture toughness approach (Lawn, 1993), which states that during mode I fracturing, the following relationship exists in 2D conditions:

$$K_{IC} = (\sigma^r - P)_Y(\pi l)^{1/2} \tag{5.6}$$

where K_{IC} is the stress intensity factor that is also a good proxy of the maximum fracture toughness at the onset of fracture propagation, $(\sigma^r - P)_Y$ is the driving stress, σ^r is the remote tensile stress normal to the crack, P is the fluid pressure inside the crack, and l is the initial half-length of the crack. The fracture toughness of untreated chert is $K_{IC} = 1.55 \pm 0.007$ MPa/m$^{1/2}$ and that of limestones like *Maiolica* is $K_{IC} = 0.35 \pm 0.007$ MPa/m$^{1/2}$ (Beauchamp and Purdy, 1986). The length of an initial crack or flaw in the chert is assumed to vary between 0.01 mm and 1 mm (Wood and Weidlich, 1982). Consequently, the effective normal stress during cracking in the chert nodule varied from 25 to 250 MPa (maximum values).

5.4.4. Modelling results

5.4.4.1. Stresses within the inclusion

The purpose of the modelling presented in this section is to show if the stresses inside the inclusion would allow the opening of tensile fractures as a function of ellipsoid shape and stress boundary conditions. The modeling results for the magnitude of the (uniform) stress components inside the inclusion are reported in Figures 5.10 and 5.11 for different ellipsoid shapes (oblate and prolate) and remote stress boundary conditions including hydrostatic stress. The stresses inside the elliptical inclusions are uniform and they are linearly related to the remote stresses as shown in Fig. 5.10.

Opening mode fracturing is most likely to occur in the chert nodules where tension develops. Tension occurs in the nodules where the ratio between the minimum inclusion stress and the maximum remote stress ($\sigma_{min}^i/\sigma_{max}^r$) is largest in absolute value and negative, because the minimum inclusion stress (σ_{min}^i) is tensile (positive) but the maximum compressional remote stress (σ_{max}^r) is compressive (negative). This shows up in the graphs of Figure 5.10 as negative values for the $\sigma_{min}^i/\sigma_{max}^r$ ratio, which is plotted vs. the minimum and maximum remote stresses ratio ($\sigma_{min}^r/\sigma_{max}^r$).

For oblate inclusions and an extensional tectonic setting (Table 5.1), Figure 5.10a reveals four key points. First, as the inclusion a/b ratio decreases, the $\sigma_{min}^i/\sigma_{max}^r$ ratio becomes more negative. Second, for $\sigma_{min}^r/\sigma_{max}^r = 0$, we observe the most negative value modeled ($\sigma_{min}^i/\sigma_{max}^r = -2.335$) for $a/b = 0.01$ and the least negative ($\sigma_{min}^i/\sigma_{max}^r = -0.0885$) for $a/b = 1$. Third, a tensile stress arises in the inclusion for $\sigma_{min}^r/\sigma_{max}^r = 0.1$ for $a/b = 1$ and for stress ratios as high as $\sigma_{min}^r/\sigma_{max}^r = 0.36$ for $a/b = 0.01$. Fourth, all extensional models have the same $\sigma_{min}^i/\sigma_{max}^r$ stress ratio (0.1775) for $\sigma_{min}^r/\sigma_{max}^r = 0.3836$.

For oblate inclusions and a contractional tectonic setting (Fig. 5.10b; Table 5.1), four key points emerge. First, the smaller the inclusion a/b ratio, the more negative the $\sigma_{min}^i/\sigma_{max}^r$ ratio. Second, where $\sigma_{min}^r/\sigma_{max}^r = 0$, we observe the most negative value modeled ($\sigma_{min}^i/\sigma_{max}^r = -1.16$) for $a/b = 0.01$ and the least negative ($\sigma_{min}^i/\sigma_{max}^r = -0.0885$) for $a/b = 1$. Third, the tensile field in the inclusion exists up to a

$\sigma_{min}^r/\sigma_{max}^r = 0.1$ for $a/b = 1$ and up to $\sigma_{min}^r/\sigma_{max}^r = 0.22$ for $a/b = 0.01$. Fourth, all compressional models have the same $\sigma_{min}^i/\sigma_{max}^r$ (0.0738) stress ratio for $\sigma_{min}^r/\sigma_{max}^r = 0.2295$.

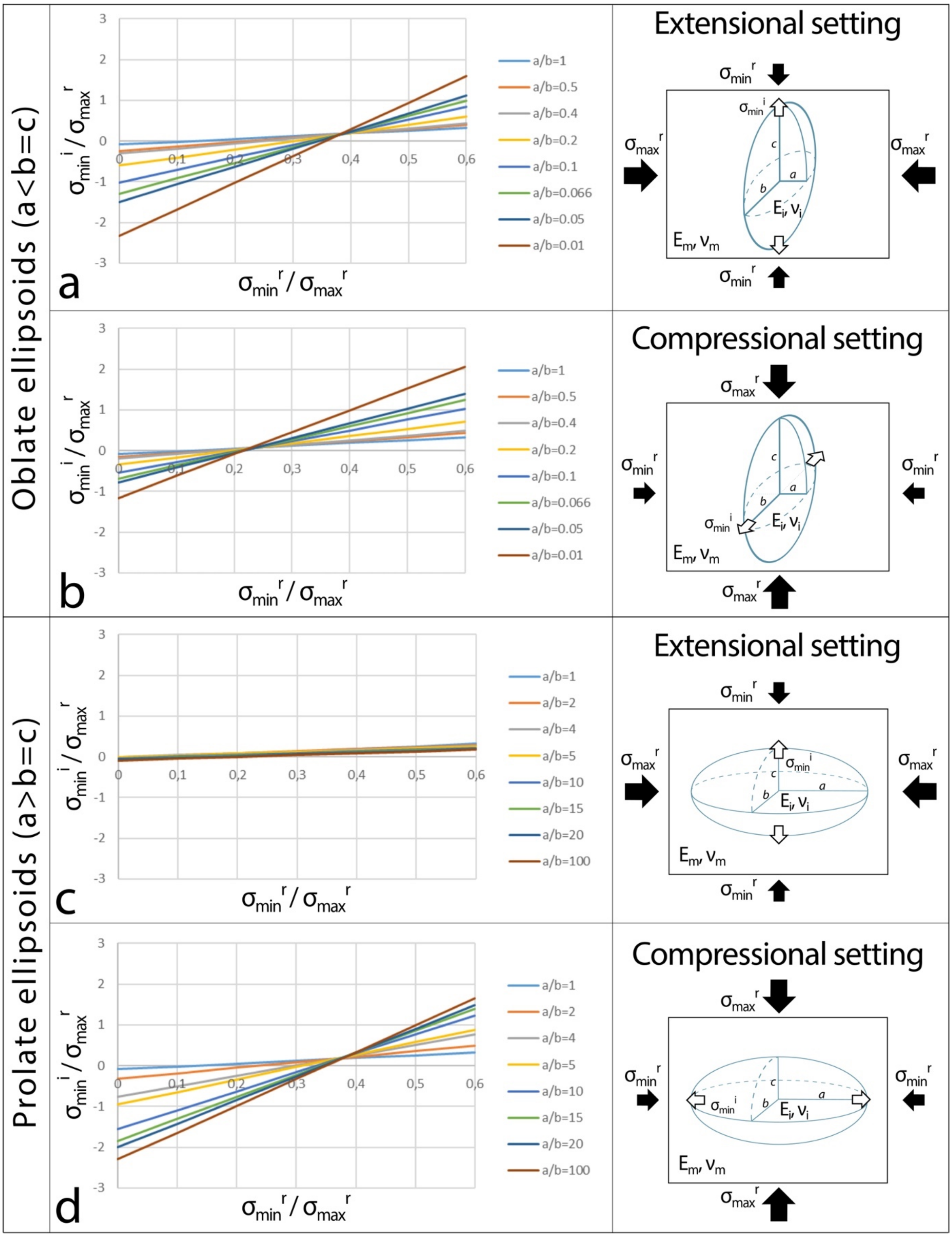

Fig. 5.10 – Normalized most tensile stress in oblate and prolate ellipsoidal inclusions for different remote stresses and various *a/b ratios* (shapes). The figures show that as *a/b* decreases, the most tensile stress in the inclusion increases. The diagrams in the right column represent the boundary conditions and the internal inclusion stresses. **(a)** Oblate inclusions in an extensional setting. **(b)** Oblate inclusions in a contractional setting. **(c)** Prolate inclusions in an extensional setting. **(d)** Prolate inclusions in a contractional setting.

For prolate inclusions and an extensional tectonic setting (Fig. 5.10c) it seems that the *a/b* ratio, which is here much larger than in the case of oblate ellipsoids, matters little on the development of tension within the inclusion. We note that the $\sigma_{min}^{i}/\sigma_{max}^{r}$ ratio is mostly positive (and therefore no tensile stresses arise) for all *a/b* and $\sigma_{min}^{r}/\sigma_{max}^{r}$ ratios examined, so that fracturing cannot take place.

For prolate inclusions and a contractional tectonic setting (Fig. 5.10d), we note four key points. First, the larger the inclusion *a/b* ratio, the more negative the $\sigma_{min}^{i}/\sigma_{max}^{r}$ ratio, the more likely the fracturing. Second, where $\sigma_{min}^{r}/\sigma_{max}^{r} = 0$, we observe the most negative value modeled ($\sigma_{min}^{i}/\sigma_{max}^{r}$ = -2,3) for $a/b = 100$ and the least negative value ($\sigma_{min}^{i}/\sigma_{max}^{r} = -0.0885$) for $a/b = 1$. Third, the tensile field in the inclusion exists for stress ratios $\sigma_{min}^{r}/\sigma_{max}^{r}$ as large as 0.1 for $a/b = 1$ and as large as $\sigma_{min}^{r}/\sigma_{max}^{r} = 0.35$ for $a/b = 100$. Fourth, all compressional models have the same $\sigma_{min}^{i}/\sigma_{max}^{r}$ stress ratio (0.1718) for $\sigma_{min}^{r}/\sigma_{max}^{r} = 0.3754$.

Figure 5.11 shows the amplification of the normal stress components within the inclusion as a function of ellipsoid shape (*a/b* ratio). This figure shows which stress component is the most tensile. The normal components of the inclusion stress (σ_x^i, σ_y^i, and σ_z^i) are normalized by the maximum vertical remote stress (σ_x^r) for the extensional setting case and by the maximum horizontal stress (σ_z^r) for the compressional setting. Also, here, given that the remote stress is negative (compression), negative ratios correspond to tensile stresses within the inclusion.

In the case of the extensional setting, there is no amplification of the σ_x^i / σ_x^r ratio for oblate ellipsoids ($a/b < 1$) whereas it can be up to a factor of 9 for prolate ellipsoids ($a/b > 1$) in weak confinement conditions (small $\sigma_z^r / \sigma_x^r \sim 0$) (Fig. 5.11a). Both σ_y^i / σ_x^r and σ_z^i / σ_x^r ratios become tensile for weak confinements ($\sigma_z^r / \sigma_x^r < 0.3$) and larger in absolute value (up to a factor 2.5) as the ellipsoid becomes more oblate (Fig. 5.11b, c).

In the case of a compressional setting (Fig. 5.11d,), no enhancement of the σ_x^i / σ_z^r ratio occurs for oblate ellipsoids ($a/b < 1$) whereas it is amplified up to a factor of -2.5 for prolate ellipsoids ($a/b > 1$) in weak confinement conditions ($\sigma_x^r / \sigma_z^r < 0.2$) (Fig. 5.11d). For oblate ellipsoids in a compressional setting, the σ_y^i / σ_z^r ratio is enhanced and it becomes tensile up to a value of -1.1 if the confinement is low ($\sigma_y^r / \sigma_z^r < 0.1$) (Fig. 5.11e). The σ_z^i / σ_z^r ratio can be enhanced up to a factor 7.8 in weak confinement conditions and oblate ellipsoid shapes (Fig. 5.11f).

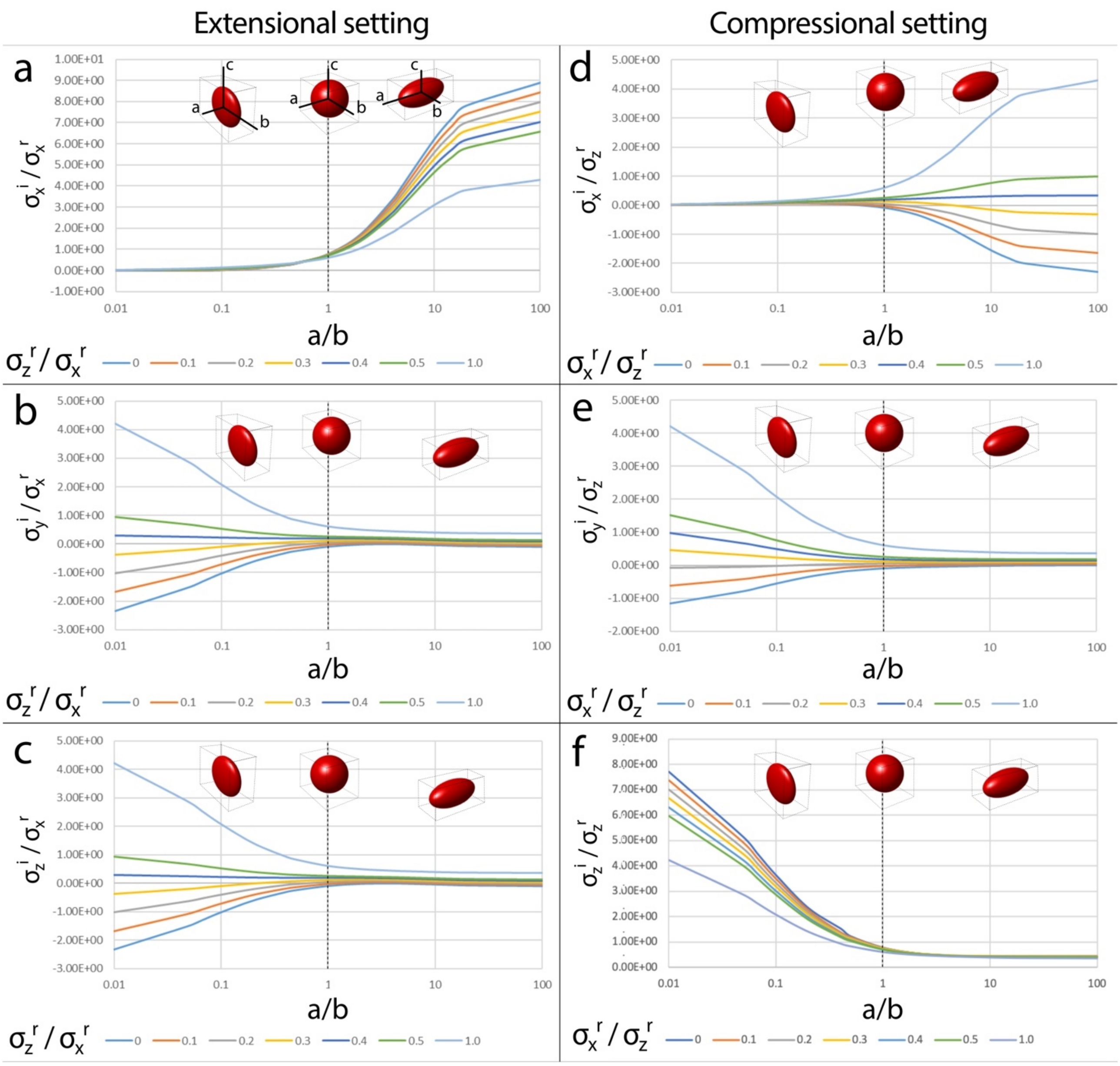

Fig. 5.11 – Amplification of the normal stress components within the chert inclusions as a function of ellipsoid shape (*a/b ratio*) and confinement conditions (σ_{min}^r / σ_{max}^r). The normal stresses components σ_x^i, σ_y^i, and σ_z^i are normalized by the maximum vertical remote stress *(σ_x^r; x-direction)* for the extensional setting case and by maximum horizontal stress (σ_z^r; *z-direction*) for the compressional setting. **(a)** σ_x^i / σ_x^r. **(b)** σ_y^i / σ_x^r. **(c)** σ_z^i / σ_x^r. **(d)** σ_x^i / σ_z^r. **(e)** σ_y^i / σ_z^r. **(f)** σ_z^i / σ_z^r. Note that a negative stress ratio corresponds to a tensile stress in the inclusion. Curves for hydrostatic stress boundary conditions are reported in each figure and correspond to the σ_{min}^r / σ_{max}^r = *1* line (or in other words to *σ_z^r / σ_x^r = 1 or to σ_x^r / σ_z^r = 1*). Note that also with hydrostatic remote stresses ($\sigma_x^r = \sigma_y^r = \sigma_z^r$), stresses within the inclusion are amplified or attenuated with respect to the remote external hydrostatic stress.

In the case of hydrostatic compression remote stresses boundary conditions ($\sigma_x^r = \sigma_y^r = \sigma_z^r$), we note that the stress σ_x^i along the short *a*-semi axis of the oblate ellipsoid is less than the applied hydrostatic stress, and it ranges from 0.02264σ_x^r at *a*/*b* = 0.01 to 0.605σ_x^r at *a*/*b* = 1 (Fig. 5.11a). On the other hand, the σ_y^i and σ_z^i stresses within the oblate ellipsoids and along their long semi-axes (*b* and c) are larger than the remote hydrostatic stresses and vary from $4.21\sigma_y^r$ (or σ_z^r) at a/b = 0.01 to $0.605\sigma_y^r$ (or σ_z^r) at a/b = 1 (Fig. 5.11b, c). In the case of prolate ellipsoids under hydrostatic stresses, we note that the stress σ_x^i along the long a-axis of the prolate ellipsoid is larger than the applied hydrostatic stress and it ranges from $0.605\sigma_x^r$ at a/b = 1 to $4.29\sigma_x^r$ at a/b = 100 (Fig. 5.11d). On the other hand, the σ_y^i and σ_z^i stresses within the prolate ellipsoids and along their short semi-axes (b and c) are smaller than the remote hydrostatic stresses and vary from $0.605\sigma_y^r$ (or σ_z^r) at a/b = 1 to $0.36\sigma_y^r$ (or σ_z^r) at a/b = 100 (Fig. 5.11e, f).

Table 5.2 reports the maximum compressive stress (σ_{max}^r), estimated with the fracture toughness approach, at the time of joint formation in the chert nodules of *Monte Conero* for different ellipsoid shapes (oblate vs. prolate) and for different tectonic settings. Given that, in nature, materials tend to fail more easily than in lab conditions (Eidelman and Reches, 1992), we used the minimum computed value of $(\sigma^r - P)_Y$, which is 25 MPa. Considering that σ_{max}^r is close to the stress caused by the overburden (Zoback, 2008), we can derive the thickness of the overburden (or depth of burial) during deformation using the simple equation $\sigma_{max}^r = \varrho g h$ where we take an average rock density ϱ of 2.1 10^3 kg/m^3. The thickness of the overburden computed with this method suggests a depth of 3.2 km for the extensional and of 5.1 km for the compressional tectonic setting (see last column in Table 5.2).

Table 5.2.
Estimated overburden depth at the time of deformation for different tectonic settings and ellipsoid shapes (oblate vs. prolate) using the fracture toughness approach.

Ellipsoid type	Tectonic setting	Range $\sigma_{min}^r/\sigma_{max}^r$	Min$(\sigma^r - P)_Y$	σ_{max}^r	Overburden
Oblate ellipsoid	*Horizontal extension*	$0<\sigma_{min}^r/\sigma_{max}^r<0.35$	25 MPa	70 MPa	3.2 km
	Horizontal contraction	$0<\sigma_{min}^r/\sigma_{max}^r<0.22$	25 MPa	113 MPa	5.1 km
Prolate ellipsoid	*Horizontal extension*	-			
	Horizontal contraction	$0<\sigma_{min}^r/\sigma_{max}^r<0.35$	25 MPa	70 MPa	3.2 km

5.4.4.2. Stresses in the host rock surrounding the inclusion

The mean stress state in the matrix near the inclusions was computed to identify areas of the host rock where fractures formed inside the chert inclusions could propagate into, or where new fractures might form. We considered only oblate inclusion shapes here, because they are the most common in nature, in general, and at *Monte Conero* in particular (Taliaferro, 1934; Diaz-General et al., 2015). The boundary conditions are listed in Table 5.1. The mean stress state ($\bar{\sigma}$) in three dimensions is graphically represented with surfaces of a constant mean stress value normalized by absolute value of the maximum compressional remote stress or so called isosurfaces (Figs. 5.12 and 5.13). The analysis for remote hydrostatic stress conditions is reported in the Appendix D.

Figure 5.12 shows some selected cases for an extensional tectonic setting with varying remote stress conditions (see Table 5.1). Note the existence of regions of either positive (tensile) mean stresses next to the ellipsoids (yellow shapes) or negative (compressive; blue shapes). The size of these regions is controlled by the *a/b* ratio of the ellipsoids and the remote stress ratio. In an extensional setting, the mean stress is positive (tensional; yellow) around the equator of the oblate ellipsoid (T_{yz}; see Fig. 5.2 for nomenclature). Keeping constant the remote stresses ($\sigma_x^r = \sigma_{max}^r$, $\sigma_y^r = 0$; $\sigma_z^r = 0$), the tensile T_{yz} volume is maximum for large *a*/b ratios (Fig. 5.12a, d) and it decreases in size as the *a/b* ratio decreases. Increasing the lateral confinement (σ_z^r/σ_x^r) in the remote stresses ($\sigma_x^r = \sigma_{max}^r$, $\sigma_y^r = 0.4\ \sigma_{max}^r$; $\sigma_z^r = 0.4\ \sigma_{max}^r$), leads to an overall decrease in tensile mean stress within the equatorial region T_{yz} (Figs. 5.12d-f). The mean stress is compressive in the polar regions of the ellipsoids (P_x region); also, these regions shrink with decreasing *a/b* ratio and increasing σ_z^r/σ_x^r ratio.

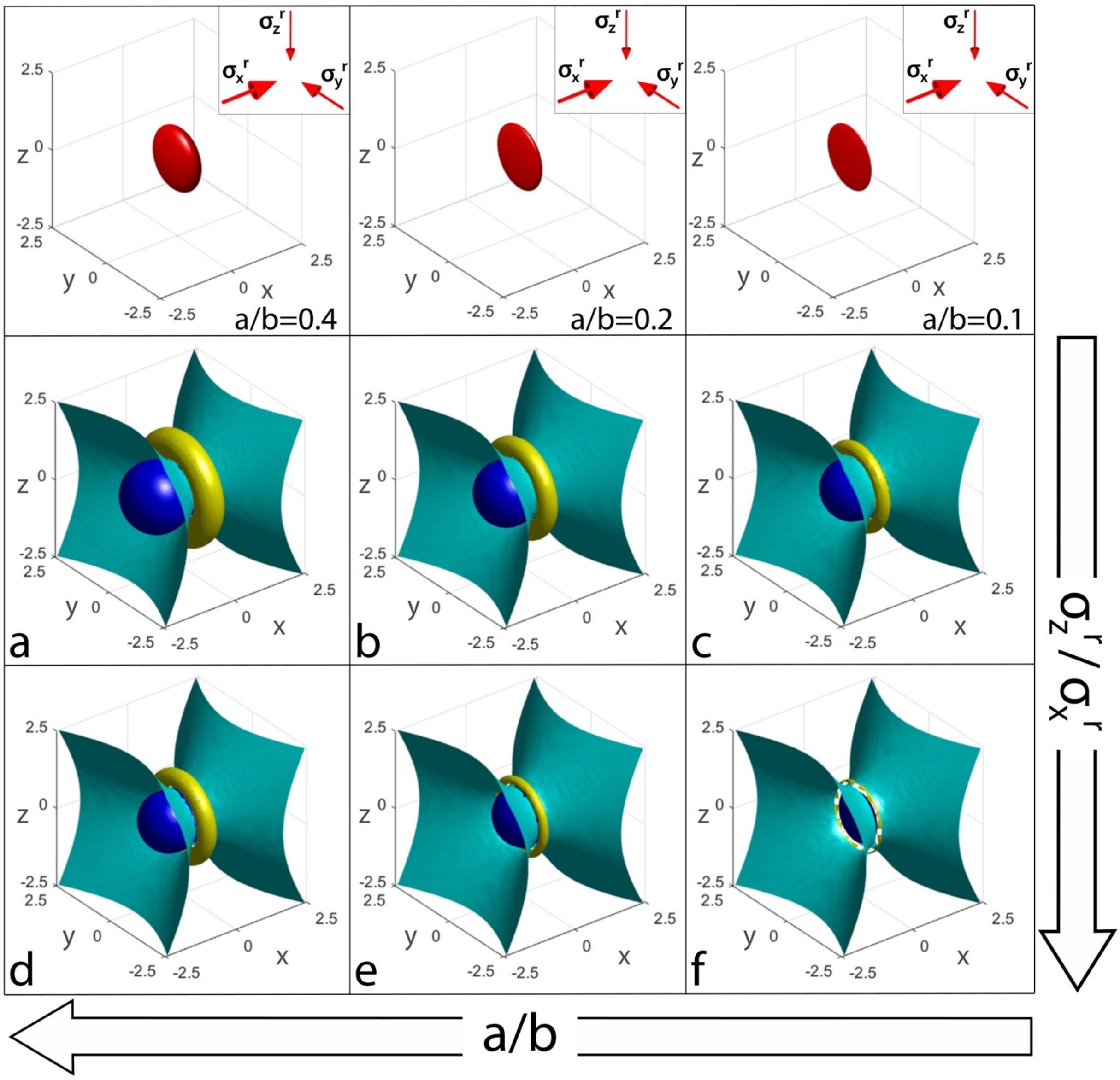

Fig. 5.12 – Modelling results of the mean stress outside the chert inclusion in an extensional tectonic setting and for different ellipsoid (inclusion) *a/b ratios* as well as different lateral confinement (σ_z^r/σ_x^r) conditions. The mean stress is represented by isosurfaces: blue is for $\sigma / |\sigma_{max}^r| = -0.025$ (*compression*); cyan is for $\sigma / |\sigma_{max}^r| = 0$; yellow is for $\sigma / |\sigma_{max}^r| = 0.025$ (tension). $b=c=1$ in all figures. **(a)** $a/b=0.4$; $a=0.4$; $\sigma_x^r = \sigma_{max}^r$, $\sigma_y^r = 0$; $\sigma_z^r = 0$. **(b)** $a/b=0.2$; $a=0.2$; $\sigma_x^r = \sigma_{max}^r$, $\sigma_y^r = 0$; $\sigma_z^r = 0$. **(c)** $a/b=0.1$; $a=0.1$; $\sigma_x^r = \sigma_{max}^r$, $\sigma_y^r = 0$; $\sigma_z^r = 0$. **(d)** $a/b=0.4$; $a=0.4$; $\sigma_x^r = \sigma_{max}^r$, $\sigma_y^r = 0.4\ \sigma_{max}^r$; $\sigma_z^r = 0.4\ \sigma_{max}^r$. **(e)** $a/b=0.2$ $a=0.2$; $\sigma_x^r = \sigma_{max}^r$, $\sigma_y^r = 0.4\ \sigma_{max}^r$; $\sigma_z^r = 0.4\ \sigma_{max}^r$. **(f)** $a/b=0.1$; $a=0.1$; $\sigma_x^r = \sigma_{max}^r$, $\sigma_y^r = 0.4\ \sigma_{max}^r$; $\sigma_z^r = 0.4\ \sigma_{max}^r$.

Figure 5.13 shows some selected cases (same ellipsoid geometry as in Fig. 5.12) for a compressional tectonic setting with different remote stresses (see Table 5.1). Note the existence of rock volumes next to the ellipsoids where the mean stress is positive (tensional, yellow) or negative (compressive, blue). The size of these volumes is controlled by both the *a*/b ratio of the ellipsoids and the remote stresses. Within a donut-shaped volume around the equator of the ellipsoid the mean stress is positive (tensional) around the oblate ellipsoid. This volume is largest for large *a*/b ratios (Fig.

5.13a, d) and it decreases as the a/b ratio decreases for constant remote stress conditions ($\sigma_x^r = 0, \sigma_y^r = 0; \sigma_z^r = \sigma_{max}^r$). Increasing the lateral confinement (σ_x^r/σ_z^r) of the remote stresses ($\sigma_x^r = 0.4\ \sigma_{max}^r$, $\sigma_y^r = 0.4\ \sigma_{max}^r; \sigma_z^r = \sigma_{max}^r$), we observe an overall decrease in tensile mean stress within the equatorial region T_{xy}. The tensile stress, however, does not disappear as it does in the extensional setting. Two regions where the mean stress is compressive (negative) are present on the y-z plane. These regions are centred on the z-semi axis (P_z region) (Fig. 5.13), which is also the direction of the maximum applied compressive remote stress.

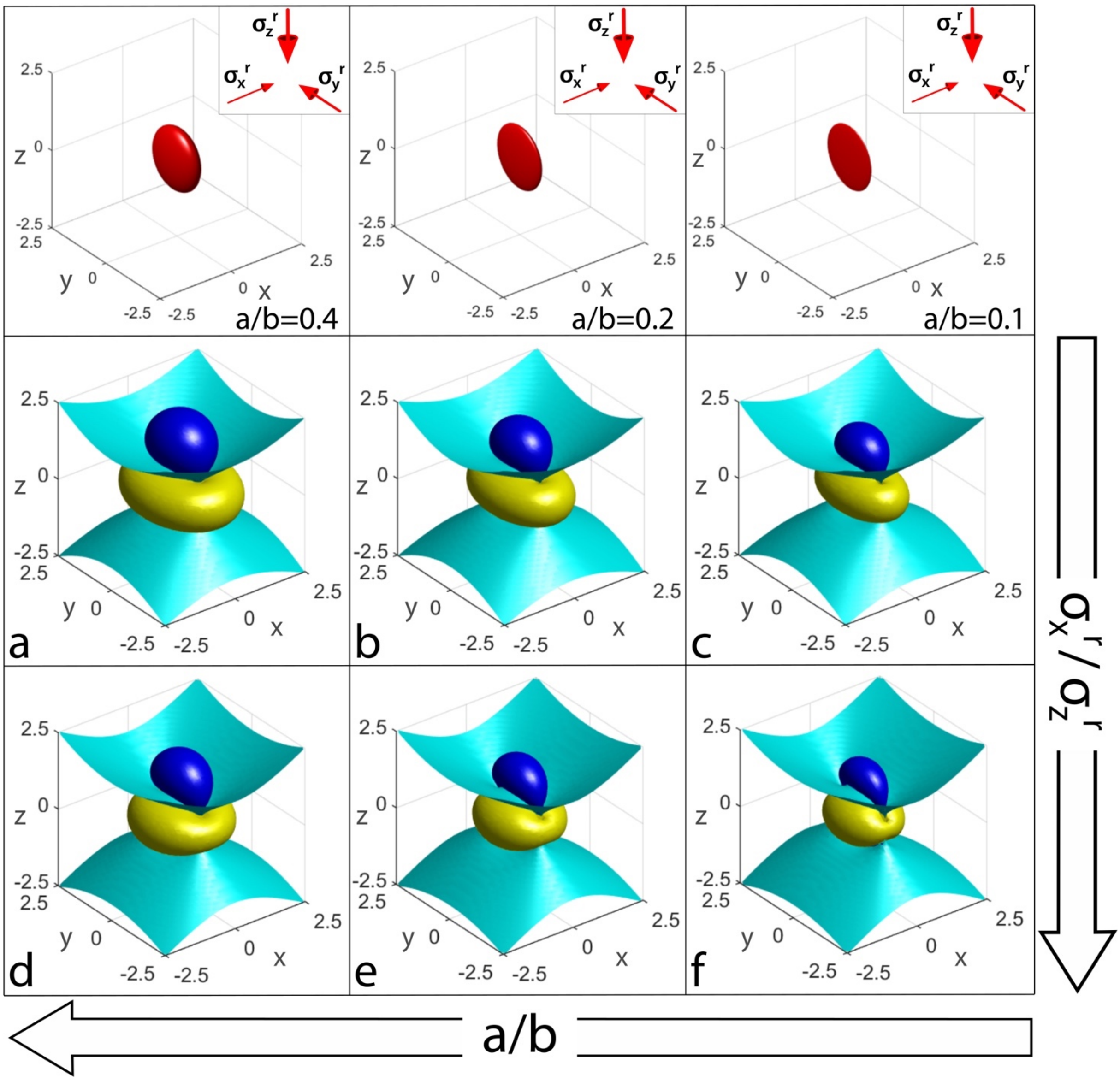

Fig. 5.13 – Modelling results of the mean stress outside the chert inclusion in a compressional tectonic setting and for different ellipsoid (inclusion) *a*/*b ratio* as well as lateral confinement (σ_x^r/σ_z^r) conditions. The mean stress is represented by isosurfaces: blue is for $\sigma / |\sigma_{max}^r| = -0.025$ (compression); cyan is for $\sigma / |\sigma_{max}^r| = 0$; yellow is for $\sigma / |\sigma_{max}^r| = 0.025$ (tension). $b=c=1$ in all figures. **(a)** $a/b=0.4; a=0.4; \sigma_x^r = 0, \sigma_y^r = 0; \sigma_z^r = \sigma_{max}^r$. **(b)** $a/b=0.2; a=0.2; \sigma_x^r = 0, \sigma_y^r = 0; \sigma_z^r = \sigma_{max}^r$. **(c)** $a/b=0.1; a=0.1; \sigma_x^r = 0, \sigma_y^r = 0; \sigma_z^r = \sigma_{max}^r$. **(d)** $a/b=0.4; a=0.4; \sigma_x^r = 0.4\ \sigma_{max}^r, \sigma_y^r = 0.4\sigma_{max}^r; \sigma_z^r = \sigma_{max}^r$. **(e)** $a/b=0.2\ a=0.2; \sigma_x^r = 0.4\sigma_{max}^r, \sigma_y^r = 0.4\sigma_{max}^r; \sigma_z^r = \sigma_{max}^r$. **(f)** $a/b=0.1; a=0.1; \sigma_x^r = 0.4\sigma_{max}^r, \sigma_y^r = 0.4\sigma_{max}^r; \sigma_z^r = \sigma_{max}^r$.

5.5. DISCUSSION

In the discussion, we address two matters. First, we compare our field and sample observations on chert nodules with the results of the geomechanical Eshelby model. Second, we discuss whether deformation structures in and around chert inclusions might be used as paleo-stress indicators.

5.5.1. Field observations and modeling results

The most striking field observation in our study is that chert nodules are more intensely fractured than the surrounding carbonate matrix in agreement with previous work (Diaz-General et al., 2015; Petracchini et al., 2015a, b). We explain this fracture concentration by extending to 3D the analyses done by others in 2D. The 3D inclusion model (Eshelby 1957), in fact, predicts an amplification (or concentration) of the stresses within the inclusion that can lead to a higher fracture density in the inclusion with respect to the surrounding matrix. This is exactly what we observed in the *Monte Conero* outcrops. The fracture distribution within the nodules might be explained by the stress state within the inclusion. The Eshelby model also predicts a homogeneous stress distribution (the stress tensor does not vary with position) in the inclusion (Eshelby, 1957) and this is what we infer based on the joint distribution within the nodules (Figs. 5.4 and 5.5). Joints in the chert inclusion have a regular spacing and they do not veer at the tip of the inclusion or at its borders (Fig. 5.5a, b).

In most nodules, we observed a set of joints parallel to bedding and one set normal to bedding (Fig. 5.8a, b) where the second set abuts against the first one (Fig. 5.4). The spacing is regular in both sets as also expected from the uniformity of stresses within the nodules predicted by the Eshelby (1957) model. The abutting normal to bedding set, therefore, probably formed after the bedding-parallel set, as is usually inferred in the literature (Wu and Pollard, 1992; Willemse and Pollard, 1998; Antonellini and Mollema, 2019). The abutting relationship is explained by the fact that the stress concentration driving joint propagation, terminates at the discontinuity represented by another joint surface (Renshaw and Pollard, 1995). We speculate that the first bedding-parallel joint set in the chert nodules formed during the compressional tectonic event leading to the formation of the *Monte Conero* anticline (with σ_3 vertical and σ_1 horizontal). The younger normal-to-bedding set probably formed during uplift and collapse of the anticline (vertical σ_1 and horizontal σ_3) as reported by Montanari et al. (2016) or is connected with tear faulting in the leading edge of the *Monte Conero* fold (Diaz-General et al., 2015).

In general, the observation that limestone and chert (for the same layer or nodule thickness) have different fracturing intensities (number of fractures per unit length) can be simply explained by the high stiffness (Young's modulus value) of the chert respect to the limestone (i.e. Table S1 and S2 in Petracchini et al., [2015b] and references therein). At the same time, the fact that fracture intensity is intermediate within the chert-rind (Fig. 5.4) may be related to the mechanical behavior of the rind, which is mostly composed of silica with a minor fraction of the surrounding limestone (Hesse, 1989).

Pressure solution seams or stylolites normal to bedding are observed in some outcrops of *Monte Conero* but are rare compared to carbonate sequences without chert nodules (Petracchini et al., 2015b). The lack of pressure solution seams in presence of chert in carbonate rocks was observed also by Petracchini et al. (2015b), who speculated that chert layers may strengthen a limestone sequence and inhibit pressure solution under layer-parallel-shortening. In this situation, the tectonic load is mostly supported by the stiff chert layers and the strain of the whole chert–limestone composite remains in the elastic field, so that pressure solution seam development is prevented in the limestone beds.

5.5.2. *Modeling of stresses inside the inclusion and implications for remote stresses at the time of chert fracturing*

A comparison of the results of the stress modeling inside of the chert inclusion (ellipsoid) with the field observations provides insight into the ratio of the principal remote stresses acting on the inclusion. This ratio, in turn, allows to infer the type of tectonic setting that was present during the formation of the fractures in the chert nodules. From the modeling, we expect that tensile fracturing is promoted in oblate ellipsoids with small *a*/*b* ratios (less than unity), and in prolate ellipsoids with large *a*/*b* ratios (greater than unity) (Fig. 5.10). This is what we observed (Fig. 5.7b). Spacing both for bedding-parallel and normal-to-bedding joints in oblate ellipsoids increases as the *a*/*b* ratio increases (Fig. 5.7b); a similar relationship is not statistically representative for the prolate ellipsoids, given the few examples that we found in the field.

The Eshelby models for oblate ellipsoids discussed above show similar behavior for both an extensional and a compressional setting. In extensional settings, however, the negative $\sigma_{min}^{i}/\sigma_{max}^{r}$ ratio is larger in absolute value than in compressional settings for oblate ellipsoids. This suggests that tensile fracturing in the chert nodules is more likely in extensional conditions (Fig. 5.10a-b). In the case of prolate ellipsoids, on the other hand, tensile fracturing seems to be possible *only* in a compressive tectonic setting (compare Fig. 5.10c-d).

The remote stresses need to be markedly different for tensile fracturing to take place, with $\sigma_{min}^{r}/\sigma_{max}^{r} < 0.35$ in the extensional setting (oblate ellipsoids) and $\sigma_{min}^{r}/\sigma_{max}^{r} < 0.22$ in the compressional one (oblate ellipsoids). Also, for this latter reason, in general, tensile fracturing in the chert nodules is more likely in extensional rather than compressional conditions within oblate ellipsoid shapes.

Figure 5.7b, which presents outcrop data for joint sets parallel to bedding and sets normal to bedding in oblate ellipsoids, shows a mild correlation ($R^2 \sim 0.33$) between fracture spacing and *a*/*b* ratio: small *a*/*b* ratios have a small fracture spacing and large *a*/*b* ratios have a large fracture spacing. This is also consistent with the modelling that predicts more persistent conditions for tensile field existence in oblate inclusions with small *a*/*b* ratios with respect to those with large *a*/*b* ratios (Fig. 5.10a, b).

Using the parameters summarized in Table 5.2, we estimate that burial depth was around 5.1 Km during the formation of the parallel-to-bedding joints in the oblate ellipsoids and around 3.2 Km during the formation of the normal-to-bedding-joints. Also, the fracture toughness approach indicates a high differential stress with $(\sigma^r - P)_Y$ around 25 MPa and $\sigma_{max}{}^r$ between 70 MPa and 113 MPa. In both instances, the deformation of the chert nodules at shallow crustal level with $\sigma_{min}{}^r / \sigma_{max}{}^r < 0.22$-0.35. The compressional phase might have occurred deeper than the extensional one by about 2 km.

Comparison of Figure 5.11d and 5.11e shows that the most tensile stress during compression is in the x-direction, so that joints may open-up parallel to the *yz*-plane (parallel-to-bedding) as we observe in the field (Fig. 5.4). Figure 5.11b, and c shows that in an extensional setting the tensile components have the same magnitude both in the *y* and *z* direction, so that it is possible to have two sets of joints parallel to the *xz* and *xy*-planes (normal-to-bedding), which is also observed in the field. Also, for chert nodules to fracture, the $\sigma_{min}{}^r$ / $\sigma_{max}{}^r$ ratio needs almost always to be less than 0.3. Furthermore, it is interesting to note that bedding-parallel joints (or veins for the limestone) are present only in the chert nodules (thanks to the enhancement of the tensile field) and not in the limestone matrix whereas veins with orientation similar to that of the normal-to-bedding joints in the nodules are also present in the *Maiolica* and *Scaglia* Fm (Diaz-General et al. 2015).

5.5.3. Modeling of stresses outside the inclusion and implications for remote stresses at the time of chert fracturing

Comparing field observations on the locations where joints propagate from the chert inclusion into the carbonate matrix with the geomechanical models for the mean stress outside the inclusion, gives insight into the orientation and magnitude of the paleo-stress at the time of joint nucleation. The field data that we collected (Fig. 5.7a), in fact, show that with increasing *a*/*b* ratio, the fracture penetration distance into the carbonate matrix increases as expected from the tensile mean stress distribution modeled in Figures 5.12 and 5.13.

Another key point is that we observed longer penetration distances into the matrix for the normal-to-bedding-joints with respect to the parallel-to bedding-ones (Fig. 5.7a). Based on this observation and the stress modelling outside the inclusion we suggest the following paleostress conditions, which also are consistent with our analysis of the stresses inside the inclusion. The first tectonic phase recorded by jointing within the nodules at *Monte Conero* and represented by the parallel-to-bedding-joints is a compressional one (forming the *Monte Conero* anticline) probably with a $0.1 < \sigma_{min}^r/\sigma_{max}^r < 0.3$ stress confinement ratio. The second tectonic phase, represented by the normal-to-bedding-joints, might record the extensional collapse of the anticline during exhumation and uplift with a $0 < \sigma_{min}^r/\sigma_{max}^r < 0.2$ confinement ratio. Most authors (Crescenti et al., 1977; Mayer et al., 2003; Sarti et al., 2011), based on the seismicity along NNE-SW trending tear faults, claim that the Pliocene-Pleistocene contraction phase at Monte Conero continued until recent times. Our data, however, seem to point out an extension phase (exhumation of the anticline) starting in the medium Pleistocene (Calabrian stage) at about 1-1.2 Ma years. At the current uplift rates (average 3 mm/year; Coltorti et al., 1987), the formation of the joints in the chert nodules could have occurred at a depth of about 3.2 Km and shallower (see Table 5.2). The recent gravitational collapse of the *Monte Conero* anticline (Pleistocene to recent), on the other hand, is well described also by Montanari et al. (2016) who relate the landslide hazard of the area to the existence of pre-existing weaknesses and intense fracturing.

Oblate nodules with only one set of open fractures (usually normal-to-bedding) (Fig. 5.5a, b) show small penetration distances of the joints into the matrix in the *x*-direction (or *z*-direction), as we expect from the 3D mean stress models (Figs. 5.12 and 5.13). In these latter models, the mean stress is compressive in the matrix above and below where the ellipsoid intersects the *x*-axis (extensional setting) or the z-axis (compressional setting). It is important to point out that a large confinement (σ_z^r / σ_x^r ratio) would suppress propagation of the joints in the volume all around the nodule more in an extensional setting than in a compressional one (see the size of extensional mean stress volumes in Figs. 5.12 and 5.13).

The nodule in Figure 5.8a shows a bedding-parallel joint set that is not propagating into the matrix along the σ_z^r direction (P_z volume) as expected from the models in Figure 5.13 (compressional setting). Near the same nodule in Figure 5.8a, a few stylolites in the carbonate matrix indicate that σ_z^r is parallel to bedding in the direction of the longer axis of the ellipsoid. Most ellipsoids with parallel-to-bedding joints have joints like this (Fig. 5.8b).

Some chert nodules show bedding-parallel joints, some of which are propagating into the carbonate matrix in the region where the stresses favoring joint propagation drop off (Fig. 5.8c). This suggests that σ_z^r is normal to the plane of the photograph (according to the compressive tectonic setting models in Fig. 5.13). A similar situation is also observed for the nodule in Figures 5.8d and 5.9.

5.5.4. Implications for fracture connectivity

The formation of chert nodules within a carbonate sequence is a diagenetic phenomenon (Hesse, 1989; Maliva and Siever, 1989; Maliva et al., 2005; Madsen and Stemmerik, 2010), so that the preferential fracturing that we observe in chert embedded in carbonate is another aspect of structural diagenesis (Laubach et al., 2010). This is another example of how diagenetic processes can control deformation characteristics and distribution in a sedimentary sequence as opposed to the case in which deformation focuses the diagenetic processes and control the distribution of diagenetic products (e.g. Del Sole and Antonellini, 2019; Chapters 2 through 4). Our study shows that chert nodules in carbonate focus fracturing and may contribute to improve fracture connectivity in a layered pelagic limestone sequence. This improvement in connectivity is dependent on how widespread the chert nodules are as well as their shape. Carbonate sequences are widespread throughout the world and they are often exploration targets for geofluids (Caineng et al., 2010; Wang et al., 2013). Furthermore, the presence of stiff rock inclusions (in a soft matrix) is a widespread phenomenon and can also be extended to conglomerates and metamorphic, volcanic, or magmatic rocks (Eidelman and Reches, 1992; Mondal and Acharyya, 2018; Acharyya and Mondal, 2019). Our model can help in predicting fracture development in and outside the inclusion as well as their evolution and connectivity in different tectonic settings.

5.6. CONCLUSIONS

This study shows how fracture distributions within and around chert nodules in a pelagic carbonate sequence are consistent with geomechanical models of stress distribution based on the 3D Eshelby solution for a stiff inclusion embedded into a soft matrix. In particular, the major conclusions of our work are:

(1) Chert is ubiquitous in the carbonate sequence exposed at *Monte Conero*. Most times the chert nodules are oblate ellipsoids with their short axis normal to the bedding plane.

(2) Evenly spaced joints concentrate in the chert nodules. Their frequency is higher in the chert than in the carbonate host rock.

(3) Two joint sets are observed in the nodules, one parallel to bedding, and one normal to bedding. The second set is always present.

(4) Joints in chert inclusions with a small *a*/*b* ratio tend to be confined within the nodule. Where the *a*/*b* ratio is large, joints propagate for short distances into the soft carbonate matrix.

(5) For the first time, we present a full 3D modeling of the stress field inside and around a chert inclusion within a carbonate matrix considering both the effects of inclusion shape and applied remote stresses to control fracture development within and about the chert nodule. The results of the modeling explain well our field observations (1) through (4).

(6) Modelling of oblate chert inclusions in an extensional or compressional tectonic setting show that they are more prone to fracturing where the *a*/*b* ratio is small.

(7) Modelling of prolate inclusions in an extensional tectonic setting shows that they cannot fracture whereas in a compressional tectonic setting they are prone to fracture for large *a*/*b* ratios.

(8) Comparing field observations with the modelling of the mean stress field outside the chert inclusions for extensional and compressional tectonic settings shows the model results are consistent with the observations. Joints propagate from the stiff inclusion into the soft matrix in a manner consistent with the spatial distribution of the mean normal stress magnitudes.

(9) The set of models presented for the stress state inside and outside the inclusions can be used to gain information on the remote stress conditions based on the propagation distance of the joints into the carbonate matrix as well as where in the 3D volume the joints will propagate about the ellipsoidal inclusion

(10) Using the field observations and a fracture toughness approach based on the geomechanical modeling results, we tried to reconstruct the paleo-stress conditions at the time of joint nucleation and propagation within the folded layered sequence outcropping at *Monte Conero*. Two different deformation phases are recognized: (i) In the first phase, bedding-parallel joints form only in the chert inclusion. These joints are probably related to a horizontal compression with an overburden of about 5.2 km. (ii) In the second phase, normal-to bedding joints form in the chert inclusion. These joints are probably related to recent extension (Calabrian stage) and gravitational collapse during exhumation of the anticline with an overburden of about 3.2 km and less.

Supplement – Supplementary material to this Chapter can be found in the Appendix D.

References – The references related to this Chapter can be found in the Bibliography.

Acknowledgments – We are grateful to Steve Martel, Andrea Billi, and an anonymous reviewer whose comments have contributed to greatly improve our manuscript, and Stephen E. Laubach for his editorial work. We thank logistical help provided by the *Ente Parco Regionale del Conero (Regional Park of the Conero Mountain)*.

6

Conclusion

Concluding remarks – Progresses, Implications, and Applications

Here, the major outcomes and progresses made with this work, their implications and practical applications to geofluids management and exploitation are synthesized.

Porous sandstones, deformation bands, and calcite nodules

We have studied compactive shear bands with cataclasis in high-porosity arkosic sandstones (*Loiano Sandstones*) associated with spatially heterogeneous calcite cement in the form of nodules in the northern Apennines (Italy) (see **Papers I-III**). The major conclusions of our work are:

- The sandstone mineralogy controls the fracturing mechanism and the cataclasis development in the DB, hence the size distribution, shape, and organization of grains within the DB in arkosic sandstone. Feldspars are characterized by a persistent cleavage that makes them weaker and more prone to fracture with respect to quartz. Feldspar contribution to the increase in fine grains content within the DB prevails with respect to the quartz. Different fracturing mechanism between feldspar (intragranular fracturing) and quartz (spalling and/or flaking of edges) explain the preferential cataclasis of feldspar grains within the DB. The cleavage controls feldspar fragments shape: elongated (high aspect ratio) and low in roundness and circularity, which are more likely to align with the DB plane during progressive shear. Quartz grains, on the other hand, do not show any preferential fracture direction, so that grain crushing will occur preferably at defects and weakness points (i.e. edges) and produce more rounded particle fragments, which are less likely to align with the DB plane. Our findings represent new insights into the deformation mechanism of DBs in arkosic sandstone (see **Paper I**).
- The joint effect of compaction and cataclasis decrease DB porosity by 1 order of magnitude with respect to the pristine host rock. The porosity and pore-size decrease within the DB causes a change in pore connectivity and a decrease in permeability up to 3 orders of magnitude from host

rock to the DB. Porosity drops by 1 order of magnitude from the host rock to the nodules. Cement precipitation within the DB enhances the reduction of porosity caused by mechanical grain-crushing, reorganization of grains, and pore collapse (see **Paper I**).

- A network of structural and diagenetic heterogeneities such as low permeability DBs and cement nodules within highly porous host sandstone (i) degrades porosity (down to < 1%) and permeability (down to 10^{-2} mD vs 10^{+3} mD in the host rock); (ii) produces a general strengthening effect (89 MPa vs 17 MPa in the host rock in average); thus (iii) imparting a strong petrophysical and mechanical heterogeneity and anisotropy to the rock volume. The association of diagenetic cementation with DBs strengthens fault rocks considerably and further increases the flow-buffering potential of these structural features (see **Paper II**).
- The variations of petrophysical and mechanical properties due to the structural (DBs) and diagenetic (calcite nodules) heterogeneities as well as their spatial distribution, thickness, continuity, and density need to be properly characterized and implemented into reservoir quality prediction modeling, reservoir simulation modeling, and geomechanical modeling, since they possibly have a strong influence on the migration, trapping, and production of geofluids in sandstone reservoirs/aquifers.
- Ground-penetrating radar (GPR) may assist and improve the subsurface imaging and characterization of sub-seismic scale structural and diagenetic heterogeneities (SDH) in outcrop analogs of faulted porous sandstone aquifers and reservoirs. Different textural, petrophysical, and geomechanical properties between host rock, DBs, and calcite nodules result in different GPR response (i.e. relative permittivity, instantaneous attributes). E.g., zones with high permittivity correspond to (outcropping) areas of positive relief, high strength, and low permeability (i.e. DBs and nodules). The GPR response, integrated with outcrop-based data, can thus be used to characterize variations in petrophysical and mechanical properties together with the organization and geometry of SDH in 3D subsurface volumes, in a way to reconstruct realistic and detailed conceptual model of outcrop analogs of faulted aquifers/reservoirs in porous sandstone (see **Paper II**).
- In two case studies, low-permeability DBs precede and control selective diagenesis recorded by carbonate cement nodules spatially associated with the bands. In *Loiano* (Northern Apennines, Italy), DBs buffered the fluid flow and promoted selective cement precipitation by "solute-sieving" across the DB and increased surface reactivity of fine-grained comminution products and small pore throats that act as nucleation sites. In *Bollène* (Provence, France), clusters of DBs hindered the cross-flow and focused fluid flow and diagenesis to parallel-to-band compartments.

Our work shows that DBs control flow patterns and foster diagenesis within a porous sandstone reservoir analog and this, in turn, affects how diagenetic heterogeneities are distributed within the rock volume. This information is invaluable to assess the uncertainties in reservoir petrophysical properties, especially where structural and diagenetic heterogeneities (SDHs) are below seismic resolution. In these cases, outcrop-based studies allow for continuous and more reliable reconstruction of their distribution. A reservoir development plan needs to take SDHs effects into account, so that the best exploitation strategy can be deployed, and bypassed pay minimized (see **Paper III**).

- A "positive feedback" between deformation, fluid flow, and diagenesis is observed in *Loiano* (see Fig. 1.1). First, the low-permeability DBs buffer the fluid flow, focus cementation, and control the distribution of calcite nodules. Because of the strengthening effect promoted by the cement and DB's material, the assemblage "DBs – nodule" is prone to a pure-fragile deformation and localizes joints that do not propagate into the "soft" host sandstone. Joints actually represent fluid flow conduits and lead to new diagenesis (veins; see **Papers II and III**, and *sec. C.8* in Appendix **C**).

Carbonate rocks, chert nodules, and fractures

We have studied the fracture network (opening mode I) concentrated in the chert nodules within a deformed layered pelagic limestone sequence (*Maiolica Fm, Scaglia Fm*) at the Mt Conero (Northern Apennines, Italy) (see **Paper IV**). The most significant conclusions of our work are:

- For the first time, we present a full 3D modelling of the stress field inside and around a (stiff) chert inclusion within a (soft) carbonate matrix, by using the 3D Eshelby solution, considering both the effects of the 3D inclusion shape (oblate or prolate ellipsoid) and the applied remote stresses (extensional or compressional tectonic setting) to control fracture development (fracture intensity and propagation) within and around the chert nodule. The results of the modelling are consistent with our field observations of fracture distribution.
- Chert nodules in a deformed layered carbonate sequence can provide important clues on (i) fracture distribution heterogeneity; (ii) temporal sequence of events; and (iii) paleo-stress conditions.
- Chert nodules in carbonate focus fracturing and may contribute to improve fracture connectivity in a layered pelagic limestone sequence. This improvement in connectivity is dependent on how widespread the chert nodules are as well as their shape. Our model can help in predicting fracture development in and outside the inclusion (e.g. clasts in conglomerate, microgranitoid enclaves) as well as their evolution and connectivity in different tectonic settings.

- To the unconventional industry, “nodulized” layers can cause troubles in hydraulic fracturing because they usually behave like either a frac or a proppant barrier. Our paper provides a new insight on the barrier mechanisms. Our quantification of stress change in the nodules can be applied to characterize the barrier strength and simulate its behavior during hydraulic fracturing.
- At the *Mt Conero,* a “positive feedback” between deformation, fluid flow, and diagenesis can be assumed (see Fig. 1.1). The chert nodules (a diagenetic phenomenon) embedded in carbonate focus fracturing (opening mode I), control fracture intensity and propagation, and may improve fracture connectivity in the deformed layered carbonate sequence. The joints represent fluid flow conduits that may subsequently focus fluid circulation and promote further diagenesis.

Suggestions for future work

As said in *Section 4.7.2* in (Chapter 4), the decrease in hydraulic conductivity in the DB dominates over the flow velocity increase caused by porosity reduction and, as a result, there is a net decrease in advective flow velocity in the DBs. A reduction in flow velocity (i.e., slower flow path in the DB than in the host rock) might increase the residence time of the fluid migrating through the reactive material within the DB. It should be tested, thus, if residence time may “kinetically” favor cement precipitation (e.g. Bott, 1995; Walker and Sheikholeslami, 2003). Moreover, we need to know the geochemical conditions of the fluids and the reaction kinetics to be able to assess the processes of cement precipitation in the band and its evolution through time. Since we have in fact never found any form of flow associated with nodules, it is likely that cement precipitation in the bands and surrounding areas is controlled primarily by the surface properties of the cataclastic material within the band (e.g. Phillips, 2009). The geochemical conditions of the fluids and the reaction kinetics are, however, very complex to assess. For these reasons, a coupled fluid flow reactive model is necessary to evaluate the effects of the flow and that of the geochemical conditions. (e.g. Parkhurst et al., 2010; Langevin et al., 2020).

Specifically, numerical flow simulations based on a deterministic fully descriptive approach (e.g. field maps) or a stochastic approach (e.g. Discrete Fracture Network model) are deemed necessary: (i) to reconstruct paleo-fluid flow pathways around DBs, thus, their effect on fluid flow and mass transport in an aqueous solution; (ii) to explore micro-scale fluid flow and diagenetic mechanisms that drive preferential calcite cement precipitation along DBs; (iii) to test the effect of both DBs prior to cement precipitation and that of structural diagenetic heterogeneities (DBs + nodules) on reservoir performance (e.g. Rotevatn et al., 2009; Antonellini et al., 2014a).

Cement precipitation modeling can be used (i) to evaluate how different initial host rock and DBs properties (e.g. porosity, permeability, grain surface area) affect cement precipitation; (ii) to explore the evolution in time of these properties during progressive calcite precipitation; and (iii) to constrain the kinetics of precipitation (e.g. De Yoreo and Vekilov, 2003; Lioliou et al., 2007; Ghezzehei, 2012; Noiriel et al., 2016).

APPENDICES

Appendix A

We provide here images and drawings that further detail the approaches, methods, and instrumentations used to investigate the mineralogical and petrographic properties of the Loiano Sandstone, the microstructure of compactive shear bands, and the petrophysical properties of host rock, nodules, and compactive shear bands.

A.1 – Manual point counting instrumentation

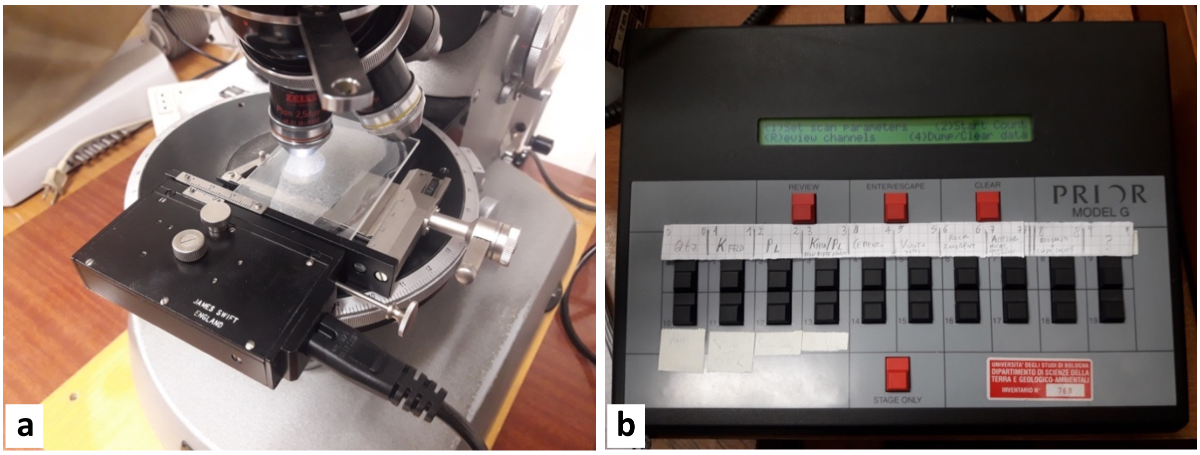

Fig. A.1 - Manual point counting was performed with **(a)** a SWIFT (England) electro-mechanical microscope slide stepper coupled via a cable with **(b)** an electronic 19-channels-point-counter.

A.2 – SEM-EDS- element distribution maps

A series of SE-SEM images (left) and SEM-EDS-element distribution maps (right) are shown below. Color coding: Silica (red; for Quartz), Aluminum (brown/green; for Feldspars), Ca (blue; for Calcite-cement), voids are indicated in black. The scale reported in the left image is the same also for the right one. The same is for the two samples: DB and Z.

Sample DB

Map1DB [Host Rock + CSB]

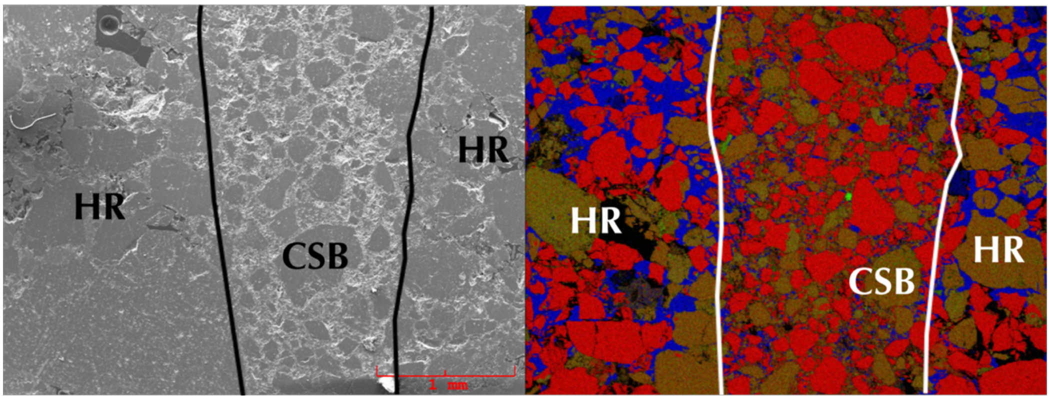

Map3HR [Host Rock]

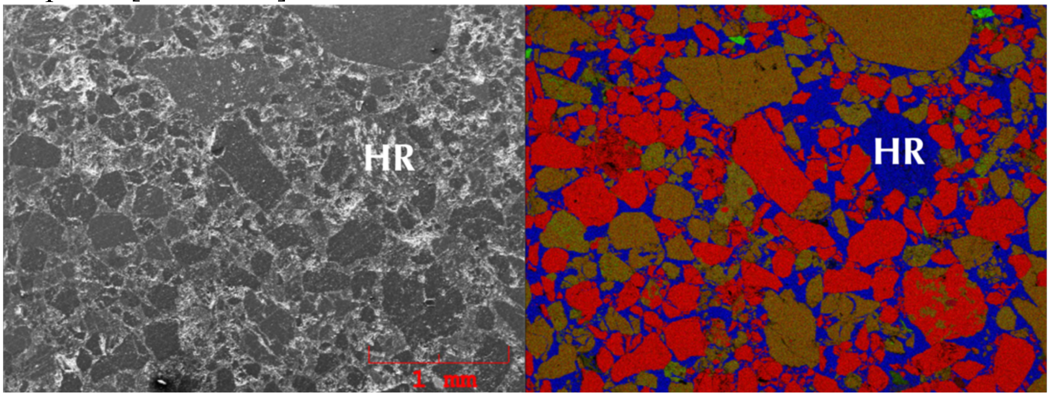

Map4HR [Host Rock]

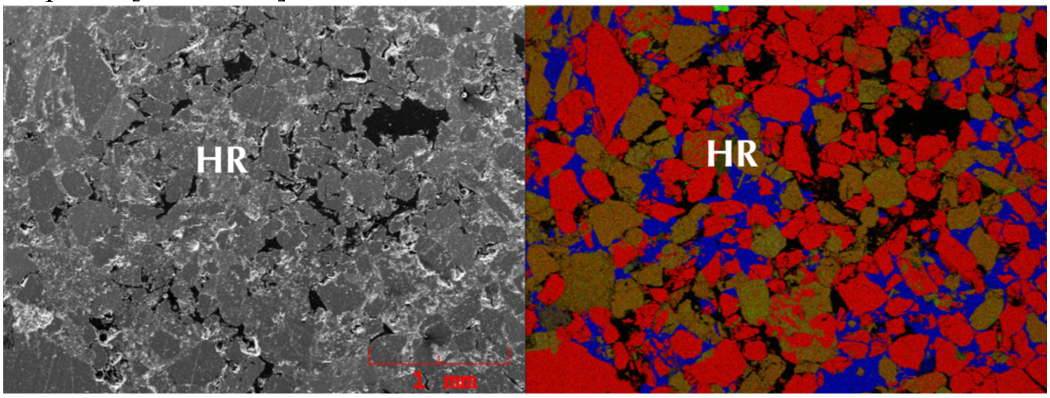

Map5DB [Host Rock + CSB]

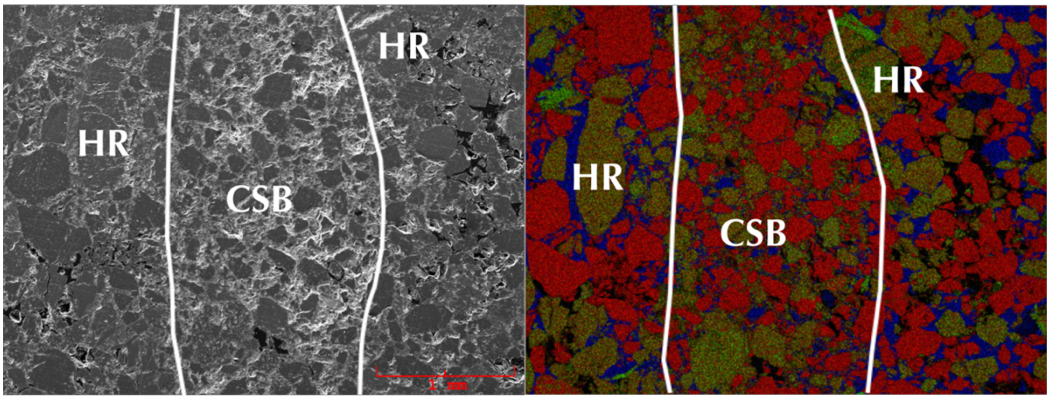

Sample Z

MapZ1 [Host Rock + CSB]

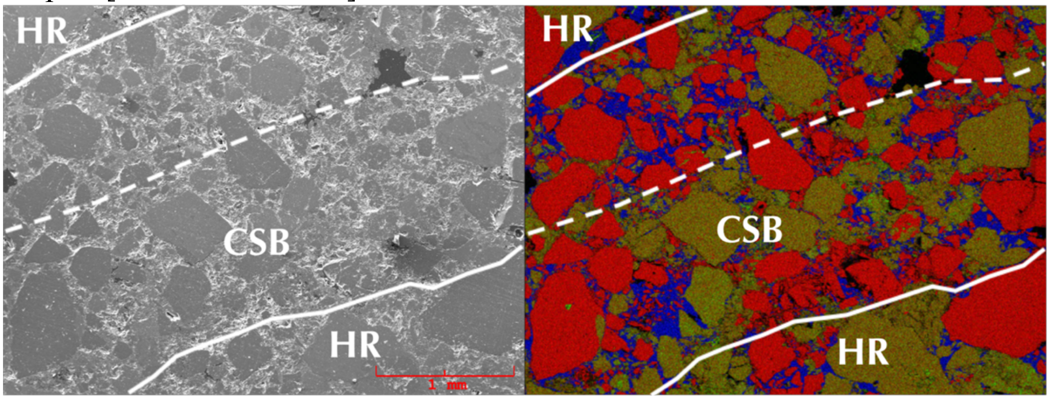

MapZ2 [Host Rock]

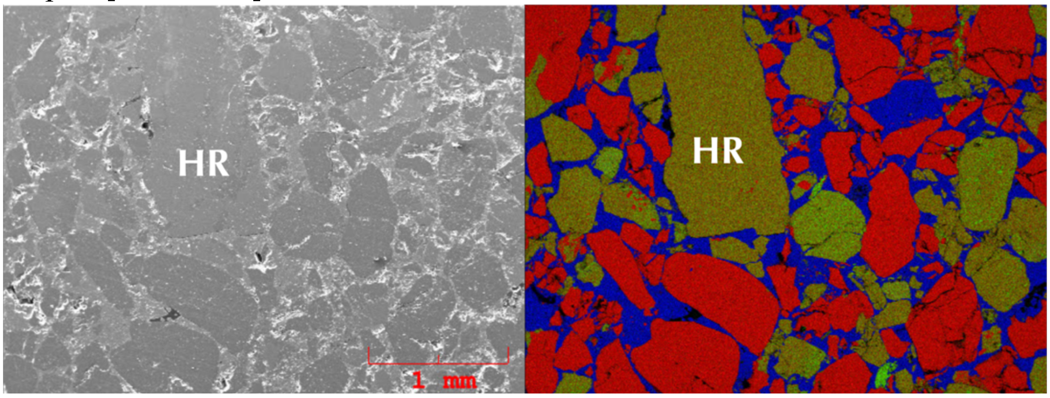

MapZ3 [Host Rock]

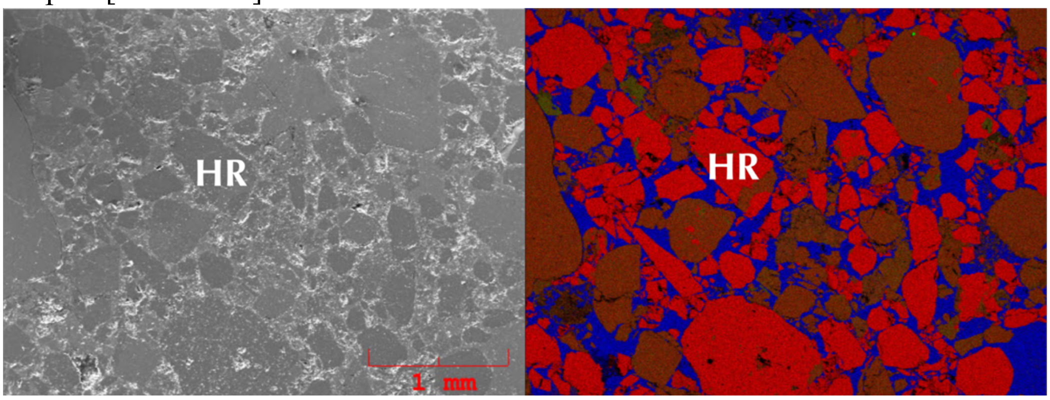

MapZ4 [Host Rock + CSB]

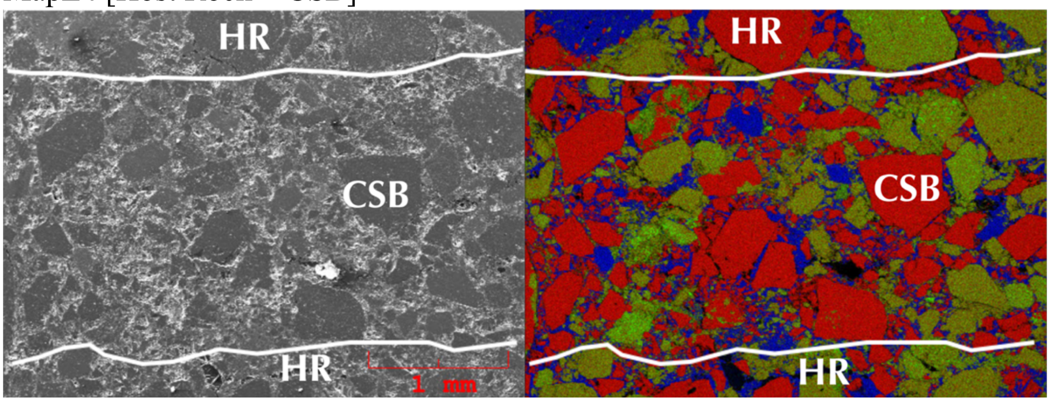

A.3 – Grain shape descriptors (*Ferreira and Rasband, 2012*)

The expression for *Roundness* is as follows:

$$Roundness = 4 \times \frac{[Particle\ Area]}{\pi \times [Particle\ Major\ axis]^2} \tag{A.1}$$

The *Aspect ratio* of the particle's fitted ellipse is expressed as follows:

$$Aspect\ ratio = \frac{[Particle\ Major\ Axis]}{[Particle\ Minor\ Axis]} \tag{A.2}$$

The *Circularity* is defined as follows:

$$Circularity = 4\pi \times \frac{[Particle\ Area]}{[Particle\ Perimeter]^2} \tag{A.3}$$

A.4 – X-ray powder diffraction analysis

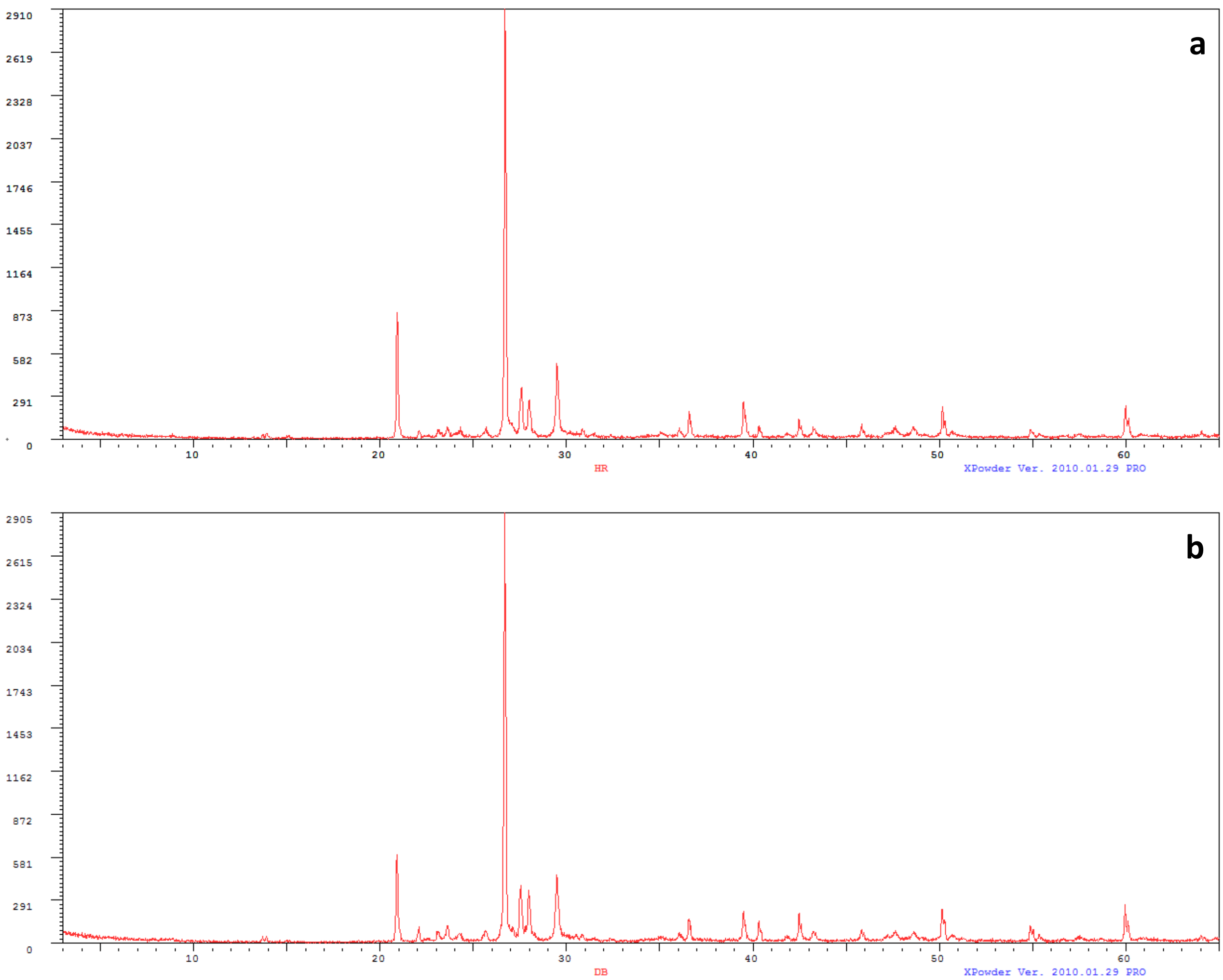

Fig. A.2 - X-ray diffractometers of **(a)** host rock and **(b)** compactive shear band samples.

A.5 – Falling head permeability test

The evaluation of permeability for the lithified HR and DB (i.e. nodules) through *falling head method* was initially thought and designed to compensate for the limits of the Kozeny-Carman relation where cement is present in the pore space (Section 2.3.3.4 in Chapter 2; Del Sole and Antonellini, 2019). Then, this limit has been overcome by measuring permeability directly *in situ* with a portable air-permeameter (Chapter 3; Del Sole et al., 2020). Therefore, only minor efforts have been dedicated to these tests. Please, consider that this tool is here presented only on an exploratory and conceptual level, and as a method for comparison with other measurements methods (Kozeny-Carman permeability, *in situ* air-permeability). More tests would be needed to validate the reliability, accuracy, and replicability of our measurements.

The *falling head test* was performed on two oriented core plugs drilled from two nodules samples collected in the field (Fig. A.3). One of the plugs was drilled in a sample (Nar) collected from a nodule without DBs, which is representative of the cemented host rock. The second plug was drilled from a sample (*CL3*) whereby the longer axis (z) is parallel to the plane of the DB. With this plug we have measured the permeability of the DB and the cement host rock that encase the DB. Some sort of *scaling* would be then needed to derive the permeability of the DB only.

The hydraulic conductivity K (m/s) has been calculated using the following relation (e.g. Dullien, 1991),

$$K = \frac{d_t^2 \times L}{d_c^2 \times \Delta t} \times \ ln \frac{h_0}{h_n} \tag{A.4}$$

where d_t and d_c are the tube and the sample diameter, respectively; L is the thickness of the rock sample, Δt is the time difference between the first measure and the *n* measure, h_0 and h_n are the initial (t_0) and final (t_n) height of the water level within the tube. First, the core plugs have been saturated under a specific head condition (saturated hydraulic conductivity - K_{sat}). Then, the pressure head declines as water passes through the core plug. The water head reference (equilibrium point) from which to calculate the water level heights ($h_0, h_1, \dots, h_n$) was fixed as the upper end of the permeability cell, because there the water level is constant (Fig. A.4). The experiment was performed at room temperature (20 °C) and distilled water was used to avoid any fluid-rock interaction (e.g. cement precipitation/dissolution) during water flow through the core plug. The hydraulic conductivity – K (m/s) was then converted into the permeability – k (m^2) as follow:

$$k = \frac{\mu}{\rho * g} \text{ K} \tag{A.5}$$

where ρ is the fluid density (998.21 Kg/m^3) and μ is the fluid dynamic viscosity (0.001 Pa*s), g is the acceleration due to gravity (~9.80 m/s^2). The estimated permeability values (Fig. A.5) are comparable with those obtained with the Kozeny-Carman approach (Chapter 2; Del Sole and Antonellini, 2019) and the air-permeameter (Chapter 3; Del Sole et al., 2020).

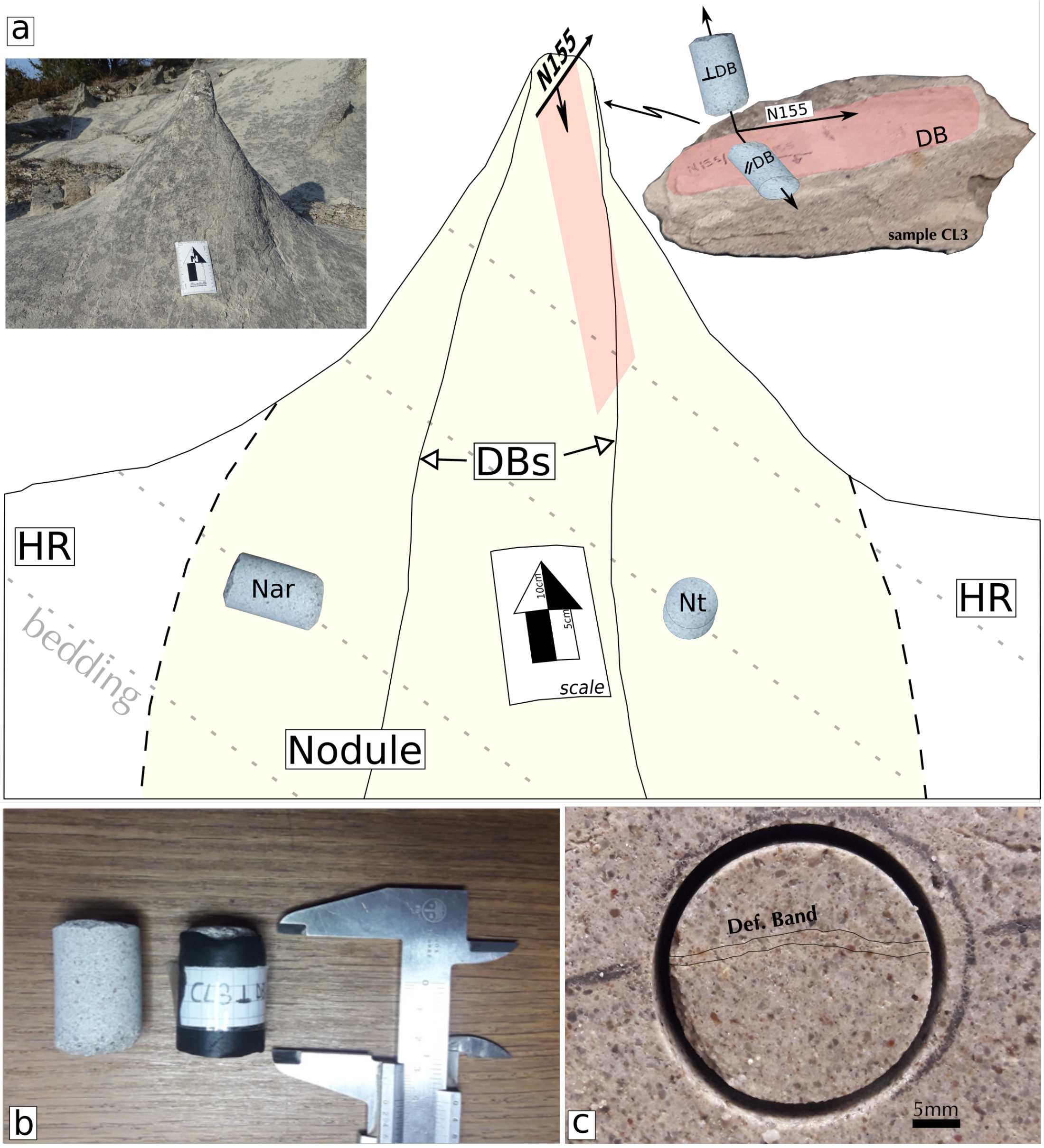

Figure A.3. (a) Sketch of the sampling method for falling head permeability test. Spatial relation between cores **(b, c)** and the local geologic framework (DB and bedding) is reported. "Nar" and "Nt" are representative of undeformed cemented host rock, while "⊥DB" and "//DB" are cores oriented normal **(b)** and parallel **(c)** to DB strike respectively, and they were drilled **(b, c)** form the sample CL3 **(a)**

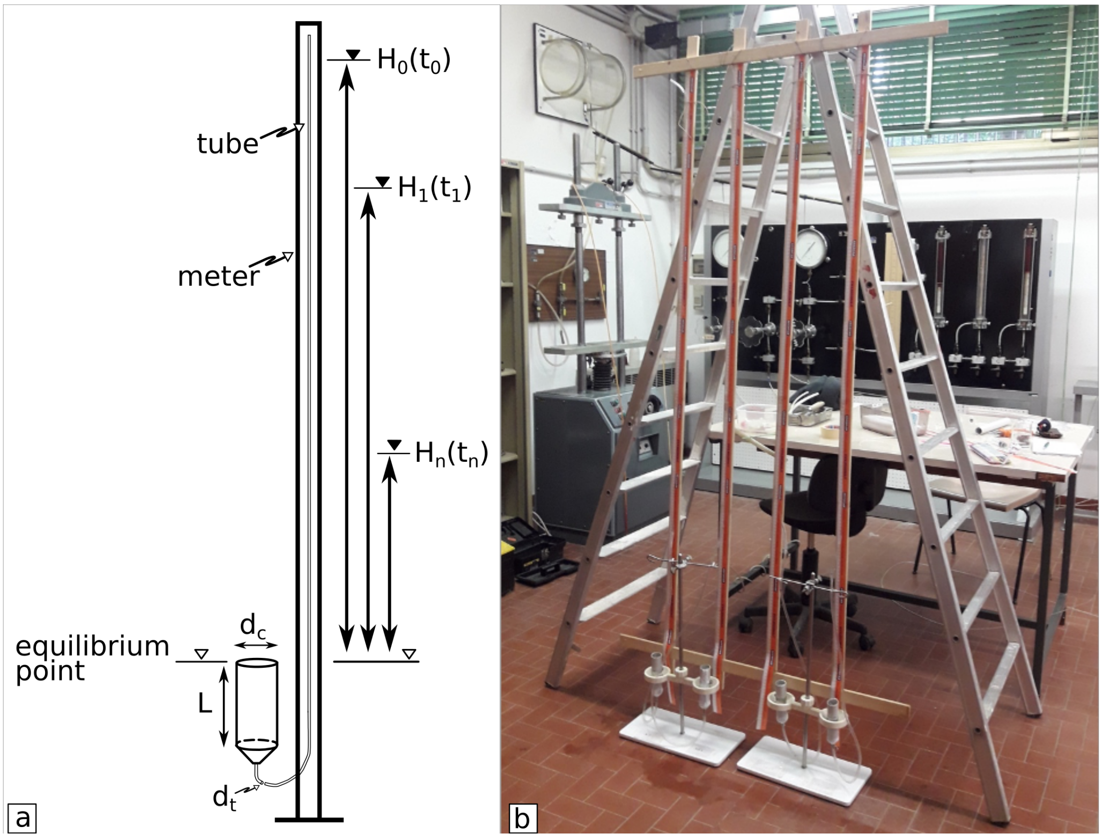

Figure A.4. (a, b) Falling head test experimental setup. The sketch **(a)** portrays the principal parameters used in the calculations. Plugs dimensions: length (L) and diameter (d_c) were measured with a caliper (Fig. A.3b). Each dimension for each plug has been measured 5 times, and the average values have been used. The diameter of the tube (d_t) is a known parameter. Height of water level has been monitored and measured during time.

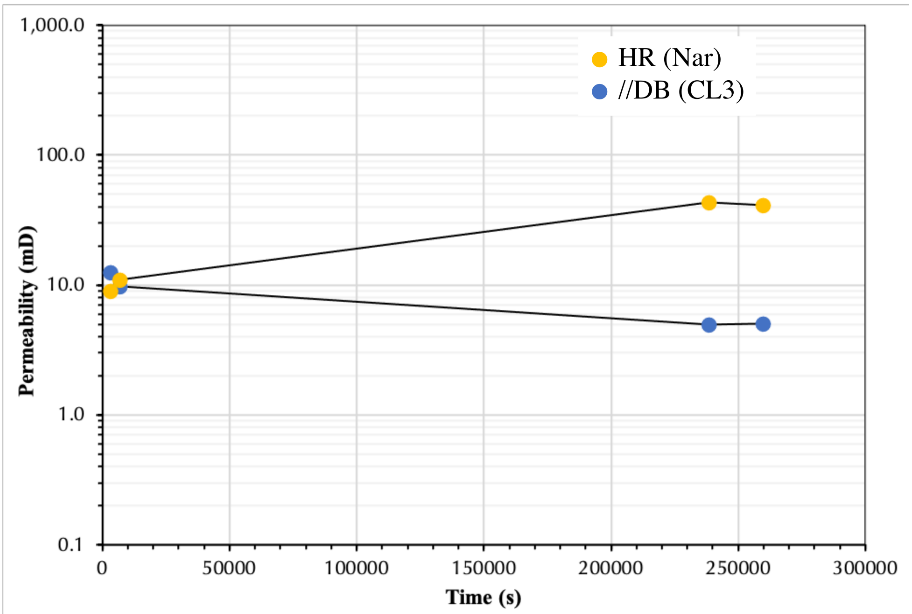

Figure A.5. Falling head test results showing 4 permeability values for each of the two core plugs. Yellow dots are referred to the cemented host rock core plug (Nar sample), whereas blue dots are referred to the core plug made of cemented host rock that encase a DB plane (see Fig. A.3) parallel to major axis of the plug, therefore to the direction of the flow. Consider that the permeability calculated for the sample CL3 refer to that of the host rock plus the DB.

Appendix B

B.1 – Dielectric permittivity, electromagnetic (EM) wave velocity, and GPR profiles resolution.

Table B.1 - EM material properties and GPR setup.

Symbol	Definition	Units	Value	Notes
ε_r (or k)	Relative permittivity (or dielectric constant)	F/m	16	ε_r was chosen considering the values suggested by the instrument and software manufacturers and from literature (e.g. Table 2.1 in Cassidy, 2009) for sandstones in similar saturation conditions. See text below for further specifics.
ε_0	Dielectric permittivity of vacuum	F/m	8.89×10^{-12}	Value from Cassidy, 2009
ε	Permittivity of the medium	F/m	1.42×10^{-10}	$\varepsilon = \varepsilon_r \times \varepsilon_0$
μ_0	Free-space magnetic permeability	H/m	1.25×10^{-6}	Value from Cassidy, 2009
μ	Magnetic permeability	H/m	1.25×10^{-6}	$\mu = \mu_0$ in this study. The assumption is valid if the amount of ferromagnetic material is minor (Cassidy, 2009)
v	EM wave velocity	m/s	7.50×10^{7}	$v = \sqrt{\frac{1}{\varepsilon * \mu}}$
f	Frequency	MHz	*channel 1:* 500 *channel 2:* 300	-
t	Time range	ns	*channel 1:* 50 *channel 2:* 100	-
λ	Wavelength	m	*channel 1:* 0.15 *channel 2:* 0.25	$\lambda = v/f$
z	depth	m	*Max depth* *channel 1:* 1.88 *channel 2:* 3.75	$z = v \times {}^{t}/_{2}$
Δz	Vertical resolution	m	see Table A1.2	$\Delta z \approx \lambda/4$; In this study, Δz is assumed to be independent of distance from the source. In practice, at larger distances, pulse dispersion and attenuation will affect vertical resolution.
Δl	Lateral resolution	m	See Table A1.2	$\Delta \mathrm{l} \approx \sqrt{z \times \lambda/2}$

Table B.2 – Vertical and lateral resolution

	Channel 1			*Channel 2*		
z (m)	$\Delta z\ (m)$	$\Delta l\ (m)$	*min. Vol. (m^3)	$\Delta z\ (m)$	$\Delta l\ (m)$	*min. Vol. (m^3)
0.1	0.0375	0.0866	0.0003	0.0625	0.1118	0.0008
0.5	0.0375	0.1936	0.0014	0.0625	0.2500	0.0039
1	0.0375	0.2739	0.0028	0.0625	0.3535	0.0078
1.5	0.0375	0.3354	0.0042	0.0625	0.4330	0.0117
1.88	0.0375	0.3755	0.0053	0.0625	0.4848	0.0147
2	-	-	-	0.0625	0.5000	0.0156
2.5	-	-	-	0.0625	0.5590	0.0195
3	-	-	-	0.0625	0.6124	0.0234
3.5	-	-	-	0.0625	0.6614	0.0273
3.75	-	-	-	0.0625	0.6846	0.0293

(*) Minimum detectable volume ($\approx \Delta z \times \Delta l^2$).

Appendix C

C.1 – Deformation bands characteristics

<u>Field and microstructural observations</u>

In Loiano, DBs occur along all the exposed sandstone sequence but display different patterns wherein the grain size, sorting or porosity differ. In poorly sorted and/or low porosity coarse-grained sandstone, deformation appears more localized, and the trace of the DBs tends to be straight and develop along a single strand (Fig. 4.5e). In well-sorted and/or high porosity fine-grained sandstone, instead, deformation is more distributed and the trace of the DBs splits into several wavy and anastomosing segments (Fig. 4.5e). A clay smear occurs where DBs cut through thin, dark-colored clay levels (Fig. 4.5e).

Grains in the DBs are fractured and angular, whereas the host rock consists of more rounded and nearly undisturbed medium- to coarse-grained sand grains (Figs. 4.9b-d and 4.10). However, some intragranular fractures are present at grain-to-grain contacts (Fig. 4.10a-b). These microfractures are common in the boundary zone of the DBs (Fig. 4.10i). Microfractures in larger grains are often filled by fine-grained clasts. Detrital calcite clasts and bioclasts are often fractured or affected by pressure solution at contact points with other framework grains (Fig. 4.10b-d). Elongated detrital mica grains (mostly biotite) are bent between other grains and they tend to be preferentially aligned parallel to the bedding (Fig. 4.10c). In some cases, where framework grains are in contact, they show straight-elongate planar to slightly undulated grain to grain contacts (Fig. 4.10b) that are also roughly parallel to the bedding. Locally, we observed partial dissolution of feldspar with formation of authigenic calcite (Fig. 4.10e). Minor calcite cement occurs also as syntaxial overgrowths around fossil shells and detrital carbonate grains (Fig. 4.10f).

Microstructural analysis in Bollène samples showed that a few intragranular fractures break framework grains at the contact-point among two or more grains (Fig. 4.11a, b). These microfractures become more frequent approaching the DB (Fig. 4.11g, h, j) and they are preferentially oriented with respect (ranging from ca. 30° to 50°) to the force chain around DB (Fig. 4.8c; see also *Section C.2*). Despite the grains being fractured in the host rock sectors close to the DB, and the reduction in grain size is limited.

Feldspar sheared grains within the bands commonly organize in highly comminuted lenses. These stripes are well recognizable both in natural-light where they appear as brown lenses (Fig. 4.11g, h) and in CL where they show a bright light blue color (Fig. 4.11h). The preferential alignment of elongated grains and stripes of detrital feldspar produce a foliated pattern that is sub-parallel to the DB.

<u>*Discussion*</u>

In both study areas, the key, common structural element are the DBs. In *Loiano*, geometric compatibility between DBs strike (Fig. 4.2d) and large-scale normal faults in this sector of the Northern Apennines (Fig. 4.2a, c; Antonellini and Mollema, 2002; Picotti et al., 2009) indicates that they might be coeval. For instance, our study outcrops are close to a high-angle normal fault striking nearly N-S and dipping W (Del Sole et al., 2020). However, the presence of multiple sets of DBs, with different trends (Fig. 4.2d), kinematics, and ambiguous crosscutting relationships (Fig. 4.3) suggests that the Loiano Sandstones recorded multiple tectonic phases (Cibin et al., 2001; Antonellini and Mollema, 2002) from the Eocene onwards. A clear sequence of deformation events has not yet been defined. In *Loiano*, the inhomogeneous mesoscale pattern and geometry of DBs along the exposed sandstone sequence is related to variations in host rock properties, such as sorting, porosity, and grain-size (Fig. 4.5e). Low porosity and/or poorly sorted coarse-grained host sandstones promote localized deformation commonly featured by a single straight-trace DB accommodating all displacement. High porosity and/or well-sorted fine-grained sandstones, instead, foster a more distributed deformation characterized by several anastomosing DB segments, where each segment accommodates part of the total displacement. Others host rock properties steering the overall DB characteristics are mineralogy, lithification, and grain roundness (Antonellini and Mollema, 2002; Fossen et al., 2017; Del Sole and Antonellini, 2019).

In the *Bollène quarry*, structural features include diachronous and differently oriented DBs and occur only in the unconsolidated Turonian sands (Fig. 4.2c). Crosscutting relationships between different sets point out that ESE-WNW reverse DBs set should be the oldest. Their kinematics, low-angle planar attitude and organization in conjugate and densely distributed networks, are typical features of DBs formed in a contractional regime (see *Section C.3*). This evidence and the compatibility between the strike of reverse DBs and larger scale E-W trending thrusts and folds in the area (Fig. 4.2a, b) would indicate that they formed contemporaneously and within a single stress field (Ballas et al., 2013, 2014; Soliva et al., 2013). In particular, these DBs are likely associated with the Paleocene to early Oligocene Pyrenean shortening (Sanchis and Séranne, 2000; Lacombe and Jolivet, 2005) (Fig. 4.2a). The NE-SW/ENE-WSW strike-slip bands displace the ENE-WSW reverse DBs, the NW-SE bands, and the NW-SE-trending carbonate cementation; hence, NE-SW/ENE-WSW strike-slip bands should be the younger set among the observed ones. They are most probably related to the (left-lateral) strike-slip reactivation of some major preexisting NE-SW faults in the region (e.g. Cevennes and Nîmes faults; Fig. 4.2a) during the Pyrenean event or in the Miocene to Quaternary age NNE-SSW Alpine contraction (Champion et al., 2000). The existence of a conjugate set of strike-slip bands with left-lateral (mostly ENE-WSW) and right-lateral (mostly NE-SW) kinematic (Fig. 4.6b; Fig. C.1) it places the maximum-compressive stress axis (σ_1) at ca. N50°E, thus, these DBs are consistent with the Miocene Alpine contraction (Fig. 4.2a). Two hypotheses can explain the occurrence of NW-SE/NNW-SSE DBs associated with cement nodules. They could have been formed as dextral strike-slip structures (Figs. 4.6b and 4.7f) during the NNE-SSW Pyrenean-Provencal shortening (Fig. 4.2a). Some of these faults could have been reactivated as normal faults during the NW-SE Oligocene-Early Miocene extension. A second possibility is related to the presence of a NE-SW map-scale normal fault, the Bollène Fault (Saillet, 2009), close to the outcrops discussed in this study (Fig. 4.2c). In this framework, the NW-SE set of normal DBs could be genetically linked to a stress perturbation (in a dilation jog or quadrant) around the large-scale Bollène fault, during its Oligocene activity.

Microstructural observations indicate that DBs in both *Loiano* and *Bollène,* developed by mechanical grain fracturing and compaction with minor contributions by shear-related grain disaggregation by rolling and grain boundary sliding. Zone of bands show a similar pattern but the degree of cataclasis is higher than single DBs. These structures can be classified as compactive shear bands (CSB) with cataclasis (Aydin et al., 2006; Fossen et al., 2017).

C.2 – Microfractures and force chains

Force chains are observed as trains of aligned grains that are in contact, and these chains are considered to represent load-bearing structures within the granular framework (Eichhubl et al., 2010; Ballas et al., 2013; Soliva et al., 2013). Microfractures and force chains are nearly parallel to each other. These structures formed approximately parallel to σ_1 (white arrows) at the time of band formation. Here, some examples of mapping of grain microfractures and force chains are reported (Fig. C.1).

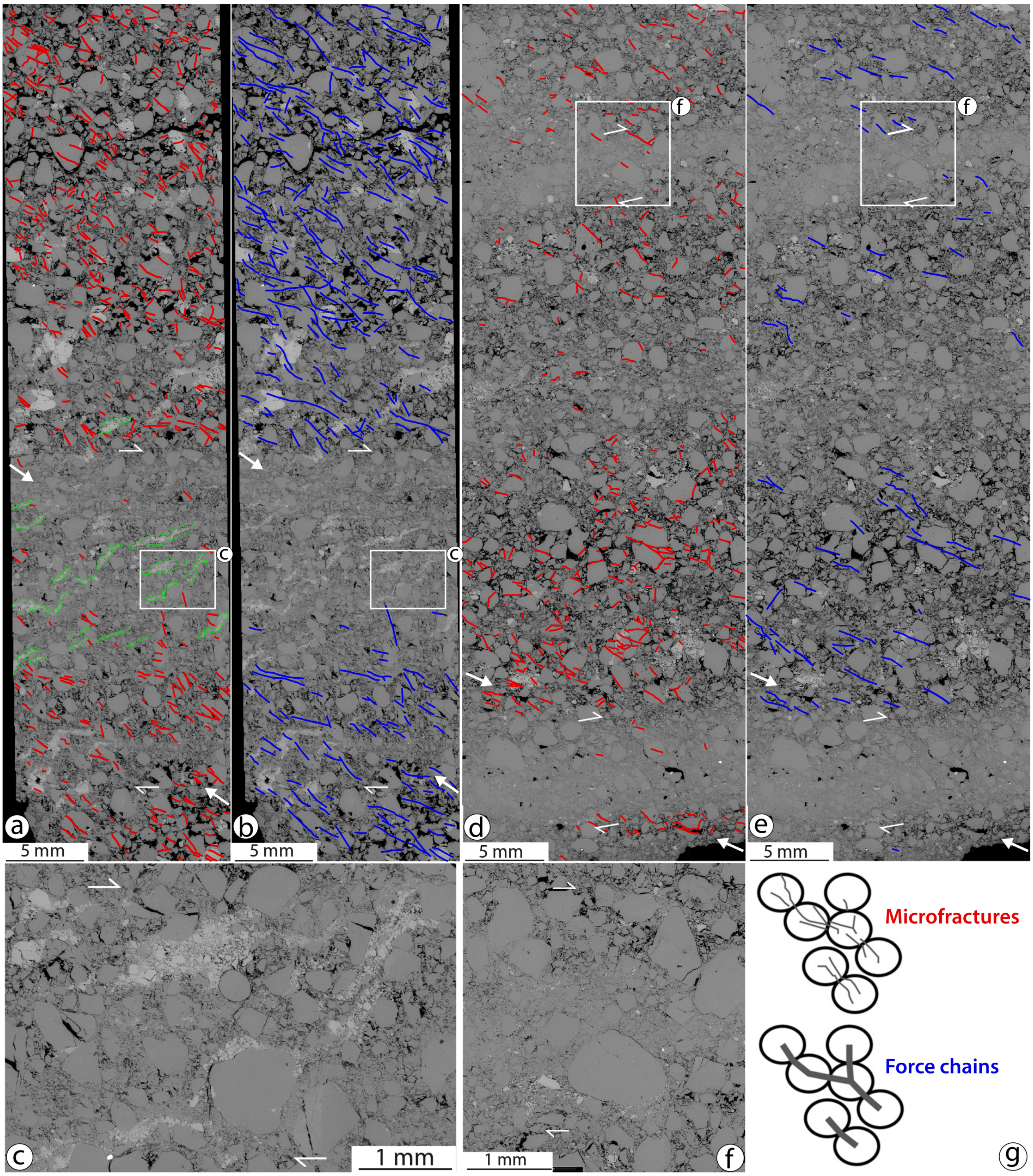

Figure C.1 – Backscattered electrons SEM photomicrographs showing the microstructures of the DBs in Bollène quarry. **(a-c)** are referred to NNW-SSE dextral strike-slip bands (sample location in Fig. 4.7f). **(d-f)** are referred to NE-SW/ENE-WSW left-lateral strike-slip bands. **(a-b, d-f)** Mapping of grain microfractures (at Hertzian contact) and force chains **(g)** performed on photographs of thin sections oriented perpendicular to the DBs. (a) Stripes of detrital feldspar (green lines) within the DB are approximately perpendicular to the microfractures. (g) Scheme showing the geometry of Hertzian microfractures and geometry of force chains as inferred from grain contact points. Modified from Soliva et al. (2013).

C.3 Reverse cataclastic shear bands

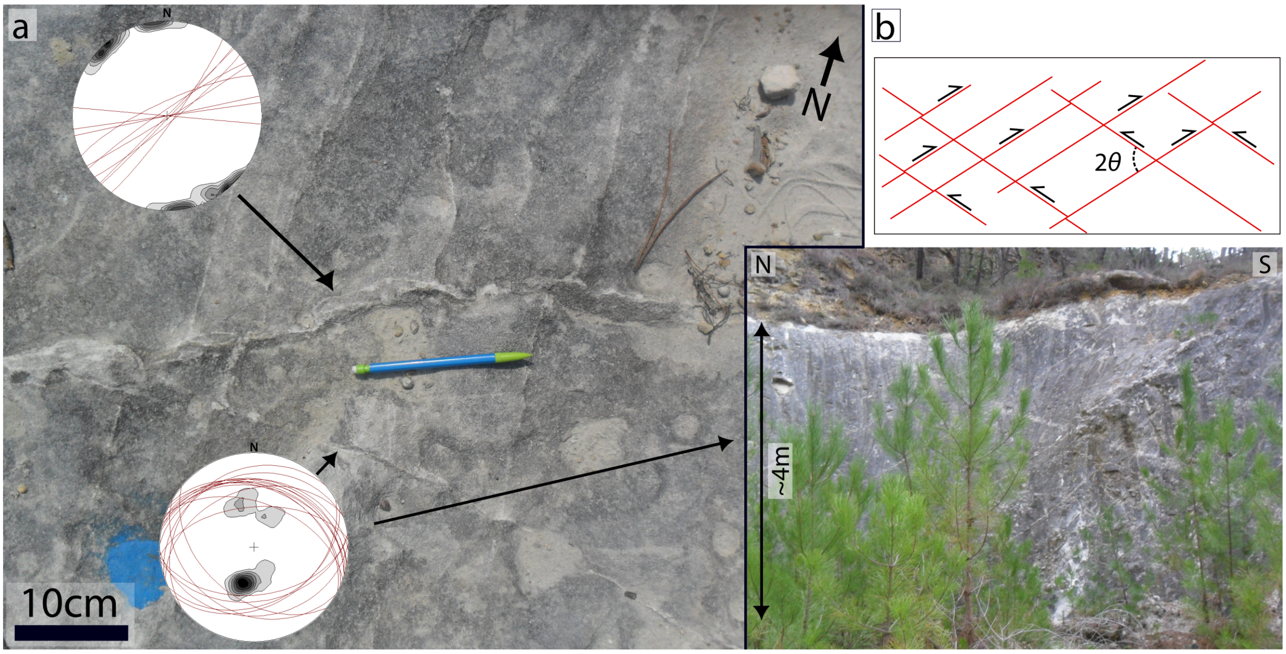

Fig. C.2 – (a) ESE-WSE reverse cataclastic shear bands (CSB) are crosscut by the NE-SW/ENE-WSW strike-slip bands. **(b)** Evenly spaced low-angle reverse CSB arranged in conjugate systems and with dihedral angle (2θ) around 69°. Figure in **(a)** and **(b)** are in plan-view and side-view, respectively. The position of **(d)** is indicated in Fig. 4.6b.

C.4 – Calcrete

In the Bollène quarry, a massive, hardened layer is exposed stratigraphically above the Turonian Sandstones, at roughly 3 meters above the quarry floor (Fig. C.3a). This layer is characterized by a tabular structure and its lower boundary is irregular, as well as its thickness (Fig. C.3a, b). The features of this weathered crust and the invariably negative $\delta^{13}C$ and $\delta^{18}O$ values of its cement (Fig. 4.12b), suggest that it is a "massive" calcrete (e.g. Alonso-Zarza, 2003). The calcrete specimen was collected along this level (Fig. C.3c, d), and the cement was sampled to compare its stable isotopes composition with that of cement in nodules (Fig. 4.12b).

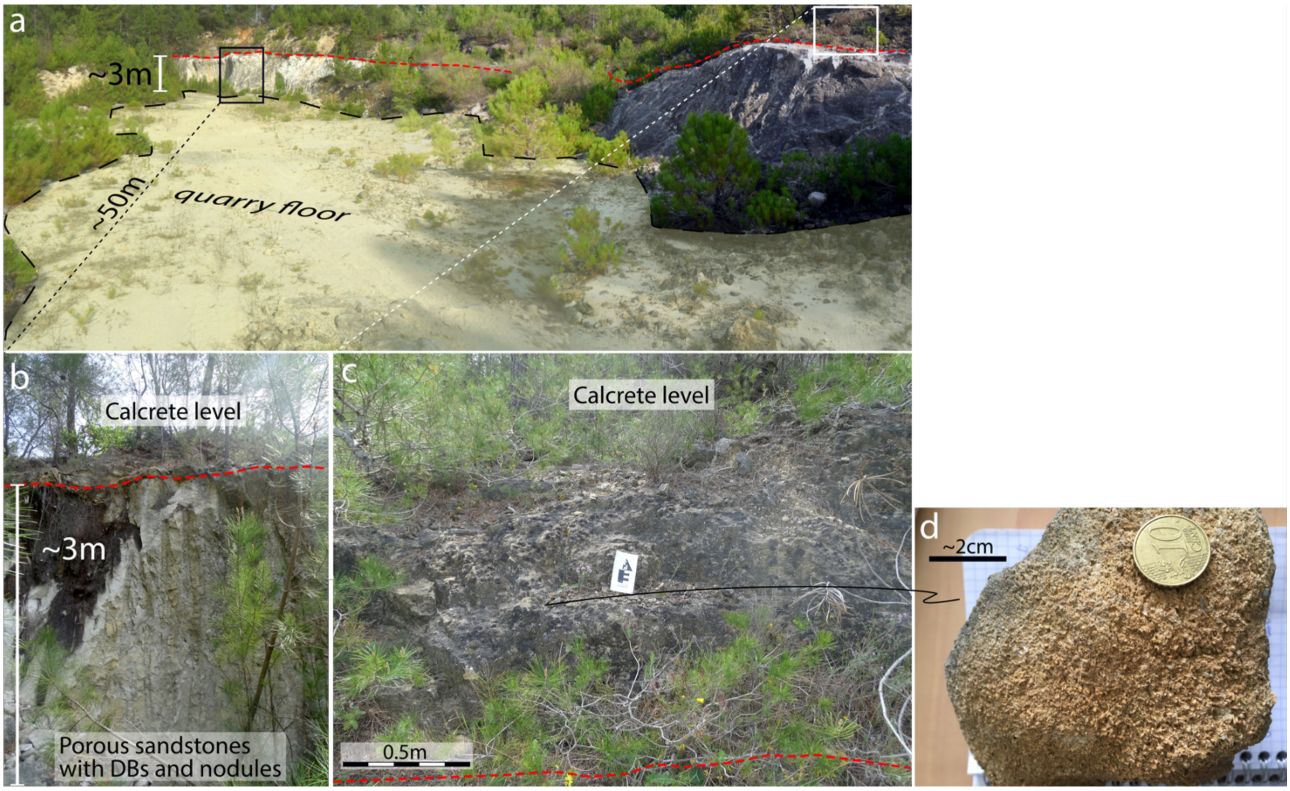

Fig. C.3 – (a) Overview photograph that show the local stratigraphic framework of the Bollène quarry. The whitish Turonian sands, with DBs and nodules, are overlain by a reddish-brown massive calcrete level **(b, c)**. **(d)** Calcrete hand specimen.

C.5 – Petrophysical data

Table C.1 Petrophysical data for the Loiano field site

(*) Kozeny-Carman (KC) permeability

Parameters			**Unit**
	HR	**DB**	
Porosity	2.24E-01	4.50E-02	-
Intrinsic permeability	2.94E+00	5.00E-03	Darcy
Hydraulic conductivity	9.60E+00	8.11E-02	K/n

(**) *In situ* air-permeability

	Feature	**Data N**	**Median**	**Mean**	**Std. Dev.**	**Min**	**Max**
Permeability (mD)	HR	174	1053.46	2963.35	5409.98	0.29	39729.44
	DB	56	17.16	38.65	80.65	0.04	522.41
	NOD	118	5.76	31.70	56.49	0.03	339.65

HR — host rock; NOD — nodule.
(*) Del Sole and Antonellini, (2019); (**) Del Sole et al., (2020a).

Table C.2 Petrophysical data for the Bollène field site (***)

Parameters				Unit
	HR	DB	DB	
Porosity (%)	22.05	10	17.46	%
Permeability (mD)	50	0.02	1.9	mD
R_{50} — Median pore access radius	9.9	0.	1	µm
R_a — Threshold pore access radius	23	2.6	7.6	µm

(***) Ballas (2013); Ballas et al., (2014).

C.6 – Formation waters ($\delta^{18}O_{fluid}$) composition

Oxygen isotope composition in minerals ($\delta^{18}O_{carb}$) are not a direct measurement of the $\delta^{18}O$ composition of the formation waters ($\delta^{18}O_{fluid}$) at the time of cement precipitation, since the oxygen isotopic fractionation between water and calcite depends on temperature (e.g. Friedman & O'Neil, 1977). To this end, we adopted the fractionation formula of Friedman and O'Neil (1977) for water-calcite system, assuming 10 °C as the temperature of superficial fluids, 200-500 m as the depth range, and a geothermal gradient of 20 °C/km for Loiano. We did the same for Bollène, assuming 400 m as the maximum burial depth (Ballas et al., 2013; Soliva et al., 2013). A temperature range of 14-20 °C for Loiano and 18 °C for Bollène has been estimated, respectively. The depth range for nodule formation in Loiano has been assumed considering that if the nodules are due to meteoric water infiltration, then the flow lines would have travelled, at most, a maximum distance from the ridges that delimit the valleys until the contact with the Liguride units (regional seal; e.g. *Monghidoro Fm.*), thus, at a maximum depth of 400-500 m. Results of the back-calculation of the $\delta^{18}O$ composition of the cementing fluids are reported in Tables C.3 and C.4 for Loiano and Bollène samples, respectively.

Table C.3 Isotopic composition of cementing fluids at Loiano

Feature	**$\delta^{18}O_{fluid}$ (‰ V-SMOW)** at 14 °C	
	Min; Max	Mean
DBs-parallel nodules	-5.42; -2.31	-3.73
Bedding-parallel nodules	-3.03; -2.26	-2.75
Feature	**$\delta^{18}O_{fluid}$ (‰ V-SMOW)** at 20 °C	
	Min; Max	Mean
DBs-parallel nodules	-4.01; -0.90	-2.33
Bedding-parallel nodules	-1.62; -0.85	-1.34

Table C.4 Isotopic composition of cementing fluids at Bollène

Feature	**$\delta^{18}O_{fluid}$ (‰ V-SMOW)**	
	Min; Max	Mean

DBs-parallel nodules	-7.85; -5.98	-7.19
Calcrete	-6.70; -6.44	-6.62

C.7 Stable isotope analysis sampling transect

In some particular case, the sampling was performed along a transect with sample spacing between 1 and 1.5 cm along the transect trace. This approach was applied to observe any possible stable isotopes variations between nodules rims and its core, between the nodule and the adjacent HR, and between nodule cement inside and outside the DB in DBs-parallel nodules (Figs. C.4b-e and C.5b-d).

Loiano – Data from sampling transects across nodules show no apparent and systematic variations in the isotopic composition along the nodule, yet carbon signature shows greater variations along a transect when compared with the oxygen trend on the same transect (Fig. C.4b-e). Graph in figure C.4b report isotopic values sampled from a DB-parallel nodule and we observe the most depleted $\delta^{18}O$ values in the DB-trace, while the outer edges have uniform and heavier isotopic signatures, symmetrically with respect to the DB-trace. In this case the $\delta^{13}C$ show a roughly constant isotopic composition. In others DB-parallel nodules there is no apparent variation in values along the DB-trace, whereas some minor variations are observed between the sectors of the nodule which are on the opposite sides of the DB (Fig. C.4c-d). For example, in figure C.4d we observe that the most depleted $\delta^{13}C$ value is in the high-porosity (low cement content) sector on the right side of the nodule with respect to the DB, that is the nodule edge. Bedding parallel nodules show the most depleted $\delta^{13}C$ isotopic signature in the overall data set, but with relatively uniform isotopic compositions, at least along the bedding trace (Fig. C.4e).

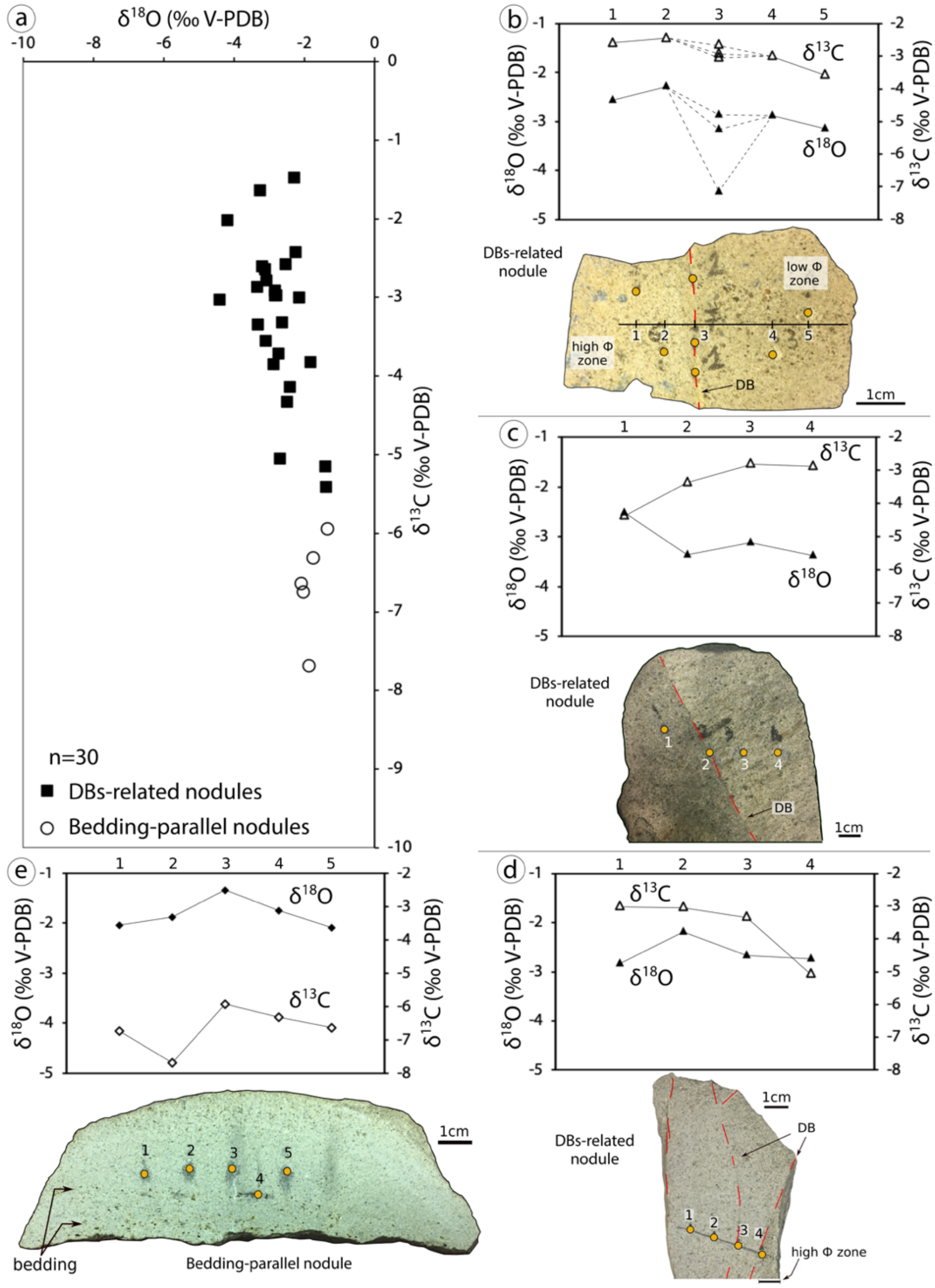

Figure C.4 – Stable isotopes analysis results. Cumulative isotopic data characterizing the DBs-related nodules (black full-dots) and bedding-parallel nodules (empty-dots) inside the Loiano Sandstones. (b-e) Sampling methods and isotopic trends on nodules hand specimen representative of (b-d) DBs-related nodules and (e) bedding-parallel nodules.

<u>**Bollène**</u>. <u>Data from sampling transects across nodules show no apparent correlation between either carbon or oxygen-isotope ratio and position within the nodule</u>, yet carbon signature show greater variations along a transect when compared with the oxygen trend on the same transect (Fig. C.5b-d). Graph in figure C.5b report isotopic values sampled from a spherical nodule associated to DBs and we observe more uniform $\delta^{13}C$ values in the nodule core, while the outer edges have both heavier (sampling point 1) and depleted (sampling point 4) carbon isotopic signature with respect to

the core. In this case $\delta^{18}O$ isotopic signature show roughly uniform composition. Graph in figure C.5c report isotopic values of a tabular nodule, that have the most depleted carbon isotopic values in the nodule edges and the heaviest one in the core with a symmetric pattern, and the $\delta^{18}O$ values are relatively constant. The sample collected in the adjacent HR (sampling point 1) gave no results (below detection level). Figure C.5d show isotopic composition of nodule crosscut by a NE-SW band, and both $\delta^{13}C$ and $\delta^{18}O$ values are heavier along the DB-trace, while the sectors of the nodule adjacent to the DB have more depleted values (Fig. C.5d).

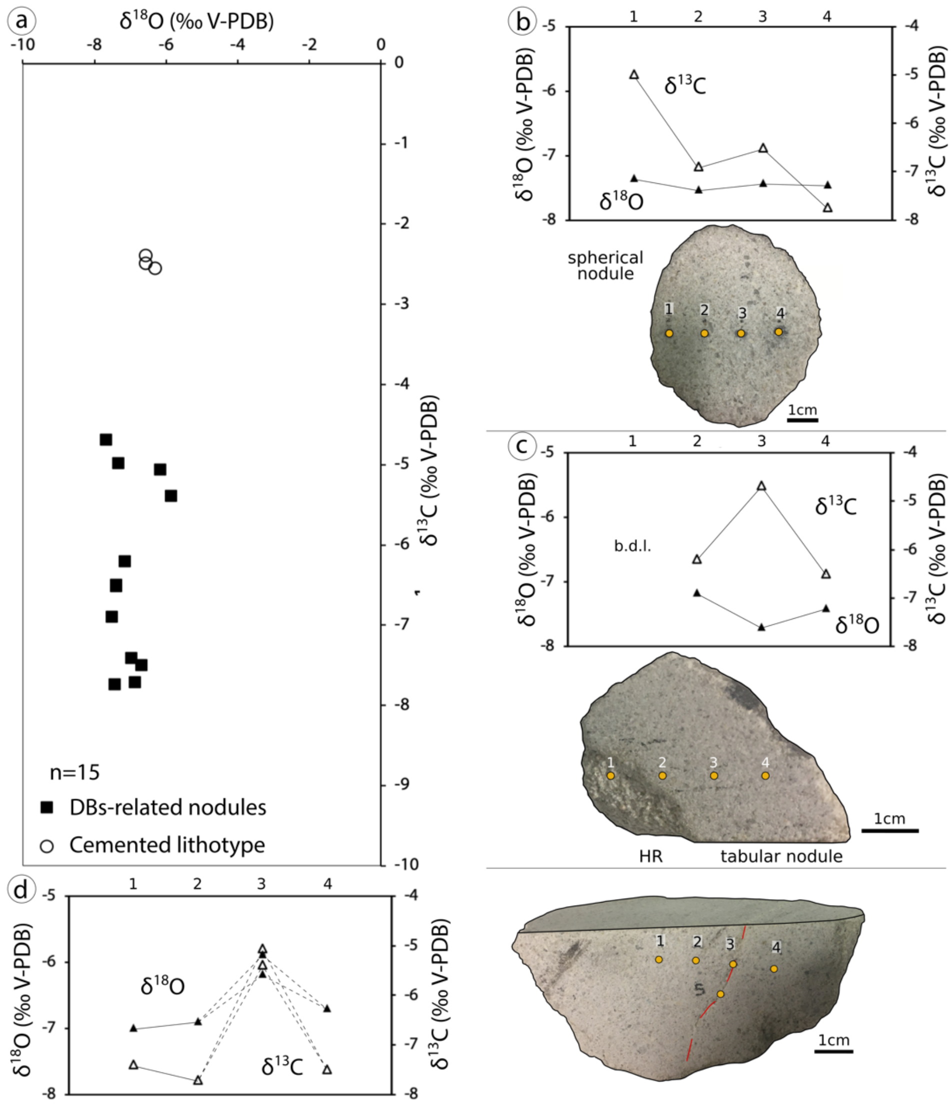

Fig. C.5 – Cumulative isotopic data characterizing the DBs-related nodules (black full-dots) and cement sampled in the cemented lithotype (empty-dots) above the Turonian Sandstones in the Bollène quarry (see Section C.4 for further details). (b-d) Sampling methods and isotopic trends on nodules hand specimen representative of (b-d) DBs-related nodules. b.d.l. – below detection level.

C.8 Post-DB and post-nodule opening-mode fractures

In Loiano, other deformation structures observed in the field are fractures and cement-filled fractures, i.e. veins (Figs. C.6, 3.4d, e, and 4.5a, b). They are not associated to shear offsets or splay structures; hence, they were classified as mode-I. Field evidence indicates that these fractures develop exclusively within the calcite nodules (Fig. C.6 a-e and 3.4d, e) and, in some case, they are observed along planes of DB (Fig. C.6f), often when associated with nodules. These fractures do not propagate into the surrounding host sandstone, and they post-date DBs and calcite nodules as indicated by cross-cutting relationships (Figs. C.6 and 3.4d, e).

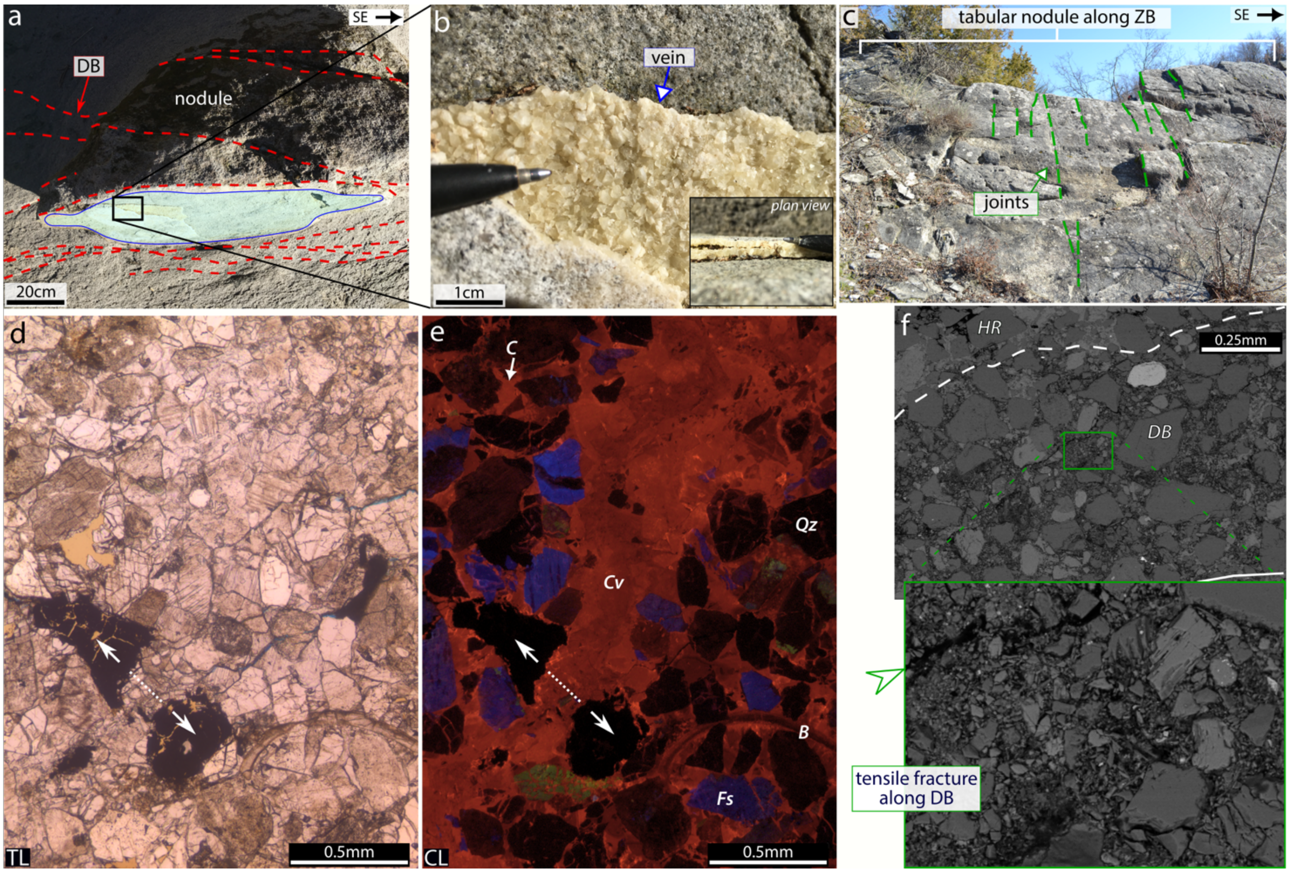

Figure C.6 Opening-mode fractures (i.e. joints) develop **(a-e)** within the cemented sandstone (nodules) and (f) along DBs. **(a, b)** DB-parallel vein in nodule. **(a-c)** Joints and cement-filled joints (veins) are confined within nodules and do not propagate into the host sandstone. **(d-e)** Natural- and CL-light photomicrographs showing the microstructure and cement textures of a vein (Cv) that cross-cut the sandstone framework grains and the nodule cement (C). Vein-filling cement is constituted by a mosaic of blocky crystals with dull-orange CL color. **(f)** Backscattered electron SEM image showing a tensile fracture that develop within a DB associate with a nodule. Qz—quartz; Fs—feldspar; B—bioclast; Cv—dull-orange CL calcite cement filling fracture; C—bright-orange CL intergranular calcite cement.

Nodules and nodules with DBs are the most indurated part of the rock volume (Chapter 3; Del Sole and Antonellini, 2019; Del Sole et al., 2020). The presence of pore-filling cement would increase the strength of the sandstone, preventing rotation and sliding of particles, and increase rock cohesion (Bernabé et al., 1992) and grain contact area, thus yielding a uniform contact stress distribution and higher stiffness (Dvorkin et al., 1991). In the DB, the combination of cataclasis and compaction increases the friction and the cohesion by clast roughening, sorting worsening, and enhancement of the packing degree (Chapter 2; Aydin and Johnson, 1978; Underhill and Woodcock, 1987; Mair et al., 2002; Kaproth et al., 2010; Del Sole and Antonellini, 2019).

The transition in the deformation style, from formation of DBs to opening-mode brittle fractures, could reflect a diagenetic (cement-related; Flodin et al., 2003; Johansen et al., 2005) and a physical (DB related; Tindall and Eckert, 2015; Del Sole and Antonellini, 2019; Pizzati et al., 2020) stiffening of the host sandstone. This process can explain why opening-mode fractures and veins do not propagate outside the cement nodule, into the "soft" and poorly consolidated host rock.

Tensile fractures overprinting DB cause the latter to behave as conduits that may focus fluid flow and localize cementation. The association between overprinted or reactivated (e.g. jointed) DBs and cementation (e.g. vein overprinting DBs) have been described by several authors (Johansen et al., 2005; Eichhubl et al., 2009; Skurtveit et al., 2015; Hodson et al., 2016;).

The interplay among deformation, pore fluids, and diagenesis control the structural diagenesis evolution of a certain rock volume (Fig. C.7). First, the low-permeability DBs buffer the fluid flow, focus cementation, and control the distribution of calcite nodules (Fig. C.7a). Because of the stiffening effect promoted by the cement and DB's material, the assemblage "DBs – nodule" control fracturing characteristics and distribution during subsequent deformation. The assemblage localizes joints that do not propagate into the "soft" host sandstone (Fig. C.7b). Joints actually represent fluid flow conduits and may lead to new diagenesis (veins; Fig. C6)

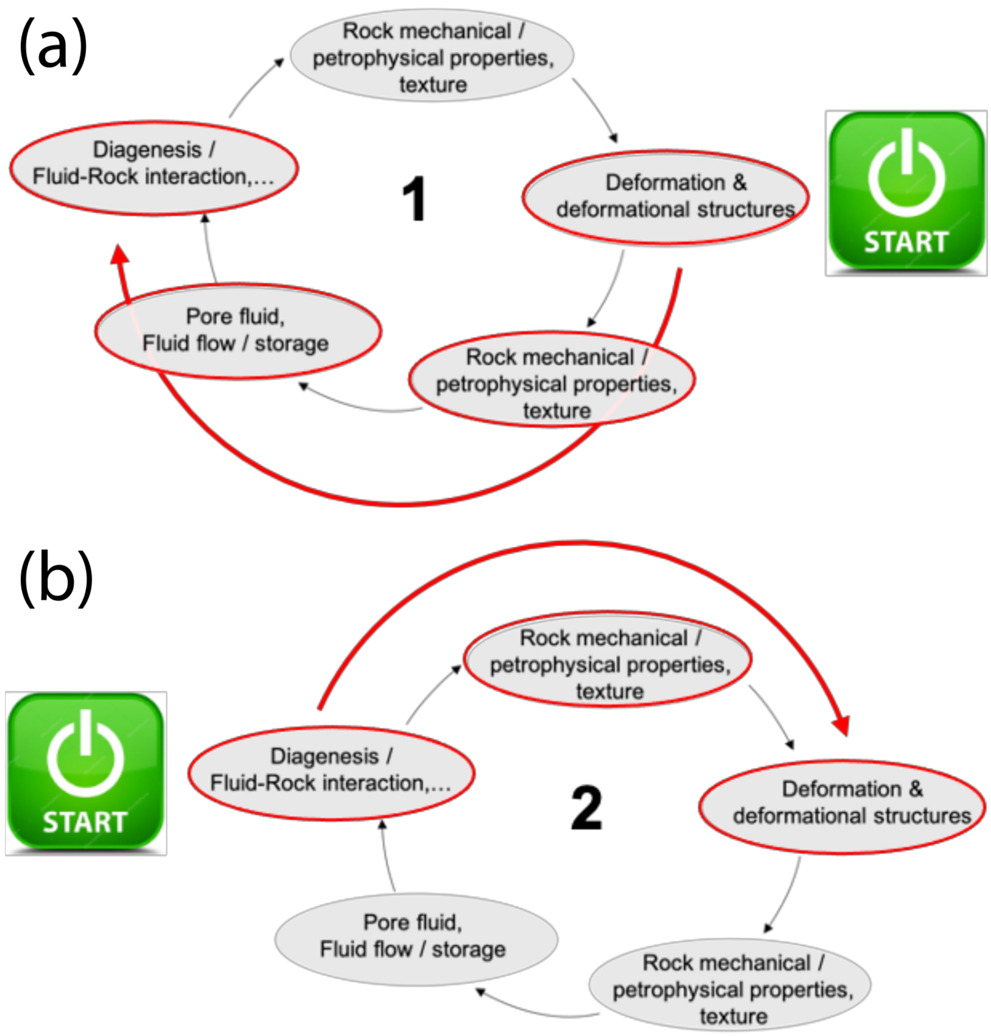

Figure C.7 Conceptual flow diagram showing the interactions between the three main topics of deformation, fluid flow, and diagenesis (see Fig. 1.1) adapted for the case of Loiano. See the text for more detail.

Appendix D

Table D.1 - ***List of Symbols and nomenclature used in the paper***

Symbol	Definition	Units	Notes
α	aspect ratio (α = length long axis / length short axis	no	Defines shape of 2D ellipse not enough for 3D
a	Length of one of the axis of an ellipse		In the case of oblate ellipsoids, $a < b = c$ and in the case of prolate ellipsoids $a > b = c$
b	Length of one of the axis of an ellipse		$b = c$ in this study
c	Length of one of the axis of an ellipse		
$\boldsymbol{C}^0$	is the stiffness tensor of the matrix		
$\boldsymbol{\varepsilon}^{\mathbf{0}}$	the remote strain		
$\boldsymbol{\varepsilon}^{**}$	the eigenstrain		
$\boldsymbol{\varepsilon}(\boldsymbol{x})$	Strain as a function of position **x**		
E	Young's modulus	GPa	see Table 5.1
$\boldsymbol{G}(\boldsymbol{x})$	a 4th-order tensor that is a function of the ellipsoid geometry, Poisson's ratio		

	of the matrix, and the coordinate position		
$\boldsymbol{I}$	the 4th-order identity tensor		
K_{IC}	Stress intensity factor - a good proxy of the maximum fracture toughness at the onset of fracture propagation		
l	the initial half-length of the crack (or flaw)		
P	the pore pressure inside the crack		
P_x	Label for a geometric description of the modeled stress field: P_x a balloon-shaped region (blue color) around the x-axis		
P_z	Label for a geometric description of the modeled stress field: P_z a balloon-shaped region (blue color) around the *z-axis*.		
$\bar{\sigma}$	the mean stress	Pa	For uncompressible materials σ is equivalent to the octahedral normal stress

σ^r	the stress normal to the crack in the fracture toughness approach		
$(\sigma^r - P)_Y$	effective stress normal to the crack during yielding		
σ_{ii}	the three normal stress components in the three cartesian directions. (σ_{xx} σ_{yy} σ_{zz})		
σ_x^r	Applied remote stress (in models) in x direction		
σ_y^r	Applied remote stress (in models) in y direction		
σ_z^r	Applied remote stress (in models) in z direction		
σ_x^i	The stresses within the inclusion (superscript I is for 'inside inclusion' σ_x^i, σ_y^i, and σ_z^i are also aligned along the x, y, and z axes respectively		
σ_y^i,	The stresses within the inclusion σ_x^i, σ_y^i, and σ_z^i are also aligned along the x, y, and z axes respectively		

σ_z^i	The stresses within the inclusion σ_x^i, σ_y^i, and σ_z^i are also aligned along the x, y, and z axes respectively		
σ_{max}^r	the largest compressive (most negative) remote stress		
σ_{min}^r	the least compressive remote stress		
σ_{min}^i	the least compressive (most tensile) stress within the inclusion.		
S	the 4-th order Eshelby tensor. ***S*** is a function of the ellipsoid dimensions and the Poisson ratio of the matrix		
T_{yz}	Label for a geometric description of the modeled stress field: T_{yz} a toroidal region (yellow color) on the *yz* plane		
T_{xy}	Label for a geometric description of the modeled stress field: T_{xy} a toroidal		

	region (yellow color) on the *xy* plane		
ν	Poisson ratio	no	see Table 5.1

D.2 – Stresses in the host rock surrounding the inclusion under hydrostatic boundary conditions.

In the case of a remote hydrostatic stress, for the material properties of inclusion and matrix reported in Table 5.1, and for *oblate* ellipsoids, the mean stress is tensile around the polar region (P_x) of the ellipsoid and compressive around the equatorial region (T_{yz}) (Fig. D.1a). These regions disappear as *a*/*b* ratio of the ellipsoid increases approaching 1 (Fig. D.1b). Under the same hydrostatic remote stress and for *prolate* ellipsoids, the mean stress is tensile around the equatorial area (T_{yz}) and compressive around the polar region (P_x) (Fig. D.1c).

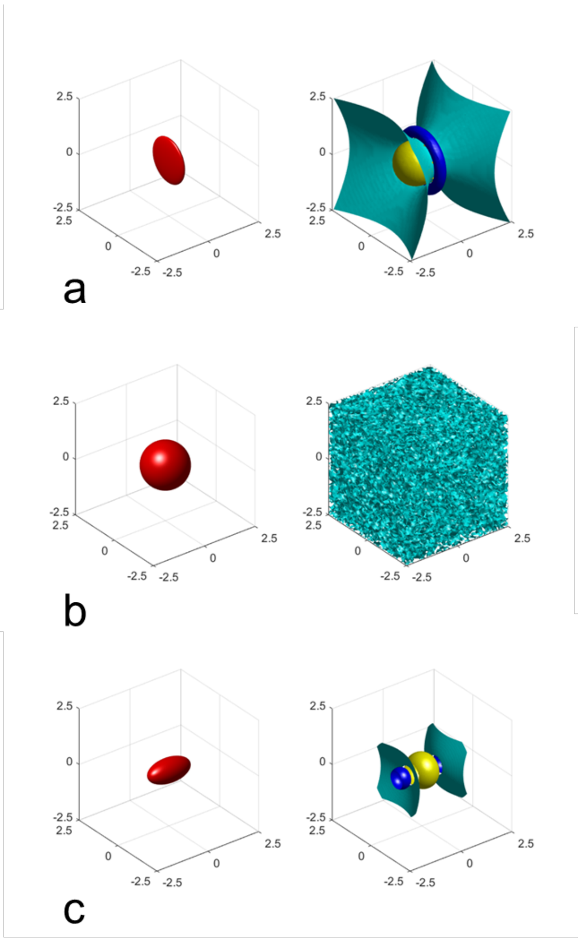

Fig. D.1 – Modelling results of the mean stress outside the chert inclusion in hydrostatic conditions and for different ellipsoid (inclusion) shapes: (a) oblate, (b) spherical, and (c) prolate. The mean stress is represented by isosurfaces: Blue is for $\sigma/|\sigma_{max}{}^r|$ = -0.025 (compression); cyan is for $\sigma/|\sigma_{max}{}^r|$ = 0; yellow is for $\sigma/|\sigma_{max}{}^r|$ = 0.025 (tension). (a) *a*/*b*=0.2; *a*=0.2 *b*=1.0 *c*=1.0. (b) *a*/*b*=1; *a*=1 *b*=1 *c*=1. (c) *a*/*b*=2; *a*=1 *b*=0.5 *c*=0.5.

BIBLIOGRAPHY

References

Acharyya, S.S., Mondal, T.K., 2019. Stress enhanced tensile fractures in elliptical clast in conglomerate. Journal of Structural Geology 122, 81–88. https://doi.org/10.1016/j.jsg.2019.02.001

Adams, A. and Diamond, L. W.: Early diagenesis driven by widespread meteoric infiltration of a Central European carbonate ramp: A reinterpretation of the Upper Muschelkalk, Sediment. Geol., 362, 37-52, https://doi.org/10.1016/j.sedgeo.2017.10.002, 2017.

Agosta, F., Alessandroni, M., Antonellini, M., Tondi, E., Giorgioni, M., 2010. From fractures to flow: A field-based quantitative analysis of an outcropping carbonate reservoir. Tectonophysics 490, 197–213, https://doi.org/10.1016/j.tecto.2010.05.005.

Al-Harthi, A. A., 1998. Effect of planar structures on the anisotropy of Ranyah sandstone, Saudi Arabia. *Engineering geology*, *50*(1-2), 49-57.

Alberti, M., Decandia F.A., Tavarnelli, E.,1998. Kinematic evolution of the outer zones of the northern Apennines, Italy: the contribution of sequential cross-section balancing techniques. Mem. Soc. Geol. It., 52, 607-616.

Alikarami, R., Torabi, A., Kolyukhin, D., Skurtveit, E., 2013. Geostatistical relationships between mechanical and petrophysical properties of deformed sandstone. *International Journal of Rock Mechanics and Mining Sciences*, *63*, 27-38.

Aliyu, M.M., Murphy, W., Lawrence, J.A., Collier, R.E.L., 2017. Engineering geological classification of flint. Quarterly Journal of Engineering Geology and Hydrogeology, 50, 133

Alonso-Zarza, A. M.: Palaeoenvironmental significance of palustrine carbonates and calcretes in the geological record, Earth Sci. Rev., 60(3-4), 261-298, https://doi.org/10.1016/S0012-8252(02)00106-X, 2003.

Alvarez, W., Engelder, T., Lowrie, W., 1976. Formation of spaced cleavage and folds in brittle limestone by dissolution. Geology, 4, 698–701.

Ambrose, W.A., Lakshminarasimhan, S., Holtz, M.H., Nunez-Lopez, V., Hovorka, S.D., Duncan, I., 2008. Geologic factors controlling CO2 storage capacity and permanence: case studies based on experience with heterogeneity in oil and gas reservoirs applied to CO2 storage. Environ. Geol. 54, 1619-1633.

An, L. J., Sammis, C.G., 1994. Particle size distribution of cataclastic materials from southern California: A 3-D study. Pure and Applied Geophysics, 143(1-3), 203-227.

Andrew, R.E.B, Gudmundsson, A., 2008. Volcanoes as elastic inclusions: Their effects on the propagation of dykes, volcanic fissures, and volcanic zones in Iceland. Journal of Volcanology and Geothermal Research 177, 1045–1054.

Annan, A. P., 2009. *Electromagnetic principles of ground penetrating radar*. In: Jol, H. M. (Ed.), Ground penetrating radar: theory and applications, Elsevier, 1-37.

Anthony, J. L., Marone, C., 2005. Influence of particle characteristics on granular friction, J. Geophys. Res., 110, B08409.

Antolini, F., Barla, M., Gigli, G., Giorgetti, A., Intrieri, E., Casagli, N., 2016. Combined Finite–Discrete Numerical Modeling of Runout of the Torgiovannetto di Assisi Rockslide in Central Italy. International Journal of Geomechanics ASCE, 04016019, 1-16.

Antonellini M., Tondi E., Agosta F., Aydin A., Cello G., 2008. Failure modes in deep-water carbonates and their impact for fault development: Majella Mountain, Central Apennines, Italy. Marine and Petroleum Geology, 25, 1074 – 1096.

Antonellini M., Mollema P. N., 2002. Cataclastic faults in the Loiano Sandstones; Northern Apennines, Italy. Bollettino della Società Geologica Italiana 121, pp. 163-178.

Antonellini, M., Pollard, D. D., 1995. Distinct element modeling of deformation bands in sandstone. *Journal of Structural Geology*, *17*(8), 1165-1182.

Antonellini, M., Aydin, A., 1994. Effect of faulting on fluid flow in porous sandstones: petrophysical properties. *AAPG Bulletin*, *78*(3), 355- 377.

Antonellini, M., Aydin, A., Orr, L., 1999. Outcrop-aided characterization of a faulted hydrocarbon reservoir: Arroyo Grande oil field, California, USA, in: Faults and Subsurface Fluid Flow in the Shallow Crust, edited by: Haneberg, W. C., Mozley, P. S., Moore, J. C., and Goodwin, L. B., American Geophysical Union, Washington, DC, 113, 7-26, https://doi.org/10.1029/GM113p0007.

Antonellini, M., Aydin, A., Pollard, D. D., 1994a. Microstructure of deformation bands in porous sandstones at Arches National Park, Utah. *Journal of structural geology*, *16*(7), 941-959.

Antonellini, M., Aydin, A., Pollard, D. D., D'Onfro, P., 1994b. Petrophysical study of faults in sandstone using petrographic image analysis and X-ray computerized tomography. *Pure and Applied Geophysics*, *143*(1-3), 181-201.

Antonellini, M., Cilona, A., Tondi, E., Zambrano, M., Agosta, F., 2014a. Fluid flow numerical experiments of faulted porous carbonates, northwest Sicily (Italy), Mar. Pet. Geol., 55, 186–201, https://doi.org/10.1016/j.marpetgeo.2013.12.003.

Antonellini, M., Del Sole, L., Mollema, P. N., 2020. Chert nodules in pelagic limestones as paleo-stress indicators: A 3D geomechanical analysis. J. Struct. Geol. 132, 103979, https://doi.org/10.1016/j.jsg.2020.103979.

Antonellini, M., Mollema, P. N., 2015. Polygonal deformation bands. *Journal of Structural Geology*, *81*, 45-58.

Antonellini, M., Mollema, P. N., Del Sole, L., 2017. Application of analytical diffusion models to outcrop observations: Implications for mass transport by fluid flow through fractures. *Water Resources Research*, *53*(7), 5545-5566.

Antonellini, M., Mollema, P. N., 2000. A natural analog for a fractured and faulted reservoir in dolomite: Triassic Sella Group, Northern Italy. AAPG Bulletin, 84, 314-344.

Antonellini, M., Mollema, P.N., 2019. Outcrop fracture network characterization for unraveling deformation sequence, geomechanical properties distribution, and slope stability in a flysch sequence (Monte Venere Formation, Northern Apennines, Italy). Int J Earth Sci (GeolRundsch) 108, 735–751. https://doi.org/10.1007/s00531-019-01685-y

Antonellini, M., Petracchini, L., Billi, A., Scrocca, D., 2014b. First reported occurrence of deformation bands in a platform limestone, the Jurassic Calcare Massiccio Fm., northern Apennines, Italy. *Tectonophysics*, *628*, 85-104.

Argnani, A., 1998. Structural elements of the Adriatic foreland and their relationships with the front of the Apennine fold-and-thrust belt. Mem. Soc. Geol. It., 52, 647-654.

Arthaud, F. and Séguret, M.: Les structures pyrénéennes du Languedoc et du Golfe du Lion (Sud de la France). Bull. Soc. Géol. Fr. 23, 51-63, 1981.

Aydin, A., 1978. Small faults formed as deformation bands in sandstones: Pure and Applied Geophysics, v. 116, p. 913-930.

Aydin, A., 2000. Fractures, faults, and hydrocarbon entrapment, migration and flow. *Marine and petroleum geology*, *17*(7), 797-814, https://doi.org/10.1016/S0264-8172(00)00020-9.

Aydin, A., 2009. ISRM Suggested method for determination of the Schmidt hammer rebound hardness: revised version. Int. J. Rock Mech. Min. Sci. 46, 627–634. https:// doi.org/10.1016/j.ijrmms.2008.01.020.

Aydin, A., Antonellini, M., Tondi, E., Agosta, F., 2010. Deformation along the leading edge of the Maiella thrust sheet in central Italy. Journal of Structural Geology, 32, 1291 – 1304.

Aydin A., Basu, A. 2005. The Schmidt hammer in rock material characterization. Eng. Geol., 81,1–14.

Aydin, A., Borja, R. I., Eichhubl, P., 2006. Geological and mathematical framework for failure modes in granular rock. *Journal of Structural Geology*, *28*(1), 83-98.

Aydin, A., Johnson, D., 1978. Development of faults as zones of deformation bands and as slip surfaces in sandstone: Pure and Applied Geophysics, v. 116, p. 931– 942.

Aydin, A., & Johnson, A. M. (1983). Analysis of faulting in porous sandstones. Journal of structural Geology, 5(1), 19-31.

Baek, S.-H., Kima, S.-S., Kwon, J.-S., Um, E.S., 2017. Ground penetrating radar for fracture mapping in underground hazardous waste disposal sites: a case study from an underground research tunnel, South Korea. Journal of Applied Geophysics 141, 24–33.

Ballas, G., 2013. Modèle structural, mécanique et pétrophysique de la localisation de la déformation dans les grès Poreux (Provence, France). Sciences de la Terre. Université Montpellier II - Sciences et Techniques du Languedoc. Français. https://tel.archives-ouvertes.fr/tel-01001389.

Ballas, G., Fossen, H., Soliva, R., 2015. Factors controlling permeability of cataclastic deformation bands and faults in porous sandstone reservoirs. *Journal of Structural Geology*, *76*, 1-21.

Ballas, G., Soliva, R., Benedicto, A., Sizun, J. P., 2014. Control of tectonic setting and large-scale faults on the basin-scale distribution of deformation bands in porous sandstone (Provence, France). *Marine and Petroleum Geology*, *55*, 142-159.

Ballas, G., Soliva, R., Sizun, J. P., Benedicto, A., Cavailhes, T., Raynaud, S., 2012. The importance of the degree of cataclasis in shear bands for fluid flow in porous sandstone, Provence, France. *AAPG bulletin*, *96*(11), 2167-2186.

Ballas, G., Soliva, R., Sizun, J. P., Fossen, H., Benedicto, A., Skurtveit, E., 2013. Shear-enhanced compaction bands formed at shallow burial conditions; implications for fluid flow (Provence, France), J. Struct. Geol., 47, 3-15, https://doi.org/10.1016/j.jsg.2012.11.008.

Balsamo F., Storti F., 2010. Grain size and permeability evolution of soft-sediment extensional sub-seismic and seismic fault zones in high-porosity sediments from the Crotone basin, southern Apennines, Italy, Mar. Pet. Geol., 27, 822-837, https://doi.org/10.1016/j.marpetgeo.2009.10.016, 2010.

Balsamo, F., Bezerra, F. H. R., Vieira, M. M., Storti, F., 2013. Structural control on the formation of iron-oxide concretions and Liesegang bands in faulted, poorly lithified Cenozoic sandstones of the Paraíba Basin, Brazil. GSA Bulletin, 125(5-6), 913-

Balsamo, F., Storti, F., Gröcke, D. R., 2012. Fault-related fluid flow history in shallow marine sediments from carbonate concretions, Crotone basin, south Italy. *Journal of the Geological Society*, *169*(5), 613-626.

Barchi, M., De Feyter, A. J. J., Magnani, M.B., Minelli, G., Pialli, G., Sotera, B.M., 1998. The structural style of the Umbra-Marche fold and thrust belt. Mem. Soc. Geol. It., 52, 557-578.

Barnaby, R.J. and Rimstidt, J.D.: Redox conditions of calcite cementation interpreted from Mn and Fe contents of authigenic calcites. Geol. Soc. Am. Bull., 101, 795–804, https://doi.org/10.1130/0016-7606(1989)101<0795:RCOCCI>2.3.CO;2, 1989.

Baud P., Louis, L., David, C., Rawling, G.C., Wong, T., 2005. Effects of bedding and foliation on mechanical anisotropy, damage evolution and failure mode. Geol Soc (Spec Publ). 245, 223–49.

Beauchamp, E.K., Purdy, B.A., 1986. Decrease in fracture toughness of chert by heat treatment. J Mater Sci 21, 1963–1966. https://doi.org/10.1007/BF00547934

Bense, V. F., Gleeson, T., Loveless, S. E., Bour, O., Scibek, J., 2013. Fault zone hydrogeology, Earth Sci. Rev., 127, 171-192, https://doi.org/10.1016/j.earscirev.2013.09.008.

Bense, V.F., Van Den Berg, E.H. Van Balen, R.T., 2003. Deformation mechanisms and hydraulic properties of fault zones in unconsolidated sediments; the Roer Valley Rift System, The Netherlands. *Hydrogeology Journal*, 11, 319–332.

Bernabé, Y., Fryer, D. T., Hayes, J. A., 1992. The effect of cement on the strength of granular rocks. *Geophysical Research Letters*, *19*(14), 1511-1514.

Berner, R. A., 1968. Calcium carbonate concretions formed by the decomposition of organic matter. *Science*, *159*(3811), 195-197.

Berner, R. A., 1980. *Early diagenesis: a theoretical approach*. Princeton University Press, Princeton, N.J.

Billi, A., Salvini, F., Storti, F., 2003. The damage zone-fault core transition in carbonate rocks: implications for fault growth, structure and permeability. *Journal of Structural geology*, *25*(11), 1779-1794.

Bjørkum, P. A., Walderhaug, O., 1990. Geometrical arrangement of calcite cementation within shallow marine sandstones. *Earth-Science Reviews*, *29*(1-4), 145-161.

Blenkinsop, T.G., 1991, Cataclasis and processes of particle size reduction: Pure and Applied Geophysics, v. 136, p. 59–86.

Bortolotti V., Castellarin, A., Cita, M.B., Dal Piaz, G.V., Praturlon, A., Ricchetti, G., Vanossi, M., 1994. Guide Geologiche Regionali - Appennino Umbro-Marchigiano, In: L. Passeri (ed.), Soc. Geol. It., BE-MA, Milano, vol. 7/1, pp. 14-78 and 207-218.

Bott, T. R.: Fouling of heat exchangers. Elsevier Science B.V. The Netherlands, 1995.

Boutt, D. F., Plourde, K. E., Cook, J., and Goodwin, L. B.: Cementation and the hydromechanical behavior of siliciclastic aquifers and reservoirs, Geofluids, 14(2), 189-199, https://doi.org/10.1111/gfl.12062, 2014.

Braathen, A., Petrie, E., Nystuen, T., Sundal, A., Skurtveit, E., Zuchuat, V., Gutierrez, M., Midtkandal, I. (2020). Interaction of deformation bands and fractures during progressive strain in monocline-San Rafael Swell, Central Utah, USA. Journal of Structural Geology, 141, 104219.

Brace, W. F. (1961, January). Dependence of fracture strength of rocks on grain size. In *The 4th US Symposium on Rock Mechanics*. American Rock Mechanics Association.

Brandenburg, J. P., Alpak, F. O., Solum, J. G., & Naruk, S. J. (2012). A kinematic trishear model to predict deformation bands in a fault-propagation fold, East Kaibab monocline, Utah. AAPG bulletin, 96(1), 109-132.

Brandes, C., Igel, J., Loewer, M., Tanner, D. C., Lang, J., Müller, K., and Winsemann, J., 2018. Visualisation and analysis of shear-deformation bands in unconsolidated Pleistocene sand using ground-penetrating radar: Implications for paleoseismological studies. Sedimentary geology, 367, 135-145.

Busch, B., Hilgers, C., Gronen, L., and Adelmann, D.: Cementation and structural diagenesis of fluvio-aeolian Rotliegend sandstones, northern England, J. Geol. Soc. London, 174(5), 855-868, https://doi.org/10.1144/jgs2016-122, 2017.

Caine, J. S., Minor, S. A., 2009. Structural and geochemical characteristics of faulted sediments and inferences on the role of water in deformation, Rio Grande Rift, New Mexico. *Geological Society of America Bulletin*, *121*(9-10), 1325-1340.

Caineng, Z., Guangya, Zhang, Shizhen, T., Suyun, H., Xiaodi, L., Jianzhong, L., Dazhong, D., Rukai, Z., Xuanjun, Y., Lianhua, H., Hui, Q., Xia, Z., Jinhua, J., Xiaohui, G., Qiulin, G., Lan, W., Xinjing, L., 2010. Geological features, major discoveries and unconventional petroleum geology in the global petroleum exploration. Petroleum Exploration and Development, 37, 129–145.

Callahan, O. A., Eichhubl, P., & Davatzes, N. C. (2020). Mineral precipitation as a mechanism of fault core growth. Journal of Structural Geology, 140, 104156.

Carman, P.C., 1937. Fluid flow through granular beds. Trans. Inst. Chem. Eng. 15, 150–167.

Carmignani, L., Decandia, F. A., Disperati, L., Fantozzi, P. L., Lazzarotto, A., Liotta, D., Oggiano, G., 1995. Relationships between the Tertiary structural evolution of the Sardinia-Corsica-Provençal Domain and the Northern Apennines. Terra Nova, 7(2), 128-137.

Cartwright, J., 2011. Diagenetically induced shear failure of fine-grained sediments and the development of polygonal fault systems. Mar. Pet. Geol. 28(9), 1593-1610.

Cashman, S., Cashman, K., 2000. Cataclasis and deformation-band formation in unconsolidated marine terrace sand, Humboldt County, California. Geology 28 (2), 111-114.

Cassidy, N.J., 2009. Electrical and magnetic properties of rocks, soils and fluids. p. 41–72. In H. M. Jol (ed.) Ground penetrating radar: Theory and applications. Elsevier, Amsterdam.

Cavailhes, T., Rotevatn, A., 2018. Deformation bands in volcaniclastic rocks–Insights from the Shihtiping tuffs, Coastal Range of Taiwan. *Journal of Structural Geology*.

Cavailhes, T., Soliva, R., Benedicto, A., Loggia, D., Schultz, R.A., Wibberley, C.A.J., 2009. Are cataclastic shear bands fluid barriers or capillarity conduits? Insight from the analysis of redox fronts in porous sandstones from Provence, France. In: 2nd EAGE International Conference on Fault and Top Seals: From Pore to Basin Scale, September 21–24, 2009 - Montpellier, France, 3 pp, https://doi.org/10.3997/2214-4609.20147185.

Cavazza, W., Braga, R., Reinhardt, E. G., Zanotti, C.: Influence of host-rock texture on the morphology of carbonate concretions in a meteoric diagenetic environment, J. Sediment. Res., 79(6), 377-388, https://doi.org/10.2110/jsr.2009.047, 2009.

Cello, G., Coppola, L.,1984. – Assetto geologico-strutturale dell'area anconetana e sua evoluzione plio-quaternaria. Boll. Soc. Geol. It., 103, 97-109.

Champion, C., Choukroune, P., and Clauzon, G.: La déformation post-miocène en Provence occidentale. Geodinamica Acta 13, 67–85, https://doi.org/10.1080/09853111.2000.11105365, 2000.

Chang, C., Zoback, M. D., Khaksar, A., 2006. Empirical relations between rock strength and physical properties in sedimentary rocks. Journal of Petroleum Science and Engineering, 51(3-4), 223-237.

Chuhan, F. A., K. Bjørlykke, C. Lowery, 2000. The role of provenance in illitization of deeply buried reservoir sand- stones from Haltenbanken and north Viking Graben, off- shore Norway: Marine and Petroleum Geology, v. 17, no. 6, p. 673–689.

Cibin, U., Cavazza, W., Fontana, D., Milliken, K. L., McBride, E. F., 1993. Comparison of composition and texture of calcite-cemented concretions and host sandstones, Northern Apennines, Italy. *Journal of Sedimentary Research*, *63*(5), 945-954.

Cibin, U., Spadafora, E., Zuffa, G. G., Castellarin, A., 2001. Continental collision history from arenites of episutural basins in the Northern Apennines, Italy. *Geological Society of America Bulletin*, *113*(1), 4-19.

Coccioni, R., Moretti, E., Nesci, O., Savelli, D., Tramontana, M., Veneri, F., Astracedi, M., 1997. Carta Geologica con itinerari escursionistici - Parco Naturale del Conero. Sabakart, Santarcangelo di Romagna.

Coltorti, M., Nanni, T., Rainone, M.L., 1987. Il contributo delle scienze della terra nell'elaborazione di un piano paesistico: l'esempio del monte Conero (Marche). Mem. Soc. Geol.It., 37/2, 629-647, 6 ff.,1 tav. Roma.

Cooke, M.L., Mollema, P.N., Pollard, D.D., Aydin, A., 1999. Interlayer slip and joint localization in the East Kaibab Monocline, Utah: field evidence and results from numerical modelling. Geological Society, London, Special Publications 169, 23–49. https://doi.org/10.1144/GSL.SP.2000.169.01.03

Cortecci, G., Dinelli, E., and Mussi, M.: Isotopic composition and secondary evaporation effects on precipitation from the urban centre of Bologna, Italy. Period. Miner. 77, 55–63, doi:10.2451/2008PM0004, 2008.

Cowie, P.A., Shipton, Z.K., 1998. Fault tip displacement gradients and process zone dimensions. Journal of Structural Geology 20, 983-997.

Crescenti, U., Nanni, T., Rampoldi, R., & Stucchi, M. (1977). Ancona: considerazioni sismotettoniche. Bollettino di Geofisica Teorica e Applicata, 73(74), 33-48.

Davatzes, N. C., Eichhubl, P., & Aydin, A. (2005). Structural evolution of fault zones in sandstone by multiple deformation mechanisms: Moab fault, southeast Utah. Geological Society of America Bulletin, 117(1-2), 135-148.

Davis, J. L., Annan, A. P., 1989. Ground penetrating radar for soil and rock stratigraphy: Geophysical Prospecting, v. 37, p. 531 – 551.

Davis, J. M., Roy, N. D., Mozley, P. S., Hall, J. S., 2006. The effect of carbonate cementation on permeability heterogeneity in fluvial aquifers: An outcrop analog study. *Sedimentary geology*, *184*(3-4), 267-280, https://doi.org/10.1016/j.sedgeo.2005.11.005.

Davis, T., Healy, D., Bubeck, A., Walker, R., 2017. Stress concentrations around voids in three dimensions: The roots of failure. Journal of Structural Geology, 102, 193-207.

De Yoreo, J. J., Vekilov, P. G., 2003. Principles of crystal nucleation and growth. Reviews in mineralogy and geochemistry, 54(1), 57-93.

Debrand-Passard, S., Courbouleix, S., and Lienhardt, M.J.: Synthèse géologique du Sud- Est de la France: stratigraphie et paléogéographie. In: Bureau de Recherches Géologiques et Minières, Mémoire, vol. 215 (Orléans), 1984.

Deiana, G., Cello, G., Chiocchini, M., Galdenzi, S., Mazzoli, S., Pistolesi, E., Potetti, M., Romano, A., Turco, E., Principi, M., 2002. Tectonic evolution of the external zones of the Umbria-Marche Apennines in the Monte San Vicino-Cingoli area. Boll. Soc. Geol. It., Spec. Vol. 1/1, 229-238.

Del Sole, L., Antonellini, M., 2019. Microstructural, petrophysical, and mechanical properties of compactive shear bands associated to calcite cement concretions in arkose sandstone. J. Struct. Geol. 126, 51–68, https://doi.org/10.1016/j.jsg.2019.05.007.

Del Sole, L., Antonellini, M., Calafato, A., 2020a. Characterization of sub-seismic resolution structural diagenetic heterogeneities in porous sandstones: Combining ground-penetrating radar profiles with geomechanical and petrophysical in situ measurements (Northern Apennines, Italy), Mar. Pet. Geol., 117, 104375, https://doi.org/10.1016/j.marpetgeo.2020.104375.

Dewhurst, D. N., Jones, R. M., 2003. Influence of physical and diagenetic processes on fault geomechanics and reactivation. *Journal of Geochemical Exploration*, *78*, 153-157, https://doi.org/10.1016/S0375-6742(03)00124-9.

Díaz General, E.N., Mollema, P.N., Antonellini, M., 2015. Fracture patterns and fault development in the pelagic limestones of the Monte Conero Anticline (Italy). Italian Journal of Geosciences, 134, 495-512. https://doi.org/10.3301/IJG.2014.33.

Diaz-General, E.N., 2013. The Influence of Fractures on Vulnerability to Pollution of a Carbonate Aquifer: Monte Conero (Italy). PhD thesis, amsdottorato.unibo.it.

Dimmen, V., Rotevatn, A., Peacock, D. C., Nixon, C. W., & Nærland, K. (2017). Quantifying structural controls on fluid flow: Insights from carbonate-hosted fault damage zones on the Maltese Islands. *Journal of Structural Geology*, *101*, 43-57.

Ding, W., Li, C., Li, C., Xu, C., Jiu, K., Zeng, W., Wu, L., 2011. Fracture development in shale and its relationship to gas accumulation. Geoscience Frontiers, 3, 97-105.

Du Bernard, X., Eichhubl, P., Aydin, A., 2002. Dilation bands: A new form of localized failure in granular media. *Geophysical Research Letters*, **29**, 2176–2179.

Dullien, F. A., 1991. Porous media: fluid transport and pore structure. Academic press. New York

Dutton, S. P., White, C. D., Willis, B. J., Novakovic, D., 2002. Calcite cement distribution and its effect on fluid flow in a deltaic sandstone, Frontier Formation, Wyoming. *AAPG bulletin*, *86*(12), 2007-2021.

Dvorkin, J., Mavko, G., and Nur, A., 1991. The effect of cementation on the elastic properties of granular material, Mechanics of Materials, 12(3-4), 207-217, https://doi.org/10.1016/0167-6636(91)90018-U.

Dvorkin, J., Nur, A., 1996. Elasticity of high-porosity sandstones: theory for two North Sea data sets. Geophysics 61, 1363–1370.

Edwards, H. E., Becker, A. D., Howell, J. A., 1993. Compartmentalization of an aeolian sandstone by structural heterogeneities: permo-Triassic Hopeman Sandstone, Moray Firth, Scotland. Geological Society, London, Special Publications, 73(1), 339-365, https://doi.org/10.1144/GSL.SP.1993.073.01.20.

Ehrenberg, S. N.: Relationship between diagenesis and reservoir quality in sandstones of the Garn formation, Haltenbanken, mid-Norwegian Continental shelf, AAPG Bull., 74(10), 1538-1558, https://doi.org/10.1306/0C9B2515-1710-11D7-8645000102C1865D, 1990.

Eichhubl, P., Davatzes, N. C., Becker, S. P., 2009. Structural and diagenetic control of fluid migration and cementation along the Moab fault, Utah. *AAPG bulletin*, *93*(5), 653-681.

Eichhubl, P., Hooker, J. N., Laubach, S. E., 2010. Pure and shear-enhanced compaction bands in Aztec Sandstone. *Journal of Structural Geology*, *32*(12), 1873-1886.

Eichhubl, P., Taylor, W. L., Pollard, D. D., Aydin, A., 2004. Paleo-fluid flow and deformation in the Aztec Sandstone at the Valley of Fire, Nevada—Evidence for the coupling of hydrogeologic, diagenetic, and tectonic processes. Geological Society of America, 116 (9-10): 1120-1136.

Eichhubl, P.: Paleo-Fluid Flow Indicators, Stanford Rock Fracture Project, Vol. 12., pp. 10, https://stacks.stanford.edu/file/druid:jp813ns8076/RFP_2001_Eichhubl.pdf (last access: 5 March 2020), 2001.

Eidelman, A., Reches, Z., 1992. Fractured pebbles—A new stress indicator. Geology, 20, 307–310. https://doi.org/10.1130/0091-7613.

Ercoli, M., Pauselli, C., Frigeri, A., Forte, E., Federico, C., 2014. 3-D GPR data analysis for high-resolution imaging of shallow subsurface faults: the Mt Vettore case study (Central Apennines, Italy). *Geophysical Journal International*, *198*(1), 609-621.

Eshelby, J. D., 1957. The determination of the elastic field of an ellipsoidal inclusion, and related problems. Proceedings of the Royal Society of London. Series A. Mathematical and Physical Sciences 241, 376–396. https://doi.org/10.1098/rspa.1957.0133

Eshelby, J. D., 1959. The elastic field outside an ellipsoidal inclusion. Proceedings of the Royal Society of London. Series A. Mathematical and Physical Sciences 252, 561–569. https://doi.org/10.1098/rspa.1959.0173

Exner, U., Tschegg, C., 2012. Preferential cataclastic grain size reduction of feldspar in deformation bands in poorly consolidated arkosic sands. Journal of structural geology, 43, 63-72.

Fachri, M., Rotevatn, A., Tveranger, J., 2013. Fluid flow in relay zones revisited: towards an improved representation of small-scale structural heterogeneities in flow models. Mar. Petrol. Geol. 46, 144-164, https://doi.org/10.1016/j.marpetgeo.2013.05.016.

Falzone, G., Falla, G.P., Wei, Z., Zhao, M., Kumar, A., Bauchy, M., Neithalath, N., Pilon, L., Sant, G., 2016. The influences of soft and stiff inclusions on the mechanical properties of cementitious composites, Cement and Concrete Composites, doi: 10.1016/j.cemconcomp.2016.05.008.

Farrell, N. J. C., Healy, D., Taylor, C. W., 2014. Anisotropy of permeability in faulted porous sandstones. *Journal of Structural Geology*, *63*, 50-67.

Faulkner, D. R., Jackson, C. A. L., Lunn, R. J., Schlische, R. W., Shipton, Z. K., Wibberley, C. A. J., and Withjack, M. O.: A review of recent developments concerning the structure, mechanics and fluid flow properties of fault zones, J. Struct. Geol., 32(11), 1557-1575, https://doi.org/10.1016/j.jsg.2010.06.009, 2010.

Ferraro, F., Agosta, F., Ukar, E., Grieco, D.S., Cavalcante, F., Belviso, C., Prosser, G., 2019. Structural diagenesis of carbonate fault rocks exhumed from shallow crustal depths: An example from the central-southern Apennines, Italy. Journal of Structural Geology 122, 58–80. https://doi.org/10.1016/j.jsg.2019.02.008

Ferreira, T., Rasband, W., 2012. ImageJ user guide. *ImageJ/Fiji*, *1*.

Ferry, S. (Ed.): Actes des Journées Scientifiques CNRS/ANDRA, Apport des forages ANDRA de Marcoule à la connaissance de la marge crétacée rhodanienne. Etude du Gard Rhodanien/EDP sciences, Bagnols-sur-Cèze, pp. 63-91, 1997.

Fetter, C.W., 2002. Applied Hydrogeology. Prentice Hall.

Filomena, C.M., Hornung, J., Stollhofen, H., 2014. Assessing accuracy of gas-driven permeability measurements: a comparative study of diverse Hassler-cell and probe permeameter devices. Solid Earth 5, 1–11. https://doi.org/10.5194/se-5-1-2014.

Fisher, Q. J., Knipe, R., 1998. Fault sealing processes in siliciclastic sediments, Geol. Soc. Spec. Publ., 147(1), 117-134, https://doi.org/10.1144/GSL.SP.1998.147.01.08.

Fisher, Q. J., Knipe, R. J., 2001. The permeability of faults within siliciclastic petroleum reservoirs of the North Sea and Norwegian Continental Shelf. *Marine and Petroleum Geology*, *18*(10), 1063-1081.

Fjær, E., Holt, R.M., Horsrud, P., Raaen, A.M., Rines, R., 2008. Petroleum Related Rock Mechanics, second ed. Elsevier Science Publ., Amsterdam.

Flodin, E., Prasad, M., and Aydin, A.: Petrophysical constraints on deformation styles in Aztec Sandstone, southern Nevada, USA, Pure and Applied Geophysics 160, 1589–1610, https://doi.org/10.1007/s00024-003-2377-1, 2003.

Flügel, E.: Microfacies of carbonate rocks: analysis, interpretation and application, Springer Science & Business Media, 2013.

Forte, E., Pipan, M., Casabianca, D., Di Cuia, R., Riva, A., 2012. Imaging and characterization of a carbonate hydrocarbon reservoir analogue using GPR attributes. *Journal of Applied Geophysics*, *81*, 76-87.

Fossen, H., Bale, A., 2007. Deformation and their influence on fluid flow: AAPG Bulletin, v. 91, p. 1685–1700.

Fossen, H., Schultz, R.A., Torabi, A., 2011. Conditions and implications for compaction band formation in the Navajo Sandstone, Utah. J. Struct. Geol. 33, 1477–1490. https://doi.org/10.1016/j.jsg.2011.08.001.

Fossen, H., Rotevatn, A. (2012). Characterization of deformation bands associated with normal and reverse stress states in the Navajo Sandstone, Utah: Discussion. *AAPG bulletin*, *96*(5), 869-876.

Fossen, H., Shultz, R. A., Shipton, Z. K., Mair, K., 2007. Deformation bands in sandstone: A review: Journal of the Geological Society of London, 164, 755–769.

Fossen, H., Zuluaga, L. F., Ballas, G., Soliva, R., Rotevatn, A., 2015. Contractional deformation of porous sandstone: Insights from the Aztec Sandstone, SE Nevada, USA: Journal of Structural Geology, v. 74, p. 172–184, doi: 10.1016/j.jsg.2015.02.014.

Fossen, H., Soliva, R., Ballas, G., Trzaskos, B., Cavalcante, C., and Schultz, R. A.: A review of deformation bands in reservoir sandstones: geometries, mechanisms and distribution, in: Subseismic-Scale Reservoir Deformation, edited by: Ashton, M., Dee, S.J., and Wennberg, O.P., Geol. Soc. Spec. Publ., 459(1), 9-33, https://doi.org/10.1144/SP459.4, 2017.

Fowles, J., Burley, S., 1994. Textural and permeability characteristics of faulted, high porosity sandstones. Marine and Petroleum Geology, 11(5), 608-623.

Fredrich, J. T., Evans, B., Wong, T. F., 1990. Effect of grain size on brittle and semibrittle strength: Implications for micromechanical modelling of failure in compression. *Journal of Geophysical Research: Solid Earth*, *95*(B7), 10907-10920.

Friedman, I., O'Neil, J. R., 1977. Compilation of stable isotope fractionation factors of geochemical interest: U.S. Geological Survey Professional Paper 440-KK, p. 1–117, https://doi.org/10.3133/pp440KK.

Gambino, S., Fazio, E., Maniscalco, R., Punturo, R., Lanzafame, G., Barreca, G., & Butler, R. W. H. (2019). Fold-related deformation bands in a weakly buried sandstone reservoir analogue: a multi-disciplinary case study from the Numidian (Miocene) of Sicily (Italy). Journal of Structural Geology, 118, 150-164.

Garden, I. R., Guscott, S. C., Burley, S. D., Foxford, K. A., Walsh, J. J., Marshall, J., 2001. An exhumed paleo-hydrocarbon migration fairway in a faulted carrier system, Entrada Sandstone of SE Utah, USA. *Geofluids*, *1*(3), 195-213.

Gaupp, R., A. Matter, J. Platt, K. Ramseyer, and J. Walzebuck, 1993, Diagenesis and fluid evolution of deeply buried Permian (Rotliegende) gas-reservoirs, northwest Germany: AAPG Bull., v. 77, p. 1111–1128.

Gazzi, P., Zuffa, G. G., 1970. Le arenarie paleogeniche dell'Appennino emiliano. *Mineralogica et Petrographica Acta*, *16*, 97-137.

Genty, D., Labuhn, I., Hoffmann, G., Danis, P.A., Mestre, O., Bourges, F., Wainer, K., Massault, M., Van Exter, S., Régnier, E., Orengo, P., Falourd, S., and Minster, B.: Rainfall and cave water isotopic relationships in two South-France sites. Geochimica et Cosmochimica Acta 131, 323–343, http://dx.doi.org/10.1016/j.gca.2014.01.043, 2014.

Gibson, R. G., 1998. Physical character and fluid-flow properties of sandstone-derived fault zones. *Geological Society, London, Special Publications*, *127*(1), 83-97.

Gier, S., R. H. Worden, W. D. Johns, Kurzweil, H., 2008. Diagenesis and reservoir quality of Miocene sandstones in the Vienna Basin, Austria: Marine and Petroleum Geology, v. 25, no. 8, p. 681–695.

Giustini, F., Brilli, M., Patera, A., 2016. Mapping oxygen stable isotopes of precipitation in Italy. *Journal of Hydrology: Regional Studies*, *8*, 162-181, https://doi.org/10.1016/j.ejrh.2016.04.001.

Ghezzehei, T. A. (2012). Linking sub-pore scale heterogeneity of biological and geochemical deposits with changes in permeability. Advances in water resources, 39, 1-6, https://doi.org/10.1016/j.advwatres.2011.12.015.

Goodwin, L. B., Tikoff, B., 2002. Competency contrast, kinematics, and the development of foliations and lineations in the crust. *Journal of Structural Geology*, *24*(6-7), 1065-1085.

Gouze, P., Luquot, L., 2011. X-ray microtomography characterization of porosity, permeability and reactive surface changes during dissolution. *Journal of contaminant hydrology*, *120*, 45-55.

Graham, B., Antonellini, M., Aydin, A., 2003. Formation and growth of normal faults in carbonates within a compressive environment. Geology, 31(1), 11-14.

Grasmueck, M., 1996, 3D ground-penetrating radar applied to fracture imaging in gneiss: Geophysics, 61, 1050–1064.

Guido, F.L., Antonellini, M., Picotti, V., 2015. Modeling ground displacement above reservoirs undergoing fluid withdrawal/injection based on an ellipsoidal inhomogeneity model. International Journal of Rock Mechanics and Mining Sciences 79, 63–69. https://doi.org/10.1016/j.ijrmms.2015.08.010.

Hall, J. S., Mozley, P., Davis, J. M., and Roy, N. D.: Environments of formation and controls on spatial distribution of calcite cementation in Plio-Pleistocene fluvial deposits, New Mexico, USA. *Journal of Sedimentary Research*, *74*(5), 643-653, https://doi.org/10.1306/020904740643, 2004.

Harper, T. and Moftah, I., 1985. Skin effect and completion options in the Ras Budran Reservoir, in: Society of Petroleum Engineers Middle East Oil Technical Conference and Exhibition. SPE, 13708, 211–226, https://doi.org/10.2118/13708-MS.

Heald, M. T., Renton, J. J., 1966. Experimental study of sandstone cementation. *Journal of Sedimentary Research*, *36*(4), 977-991.

Healy, D., 2009. Elastic field in 3D due to a spheroidal inclusion-MATLABTM code for Eshelby's solution. Computers and Geosciences 35, 2170–2173. https://doi.org/10.1016/j.cageo.2008.11.012

Hesse, R., 1989. Silica diagenesis: origin of inorganic and replacement cherts. Earth-Science Reviews 26, 253–284. https://doi.org/10.1016/0012-8252(89)90024-X.

Hesthammer, J., Fossen, H. 2001. Structural core analysis from the Gullfaks area, northern North Sea. Marine and Petroleum Geology, 18, 411–439, https://doi.org/10. 1016/S0264-8172(00)00068-4

Hiatt, E. E. and Pufahl, P. K.: Cathodoluminescence petrography of carbonate rocks: a review of applications for understanding diagenesis, reservoir quality and pore system evolution. Short Course, 45, 75-96, 2014.

Hodson, K. R., Crider, J. G., & Huntington, K. W. (2016). Temperature and composition of carbonate cements record early structural control on cementation in a nascent deformation band fault zone: Moab Fault, Utah, USA. Tectonophysics, 690, 240-252.

Hudson, J.D.: Stable isotopes and limestone lithification, J. Geol. Soc. London, 133, 637–660, https://doi.org/10.1144/gsjgs.133.6.0637, 1977.

Huggenberger, P., 1993. Radar facies: recognition of facies patterns and heterogeneities within Pleistocene Rhine gravels, NE Switzerland. *Geological Society, London, Special Publications*, *75*(1), 163-176.

Hustoft, S., Mienert, J., Bunz, S., Nouze, H., 2007. High-resolution 3D-seismic data indicate focused fluid migration pathways above polygonal fault systems of the mid-Norwegian margin. Mar. Geol. 245, 89-106.

Jaeger, J.C., Cook, N.G.W., 1979. Fundamentals of rock mechanics. Chapman and Hall.

Jasechko, S.: Global isotope hydrogeology—Review. *Reviews of Geophysics*, *57*(3), 835-965, DOI:10.1029/2018RG000627, 2019.

Johansen, T. E. S., Fossen, H., Kluge, R., 2005. The impact of syn-faulting porosity reduction on damage zone architecture in porous sandstone: an outcrop example from the Moab Fault, Utah. *Journal of Structural Geology*, *27*(8), 1469-1485.

Jones, R. M., 2014. *Mechanics of composite materials*. CRC press.

Jones, R. R., Mccaffrey, K. J., Imber, J., Wightman, R., Smith, S. A., Holdsworth, R. E., Clegg, P., De Paola, N., Healy, D., Wilson, R. W., 2008. Calibration and validation of reservoir models: the importance of high resolution, quantitative outcrop analogues. Geological Society, London, Special Publications, 309(1), 87–98.

Jourde, H., Flodin, E. A., Aydin, A., Durlofsky, L. J., Wen, X. H., 2002. Computing permeability of fault zones in eolian sandstone from outcrop measurements. AAPG Bull. *86*(7), 1187-1200.

Ju, J. W., Sun, L. Z., 2001. Effective elastoplastic behavior of metal matrix composites containing randomly located aligned spheroidal inhomogeneities. Part I: micromechanics-based formulation. *International Journal of Solids and Structures*, *38*(2), 183-201.

Ju, J.W., Sun, L.Z., 1999. A Novel Formulation for the Exterior-Point Eshelby's Tensor of an Ellipsoidal Inclusion. Journal of Applied Mechanics 66, 570. https://doi.org/10.1115/1.2791090.

Kantorowicz, J.D., Bryant, I.D., Dawans, J.M., 1987. Controls on the Geometry and Distribution of Carbonate Cements in Jurassic Sandstones: Bridport Sands, Southern England and Viking Group, Troll Field, Norway Geol. Soc. Spec. Publ., 36, 103-118, https://doi.org/10.1144/GSL.SP.1987.036.01.09.

Kaproth, B. M., Cashman, S. M., Marone, C., 2010. Deformation band formation and strength evolution in unlithified sand: The role of grain breakage, J. Geophys. Res., 115, B12103.

Katsman, R., 2010. Extensional veins induced by self-similar dissolution at stylolites: analytical modeling. Earth and Planetary Science Letters 299, 33–41. https://doi.org/10.1016/j.epsl.2010.08.009

Katz, O., Reches, Z., Roegiers, J. C., 2000. Evaluation of mechanical rock properties using a Schmidt Hammer. *International Journal of rock mechanics and mining sciences*, *37*(4), 723-728.

Knipe, R. J., Fisher, Q. J., Jones, G., Clennell, M. B., Farmer, A. B., Harrison, A., Kidd, B., Mcallister, E., Porter, J.R., White, E.A., 1997. Fault seal analysis: Successful methodologies, application and future directions. In P. Moller-Pederson & A. G. Koestler et al. Hydrocarbon seals: Importance for exploration and production. NPF Special Publication, 7, 15-38. https://doi.org/10.1016/S0928-8937(97)80004-5

Knoll, M.D., Knight, R., 1994. Relationships between dielectric and hydrogeologic properties of sand-clay mixtures. In: GPR '94 - Proceedings of the 5th International Conference on Ground Penetrating Radar (Eds: J.D. Redman, A.P. Annan, J.P. Greenhouse, T. Klym and J.R. Rossiter), 1, 45-61. Waterloo Center for Groundwater Research, Kitchener, Ontario.

Korneva, I., Bastesen, E., Corlett, H., Eker, A., Hirani, J., Hollis, C., Gawthorpe, R.L., Rotevatn, A., Taylor, R., 2017. The effects of dolomitization on petrophysical properties and fracture distribution within rift-related carbonates (Hammam Faraun Fault Block, Suez Rift, Egypt). J. Struct. Geol., 108, 108-120.

Kozeny, J., 1927. Uber kapillare Leitung des Wassers im Boden. Sitz. Akad. Wiss. 136, 271–306.

La Bruna, V., Lamarche, J., Agosta, F., Rustichelli, A., Giuffrida, A., Salardon, R., and Marié, L.: Structural diagenesis of shallow platform carbonates: Role of early embrittlement on fracture setting and distribution, case study of Monte Alpi (Southern Apennines, Italy), J. Struct. Geol., 131, 103940, https://doi.org/10.1016/j.jsg.2019.103940, 2020.

Labaume, P., and Moretti, I.: Diagenesis-dependence of cataclastic thrust fault zone sealing in sandstones. Example from the Bolivian Sub-Andean Zone, J. Struct. Geol. 23, 1659-1675, https://doi.org/10.1016/S0191-8141(01)00024-4, 2001.

Lacombe, O., Jolivet, L., 2005. Structural and kinematic relationships between Corsica and the Pyrenees-Provence domain at the time of the Pyrenean orogeny, Tectonics, 24(1), https://doi.org/10.1029/2004TC001673.

Lander R.H., and Laubach, S.E., 2015. Insights into rates of fracture growth and sealing from a model for quartz cementation in fractured sandstones. Geological Society of America Bulletin 127 (3-4), 516-538. doi:10.1130/B31092.1.

Lander, R. H., Larese, R. E., Bonnell, L. M., 2008. Toward more accurate quartz cement models: The importance of euhedral versus noneuhedral growth rates. *AAPG bulletin*, *92*(11), 1537-1563.

Lander, R.H., Solano-Acosta, W., Thomas, A.R., Reed, R.M., Kacewicz, M., Bonnell, L.M., and Hooker, J.N.: Simulation of fault sealing from quartz cementation within cataclastic deformation zones, in: AAPG Hedberg Conference Basin and Petroleum Systems Modeling: New Horizons in Research and Applications, May 3-7, 2009 - Napa, California, USA, 2 pp, 2009.

Langevin, C.D., Hughes, J.D., Banta, E.R., Provost, A.M., Niswonger, R.G., and Panday, S., 2020. MODFLOW 6 Modular Hydrologic Model version 6.1.1: U.S. Geological Survey Software Release, 12 December 2019, https://doi.org/10.5066/F76Q1VQV

Laubach, S. E., Eichhubl, P., Hilgers, C., Lander, R. H., 2010. Structural diagenesis. *Journal of Structural Geology*, *32*(12), 1866-1872.

Laubach, S. E., Olson, J. E., and Gross, M. R.: Mechanical and fracture stratigraphy, AAPG Bull., 93(11), 1413-1426, https://doi.org/10.1306/07270909094, 2009.

Laubach, S.E., Eichhubl, P., Hilgers, C., Lander, R.H., 2010. Structural diagenesis. Journal of Structural Geology, Structural Diagenesis 32, 1866–1872. https://doi.org/10.1016/j.jsg.2010.10.001.

Lavenu, A. P., Lamarche, J., Salardon, R., Gallois, A., Marié, L., & Gauthier, B. D. (2014). Relating background fractures to diagenesis and rock physical properties in a platform–slope transect. Example of the Maiella Mountain (central Italy). Marine and Petroleum Geology, 51, 2-19.

Lawn, B., 1993. Fracture of Brittle Solids. Cambridge University Press.

Leandro, C. G., Barboza, E. G., Caron, F., de Jesus, F. A., 2019. GPR trace analysis for coastal depositional environments of southern Brazil. *Journal of Applied Geophysics*, *162*, 1-12.

Lee, K., Gani, M. R., McMechan, G. A., Bhattacharya, J. P., Nyman, S. L., Zeng, X., 2007. Three-dimensional facies architecture and three-dimensional calcite concretion distributions in a tide-influenced delta front, Wall Creek Member, Frontier Formation, Wyoming. *AAPG bulletin*, *91*(2), 191-214. https://doi.org/10.1306/08310605114

Lemke, S. R., and L. C. Mankowski, 2000, GPR attribute analysis: Proceedings of the Symposium on the Application of Geo- physics to Engineering and Environmental Problems, Environ- mental and Engineering Geophysical Society, Wheat Ridge, Colorado, Arlington, Virginia, February 20 – 24, 2000, p. 263 – 272.

Leveille, G. P., Knipe, R., More, C., Ellis, D., Dudley, G., Jones, G., Fisher, Q.J., and Allinson, G.: Compartmentalization of Rotliegendes gas reservoirs by sealing faults, Jupiter Fields area, southern North Sea, Geol. Soc. Spec. Publ., 123(1), 87-104, https://doi.org/10.1144/GSL.SP.1997.123.01.06, 1997.

Lewis, H. and Couples, G. D.: Production evidence for geological heterogeneities in the Anschutz Ranch East field, western U.S.A., in: Characterization of fluvial and eolian reservoirs, edited by: C. P. North and D. J. Prosser, Geol. Soc. Spec. Publ., 73, p. 321–338, https://doi.org/10.1144/GSL.SP.1993.073.01.19, 1993.

Lioliou, M. G., Paraskeva, C. A., Koutsoukos, P. G., Payatakes, A. C. (2007). Heterogeneous nucleation and growth of calcium carbonate on calcite and quartz. Journal of colloid and interface science, 308(2), 421-428, https://doi.org/10.1016/j.jcis.2006.12.045.

Liu, M., Yund, R. A., 1995. The elastic strain energy associated with the olivine-spinel transformation and its implications. Physics of the Earth and Planetary Interiors, 89, 177-197.

Liu, Z., and Sun, Y., 2020. Characteristics and formation process of contractional deformation bands in oil-bearing sandstones in the hinge of a fold: A case study of the Youshashan anticline, western Qaidam Basin, China, Journal of Petroleum Science and Engineering, 106994, https://doi.org/10.1016/j.petrol.2020.106994.

Lohr, T., Krawczyk, C.M., Tanner, D.C., Samiee, R., Endres, H., Thierer, P.O., Oncken, O., Trappe, H., Bachmann, R., Kukla, P.A., 2008. Prediction of subseismic faults and fractures: integration of three-dimensional seismic data, three-dimensional retro deformation, and well data on an example of deformation around an inverted fault. AAPG Bull. 92, 473-485.

Lommatzsch, M., Exner, U., Gier, S., Grasemann, B., 2015. Structural and chemical controls of deformation bands on fluid flow: interplay between cataclasis and diagenetic alteration: structural and Chemical Controls of Deformation Bands on Fluid Flow, AAPG Bull., 99 (4), 689–710, DOI: 10.1306/10081413162.

Longman, M.W.: Carbonate diagenetic textures from nearsurface diagenetic environments, AAPG Bull., 64, 461–487, https://doi.org/10.1306/2F918A63-16CE-11D7-8645000102C1865D, 1980.

Lothe, A. E., Gabrielsen, R. H., Hagen, N. B., Larsen, B. T., 2002. An experimental study of the texture of deformation bands: effects on the porosity and permeability of sandstones. *Petroleum Geoscience*, *8*(3), 195-207.

Machel, H. G.: Application of cathodoluminescence to carbonate diagenesis, in: Cathodoluminescence in geosciences, edited by: Pagel, M., Barbin, V., Blanc, P., and Ohnenstetter D., Springer, Berlin, Heidelberg, pp. 271-301, DOI:10.1007/978-3-662-04086-7, 2000.

Madsen, H.B., Stemmerik, L., 2010. Diagenesis of flint and porcellanite in the Maastrichtian chalk at Stevns Klint, Denmark. Journal of Sedimentary Research, 80, 578-588.

Maerten, L., Gillespie, P., Daniel, J.M., 2006. Three-dimensional geomechanical modeling for constraint of sub-seismic fault simulation. AAPG Bull. 90, 1337-1358.

Maerten, L., Legrand, X., Castagnac, C., Lefranc, M., Joonnekindt, J. P., Maerten, F., 2019. Fault-related fracture modeling in the complex tectonic environment of the Malay Basin, offshore Malaysia: An integrated 4D geomechanical approach. *Marine and Petroleum Geology*, *105*, 222-237.

Magalhães, A. J. C., Lima-Filho, F. P., Guadagnin, F., Silva, V. A., Teixeira, W. L. E., Souza, A. M., Raja Gabaglia, G., P., Catuneanu, O., 2017. Ground penetrating radar for facies architecture and high-resolution stratigraphy: Examples from the Mesoproterozoic in the Chapada Diamantina Basin, Brazil. *Marine and Petroleum Geology*, *86*, 1191-1206.

Main, I. G., Kwon, O., Ngwenya, B. T., and Elphick, S. C.: Fault sealing during deformation-band growth in porous sandstone. Geology, 28(12), 1131-1134, https://doi.org/10.1130/0091-7613(2000)28<1131:FSDDGI>2.0.CO;2, 2000.

Main, I., Mair, K., Kwon, O., Elphick, S., Ngwenya, B., 2001. Experimental constraints on the mechanical and hydraulic properties of deformation bands in porous sandstones: a review. Geological Society, London, Special Publications, 186(1), 43-63.

Mair, K., Frye, K. M., Marone, C., 2002. Influence of grain characteristics on the friction of granular shear zones, J. Geophys. Res., 107(B10), 2219.

Mair, K., Main, I., Elphick, S., 2000. Sequential growth of deformation bands in the laboratory. *Journal of Structural Geology*, *22*(1), 25-42.

Mal, A.K., Singh, S.J., 1991. Deformation of Elastic Solids, Prentice-Hall, Englewood Cliffs, NJ.

Maliva, R.G., Knoll, A.H., Simonson, B.M.,2005. Secular change in the Precambrian silica cycle: insights from chert petrology. Geological Society of America Bulletin, 117, 835-845.

Maliva, R.G., Siever, R., 1989. Nodular Chert Formation in Carbonate Rocks. The Journal of Geology 97, 421–433. https://doi.org/10.1086/629320

Manzocchi, T., Ringrose, P. S., and Underhill, J. R., 1998. Flow through fault systems in high-porosity sandstones. Geol. Soc. Spec. Publ., 127(1), 65-82, https://doi.org/10.1144/GSL.SP.1998.127.01.06.

Marrett, R., Allmendinger, R.W., 1992. Amount of extension on “small” faults: an example from the Viking graben. Geology 20, 47-50.

Marroni, M., Meneghini, F., and Pandolfi, L.: A revised Subduction inception model to explain the late cretaceous, double-vergent orogen in the precollisional Western Tethys: Evidence from the Northern Apennines, Tectonics, 36, 2227–2249. https://doi.org/10.1002/2017TC004627, 2017.

Marshall, D.J.: Cathodoluminescence of geological Materials. Unwin Hyman, Boston, 1988.

Matthai, S.K., Aydin, A., Pollard, D.D. Roberts, S.G., 1998. Numerical simulation of departures from radial drawdown in faulted sandstone reservoir with joints and deformation bands. Geological Society, London, Special Publications, 147, 157–192.

Mayer, L., Menichetti, M., Nesci, O., Savelli, D., 2003. Morphotectonic approach to the drainage analysis in the North Marche region, central Italy. Quaternary International, 101–102, 157–167.

Mazzoli S., Deiana, G., Galdenzi, S., Cello, G., 2002. Miocene fault-controlled sedimentation and thrust propagation in the previously faulted external zones of the Umbria-Marche Apennines, Italy. EGU Stephan Mueller Special Publication Series, 1, 195-209.

McBride E. F., Milliken K. L, Cavazza W., Cibin U., Fontana D., Picard M. D., Zuffa G. G., 1995. Heterogeneous Distribution of Calcite Cement at the Outcrop Scale in Tertiary Sandstones, Northern Apennines, Italy. AAPG Bulletin, 79(7), 1044-1063.

McBride, E. F., 1996. How predictable are patterns of calcite cement in sandstones? (abs.): AAPG Annual Meeting Program, v. 5, p. A79.

Medeiros, W. E., Do Nascimento, A. F., da Silva, F. A., Destro, N., Demétrio, J. G. A., 2010. Evidence of hydraulic connectivity across deformation bands from field pumping tests: two examples from Tucano Basin, NE Brazil. *Journal of Structural Geology*, *32*(11), 1783-1791.

Medici, G., West, L. J., Mountney, N. P., and Welch, M.: Permeability of rock discontinuities and faults in the Triassic Sherwood Sandstone Group (UK): insights for management of fluvio-aeolian aquifers worldwide. Hydrogeology Journal, 27(8), 2835-2855, https://doi.org/10.1007/s10040-019-02035-7, 2019.

Menditto, G., Bufarini, S., D'Aria, V., 2013. Risultati di una campagna sperimentale per il tracciamento delle curve di correlazione per lo sclerometro per roccia. Articolo tecnico – GeoHAMMER. DRC Srl. https://www.drcitalia.it/en/.

Menéndez, B., Zhu, W., Wong, T.F., 1996. Micromechanics of brittle faulting and cataclastic flow in Berea sandstone: Journal of Structural Geology, v. 18, p. 1–16.

Mercier, S., Jacques, N., Molinari, A., 2005. Validation of an interaction law for the Eshelby inclusion problem in elasto-viscoplasticity. International Journal of Solids and Structures, 42, 1923-1941.

Mercier, S., Molinari, A., Berbenni, S., Berveiller, M., 2012. Comparison of different homogenization approaches for elastic–viscoplastic materials. Modelling Simul. Mater. Sci. Eng. 20, 024004. https://doi.org/10.1088/0965-0393/20/2/024004.

Michie, E. A. H., Haines, T. J., Healy, D., Neilson, J. E., Timms, N. E., & Wibberley, C. A. J. (2014). Influence of carbonate facies on fault zone architecture. Journal of Structural Geology, 65, 82-99.

Milliken, K. L., Reed, R. M., and Laubach, S. E.: Quantifying compaction and cementation in deformation bands in porous sandstones, in: Faults, fluid flow, and petroleum traps, edited by: R. Sorkhabi and Y. Tsuji, AAPG Mem., 85, 237–249, DOI:10.1306/1033726M85252, 2005.

Milliken, K.L., McBride, E.F., Cavazza, W., Cibin, U., Fontana, D., Picard, M.D., and Zuffa, G.G., 1998. Geochemical history of calcite precipitation in Tertiary sandstones, northern Apennines, Italy, in: Carbonate cementation in sandstones, edited by: Morad, S., International Association of Sedimentologists Special Publication 26, pp. 213–239, https://doi.org/10.1002/9781444304893.ch10.

Mollema, P. N., Antonellini, M. A., 1996. Compaction bands: a structural analog for anti-mode I cracks in aeolian sandstone. *Tectonophysics*, *267*(1-4), 209-228.

Mollema, P.N., Antonellini, M., 1999. Development of strike-slip faults in the dolomites of the Sella Group, Northern Italy. Journal of Structural Geology, 21, 273-292.

Mondal, T.K., Acharyya, S.S., 2018. Fractured micro-granitoid enclaves: A stress marker. Journal of Structural Geology 113, 33–41. https://doi.org/10.1016/j.jsg.2018.05.011

Montanari, A., Mainiero, M., Coccioni, R., Pignocchi, G., 2016. Catastrophic landslide of medieval Portonovo (Ancona, Italy). GSA Bulletin, 128, 1660-1678.

Montanari, A., Sandroni, P., 1995. Le Rocce del Conero: Una guida geologica del Parco del Conero. Ed. Parco Naturale del Conero, Sirolo, Aniballi Grafiche S.r.l. Ancona, 63 pp.

Moore, C.H.: Carbonate Diagenesis and Porosity, Elsevier, Amsterdam, 1989.

Morad, S. (Ed.) 1998, Carbonate cementation in sandstones. International Association of Sedimentologists Special Publication 26, John Wiley & Sons.

Morad, S., Al-Ramadan, K., Ketzer, J. M., and De Ros, L. F.: The impact of diagenesis on the heterogeneity of sandstone reservoirs: A review of the role of depositional facies and sequence stratigraphy, AAPG Bull., 94(8), 1267-1309, https://doi.org/10.1306/04211009178, 2010.

Morad, S., Ketzer, J. R. M., De Ros, L. F., 2000. Spatial and temporal distribution of diagenetic alterations in siliciclastic rocks: implications for mass transfer in sedimentary basins. *Sedimentology*, *47*, 95-120.

Mozley, P. S. and Davis, J. M.: Relationship between oriented calcite concretions and permeability correlation structure in an alluvial aquifer, Sierra Ladrones Formation, New Mexico, J. Sediment. Res., 66(1), 11-16, https://doi.org/10.1306/D4268293-2B26-11D7-8648000102C1865D, 1996.

Mozley, P. S., Davis, J. M., 2005. Internal structure and mode of growth of elongate calcite concretions: Evidence for small-scale, microbially induced, chemical heterogeneity in groundwater. *Geological Society of America Bulletin*, *117*(11-12), 1400-1412.

Mozley, P. S., Goodwin, L. B., 1995. Patterns of cementation along a Cenozoic normal fault: A record of paleoflow orientations. *Geology*, *23*(6), 539-542.

Mura, T., 2012. Micromechanics of Defects in Solids. Springer Science & Business Media.

Neal, A., 2004. Ground-penetrating radar and its use in sedimentology: principles, problems and progress. *Earth-science reviews*, *66*(3-4), 261-330.

Nelson, C.S. and Smith, A.M.: Stable oxygen and carbon isotope compositional fields for skeletal and diagenetic components in New Zealand Cenozoic nontropical carbonate sediments and limestones: a synthesis and review, New Zealand Journal of Geology and Geophysics, 39, 93–107, https://doi.org/10.1080/00288306.1996.9514697, 1996.

Nicchio, M. A., Nogueira, F. C., Balsamo, F., Souza, J. A., Carvalho, B. R., Bezerra, F. H., 2018. Development of cataclastic foliation in deformation bands in feldspar-rich conglomerates of the Rio do Peixe Basin, NE Brazil. Journal of Structural Geology

Nichols, G. 2009. *Sedimentology and stratigraphy*. John Wiley & Sons.

Noiriel, C., 2015. Resolving time-dependent evolution of pore-scale structure, permeability and reactivity using X-ray microtomography. *Reviews in Mineralogy and Geochemistry*, *80*(1), 247-285.

Noiriel, C., Luquot, L., Madé, B., Raimbault, L., Gouze, P., Van Der Lee, J., 2009. Changes in reactive surface area during limestone dissolution: An experimental and modelling study. *Chemical Geology*, *265*(1-2), 160-170.

Noiriel, C., Steefel, C. I., Yang, L., Ajo-Franklin, J., 2012. Upscaling calcium carbonate precipitation rates from pore to continuum scale. *Chemical Geology*, *318*, 60-74.

Noiriel, C., Steefel, C. I., Yang, L., and Bernard, D.: Effects of pore-scale precipitation on permeability and flow. Advances in water resources, 95, 125-137, https://doi.org/10.1016/j.advwatres.2015.11.013, 2016.

Ogilvie, S. R. and Glover, P.W.: The petrophysical properties of deformation bands in relation to their microstructure, Earth Planet. Sci. Lett., 193(1-2), 129-142, https://doi.org/10.1016/S0012-821X(01)00492-7, 2001.

Olhoeft, G. R. (1998, May). Electrical, magnetic and geometric properties that determine ground penetrating radar performance. In *Proceedings of GPR* (Vol. 98, pp. 177-182).

Olsson, O., Falk, L., Forslund, O., Lundmark, L., Sandberg, E., 1992. Borehole radar applied to the characterization of hydraulically conductive fracture zones in crystalline rock. *Geophysical prospecting*, 40(2), 109-142.

Pabst, W., Gregorova, E., 2007. Characterization of particles and particle systems. Prague: ICT, 27- 29.

Pabst, W., Gregorová, E., 2013. Elastic properties of silica polymorphs – A review. Ceramics – Silikáty, 57, 167-184.

Papani, L., 1998. Le arenarie di Loiano nel contesto dell'Appennino settentrionale. PhD thesis. Università di Bologna, Bologna, pp. 40.

Parkhurst, D. L., Kipp, K. L., & Charlton, S. R. (2010). PHAST Version 2—A program for simulating groundwater flow, solute transport, and multicomponent geochemical reactions. US Geological Survey Techniques and Methods, 6, A35.

Parnell, J., Watt, G. R., Middleton, D., Kelly, J., and Baron, M.: Deformation band control on hydrocarbon migration, J. Sediment. Res., 74(4), 552-560, https://doi.org/10.1306/121703740552, 2004.

Parry, W. T., Chan, M. A., and Beitler, B.: Chemical bleaching indicates episodes of fluid flow in deformation bands in sandstone, AAPG Bull., 88(2), 175-191, https://doi.org/10.1306/09090303034, 2004.

Paxton, S. T., Szabo, J. O., Ajdukiewicz, J. M., Klimentidis, R. E., 2002. Construction of an intergranular volume compaction curve for evaluating and predicting compaction and porosity loss in rigid-grain sandstone reservoirs. AAPG bulletin, 86(12), 2047

Pei, Y., Paton, D. A., Knipe, R. J., Wu, K., 2015. A review of fault sealing behaviour and its evaluation in siliciclastic rocks. Earth Sci. Rev., 150, 121-138, http://dx.doi.org/10.1016/j.earscirev.2015.07.011.

Perras, M.A., Diederichs, M.S., 2014. A Review of the Tensile Strength of Rock: Concepts and Testing. Geotech GeolEng 32, 525–546. https://doi.org/10.1007/s10706-014-9732-0

Petracchini, L., Antonellini, M., Billi, A., Scrocca, D., 2015a. Syn-thrusting polygonal normal faults exposed in the hinge of the Cingoli anticline, northern Apennines, Italy. Front. Earth Sci. 3. https://doi.org/10.3389/feart.2015.00067

Petracchini, L., Antonellini, M., Billi, A., Scrocca, D., Trippetta, F., Mollo, S., 2015b. Pressure solution inhibition in a limestone–chert composite multilayer: Implications for the seismic cycle and fluid flow. Tectonophysics 646, 96–105. https://doi.org/10.1016/j.tecto.2015.02.005

Petrie, E. S., Petrie, R. A., and Evans, J. P.: Identification of reactivation and increased permeability associated with a fault damage zone using a multidisciplinary approach. J. Struct. Geol., 59, 37-49, https://doi.org/10.1016/j.jsg.2013.11.008, 2014.

Philit, S., Soliva, R., Ballas, G., Chemenda, A., and Castilla, R., 2019. Fault surface development and fault rock juxtaposition along deformation band clusters in porous sandstones series. AAPG Bull., 103(11), 2731-2756, doi: 10.1306/01211917256.

Philit, S., Soliva, R., Castilla, R., Ballas, G., Taillefer, A., 2018. Clusters of cataclastic deformation bands in porous sandstones, Journal of Structural Geology.

Philit, S., Soliva, R., Labaume, P., Gout, C., Wibberley, C., 2015. Relations between shallow cataclastic faulting and cementation in porous sandstones: first insight from a groundwater environmental context. *Journal of Structural Geology*, *81*, 89-105.

Phillips, O. M., 2009. *Geological fluid dynamics: sub-surface flow and reactions*. Cambridge University Press.

Picotti, V. and Pazzaglia, F. J.: A new active tectonic model for the construction of the Northern Apennines mountain front near Bologna (Italy). J. Geophys. Res.: Solid Earth, 113(B8), doi:10.1029/2007JB005307, 2008.

Picotti, V., Ponza, A., Pazzaglia, F. J., 2009. Topographic expression of active faults in the foothills of the Northern Apennines. Tectonophysics, 474(1-2), 285-294, doi:10.1016/j.tecto.2009.01.009.

Pizzati, M., Balsamo, F., Storti, F., Iacumin, P., 2020. Physical and chemical strain-hardening during faulting in poorly lithified sandstone: The role of kinematic stress field and selective cementation. Geol. Soc. Am. Bull., 132 (5-6): 1183–1200, https://doi.org/10.1130/b35296.1.

Pollard, D.D., Aydin, A., 1988. Progress in understanding jointing over the past century. Geological Society of America Bulletin, 100(8), 1181-1204.

Pollard, D.D., Fletcher, R.C., 2005. Fundamentals of structural geology. Cambridge University Press.

Pollard, D.D., Segall, P., 1987. Theoretical displacements and stresses near fractures in rock: with applications to faults, joints, veins, dikes, and solution surfaces. In: *Fracture Mechanics of Rock* (edited by Atkinson, B. K.). Academic Press, London, 277-349.

Pontes, C. C., Nogueira, F. C., Bezerra, F. H., Balsamo, F., Miranda, T. S., Nicchio, M. A., Souza, J. A., Carvalho, B. R., 2019. Petrophysical properties of deformation bands in high porous sandstones across fault zones in the Rio do Peixe Basin, Brazil. *Int. J. Rock Mech. Min. 114*, 153-163.

Priest, S.D., Hudson, J.A., 1976. Discontinuity spacing in rock. International Journal of Rock Mechanics and Mining Science, and Geomechanics Abstracts, 13, 135-148.

Priest, S.D., Hudson, J.A.,1981. Estimation of discontinuity spacing and trace length using scanline surveys. International Journal of Rock Mechanics and Mining Science, and Geomechanics Abstracts, 18, 183-197.

Přikryl, R., 2001. Some microstructural aspects of strength variation in rocks. *Int. J. Rock Mech. Min. 38*(5), 671-682.

Qu, D., Tveranger, J., 2016. Incorporation of deformation band fault damage zones in reservoir models. AAPG Bull., 100(3), 423-443, DOI:10.1306/12111514166.

Qu, D., Tveranger, J., Fachri, M., 2017. Influence of deformation-band fault damage zone on reservoir performance. *Interpretation*, *5*(4), SP41-SP56.

Quesada, D., Leguillon, D., Putot, C., 2009. Multiple failures in or around a stiff inclusion embedded in a soft matrix under a compressive loading. European Journal of Mechanics A/Solids. 28, 668–679.

R Core Team, 2018. R: A language and environment for statistical computing. R Foundation for Statistical Computing, Vienna, Austria.

Rath, A., Exner, U., Tschegg, C., Grasemann, B., Laner, R., Draganits, E., 2011. Diagenetic control of deformation mechanisms in deformation bands in a carbonate grainstone. *AAPG bulletin*, *95*(8), 1369-1381.

Rawling, G. C., Goodwin, L. B., 2003. Cataclasis and particulate flow in faulted, poorly lithified sediments. Journal of Structural Geology, 25(3), 317-331.

Rawling, G.C., Goodwin, L.B., Wilson, J.L., 2001. Internal architecture, permeability structure, and hydrologic significance of contrasting fault-zone types. Geology 29, 43-46.

Reis, J.C., Acock, A.M., 1994. Permeability reduction models for the precipitation of inorganic solid in Berea sandstone. In Situ; 18:347–68.

Renshaw, C.E., Pollard, D.D., 1995. An experimentally verified criterion for propagation across unbounded frictional interfaces in brittle, linear elastic materials. International Journal of Rock Mechanics and Mining Sciences & Geomechanics Abstracts 32, 237–249. https://doi.org/10.1016/0148-9062(94)00037-4.

Ricci Lucchi, F., 1986. The Oligocene to Recent foreland basins of the Northern Apennines. International Association of Sedimentologists. Special Publication 8, 165–185.

Roatta, A., Bolmaro, R.E., 1997a. An Eshelby inclusion based model for the study of stresses and plastic strain localization in metal matrix composites II. Fiber reinforcement and lamellar inclusions. Materials Science and Engineering: A, 229, 192–202, https://doi.org/10.1016/S0921-5093(96)10843-1.

Roatta, A., Bolmaro, R.E., 1997b. An Eshelby inclusion-based model for the study of stresses and plastic strain localization in metal matrix composites I: General formulation and its application to round particles. Materials Science and Engineering: A 229, 182–191. https://doi.org/10.1016/S0921-5093(96)10845-5

Romano, C. R., Zahasky, C., Garing, C., Minto, J. M., Benson, S. M., Shipton, Z. K., and Lunn, R. J.: Sub-core scale fluid flow behavior in a sandstone with cataclastic deformation bands. Water Resour. Res., DOI:10.1029/2019WR026715, 2020.

Rotevatn, A., Fossen, H., 2011. Simulating the effect of subseismic fault tails and process zones in a siliciclastic reservoir analogue: Implications for aquifer support and trap definition. *Marine and Petroleum Geology*, *28*(9), 1648-1662, doi:10.1016/j.marpetgeo.2011.07.005.

Rotevatn, A., Fossmark, H. S., Bastesen, E., Thorsheim, E., Torabi, A., 2017. Do deformation bands matter for flow? Insights from permeability measurements and flow simulations in porous carbonate rocks. *Petroleum Geoscience*, *23*(1), 104-119.

Rotevatn, A., Sandve, T. H., Keilegavlen, E., Kolyukhin, D., & Fossen, H. 2013. Deformation bands and their impact on fluid flow in sandstone reservoirs: the role of natural thickness variations. *Geofluids*, *13*(3), 359-371, https://doi.org/10.1111/gfl.12030.

Rotevatn, A., Thorsheim, E., Bastesen, E., Fossmark, H. S., Torabi, A., Sælen, G., 2016. Sequential growth of deformation bands in carbonate grainstones in the hangingwall of an active growth fault: implications for deformation mechanisms in different tectonic regimes. *Journal of Structural Geology*, *90*, 27-47. https://doi.org/10.1016/j.jsg.2016.07.003

Rotevatn, A., Torabi, A., Fossen, H., Braathen, A., 2008. Slipped deformation bands: A new type of cataclastic deformation bands in Western Sinai, Suez rift, Egypt. *Journal of Structural Geology*, *30*(11), 1317-1331.

Rotevatn, A., Tveranger, J., Howell, J.A., Fossen, H., 2009. Dynamic investigation of the effect of a relay ramp on simulated fluid flow: geocellular modelling of the Delicate Arch Ramp, Utah. Petroleum Geoscience 15, 45-58.

Roure, F., Brun, J.P., Colletta, B., and Van den Driessche, J.: Geometry and kinematics of extensional structures in the Alpine Foreland Basin of southeastern France. J. Struct. Geol., 14, 503-519, https://doi.org/10.1016/0191-8141(92)90153-N, 1992.

Ruiz, F., Cheng, A., 2010. A rock physics model for tight gas sand. The Leading Edge, 29, 1484-1489.

Saillet, E.: La localisation de la déformation dans les grès poreux: caractérisation d'un analogue de réservoir gréseux et faillé dans le Bassin du Sud-Est, Provence, France. Unpublished Docteur en Sciences thesis, Université de Nice-Sophia Antipolis, 2009.

Saillet, E. and Wibberley, C.A.J.: Evolution of cataclastic faulting in high-porosity sandstone, Bassin du Sud-Est, Provence, France. J. Struct. Geol., 32, 1590-1608, https://doi.org/10.1016/j.jsg.2010.02.007, 2010.

Salvi, S., Cinti, F.R., Colini, L., D'Addezio, G., Doumaz, F., Pettinelli, E., 2003. Investigation of the active Celano-L'Aquila fault system, Abruzzi (central Apennines, Italy) with combined ground-penetrating radar and palaeoseismic trenching, *Geophys. J. Int.,* 155(3), 805–818.

Salvini, F., 2004. Daisy 3: The Structural Data Integrated System Analyzer Software. University of Roma Tre, Rome, available at: http://host.uniroma3.it/progetti/fralab/Downloads/Programs/ (last access: 25 August: 25 August 2020).

Sammis, C., King, G., Biegel, R., 1987. The kinematics of gouge deformation. *Pure and Applied Geophysics*, *125*(5), 777-812.

Sample, J. C., Woods, S., Bender, E., and Loveall, M.: Relationship between deformation bands and petroleum migration in an exhumed reservoir rock, Los Angeles Basin, California, USA. Geofluids, 6(2), 105-112, doi:10.1111/j.1468-8123.2005.00131.x, 2006.

Sanchis, E. and Séranne, M.: Structural style and tectonic evolution of a polyphase extensional basin of the Gulf of Lion passive margin: the Tertiary Alès basin, southern France. Tectonophysics 322, 219-242, https://doi.org/10.1016/S0040-1951(00)00097-4, 2000.

Sarti, M., Coltorti, M., Budini, A., Mattioni, M., Pieruccini, P., & Rossini, L., 2011. Carta Geologica d'Italia alla scala 1: 50.000 Foglio 293 Osimo.

Schmidt, R.A., 1976. Fracture-toughness Testing of Limestone. Experimental Mechanics, 8, 161-167.

Schöpfer, M. P., Abe, S., Childs, C., Walsh, J. J., 2009. The impact of porosity and crack density on the elasticity, strength and friction of cohesive granular materials: insights from DEM modelling. *International Journal of Rock Mechanics and Mining Sciences*, *46*(2), 250-261. https://doi.org/10.1016/j.ijrmms.2008.03.009.

Schueller, S., Braathen, A., Fossen, H., Tveranger, J., 2013. Spatial distribution of deformation bands in damage zones of extensional faults in porous sandstones: Statistical analysis of field data. Journal of Structural Geology, 52, 148-162.

Schultz, R.A., Fossen, H., 2008. Terminology for structural discontinuities. AAPG Bulletin 92, 853–867. https://doi.org/10.1306/02200807065

Séranne, M., Benedicto, A., Labaume, P., Truffert, C., and Pascal, G.: Structural style and evolution of the gulf of Lion Oligo-miocene rifting: role of the Pyrenean orogeny. Mar. Pet. Geol. 12 (8), 809-820, https://doi.org/10.1016/0264-8172(95)98849-Z, 1995.

Shipton, Z. K., Cowie, P. A., 2001. Damage zone and slip-surface evolution over μm to km scales in high-porosity Navajo sandstone, Utah. *Journal of Structural Geology*, *23*(12), 1825-1844.

Shipton, Z. K., Cowie, P. A., 2003. A conceptual model for the origin of fault damage zone structures in high-porosity sandstone. *Journal of Structural Geology*, *25*(3), 333-344.

Shipton, Z. K., Evans, J. P., Robeson, K. R., Forster, C. B., Snelgrove, S., 2002. Structural heterogeneity and permeability in faulted eolian sandstone: Implications for subsurface modeling of faults. AAPG bulletin, 86(5), 863-883, https://doi.org/10.1306/61EEDBC0-173E-11D7-8645000102C1865D.

Shipton, Z.K., Evans, J.P., and Thompson, L.B.: The geometry and thickness of deformation-band fault core and its influence on sealing characteristics of deformation-band fault zones, in: Faults, fluid flow, and petroleum traps, edited by: R. Sorkhabi and Y. Tsuji, AAPG Mem., 85, 181-195, DOI:10.1306/1033723M853135, 2005.

Sigda, J. M., Goodwin, L. B., Mozley, P. S., and Wilson, J. L.: Permeability alteration in small-displacement faults in poorly lithified sediments: Rio Grande Rift, Central New Mexico, in: Faults and Subsurface Fluid Flow in the Shallow Crust, edited by: Haneberg, W. C., Mozley, P. S., Moore, J. C., and Goodwin, L. B., American Geophysical Union, Washington, DC, 51-68, https://doi.org/10.1029/GM113p0051, 1999.

Sigda, J.M., Wilson, J.L., 2003. Are faults preferential flow paths through semiarid and arid vadose zones? Water Resour. Res. 39 (8), https://doi.org/10.1029/2002WR001406.

Skurtveit, E., Torabi, A., Alikarami, R., Braathen, A. 2015. Fault baffle to conduit developments: reactivation and calcite cementation of deformation band fault in aeolian sandstone. Petroleum Geoscience, 21(1), 3-16.

Slater, L., Comas, X., 2009. The contribution of ground penetrating radar to water resource research. In: Jol, H. M. (Ed.), Ground penetrating radar: theory and applications, Elsevier, 203-246.

Slater, L., Niemi, T. M., 2003. Ground-penetrating radar investigation of active faults along the Dead Sea Transform and implications for seismic hazards within the city of Aqaba, Jordan. *Tectonophysics*, *368*(1-4), 33-50.

Smith, I. B., Holt, J. W., 2015. Spiral trough diversity on the north pole of Mars, as seen by Shallow Radar (SHARAD). *Journal of Geophysical Research: Planets*, *120*(3), 362-387.

Soliva, R., Ballas, G., Fossen, H., Philit, S., 2016. Tectonic regime controls clustering of deformation bands in porous sandstone. *Geology*, *44*(6), 423-426.

Soliva, R., Schultz, R. A., Ballas, G., Taboada, A., Wibberley, C., Saillet, E., Benedicto, A., 2013. A model of strain localization in porous sandstone as a function of tectonic setting, burial and material properties; new insight from Provence (southern France). *Journal of Structural Geology*, *49*, 50-63. https://doi.org/10.1016/j.jsg.2012.11.011

Soltanzadeh, H., Hawkes, C.D., 2008. Semi-analytical models for stress change and fault reactivation induced by reservoir production and injection. Journal of Petroleum Science and Engineering 60, 71–85, https://doi.org/10.1016/j.petrol.2007.05.006.

Sone, H., Zoback, M.D., 2013. Mechanical properties of shale-gas reservoir rocks — Part 2: Ductile creep, brittle strength, and their relation to the elastic modulus. Geophysics, 78, D393–D402. 10.1190/GEO2013-0051.1.

Sternlof, K. R., Chapin, J. R., Pollard, D. D., and Durlofsky, L. J., 2004. Permeability effects of deformation band arrays in sandstone. AAPG Bull., 88(9), 1315-1329, https://doi.org/10.1306/032804.

Sternlof, K.R., Rudnicki, J.W., Pollard, D.D., 2005. Anticrack inclusion model for compaction bands in sandstone: anticrack bands. J. Geophys. Res. 110. https://doi.org/10.1029/2005JB003764

Stockmann, G. J., Wolff-Boenisch, D., Bovet, N., Gislason, S. R., and Oelkers, E. H.: The role of silicate surfaces on calcite precipitation kinetics. *Geochimica et Cosmochimica Acta*, *135*, 231-250, https://doi.org/10.1016/j.gca.2014.03.015, 2014.

Sulem, J., Ouffroukh, H., 2006. Shear banding in drained and undrained triaxial tests on a saturated sandstone: Porosity and permeability evolution. *International journal of rock mechanics and mining sciences*, *43*(2), 292-310.

Szerbiak, R. B., McMechan, G. A., Corbeanu, R., Forster, C., Snelgrove, S. H., 2001. 3-D characterization of a clastic reservoir analog: From 3-D GPR data to a 3-D fluid permeability model. *Geophysics*, *66*(4), 1026-1037.

Taliaferro, N.L., 1934. Contraction phenomena in cherts. Bulletin of the Geological Society of America, 48, 189-232.

Tavani, S., Granado, P., Balsamo, F., Pizzati, M., Cantarero, I., Corradetti, A., Muñoz, J. A., 2018. Shear-enhanced compaction-solution bands in quartz-rich calcarenites of the Cotiella Massif (Spanish Pyrenees). *Journal of Structural Geology*, *114*, 274-279. https://doi.org/10.1016/j.jsg.2017.11.018

Taylor, W. L. and Pollard, D. D.: Estimation of in situ permeability of deformation bands in porous sandstone, Valley of Fire, Nevada. Water Resour. Res. 36(9), 2595-2606, https://doi.org/10.1029/2000WR900120, 2000.

Teng, H.H., Dove, P.M., De Yoreo, J.J., 2000. Kinetics of calcite growth: surface processes and relationships to macroscopic rate laws. Geochim Cosmochim Acta; 64: 2255–66.

Tenthorey, E., Scholz, C.H., Aharonov, E., and Leger, A.: Precipitation sealing and diagenesis 1. Experimental results. J. Geophys. Res.: Solid Earth 103 (B10), 23951-23967, https://doi.org/10.1029/98JB02229, 1998.

Theune, U., Rokosh, D., Sacchi, M.D., Schmitt, D.R., 2006. Mapping fractures with GPR: A case study from Turtle Mountain. Geophysics 71, B139–B150.

Tondi, E., Antonellini, M., Aydin, A., Marchegiani, L., Cello, G., 2006. The role of deformation bands, stylolites and sheared stylolites in fault development in carbonate grainstones of Majella Mountain, Italy. Journal of Structural Geology, 28(3), 376-391.

Tondi, E., Cilona, A., Agosta, F., Aydin, A., Rustichelli, A., Renda, P., & Giunta, G. (2012). Growth processes, dimensional parameters and scaling relationships of two conjugate sets of compactive shear bands in porous carbonate grainstones, Favignana Island, Italy. Journal of Structural Geology, 37, 53-64.

Topp, G.C., Davis, J.L., Annan, A.P., 1980. Electromagnetic determination of soil water content: measurements in coaxial transmission lines. Water Resources Res., 16, 574-582.

Torabi, A., A. Braathen, F. Cuisiat, Fossen, H., 2007. Shear zones in porous sand: Insights from ring-shear experiments and naturally deformed sandstones: Tectonophysics, v. 437, p. 37–50.

Torabi, A., Alaei, B., Ellingsen, T. S. S., 2018. Faults and fractures in basement rocks, their architecture, petrophysical and mechanical properties. *Journal of Structural Geology*.

Torabi, A., Alikarami, R., 2012. Heterogeneity within deformation bands in sandstone reservoirs. In *46th US Rock Mechanics/Geomechanics Symposium*. American Rock Mechanics Association.

Torabi, A., Fossen, H., 2009. Spatial variation of microstructure and petrophysical properties along deformation bands in reservoir sandstones. AAPG *Bulletin*, *93*(7), 919-938.

Torabi, A., H. Fossen, Alaei, B., 2008. Application of spatial correlation functions in permeability estimation of deformation bands in porous rocks, J. Geophys. Res., 113, B08208.

Tucker, M. E., 2003. *Sedimentary rocks in the field*. John Wiley & Sons.
Tueckmantel, C., Fisher, Q. J., Grattoni, C. A., and Aplin, A. C.: Single-and two-phase fluid flow properties of cataclastic fault rocks in porous sandstone. *Marine and Petroleum Geology*, 29(1), 129-142, doi:10.1016/j.marpetgeo.2011.07.009, 2012.
Tueckmantel, C., Fisher, Q. J., Knipe, R. J., Lickorish, H., Khalil, S. M., 2010. Fault seal prediction of seismic-scale normal faults in porous sandstone: a case study from the eastern Gulf of Suez rift, Egypt. *Marine and Petroleum Geology*, *27*(2), 334-350.
Tullis, J., Yund, R.A., 1987. Transition from cataclastic flow to dislocation creep of feldspar: mechanisms and microstructures. Geology 15, 606–609.
Turcotte, D.L., 1997. Fractals and Chaos in Geology and Geophysics. Cambridge University Press.
Underhill, J. R., Woodcock, N. H., 1987. Faulting mechanisms in high-porosity sandstones; new red sandstone, Arran, Scotland. *Geological Society, London, Special Publications*, *29*(1), 91-105.
Vai, G. B., Martini, I. P. (Eds.): Anatomy of an orogen: The Apennines and Adjacent Mediterranean Basins, p. 637, Dordrecht, Netherlands, Kluwer Academic Publishers, 2001.
van Noort, R., Yarushina, V., 2019. Water, CO 2 and argon permeabilities of intact and fractured shale cores under stress. Rock Mech. Rock Eng. 52, 299–319. https://doi. org/10.1007/s00603-018-1609-8.
Verschuren, M., 2019. Outcrop evidence of polygonal faulting in Ypresian marine clays (Southern North Sea Basin) leads to a new synthesis. *Marine Geology*, *413*, 85-98.
Walderhaug, O., 1996. Kinetic modeling of quartz cementation and porosity loss in deeply buried sandstone reservoirs. AAPG bulletin, 80(5), 731-745.
Walderhaug, O.: Modeling quartz cementation and porosity in middle Jurassic Brent Group sandstones of the Kvitebjørn field, Northern North Sea, AAPG Bull., 84, 1325-1339, 2000.
Walker, P. and Sheikholeslami, R.: Assessment of the effect of velocity and residence time in CaSO4 precipitating flow reaction. Chemical engineering science, 58(16), 3807-3816, https://doi.org/10.1016/S0009-2509(03)00268-9, 2003.
Walsh, J.J., Watterson, J., Heath, A., Gillepsie, P.A., Childs, C., 1998. Assessment of the effects of sub-seismic faults on bulk permeabilities of reservoir sequences. In: Geological Society of London, Special Publications, vol. 127, pp. 99-114.
Wang, Z., Su, J., Zhu, G., Han, J., Wang, Y., 2013. Characteristics and accumulation mechanism of quasi-layered Ordovician carbonate reservoirs in the Tazhong area, Tarim Basin.
Wänstedt, S., Carlsten, S., Tirén, S., 2000. Borehole radar measurements aid structure geological interpretations. *Journal of Applied Geophysics*, *43*(2-4), 227-237.
Wennberg, O.P., Svånå, T., Azizzadeh, M., Aqrawi, A.M.M., Brockbank, P., Lyslo, K.B., Ogilvie, S., 2006. Fracture intensity vs. mechanical stratigraphy in platform top carbonates: the Aquitanian of the Asmari Formation, Khaviz Anticline, Zagros, SW Iran. Petroleum Geoscience 12, 235–246. https://doi.org/10.1144/1354-079305-675.
Whitworth, T. M., Haneberg, W. C., Mozley, P. S., and Goodwin, L. B.: Solute-sieving-induced calcite precipitation on pulverized quartz sand: experimental results and implications for the membrane behavior of fault gouge, in: Faults and Subsurface Fluid Flow in the Shallow Crust, edited by: Haneberg, W. C., Mozley, P. S., Moore, J. C., and Goodwin, L. B., American Geophysical Union, Washington, DC, 149-158, https://doi.org/10.1029/GM113p0149, 1999.
Wibberley, C.A.J., Petit, J.-P., and Rives, T.: The mechanics of fault distribution and localization in high-porosity sands, Provence, France, Geol. Soc. Spec. Publ., 289, 19-46, DOI:10.1144/SP289.3, 2007.
Wickham, H., 2016. ggplot2: Elegant Graphics for Data Analysis. Springer-Verlag New York.
Wierer, U., Bertola, S., 2016. The Sauveterrian Chert Assemblage of Galgenbühel, Dos de la Forca (Adige Valley, South Tyrol, Italy): Procurement Areas, Reduction Sequences, Tool Making. In Ressources lithiques, productions et transferts entre Alpes et Méditerranée. Séances de la Sociétè préhistorique francaise.

Wilkins, S. J., Davies, R. K., and Naruk, S. J.: Subsurface observations of deformation bands and their impact on hydrocarbon production within the Holstein Field, Gulf of Mexico, USA, Geol. Soc. Spec. Publ., 496, https://doi.org/10.1144/SP496-2018-139, 2019.

Wilkinson, M., Dampier, M. D., 1990. The rate of growth of sandstone-hosted calcite concretions. *Geochimica et Cosmochimica Acta*, *54*(12), 3391-3399.

Willemse, E.J.M., Pollard, D.D., 1998. On the orientation and patterns of wing cracks and solution surfaces at the tips of a sliding flaw or fault. Journal of Geophysical Research: Solid Earth 103, 2427–2438, https://doi.org/10.1029/97JB01587.

Williams, R. T., Goodwin, L. B., Mozley, P. S., 2016. Diagenetic controls on the evolution of fault-zone architecture and permeability structure: Implications for episodicity of fault-zone fluid transport in extensional basins. Geol. Soc. Am. Bull., 129(3-4), 464-478, https://doi.org/10.1130/B31443.1.

Williams, R.T., Farver, J.R., Onasch, C.M., Winslow, D.F., 2015. An experimental investigation of the role of microfracture surfaces in controlling quartz precipitation rate: applications to fault zone diagenesis. J. Struct. Geol., 74, 24-30, https://doi.org/10.1016/j.jsg.2015.02.011.

Wilson, J. E., Goodwin, L. B., and Lewis, C. J.: Deformation bands in nonwelded ignimbrites: Petrophysical controls on fault-zone deformation and evidence of preferential fluid flow. Geology, 31(10), 837-840, https://doi.org/10.1130/G19667R.1, 2003.

Wilson, J. E., Goodwin, L. B., Lewis, C., 2006. Diagenesis of deformation band faults: Record and mechanical consequences of vadose zone flow and transport in the Bandelier Tuff, Los Alamos, New Mexico. Journal of Geophysical Research: Solid Earth, 111(B9).

Wollast, R., 1971. Kinetic aspects of the nucleation and growth of calcite from aqueous solutions, *in*: Bricker, O.P., Mackenzie, F.T., (*Eds*.), Carbonate Cements, J. Hopkins Press, 79, 264–273.

Wong, T.-f., David, C. & Zhu, Q. 1997. The transition from brittle faulting to cataclastic flow in porous sandstones: mechanical deformation. Journal of Geophysical Research, 102, 3009–3025.

Wood, M.M., Weidlich, J.E., 1982. Empirical evaluation of fracture toughness: the toughness of quartz. American Mineralogist, 67, 1065-1066.

Worden, R. H., Armitage, P. J., Butcher, A. R., Churchill, J. M., Csoma, A. E., Hollis, C., Lander, R. H., Omma, J. E., 2018. Petroleum reservoir quality prediction: overview and contrasting approaches from sandstone and carbonate communities. Geol. Soc. Lond. Spec. Publ. 435(1), 1-31.

Wu, H., Pollard, D.D., 1992. Propagation of a set of opening-mode fractures in layered brittle materials under uniaxial strain cycling. Journal of Geophysical Research: Solid Earth 97, 3381–3396. https://doi.org/10.1029/91JB02857

Xu, P., Yu, B., 2008. Developing a new form of permeability and Kozeny–Carman constant for homogeneous porous media by means of fractal geometry. *Advances in water resources*, *31*(1), 74-81.

Young, R. A., Slatt, R. M., Staggs, J. G., 2003. Application of ground penetrating radar imaging to deepwater (turbidite) outcrops. *Marine and Petroleum Geology*, *20*(6-8), 809-821.

Zoback, M. D., 2010. *Reservoir geomechanics*. Cambridge University Press.

Zuluaga, L. F., Fossen, H., & Rotevatn, A. (2014). Progressive evolution of deformation band populations during Laramide fault-propagation folding: Navajo Sandstone, San Rafael monocline, Utah, USA. Journal of Structural Geology, 68, 66-81.

Zuluaga, L. F., Rotevatn, A., Keilegavlen, E., Fossen, H., 2016. The effect of deformation bands on simulated fluid flow within fault-propagation fold trap types: Lessons from the San Rafael monocline, Utah. *AAPG Bull*. *100*(10), 1523-1540.